PART FOUR OF THE RHODES UNIVERSITY SKYMAP PROGRAM

THESIS
Submitted in Fulfilment of the
Requirements for the Degree of
MASTER OF SCIENCE
of Rhodes University

by
MICHAEL ROBERT WRIGHT

January 1989

This work is dedicated to

the true Master of Science and

Creator of the universe,

Jesus Christ.

Acknowledgements

There are a great many people to whom thanks are due for help, encouragement and support during the course of my work.

I am most grateful for the help and guidance afforded me by my supervisors, Professor E. E. Baart and Justin Jonas. Justin's "on-the-spot" advice and explanations were always most welcome.

For the use of the facilities at the Hartebeesthoek Radio Astronomy Observatory, thanks are due to the Director of the Observatory, Dr. G Nicolson.

I am indebted to the Department of Physics and Electronics of Rhodes University for the use of the word processor and laser printer used to produce the text and maps of this thesis.

Special thanks must go to my parents for their continual encouragement and for the financial assistance which they freely offered.

Finally, I would like to express my extreme appreciation to my wife, Diane, for her unfailing support, encouragement and love.

Michael Wright

Contents

List of Illustrations

List of Tables

Abstract

The results of the fourth part of the Rhodes University Skymap Program are presented. The observations cover the area of sky between right ascension $14^h\ 00^m$ and $02^h\ 30^m$ and declination -26° and +13° at a frequency of 2.3 GHz. Contour maps of this region, with a resolution of 0.38°, are presented.

Various methods of reducing the effect of the Galactic disc emission are analyzed. The results demonstrate the effectiveness of one of these methods in the production of a flat base level.

The filamentary structure of the North Polar Spur is enhanced and results are obtained which support current theories of the origin of this object. The HII region surrounding ζ Ophiuchi is examined in detail. A number of parameters are derived for the HII region. The spur associated with the HII region S54 is also examined.

A listing of 1105 point sources appearing in the maps is presented. The limiting flux density of this listing is 0.5 Jy.

Chapter One - Introduction

Since the earliest days of radio astronomy, numerous large-scale surveys of the whole sky or a major part of the sky have been carried out. The first such survey was undertaken by Grote Reber at a frequency of 160 MHz, and the resulting maps were published in The Astrophysical Journal for November 1944. Since then, maps have been published at frequencies ranging from as low as 30 MHz to as high as 5000 MHz. However, the trend in more recent years has generally been away from large-scale maps, since radio astronomers are continually striving for higher resolution and higher quality radio images of small-scale sources. To this end, individual radio telescopes have become large and unwieldy when it comes to large-scale mapping, the emphasis being placed on small-scale observations. Also, many telescopes have been included or are being built for inclusion in radio interferometer systems (again aimed at an improvement in resolution), allowing little or no opportunity for the more time-consuming large-scale mapping projects.

One of the major problems with small-scale maps of individual sources is that, if any large-scale structure were evident in the initial map, it would be subtracted out as part of the background. One of the major results of large-scale surveys is that they allow structure, such as large radio loops and spurs, to be seen where no structure appears on the small-scale maps. However, even in the case of large-scale maps the resolution is important. Thus, there is a need for large-scale maps of the sky with higher resolution to study the known large-scale structure and detect new structure. This, along with the availability of a suitable telescope, prompted the Rhodes University Radio Astronomy Research Group to embark on a new 2.3 GHz southern sky survey - hereafter referred to as Skymap.

Since the inception of the Rhodes University Skymap Program, a relatively large percentage of the southern sky and a small amount of the northern sky has been mapped at 2.3 GHz. The first part of the Skymap program consisted of a region containing the Magellanic Clouds (Mountford *et al* 1987). The second part of the program covered the region from $12^h\ 00^m$ to $22^h\ 04^m$ in right ascension and -24° to -63° in declination (Jonas 1982, Jonas *et al* 1985). This region included a large part of the

southern Milky Way, including the Galactic centre. The third part of the Skymap program included the region of sky at lower right ascensions than Jonas' region, while keeping within the same declination bounds (Woermann 1988). This region also contains a large part of the southern Milky Way, including the Vela supernova remnant and the Gum nebula region.

This thesis presents the results of the fourth part of the Rhodes University Skymap Program. Chapter Two briefly describes the telescope and observing method used to obtain the data for this region and discusses the initial stages of the data reduction. Many of the large-scale sources have a very low intrinsic brightness. This fact presents many problems when it comes to observations made close to the Galactic plane since the Galactic disc emission is very overpowering and tends to hide the low-level, large-scale structure. Chapter Three discusses a number of methods by which the Galactic disc emission may be removed - some more effective than others. The most effective method for most applications is described in a little more detail, and the results of this method are presented.

As with most astronomical observations, the results of observation of particular sources or structure within the map and comparison of such structure with other observations quoted in the literature are interesting and important. Chapter Four deals with a number of specific objects that appear on the maps of this region, as well as mentioning other objects which could bear further investigation. Appendix One contains a series of contour maps covering the survey region, while Appendix Two contains contour maps of the North Polar Spur region after the subtraction of the Galactic disc emission. Appendix Three discusses in some detail the sources used to calibrate the data and Appendix Four contains a listing of 1105 sources with flux densities greater than 0.5 Jy.

A discussion of the results of the survey is presented in Chapter Five. The validity of the Galactic disc emission removal procedures is discussed and suggestions for possible improvement are made. The results of this part of the Skymap survey have again proven the importance of medium resolution, large-scale surveys with regards the understanding of our Galaxy.

Chapter Two - The Telescope and Observations

This chapter describes the telescope and discusses the observing method used to produce the maps (see Appendix One) of the fourth part of the Rhodes University Skymap Program. Section 2.1 briefly discusses the telescope used in the survey along with the associated apparatus used to gather and store the data. Section 2.2 discusses the methods used to guide the telescope through an observing session and the method for the initial processing of the data is explained. A grey-scale image of the raw map is presented at the end of Section 2.2.

2.1 - The Observing Apparatus

The observations for the fourth part of the Rhodes University Skymap Program were made over the period from the beginning of July to the middle of August 1986. A total of seventeen nights were used to observe the whole area of sky included in the contour maps in Appendix One. These observations were carried out using the 26m telescope of the Radio Astronomy Observatory at Haartebeesthoek. The observatory is run by the South African National Institute for Telecommunications Research and operates receivers at four frequencies, the 2.3 GHz receiver being used for this project. Reasons for the choice of this receiver for the survey are that it has good properties for large scale mapping and no other survey has been carried out at this particular frequency. The antenna, receivers and other related apparatus have been discussed in detail by various members of the staff of the Radio Astronomy Observatory. Jonas (1982) has described the apparatus that is relevant to the Skymap observations, and so this section is only included for the sake of completeness, most of the factual information being taken from Jonas' thesis.

2.1.1 - The Antenna

The antenna at the Radio Astronomy Observatory is a parabolic Cassegrain reflector with a diameter

of 26 meters. It is mounted equatorially, resulting in one axis of rotation corresponding to right ascension and the other axis corresponding to declination. The antenna is capable of being driven at high speeds ($0.5°s^{-1}$ in declination) allowing large areas of sky to be covered in a short space of time. To ensure that the observed brightness distribution is oversampled, a scan spacing of 0.1° is sufficient, again allowing large areas to be mapped in a short space of time. The resolution of the antenna at 2.3 GHz (the half-power beam width) is 20′ of arc. All of these properties are ideal for large scale mapping.

The driving of the antenna is controlled automatically by a Hewlett-Packard 21MX minicomputer. The program used in the control, STEER, updates the position of the antenna every 100 milliseconds. To ensure safe control of the antenna, STEER continually checks that the coordinates of the antenna are within the safe operating region of the antenna. STEER receives its commands from a program called COMND. STEER and COMND are the two main programs involved with driving the antenna.

2.1.2 - The Receiver and Radiometer

The 2.3 GHz receiver at the Radio Astronomy Observatory is a cryogenically cooled, Gallium Arsenide field-effect transistor (GaAsFET). It has a low noise temperature and good gain stability. These two properties are also suitable for large scale mapping, the low noise allowing shorter integration times to produce a desired signal to noise ratio and the gain stability minimising unwanted variations in the radiometer output during an observing session.

The radiometer output is proportional to any change in the noise temperature and independent of any changes in system gain or bandwidth. The system temperature, T_e, recorded by the radiometer is given by the following expression (Jonas 1982)

$$T_e = T_{cosmic} + T_b + T_{terr} + T_{loss} + T_{fet} + T_{mix} / G_{fet} \quad \ldots\ldots 2.1$$

where T_{cosmic} is the temperature of the cosmic background, T_b is the temperature of radio sources, T_{terr} is the contribution from terrestrial sources such as the atmosphere and antenna spillover, T_{loss} is the attenuation in the system, T_{fet} is the noise temperature of the GaAsFET, T_{mix} is the noise temperature of various other stages of the receiver (mainly from the mixer) and G_{fet} is the gain of the GaAsFET. Each of these contributing temperatures (except for the first two) must be kept as stable as possible if-a stable baseline is to obtained at the output. The only control available over T_{terr} is to ensure observations are carried out during cloudless nights. T_{loss} is kept stable by keeping the feed cone of the antenna constant to within two degrees Celsius. T_{fet} is dependent on the physical temperature of the GaAsFET, hence the cryogenic cooling. The last term in equation 2.1 is minimal due to the high value of G_{fet}.

The r.m.s. noise temperature, or minimum detectable temperature, for the radiaometer is given by (Nicolson 1970)

$$dT_e = 2T_e(1 + T_e/T_n)/(2B\tau)^{0.5} \quad \ldots\ldots 2.2$$

where T_n is the noise temperature of the noise diode, B is the system bandwidth and τ is the post-detection time constant. For these observations, the bandwidth was approximately 38.5 MHz, the noise temperature of the noise diode was about 71K and the system temperature was 41.1K. Thus, the minimum detectable temperature was about 14.8 mK, assuming τ to be 1 second.

The output of the radiometer is connected to a computer-controlled, integrating digital voltmeter, allowing a sampled radiometer output to be recorded on magnetic tape, along with coordinate and other relevant information.

2.2 - The Observations

In order to obtain the observations presented in this thesis, a particular observing method was used.

This method has been discussed by Jonas (1982) in some detail and, as with the previous section, is included for completeness.

2.2.1 - The observing method

The observations presented in this thesis were obtained by a scanning technique, scanning taking place in declination while the right ascension remained constant. Scanning proceeds alternately in both directions - that is, one scan proceeds from south to north (up scan) and the next scan proceeds from north to south (down scan). The rotation of the celestial sphere is used to advance the right ascension for each scan. Due to the form of the observations (up-down-up-down...), one nights observation is called a raster.

As was mentioned in the previous section, the contribution to the system temperature due to terrestrial noise cannot be controlled - the atmosphere cannot be removed for the benefit of radio astronomers! However, constraints can be placed on the observing method to minimize this contribution, or at least to keep the contribution stable so that it may be subtracted out of the data at a later stage. The terrestrial noise contribution is a function of antenna altitude, a fact which suggests a simple constraint on the observing method. If the individual scans can be organized in such a way that the antenna tracks the same path in the altitude-azimuth or hour angle-declination plane, the terrestrial noise contribution will be the same for each scan. Since the hour angle is different for the up and down scans, the terrestrial noise contribution will be different for scans in opposite directions, but the same for scans in the same direction.

The separation between the up and down scans of a single raster is 0.8° for the observations presented here. Therefore, in order to obtain the 0.1° scan separation mentioned in the previous section, it was necessary to observe eight rasters, each raster being shifted 0.1° in right ascension from the previous raster. Since adjacent scans are independent of each other, systematic effects are reduced. Each raster was observed twice to ensure reliable data and to increase the signal to noise ratio. Thus, a minimum of 16 nights of observation were required to obtain the data for the map

presented in Appendix One. One raster was observed three times due to the fact that one of the nights had interference caused by the moon. This interference is evident in some of the grey scale images presented in the thesis as a relatively small (about 3°) circular region crossed by lines in the direction of the scans. Therefore, the number of nights of observations totalled to 17.

2.2.2 - Preliminary data reduction

In order to obtain a complete map of the scanned area, the individual rasters need to be combined together. However, before this can be done, a number of preliminary steps have to be completed. These steps fall into three categories: binning and reformatting, drift removal and removal of the terrestrial contribution to the system temperature. The preliminary data reduction was performed on the Rhodes University C.D.C. CY-825 (Cyber) computer. Further data reduction (to be discussed in Chapter Three) was performed on the Rhodes University Physics Department VAX-11/730 (VAX) minicomputer.

The first step in the processing of the raw data is to convert the ASCII contents of the tapes to six bit CDC characters. The data in the resulting CDC character file are then binned into 0.1° declination bins with one record per scan. Two records associated with each record of binned data contain the average right ascension deviations for each bin and the number of samples that went into each bin. Each record also contains important information such as observation number and starting right ascension.

The next step in the processing involves the removal of a background or base surface from each observation. There are two stages to this step - the removal of the terrestrial background and the removal of drift. The terrestrial background contribution is declination dependent since the antenna tracked through 39° of declination for each scan while tracking a constant right ascension. The drift is right ascension dependent since it is caused by factors such as the gradual cooling of the telescope environment during a nights observation. This causes the right ascension temperature cross section to gradually diminish throughout the night. Figure 2.1 gives an indication of the effects of the

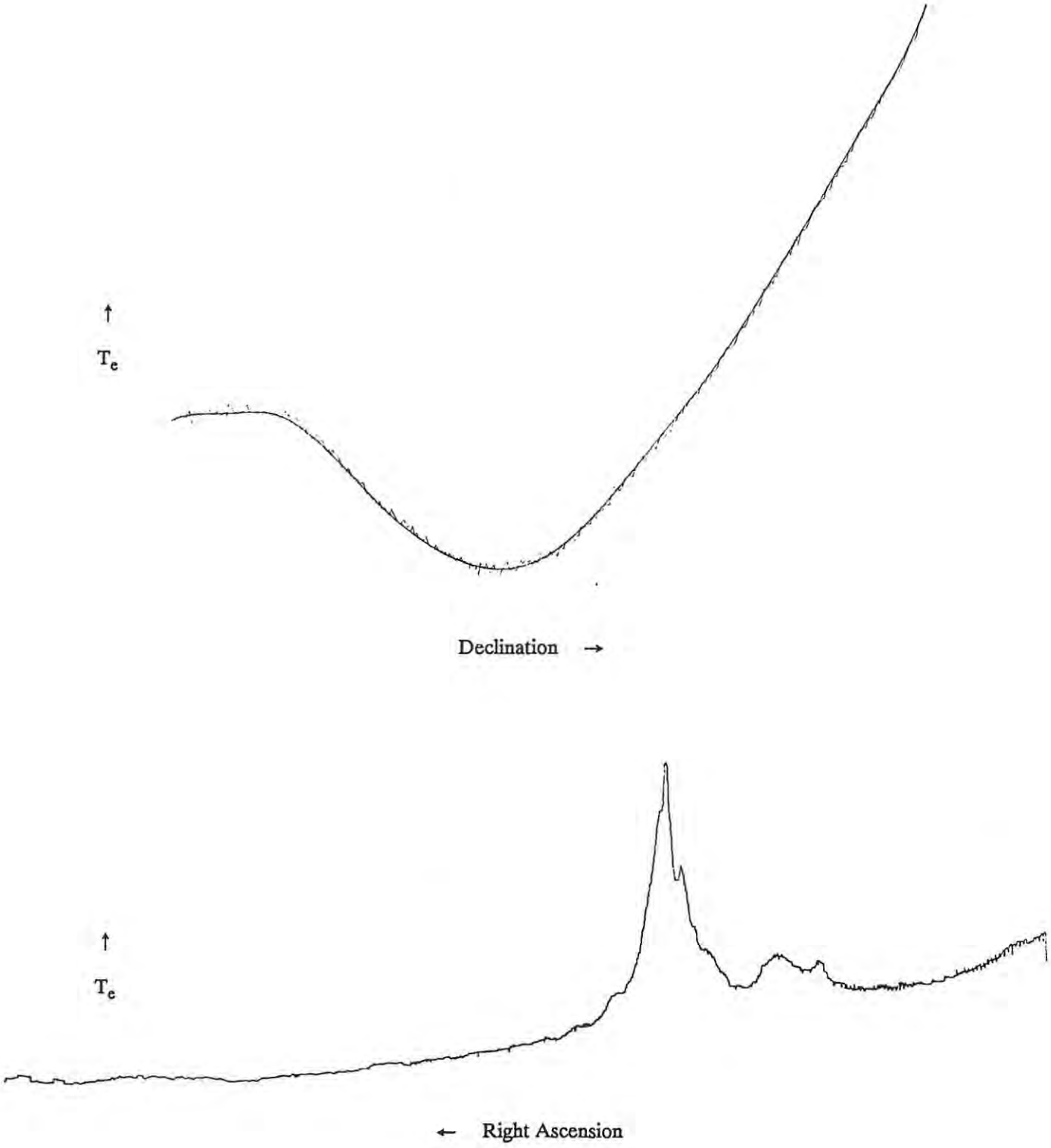

Figure 2.1 - Typical profiles of the terrestrial background contribution to the system temperature and the drift (top and bottom respectively).

terrestrial and drift contributions.

In order to model the terrestrial background component, scans from the same observation and in the same direction are treated as groups (ie - up scans and down scans), and the scans in each group are assumed to have the same background (see the previous section). The terrestrial background is then modelled by taking the tenth lowest sample at each declination and fitting a cubic spline to these points to produce a smooth background. This background profile is then subtracted from the relevent scans in the relevent observation.

The drift contribution is removed interactively. The drift removal program requires the user to indicate specific points on a cross section, such as that shown in Figure 2.1, which it assumes are representative of the drift for that cross section. The program then fits a smooth curve to these points, the curve being a combination of two exponential functions. When the user is happy that the fitted drift profile is reasonable, the profile is subtracted from the data.

On completion of the background and drift removal procedures, an essentially flat surface remains. The final step, therefore, is to combine the rasters together to produce the completed raw map. This involves creating a rectangular grid of temperatures from the binned data. The raw map is written to magnetic tape in a format readable by the VAX. All further processing and enhancement of the data takes place on the VAX.

Appendix One contains a contour map of the raw data smoothed to a half-power beam width of 0.38° and precessed to epoch 1950.0 coordinates. Figure 2.2 is a grey-scale image of the same smoothed data and effectively demonstrates the overwhelming contribution of the Galactic disc emission. Note that this grey-scale image does not cover the whole area surveyed, but only the region of the plane. The contour levels on the overlay are 350mK, 500mK, 750mK, 1K, 1.5K, 2K, 3.5K, 5K, 10K, 20K, 35K and 50K. The enhancement of small scale structure near the Galactic plane by the removal of this Galactic disc emission is discussed in the next chapter. In Chapter 4, a number of results of the Galactic disc removal are discussed.

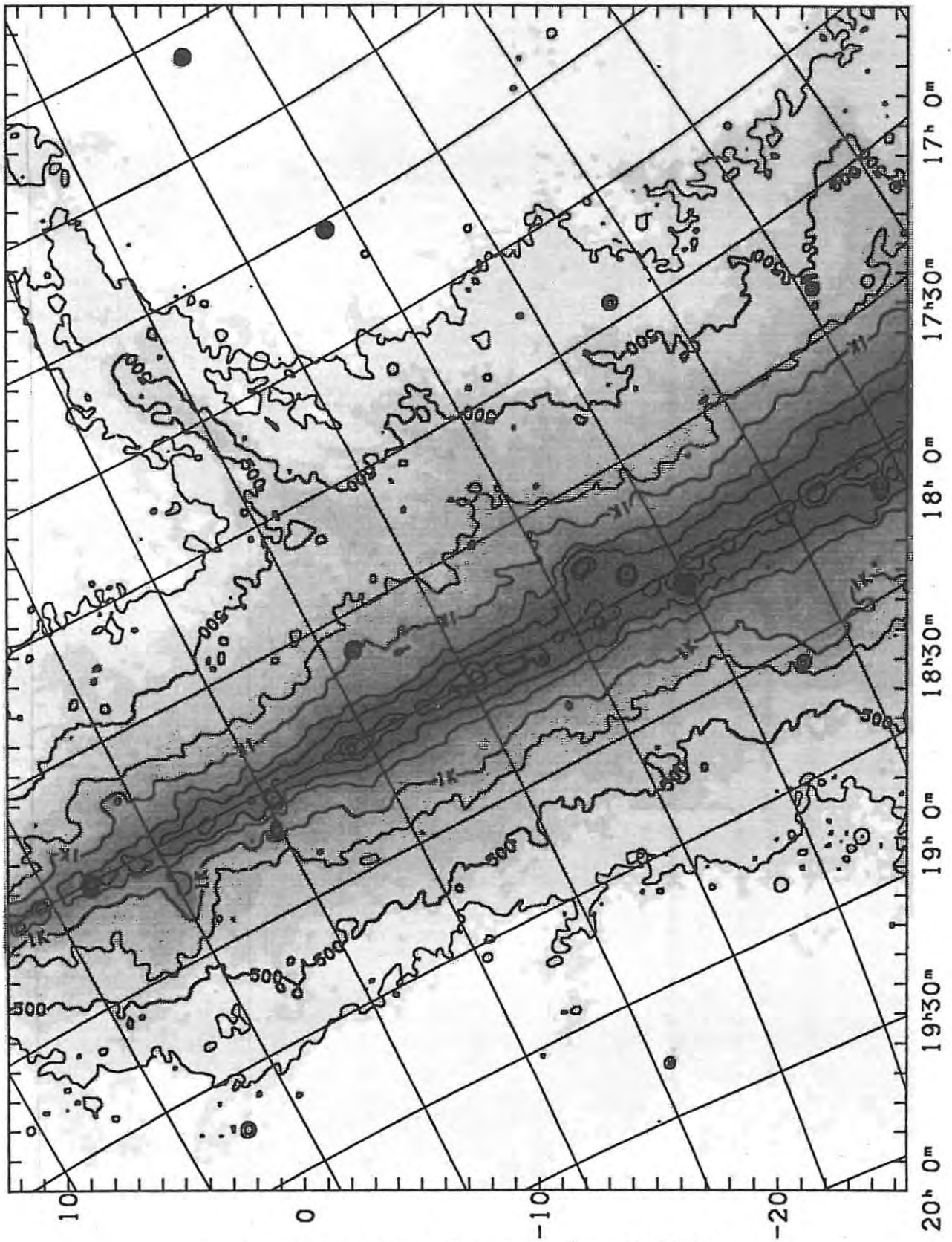

Figure 2.2 - Grey-scale image of the raw map presented in this thesis.

Chapter Three - Galactic Disc Emission Removal

On completion of the initial data processing described in the previous section, a raw map of the surveyed region was available. In the original epoch of the observations (1986.5), the region fell between $13^h\ 58^m\ 48^s$ and $2^h\ 00^m$ in right ascension, passing through $0^h\ 00^m$, and between -26° and 13° declination. The maps of the raw data presented in Appendix One fall between $13^h\ 56^m\ 48^s$ and $2^h\ 28^m\ 24^s$ right ascension, and -26° 12′ and 13° 12′ declination due to the fact that they have been precessed to 1950.0 coordinates. In its raw form, this map is of little use as far as measurements of flux density of sources is concerned.

Cutting across this map (and clearly visible in both the grey-scale image of figure 2.2 and the contour maps of Appendix One) is a 45° strip of the Galactic plane. The effect of the Galactic plane is very clear - it is first thing one sees when looking at figure 2.2 and, due to its presence, other sources apppear to get lost in its overpowering emission. An ideal example of this is the north polar spur, a radio loop which does not appear to be swamped by the disc emission. It can be seen in figure 2.2 apparently emerging from the disc emission and moving towards the top right of the image. This feature will be discussed in detail in a later chapter, but an important point to note at this stage is that, on removal of the Galactic disc emission, the north polar spur can be traced to within 3° of the plane of the Galaxy. This means that in figure 2.2, about 10° of the spur is apparently lost in the disc emission.

Like the moon in the visual astronomer's night sky, the Galctic plane can either be a blessing or a curse to radio astronomers. If one is interested in studying the Galactic plane itself, the relative brightness of the plane is a blessing. However, if one is interested in studying the fine detail of individual sources near the plane, the disc emission just interferes. One of the primary objectives of the research discussed in this thesis is to remove the interfering disc emission in such a way as to enhance small-scale structure located within a few degrees of the plane and, more importantly, to enhance low-brightness, large-scale structure in the region of the plane. The aim is, of course, to

model the plane in such a way that, on subtraction of this model from the raw map, any structure not directly associated with the disc emission (for example, the north polar spur) will remain totally unaffected by the process of disc emission removal.

In this chapter, four methods of disc emission removal will be described and discussed. All of these methods can be credited with some merit, but three of them also have major areas of weakness. Therefore, one method (the most promising one) is discussed in a little more detail than the others, and it is this method which is used in the following chapters. In section 3.1, the model of Flanagan (1981) is discussed followed by a discussion of Wright's (1985) model in section 3.2. The model of Sofue and Reich (1979) is discussed in section 3.3. The model discussed in section 3.4 is, in many respects, similar to Flanagan's model and could be termed an extension of this model. The results of this model are presented in section 3.5. Note that throughout this thesis, and especially throughout this chapter, the terms "Galactic plane", "plane", "Galactic disc emission" and "disc emission" are used extensively. Even though the first two terms refer more to the general physical structure of the plane, they are often used to refer to the Galactic disc emission.

3.1 - Plane Modelling by Fitted Gaussians

The first method of disc emission removal was investigated by Flanagan (1981) for her Honours project at Rhodes University. She tested her method on the data of the second part of the Skymap survey.

Method one involves the modelling of the Galactic disc emission by a series of Gaussian profiles fitted to constant-longitude cross-sections of the plane. The reason for the choice of Gaussians becomes evident upon examination of cross-sections of the plane (see, for example, figure 3.1) - the plane appears as a sharply defined ridge, peaking at approximately 0° Galactic latitude, initially falling away sharply, and then after a few degrees on either side of the plane, beginning to level off to eventually merge with the cold sky far from the plane. However, as was stated by Flanagan, it is

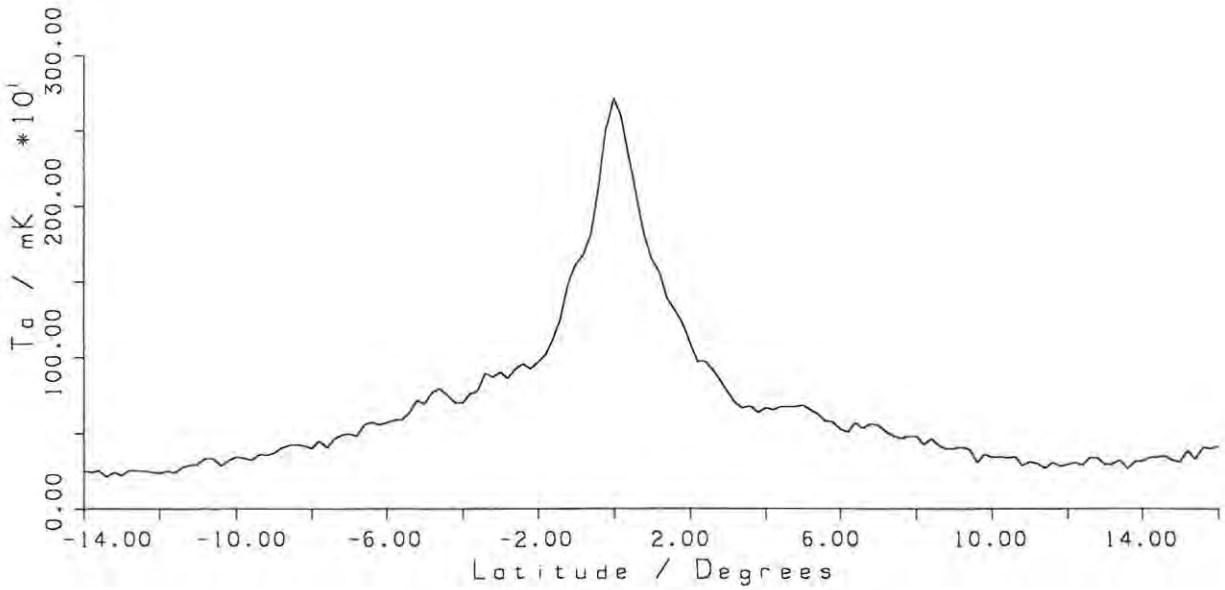

Figure 3.1 - Cross-section of the Galactic plane through longitude 32.5°. Cross-sections such as this can be modelled fairly accurately by Gaussian profiles.

apparent that a single Gaussian profile will not accurately model the disc emission at all latitudes - close to the plane the Gaussian would have to be very steep, but this would not adequately model the gradual decline of brightness even 10° on either side of the plane. A more accurate model may well be obtained by combining a steep, high Gaussian and a wide, low Gaussian. Flanagan's model, however, made use of one low, wide Gaussian with the aim of enhancing structure away from the plane but still within the influence of the disc emission. In order to fit the profiles to the cross-sections, a series of points defining a lower envelope for each cross-section were specified. The resulting Gaussian profile was then lower than the data points at all latitudes. In order to create a surface, a number of profiles were produced by the use of a running minimum over 2° (1° on either side of the current cross-section). The result was a series of profiles spaced at approximately 1° intervals. In order to smooth the final base surface, each profile was replaced by a running mean of three profiles. The final base surface was produced by linear interpolation between the profiles.

There are a number of improvements which could be made to this method which would increase its degree of usefulness. As mentioned before, a more accurate representation of the disc emission

could be obtained by the use of more than one Gaussian in modelling a profile. Also, the lower envelope for the Gaussian fitting routine was too low, resulting in disc emission still being present in the final map. These and other improvements could quite easily be made to method one, but one major problem with the method still exists - by assuming that the cross-section of the Galactic plane has the form of a Gaussian, one is assuming an idealized situation. There is no physical reason why the cross-section should have this or any other symmetric, well-defined form since there are many irregularities in the Galactic plane. Therefore, another more practical method needs to be sought.

3.2 - Removal of Disc Emission from Localized Areas

Method two was investigated by Wright (1985 - hereafter referred to as paper 1) for his honours project at Rhodes University. Again, the data from part two of the Skymap program was used to test this method. The major difference between methods one and two is that method two does not take into account the Galactic disc emission as a whole when defining a base surface. In fact, method two is primarily suited to the investigation of small-scale sources, large-scale structure being effectively subtracted out as part of the disc emission.

In method two, a box is defined around a specified source, the box size and source position both being input parameters, and a base surface is subtracted from the box. This base surface is dependent only on the data contained within the boundaries of the box. The method used in paper 1 to define the base surface was simply to linear interpolate between the left and right edges of the box.

There are numerous problems associated with this method of disc emission removal, as was pointed out in paper 1. The major problems may be summarized as follows:

1. The box size must not be too small otherwise some of the source being investigated will be chopped off. Neither must the box be too large otherwise nearby sources will be included within the boundaries of the box and will start to interfere. The problem with this is that, in some cases, nearby sources are too close to the source under

investigation not to be included in the box, and their influence is clearly seen in the resulting base surface.

2. Localized variations in the Galactic disc emission are not taken into account in this method.

3. Linear interpolation is far from ideal in the production of a base surface, especially when the effects of nearby sources are considered.

Since this method is not suitable in the present context, due to the fact that it eliminates low-level, large-scale structure, it is not considered as a viable method, and no further use of this method is discussed.

3.3 - Plane Modelling by Convolution

This method was developed by Sofue and Reich (1979) in order to remove the Galactic disc emission from their 1420 MHz data of the north polar spur. Their aim was to investigate the extension of the north polar spur toward the plane (recall a previous statement made in this thesis to the effect that the north polar spur can by traced to within 3° of the plane).

Method three involves the production of a smooth model of the disc emission by convolution of the raw data with a Gaussian beam of specified half-power beam width. Since this method was investigated in detail and tested on the Skymap data, it is described in detail here. Let the original raw map of antenna temperatures be referred to as T_a. This data set is convolved with a Gaussian beam of user specified half-power beam width - in the case of the Skymap processing, the half-power beam width was chosen to be 2° by trial and error. Since the Gaussian is the key to this method, it is vitally important that the right half-power beam width is chosen. If this value is too small then the resulting plane model will have too much small-scale structure still evident. If the value is too large, the peak intensity of the disc emission will be smoothed too much and will eventually result in sources close to the plane being subtracted away with the disc emission. Let the data set remaining

after convolution be called $\overline{T_a'}$.

From these two maps, a map of residual temperatures is formed according to the expression

$$\Delta T_a' = T_a - \overline{T_a'} \qquad \ldots\ldots 3.1$$

These residual temperatures represent small-scale structure in the original map, but due to the smoothing effect of the Gaussian convolution, much of the small-scale structure has been subtracted out of the map. Figure 3.2 demonstrates this fairly clearly. The top diagram shows a latitude scan of the original data at 18.5° longitude. This cut was chosen as an example specifically due to the large off-plane source, Sharpless 54 (Messier 16), which peaks at latitude 2°. The middle diagram shows a latitude scan of the resulting plane model after convolution with a 2° beam. Note that S54 has caused the plane model at this point to extend towards positive latitudes, resulting in (bottom diagram) S54 being cut off at its base. Note also that, in the bottom diagram, small-scale structure away from the plane is almost non-existent and, more specifically, within about 6° of the plane, all but the strongest structure has been subtracted away completely. This is due to the smoothing effect of the convolution method on the strong peak of the Galactic disc emission itself. As will be explained below, the effect of strong discrete sources such as S54 can be minimized in the final version, but the effect of the disc emission on structure close to the plane cannot be entirely eliminated in this method.

In order to reduce the effects of strong discrete sources, the whole convolution process must be repeated with the offending strong sources removed. A new map of antenna temperatures, T_a'', is produced according to the following constraints on the residual temperature map:

$$\text{If } \Delta T_a' > 0 \rightarrow T_a'' = \overline{T_a'} \qquad \ldots\ldots 3.2$$

$$\text{If } \Delta T_a' \leq 0 \rightarrow T_a'' = T_a \qquad \ldots\ldots 3.3$$

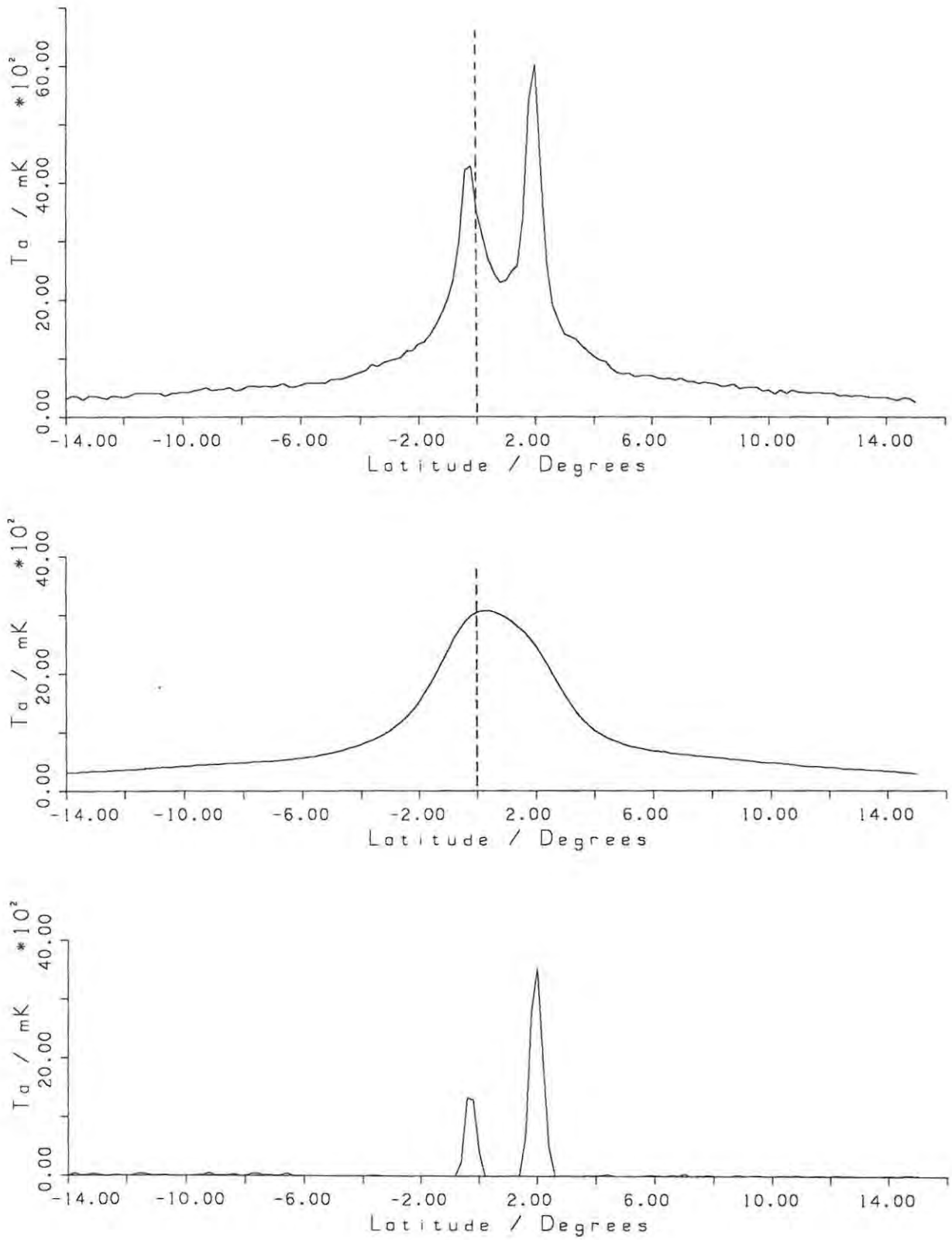

Figure 3.2 - Cross-sections through 18.5° longitude of the original data (top), the plane model (middle) and the residual map (bottom).

Hence, T_a'' is identical to T_a except that all the small-scale structure (including the strong, discrete sources) have been cut off at level $\overline{T_a'}$. This map is now convolved with the same beam as previously to get a new model of the disc emission, $\overline{T_a''}$. Another map of residual temperatures is formed by subtracting the new disc emission model from the original map - that is,

$$\Delta T_a'' = T_a - \overline{T_a''} \qquad .....3.1$$

This process may be repeated a number of times. After each iteration, the model of the disc emission will have improved and the small-scale structure will be less affected by the subtraction of the model from the original data. This is demonstrated in figure 3.3. The top diagram is a latitude scan of the original data with the residual map of the third iteration subtracted. The source S54 is still evident in the asymmetry in the direction of positive latitude, but its effect has been greatly reduced. The middle diagram shows the model of the disc emission obtained by convolving this data by the usual 2° Gausian beam, and the bottom diagram is a scan of the resulting residual temperatures after subtraction of this disc model from the original map. It is clear by comparison of this diagram with the bottom diagram of figure 3.2 that an improvement has been made. Neither S54 nor the strong source situated almost on the plane appear to have been subtracted away, and structure such as the spur emerging from S54 at $\sim 3°$ (see section 4.5 for a full discussion of this spur) is now evident. Note that, as expected, the structure within 6° of the plane has still been over-subtracted.

This method has so far proven to be the most successful method investigated, even though it tends to oversubtract. There is only one major problem associated with the method which lowers its usefulness as far as enhancing small-scale structure is concerned - the smoothing effect of the convolution filtering will always allow some of the small-scale structure and most of the extended structure not associated with the disc emission to be subtracted from the original map along with the disc emission. This problem is especially evident in the data for the fourth part of the Skymap program. Figure 3.4 is a contour plot of the final disc emission model obtained for this region of the sky (note that plot does not include the complete area surveyed, but only the region around the

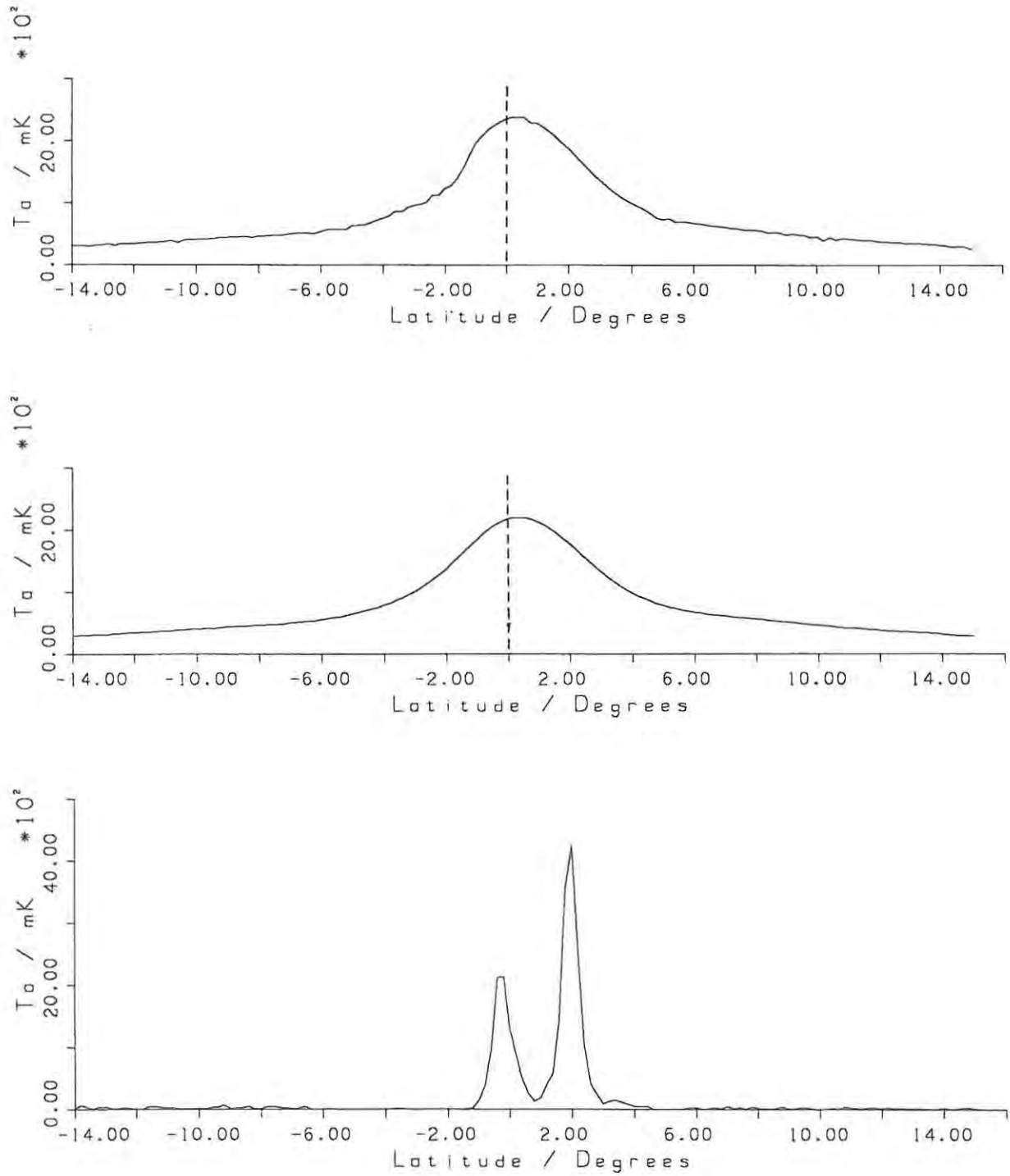

Figure 3.3 - Cross-sections through 18.5° longitude of the original data with the residual temperatures of the third iteration (see text) subtracted (top), the plane model for the above data (middle) and the residual map (bottom).

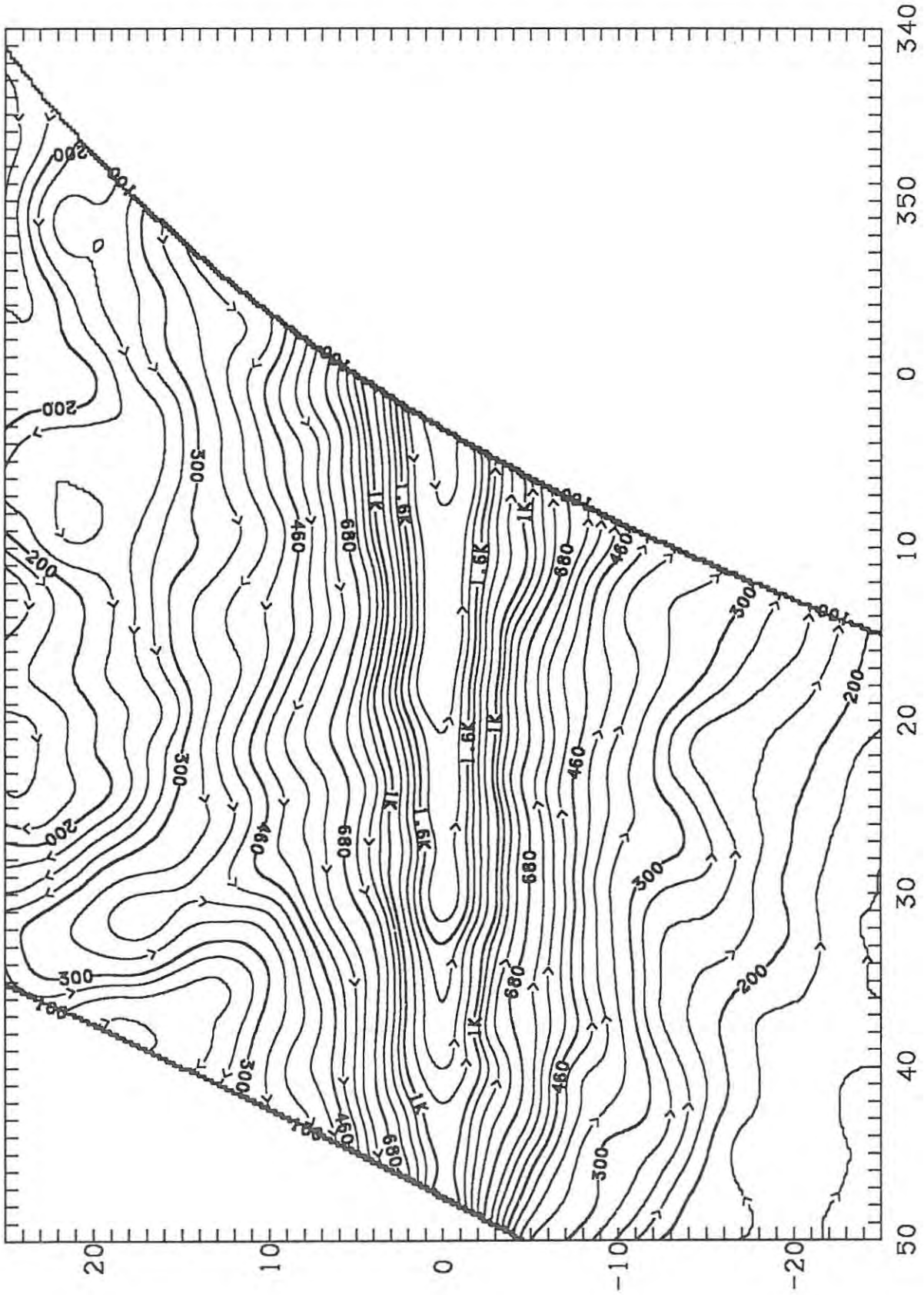

Figure 3.4 - Contour map of the plane model

after four iterations (see text).

Galactic plane). The contours levels are listed in Appendix One. Emerging from the top of the plane, and extending towards the top of the map is clear evidence of the north polar spur. This is a clear indication that there is still a need for an improved method of modelling the disc emission.

3.4 - Plane Modelling using Cubic Splines

The fourth method for the removal of the Galactic disc emission was developed in an attempt to improve upon the three methods already discussed, bearing in mind the problems pertaining to each method. The main objectives in the development of the new method were as follows:

1. A *reasonable* model of the plane must be produced, and not an idealized model in which the cross-sections are Gaussian.
2. The model must affect small-scale structure near the plane (ie - within a few degrees) as little as possible.
3. Any extended features (for example, the north polar spur) must be affected as little as possible.
4. The final model of the plane should not have been affected in any way by strong, discrete sources, such as S54.

It is an obvious statement to say that the Galactic disc emission cannot be stronger at any point on a map than the data value at that point. Figure 3.5 is a section of the Galactic plane ($b_{II} = 0°$) between $l_{II} = 20°$ and 35°. In this section of the plane, the peak at 30.8° is the thermal source W43, while the peaks at 21.9°, 22.7°, 23.5°, 27.3°, 29.7°, 31.9°, 32.9°, 33.6° and 34.8° are all supernova remnants (Clark and Caswell 1976). Other unidentified peaks are more likely to be identified with discrete sources superimposed on the Galactic disc emission rather than small-scale fluctuations in the disc emission itself. The points of interest as regards modelling the plane in this region, however, are the points labelled 1, 2, 3. It is quite safe to assume that the plane does not rise above the level of these points in this section of the plane. Of course, the plane could be substantially lower than this but it would be impossible to determine this from this set of data. Therefore, the dashed line shown

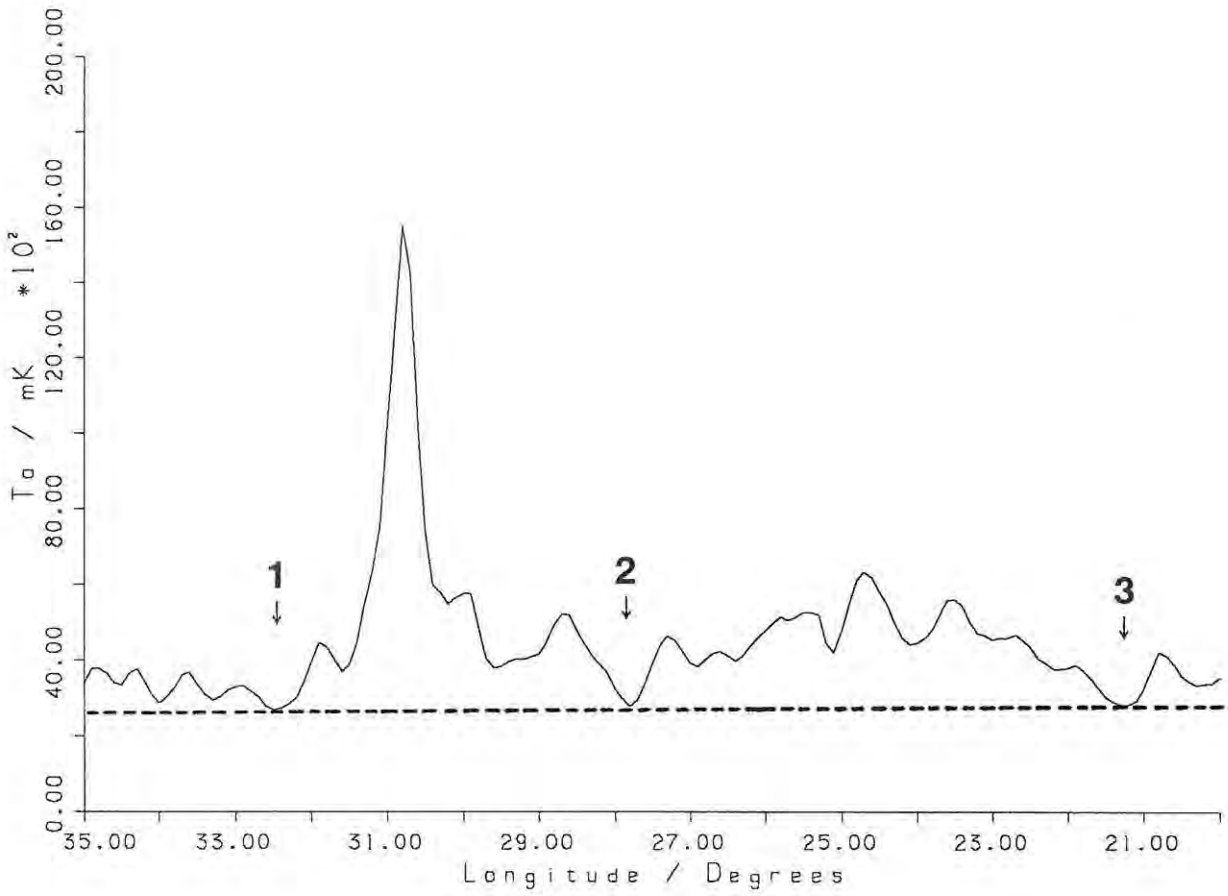

Figure 3.5 - Section of the Galactic plane showing many sources superimposed on an upper limit to the disc emission (dashed line).

in figure 3.5 is probably about as close as one is going to get to modelling the plane in this section. If one were to take a horizontal line through the lowest of these three points (point 1), the result would be just as adequate as the dashed line.

If similar sections were made at other latitudes for the same longitude range as figure 3.5, each one would have a "lowest point" for the disc emission at that particular latitude. These values for the disc emission could then be combined to give a cross section of the disc emission for this longitude range. If the same process is repeated for adjacent sections of the plane, and the resulting cross-sections taken as being representative of the central points of the sections, a simple linear interpolation should produce a very adequate model of the whole Galactic plane.

A simple algorithm to implement this is as follows:

1. Bin the data into 10° (say) longitude bins. Note that the data does not need to be binned in latitude, as each latitude will be considered separately).
2. For each bin: For each latitude, determine the lowest point in longitude.
3. For each bin: The centre of each bin (in longitude) represents the bin as a whole. A cross-section for the bin is obtained by combining all the values obtained in step 2.
4. Perform a simple linear interpolation (or some more complicated interpolation, if desired) between the (centres of the) bins. Extrapolate to the edges of the map is this is necessary. This is the model of the disc emission.
5. Subtract this model from the original data to get a map of small-scale structure.

On initial implementation of the above algorithm it was noticed that the linear interpolation of step 4 introduced rather severe horizontal "scanning" effects. In order to minimize this and obtain a smoother model, a further step is needed between steps 3 and 4 - each of the cross-sections representing each of the bins is smoothed using cubic slines. Originally an attempt was made to fit one cubic spline per cross-section, but this proved to be inadequate due to the fact that the splines could not model the sharp peak of the plane. The most recent version of this method fits two cubic splines to each cross-section - one spline for each side of the peak in the disc emission.

The results of this method are admirable. The method fits a model of the plane to the data without making any assumptions as to the form of the cross-section (ie - whether or not a Gauusian function, or any other function, is a good approximation to the disc emission), thus satisfying the first objective stated above. It also satisfies the other three objectives simultaneously by its method of binning into longitude bins of a specified width and then taking the *lowest* value for each latitude in each bin. Provided the bin width is large enough (the standard width used in the processing of the data presented in this thesis was 10°), no small-scale structure and very little extended structure should be affected in the final map of residual temperatures.

In the following section, some general results of this method are presented. Also, a comparison of the results of this method, method three and method one for a region of the sky falling within the boundaries of the second part of the Skymap survey is presented.

3.5 - Preliminary Results of the Plane Modelling Methods

Of all the disc emission removal methods investigated, method four is by far the most promising. The results obtained from this method are a good indication of the accuracy of the method. Figure 3.6 shows cross-sections of the orignal data (top diagram), the plane model (middle diagram) and the residual temperatures after subtraction of the plane model from the original data. The longitude of these cross-sections is 25°. Note that in the bottom diagram, the effect of the Galactic disc emission appears to have been subtracted away entirely, resulting in a completely flat base level to this cross-section. A comparison of the top and bottom diagrams also shows that the small-scale structure in this region has hardly been affected at all - in fact, a source seems to have appeared where no source was previously visible, peaking at -2.5° (whether or not this is a valid source has yet to be established). Note also that the cross-section of the plane model does not resemble a Gaussian function too accurately - this was to be expected.

In order to compare this method to the method of Sofue and Reich (method three), figure 3.7 contains cross-sections through the same longitude (18.5°) as figures 3.2 and 3.3. In the case of figure 3.7, however, the latitude range is from -30° to 45° in order to show the effects of method four further from the plane. The top diagram is a profile of the original data (identical to the top diagram of

---

Figure 3.6 - Overleaf are cross-sections at 25° longitude of the original data (top), the plane model (middle) and the residual map (bottom).

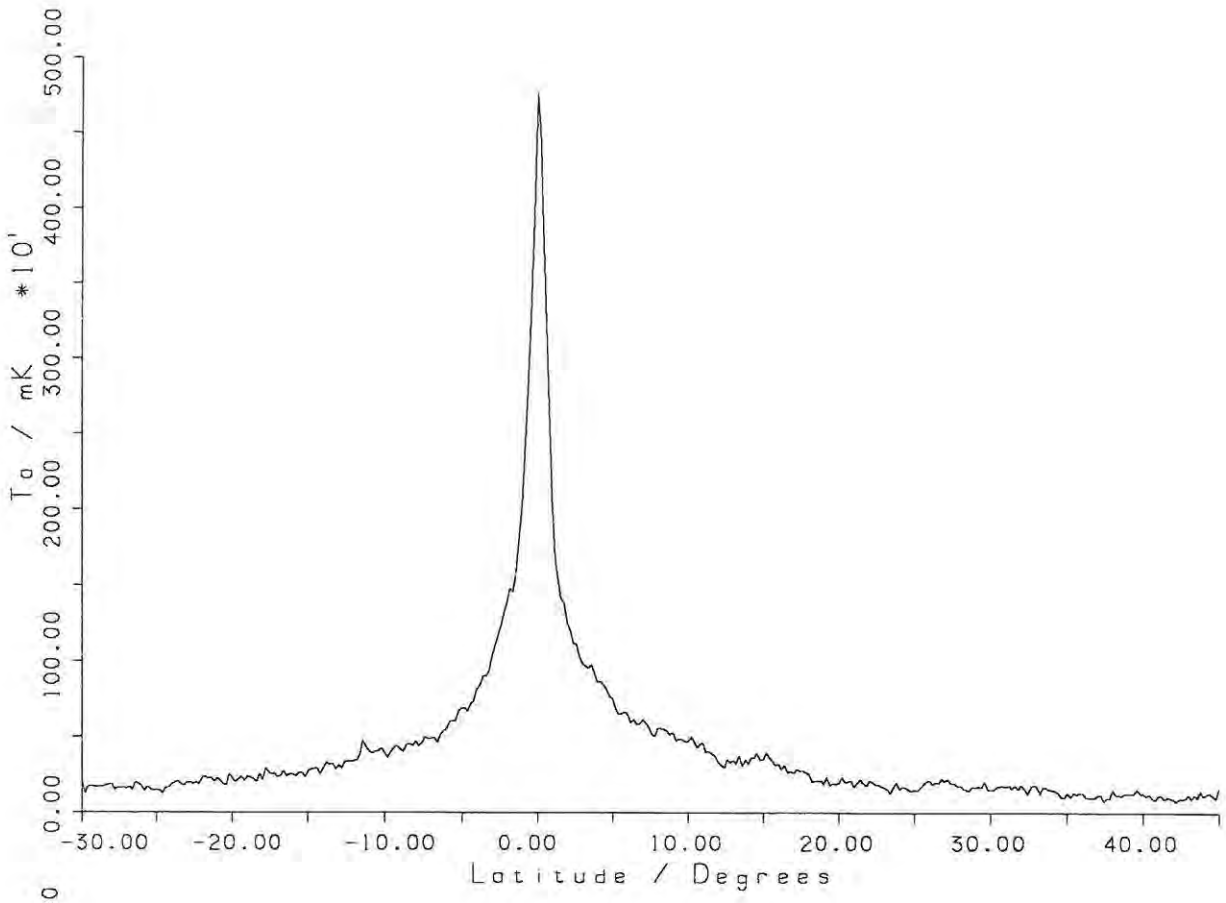
Ta / mK *10'
0.00
100.00
200.00
300.00
400.00
500.00
-30.00
-20.00
-10.00
0.00
10.00
20.00
30.00
40.00
Latitude / Degrees

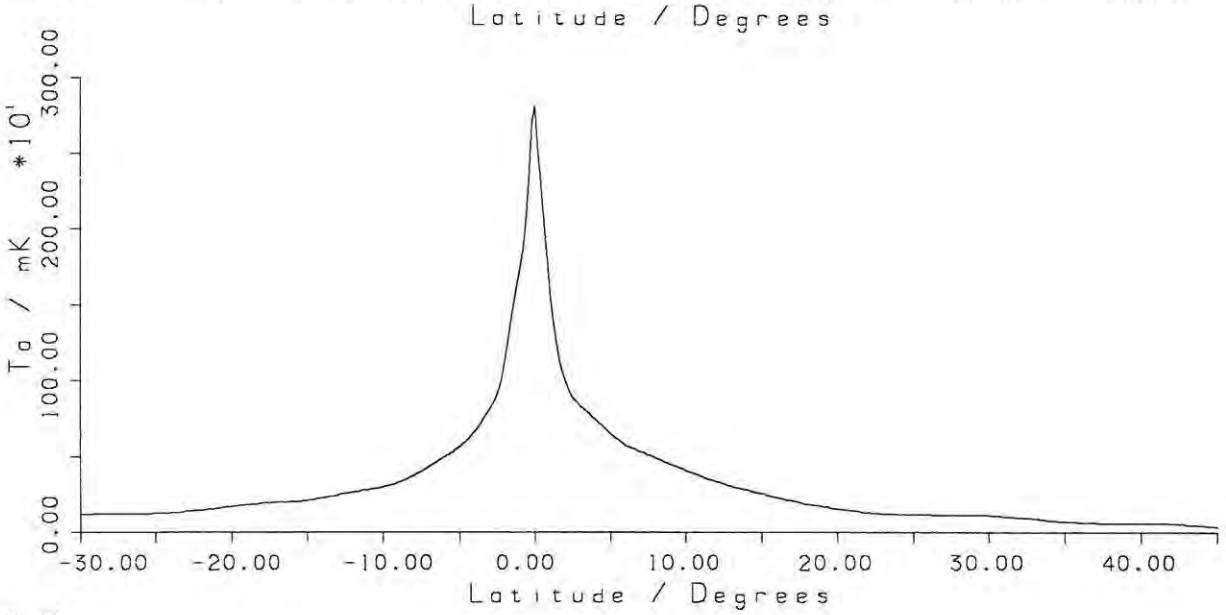
Ta / mK *10'
0.00
100.00
200.00
300.00
-30.00
-20.00
-10.00
0.00
10.00
20.00
30.00
40.00
Latitude / Degrees

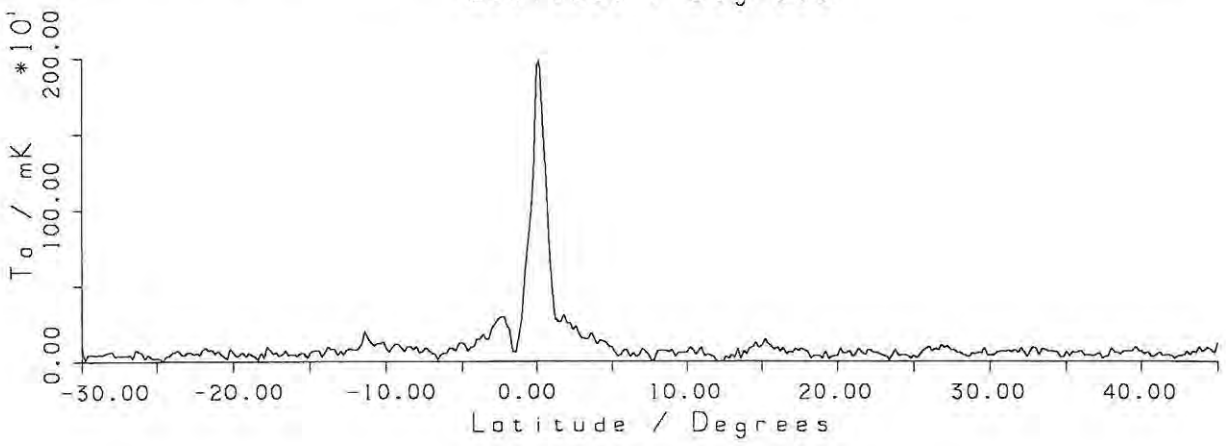
Ta / mK *10'
0.00
100.00
200.00
-30.00
-20.00
-10.00
0.00
10.00
20.00
30.00
40.00
Latitude / Degrees

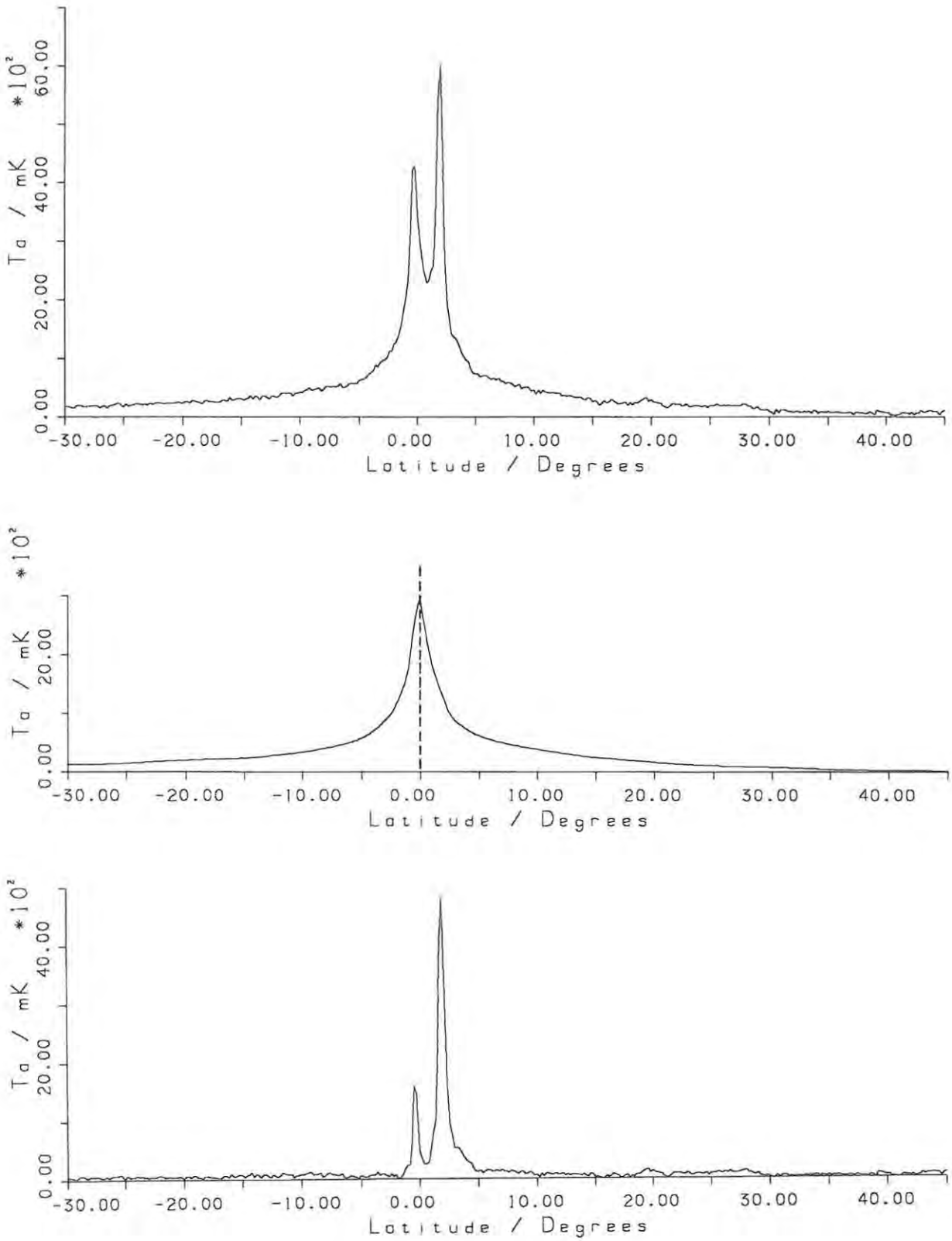

Figure 3.7 - Cross-sections through 18.5° longitude of the original data (top), the plane model (middle), the the residual map (bottom).

figure 3.2, except for the range in latitude), the middle diagram is a profile of the plane model produced by method four, and the bottom diagram is a profile of the residual data after subtraction of the plane model from the original data. Note that the peak of the plane model now occurs at exactly 0°, and there does not appear to be any extension towards positive latitudes due to the presence of the source S54. Again, the small-scale structure seems to be unaffected by the subtraction of the disc emission, and the spur associated with S54 is now clearly visible, apparently being connected to S54 and extending to about 10° latitude.

Shown in figure 3.8 are longitudinal sections of the original data, plane model and residual map through latitude 3.45° (arbitrarily chosen to include the peak of the HII region at longitude 29°). Note that these sections were produced from a map which includes data from parts two, three and four of the Skymap program. The top diagram shows a section through the original map with the section through the plane model shown as the dashed line. Note that the plane model appears to fit the data fairly accurately and only in a small number of cases does it rise above the level of the original data. These factors indicate that the linear interpolation performed between the individual cross-sections in the plane modelling algorithm is quite adequate. The bottom diagram shows a section through the residual map, and again clearly shows that the small-scale structure has not suffered due to the subtraction of the plane from the original data - the peak centred at 18.5° is a cut through the spur associated with the source S54 (mentioned previously).

An interesting comparison can be made between the work of Phillips *et al* (1981) and the current work. Phillips *et al* used the 408 MHz data of Haslam *et al* (1982) to study the large-scale distribution of Galactic synchrotron emissivity. In their work, they removed from their longitudinal profiles of the plane all contributions due to known discrete sources (whether extragalactic or Galactic) and produced a lower envelope of the plane profile. Their figure 1 is shown here in figure 3.9 (top diagram) and is a section through the Galactic plane. The contributions due to known discrete sources have been blacked in and the lower envelope for the plane profile is indicated by the dashed line. In the bottom diagram of figure 3.9, an equivalent section of the Galactic plane from the data sets of the second, third and fourth parts of the Skymap program is shown. The range in

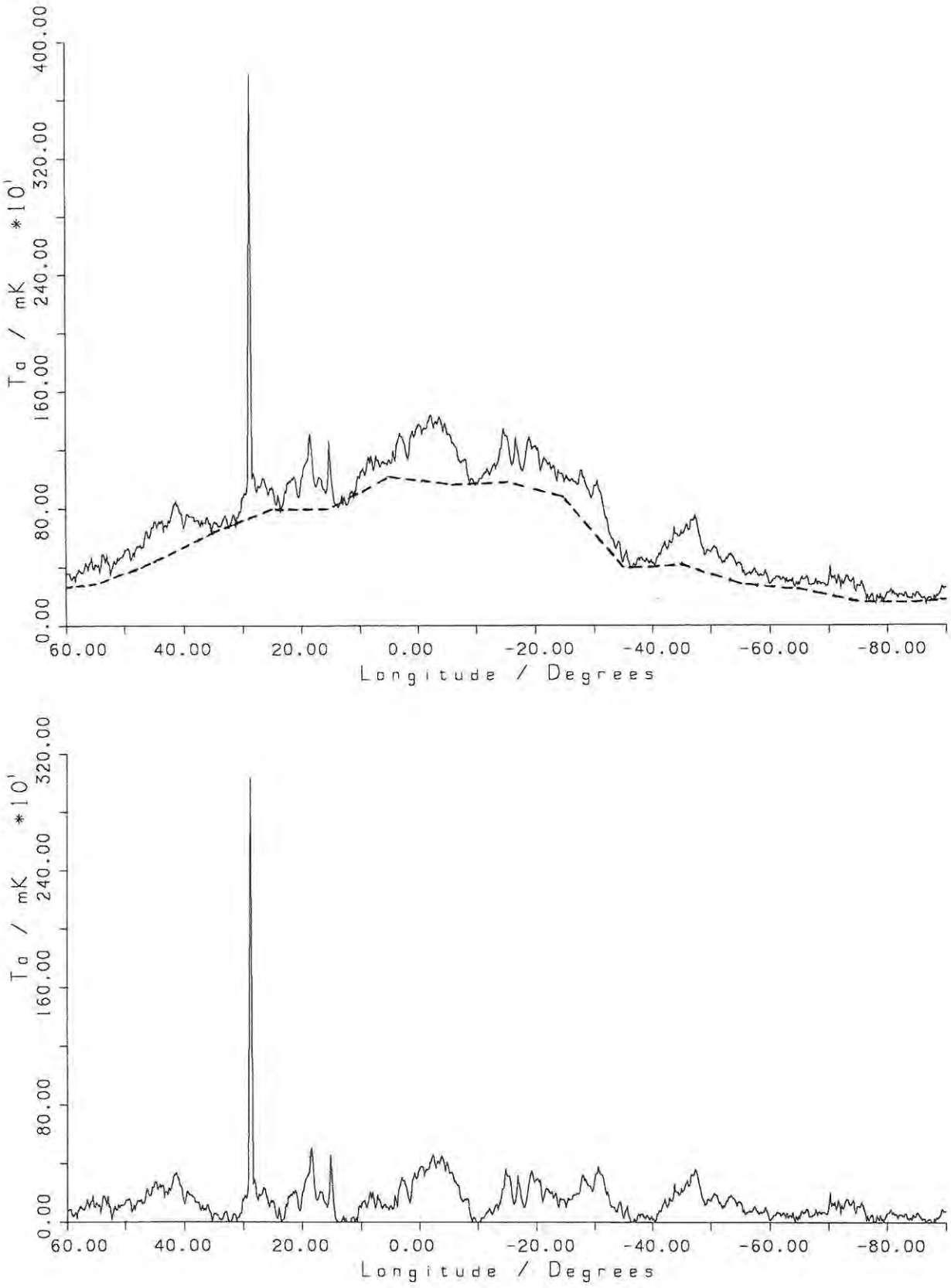

Figure 3.8 - Sections through latitude 3.45°

of the original data and plane profile

(dashed) (top) and the residual map (bottom).

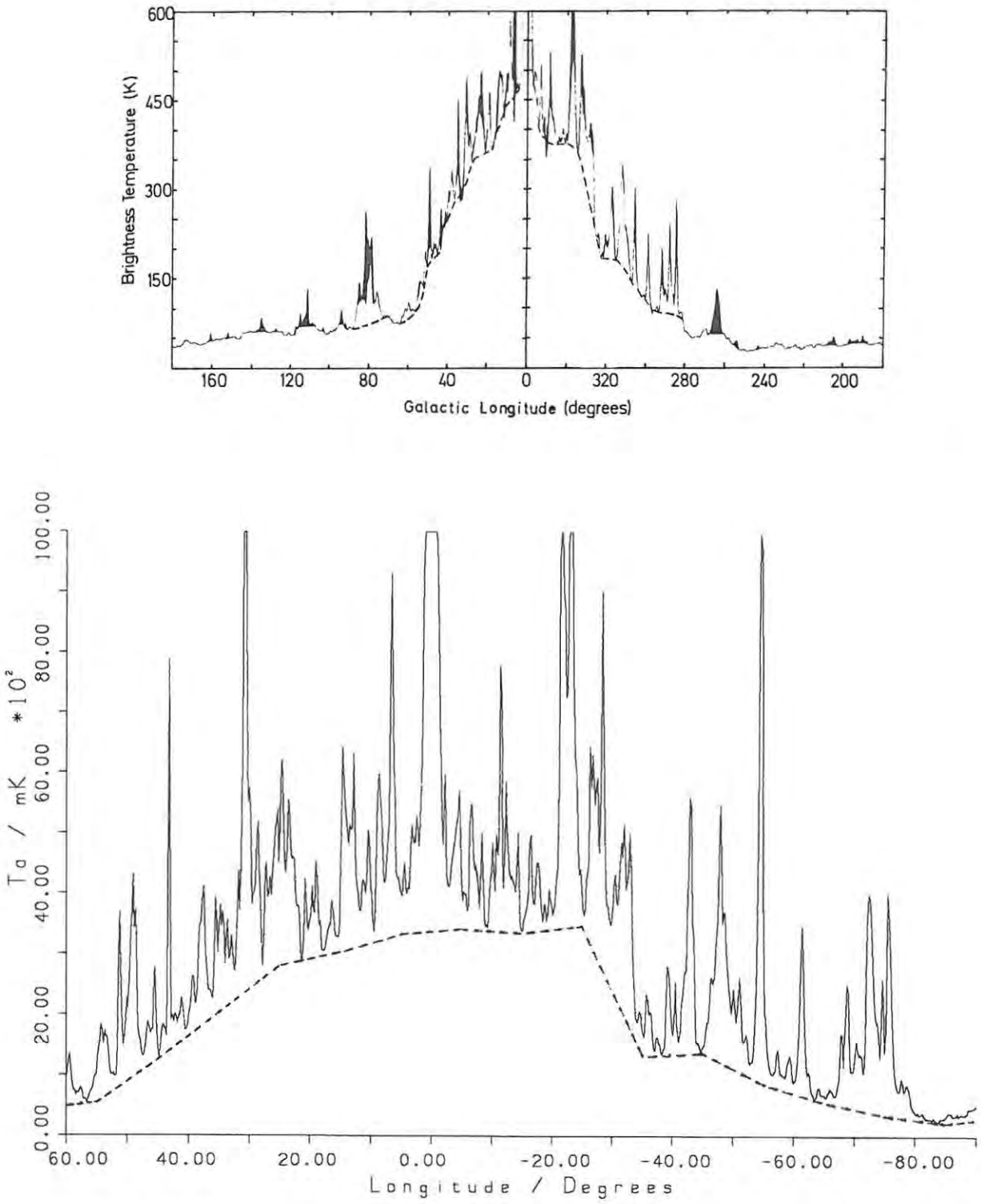

Figure 3.9 - Sections of the Galactic plane from Phillips et al (1981) (top) and the Skymap data (bottom). Profiles of the Galactic disc emission are shown as dashed lines in both diagrams.

longitude is not the same as Phillips *et al*, but includes the central part of their diagram. In the bottom diagram, the plane model produced by method four of this thesis is shown by the dashed line. The plane profiles in each diagram compare favourably, especially in the position of the well-known step in the disc emission occuring between ~325° and 335° and the flat region centred on 320°.

From figure 3.9, a rough determination of the spectral index of the Galactic disc emission can be obtained. Table 3.1 contains approximate values of the brightness temperature of the disc emission at 408 MHz and 2.3 GHz, measured directly from the profiles in figure 3.9 (with a conversion factor of 1.51 between antenna temperature and brightness temperature for the 2.3 GHz data - see the next chapter for further details of this). In column three are the calculated values of the spectral index, α. From these values it can be seen that the disc emission could be attributed to a synchrotron mechanism, although it must be remembered that this is a very rough estimate and that the true mechanism for the production of the disc emission is more than likely a combination of thermal and non-thermal components (Phillips *et al* quote a value of ~20% for the thermal component).

Table 3.1 - Spectral index of the Galactic disc emission.

Lat.	T_b(408)	T_b(2300)	α
60°	81K	0.77K	-0.7
40°	247K	2.54K	-0.6
20°	364K	4.44K	-0.5
340°	374K	5.18K	-0.5
320°	182K	2.05K	-0.6
300°	111K	1.12K	-0.7
280°	61K	0.48K	-0.8

The final comparison to be made in this section is between three of the methods discussed previously - methods one, three and four. For the purpose of this comparison, contour maps were plotted of the plane models produced by methods three and four for the same area of sky as Flanagan's (1981) figure 9. The region lies between longitudes 305° and 350° and latitudes -15° and +15° and the contour plots for methods one, three and four are shown in figures 3.10, 3.11 and 3.12 respectively. The contour levels for figures 3.11 and 3.12 are the same as for figure 3.10 to facilitate easy comparison. Table 3.2 lists the contour levels and associated labels. Note the differences in position

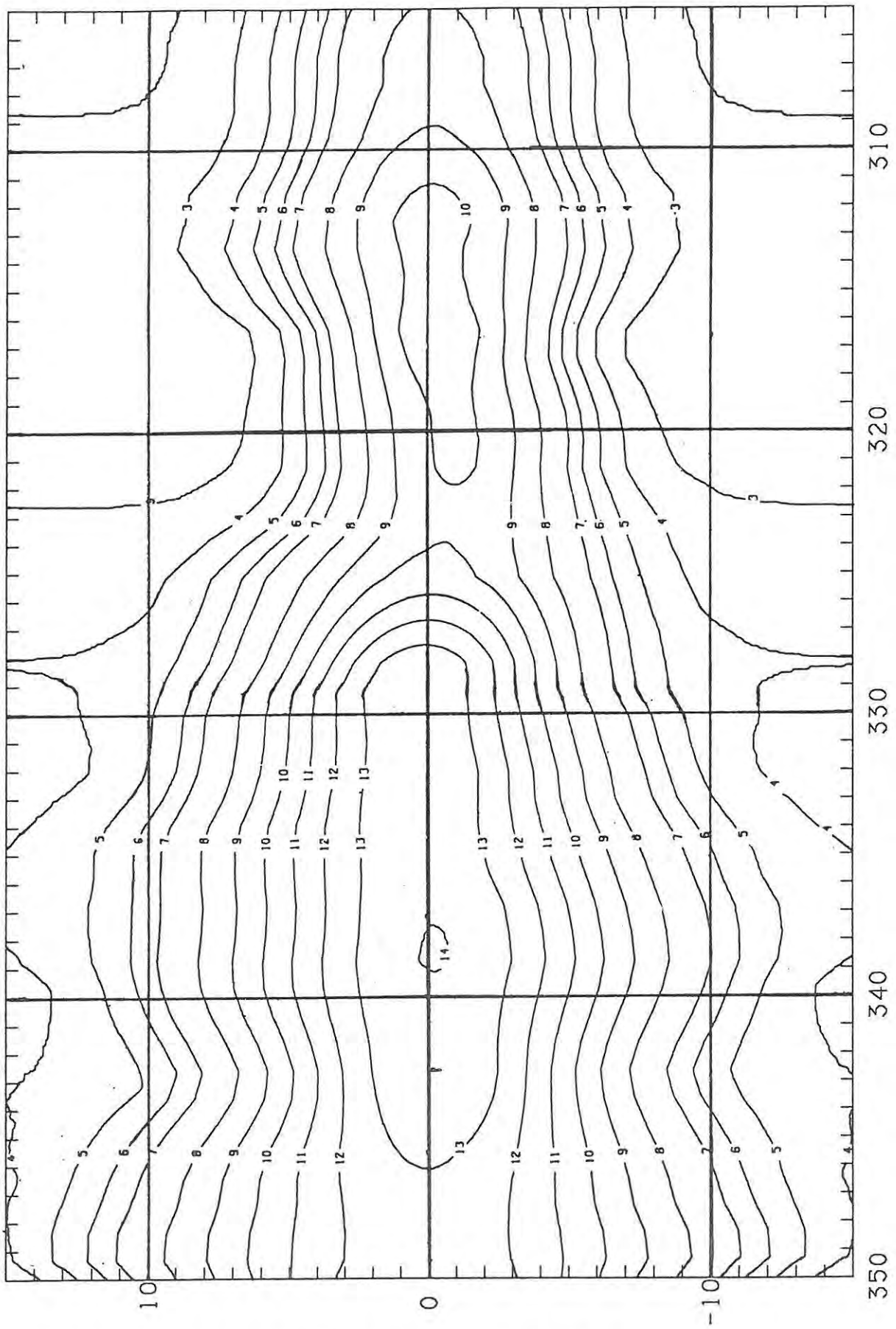

Figure 3.10 - Plane model using method one

(after Flanagan 1981).

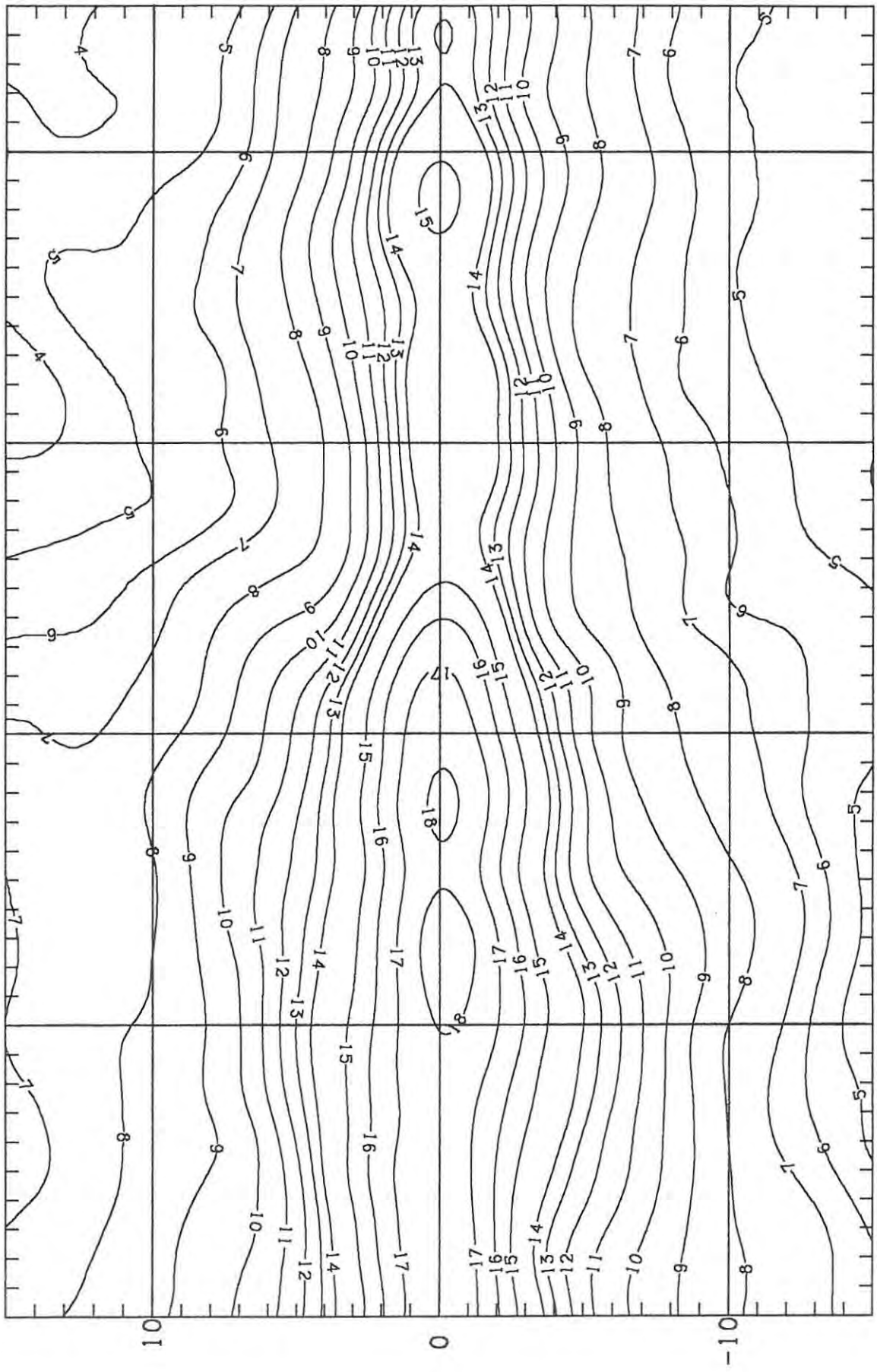

Figure 3.11 - Plane model using method three.

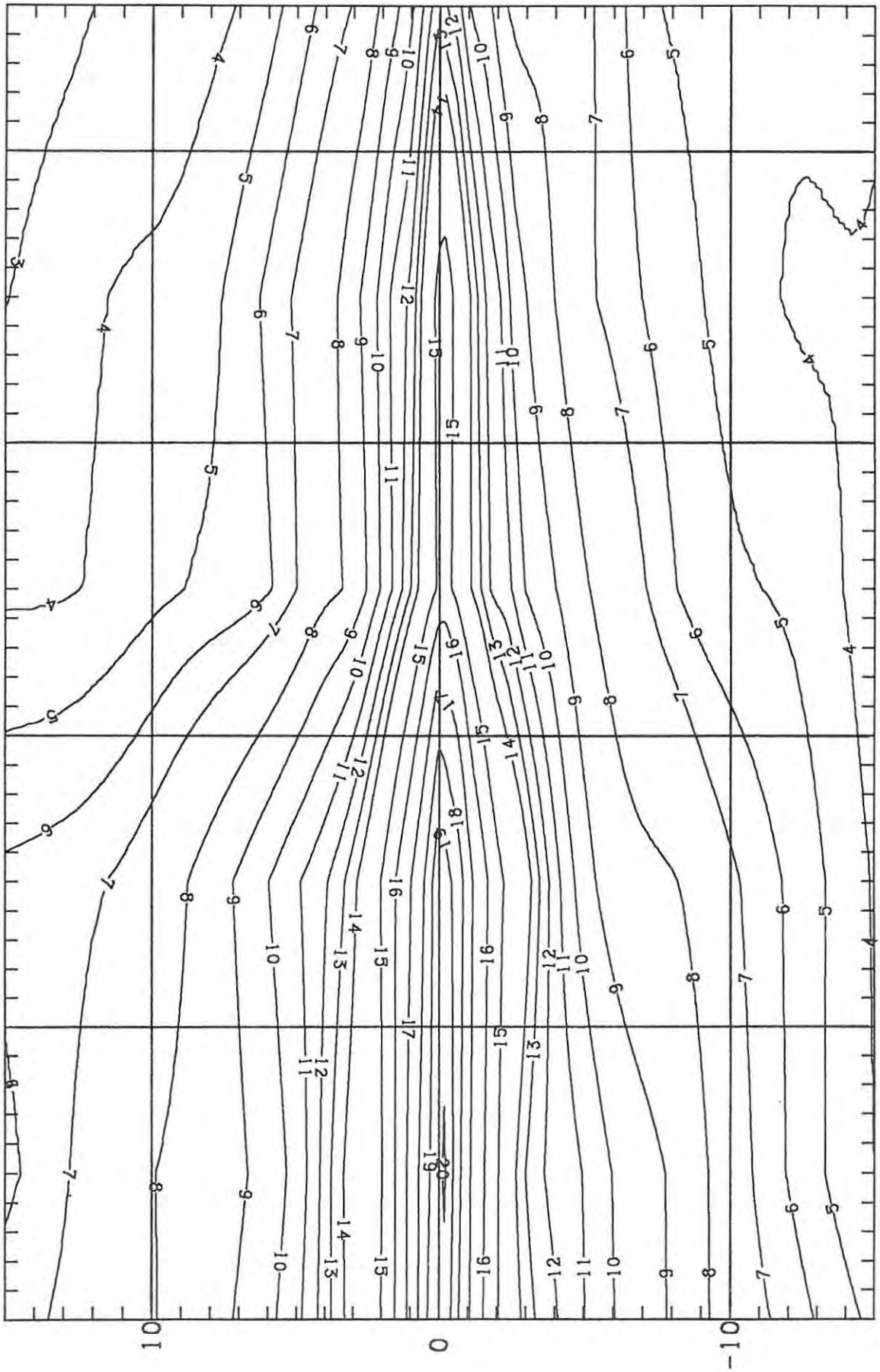

Figure 3.12 - Plane model using method four.

Table 3.2 - Contour levels for figures 3.10, 3.11 and 3.12.

Contour Level Ta / mK	Contour Label	Contour Level Ta / mK	Contour Label
0	1	700	11
50	2	800	12
100	3	900	13
150	4	1000	14
200	5	1300	15
250	6	1600	16
300	7	2000	17
400	8	2500	18
500	9	3000	19
600	10	3500	20

and height of the peaks of the maps - method four producing the highest peak and method one the lowest. Note also that the plane model produced by method three is being influenced by the presence of the very strong source Centaurus A, situated just outside of the region shown at the top right-hand corner. An interesting feature of all of the maps is the presence of the step in the disc emission at $-330°$.

Figure 3.13 is a contour map of the final plane model produced by method four for the region of the fourth part of the Skymap survey. Contour levels are listed in Appendix One. Figure 3.14 is a grey scale image of the final residual temperatures map after subtraction of the above plane model. The contour plot on the overlay has been smoothed by a Tukey filter and is intended only to highlight certain features, such as the north polar spur and the large supernova remnant below the left-hand end of the plane. In the next chapter, a number of the prominent features in this area will be discussed in full detail.

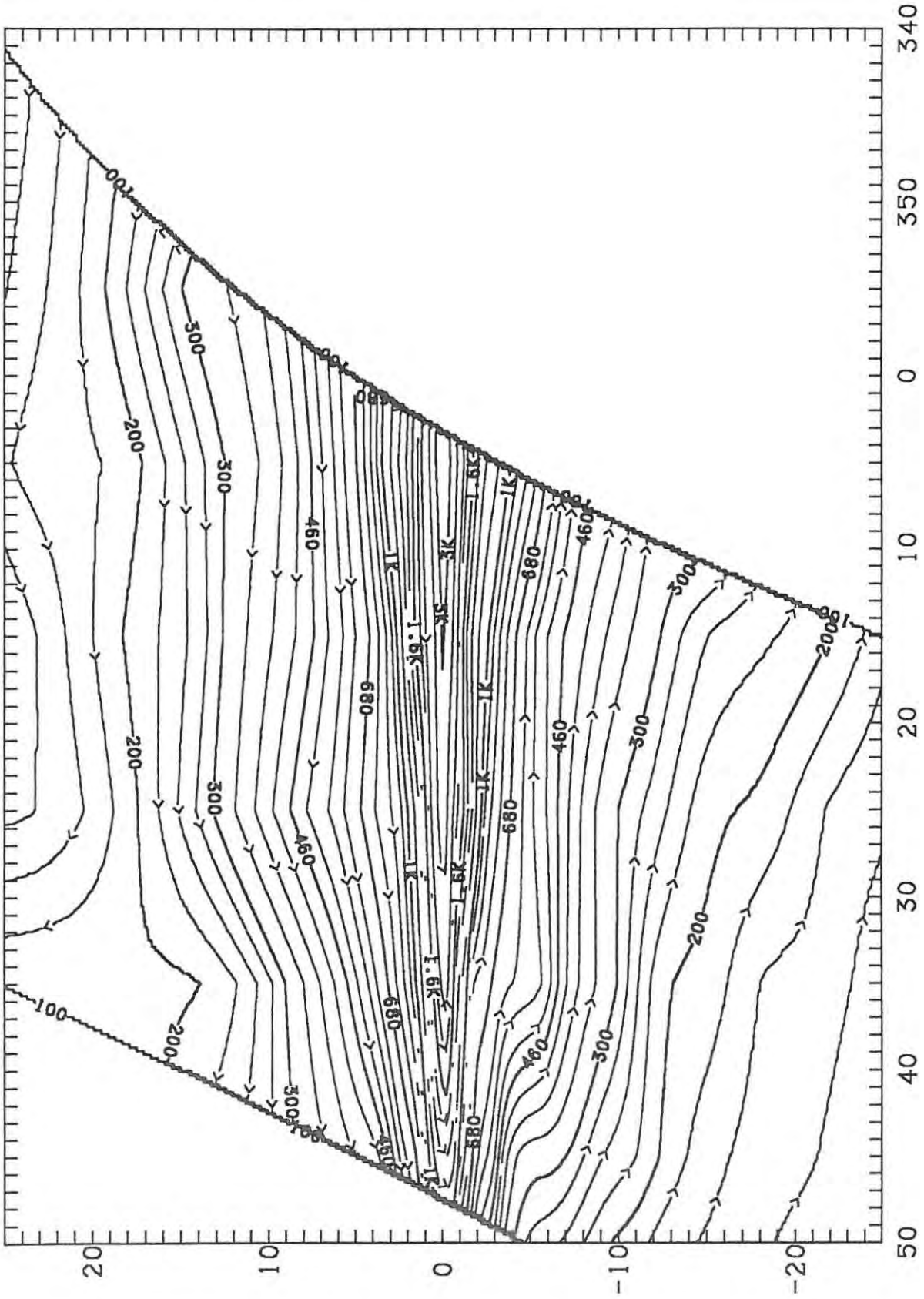

Figure 3.13 - Contour map of the final plane model produced by method four.

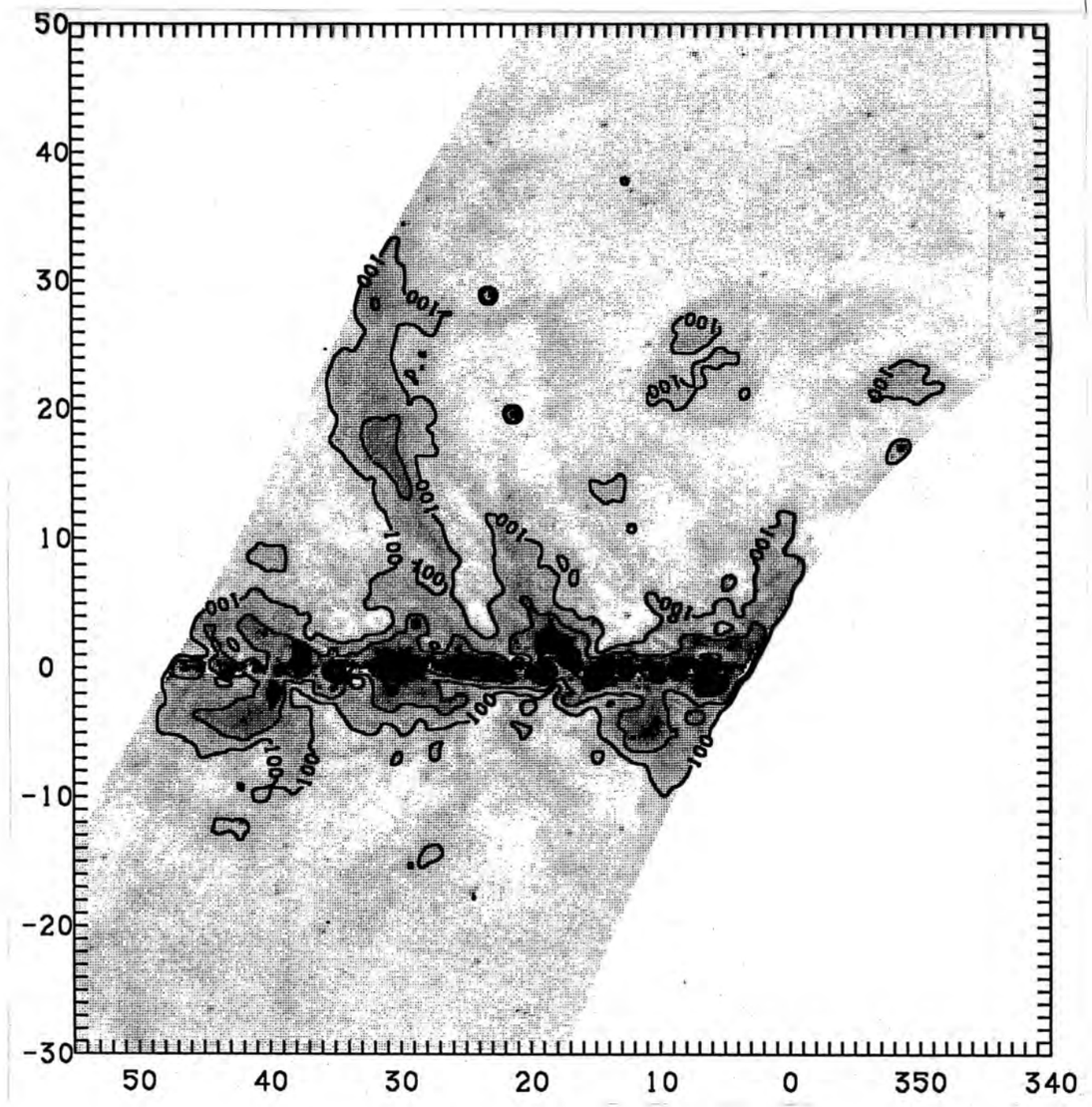

Figure 3.14 - Grey-scale image of the map resulting after subtraction of the model shown in figure 3.13 from the original data. Contour levels are 100mK, 200mK, 500mK, 1K, 2K and 5K.

Chapter Four - Results

This chapter contains in depth discussion on a number of interesting objects contained within the area of the fourth part of the Skymap survey. In section 4.2, the HII region surrounding the star Zeta Ophiuchi is discussed with extensive reference to the literature available on this well-studied object. A number of results are obtained for this source from the data presented in this thesis. In section 4.3, the north polar spur discussed, again with extensive reference to the literature. In section 4.4, the thermal spur associated with the HII region S54 is examined. Since this spur was only discovered fairly recently, only one reference was found to contain any useful information on this object. Therefore, this section deals mainly with the results of the present survey. Section 4.5 makes mention of some other objects which have not been studied in great detail using this data. However, before entering into any discussion of the characteristics of these objects, a discussion of some of the fundamentals of radio astronomy is required, along with the derivation of some of the parameters of the radio telescope and the observations.

4.1 - Fundamentals of Radio Astronomy

This section is not intended to be an exhaustive discussion of every principle of radio astronomy, but merely to outline the principles relevant to the following sections. The principle source for the material in this section was Kraus (1966), especially in the section dealing with the theory of synchrotron radiation. Other primary references were Jonas (1982) and Mezger and Henderson (1967). For a more detailed discussion of the theory discussed in this section, reference may be made to these and the many other books and papers on the subject.

4.1.1 - Parameters of the telescope

In radio astronomy, the antenna is the equivalent of the parabolic mirror of visual astronomy - the

mirror is designed to collect light from distant stars, planets and other objects and focus this light at the eyepiece of the telescope, while the antenna is designed to collect radio waves from radio sources and focus them on the feed of the antenna. A common term used in radio astronomy is the antenna pattern (sometimes referred to as the field pattern or power pattern, depending on whether it is expressed in terms of the field or radiation intensity). The antenna pattern is the response of the antenna in a given direction and normally has the form of a single, strong main lobe surrounded by smaller side lobes. Figure 4.1 shows a typical antenna pattern in polar coordinates.

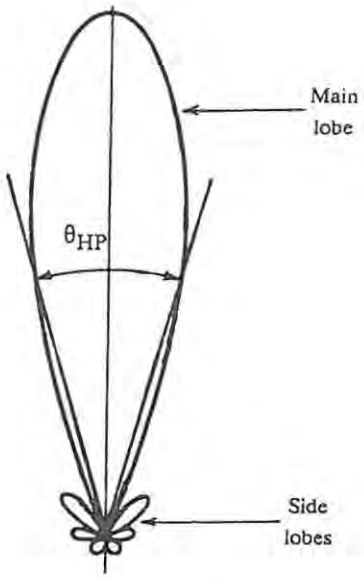

Figure 4.1 - A typical antenna pattern plotted in polar coordinates (after Kraus 1966).

The effect of the antenna pattern on the observations can be seen clearly in the vicinity of relatively strong point sources. Figure 4.2 is a contour map of the strong source 3C 353, situated at right ascension 17^h 18^m and declination -0° 54′ (1950 coordinates). The flux density of this source measured from the data presented in this thesis is 39.6 Jy (see Appendices Three and Four). 3C 353 is a radio galaxy with a spectral index of -0.69 (see the following sub-section for an explanation of flux density and spectral index). The map is centred on the peak emission of the source and at a radius of about 40′ of arc from the peak (dashed circle) four side lobes can be seen. This map has been plotted from the raw data smoothed with a Tukey filter - no base surface due to disc emission has been subtracted.

The half-power beam width of an antenna (θ_{HP}) is defined, as the name suggests, as the angle at the level of half of the peak power. This is indicated in figure 4.1. The beam solid angle is, for the case of a point source located in cold sky, the angle through which all of the incoming radiation would flow if the radiation were constant over this angle and equal to the maximum value. It is given by

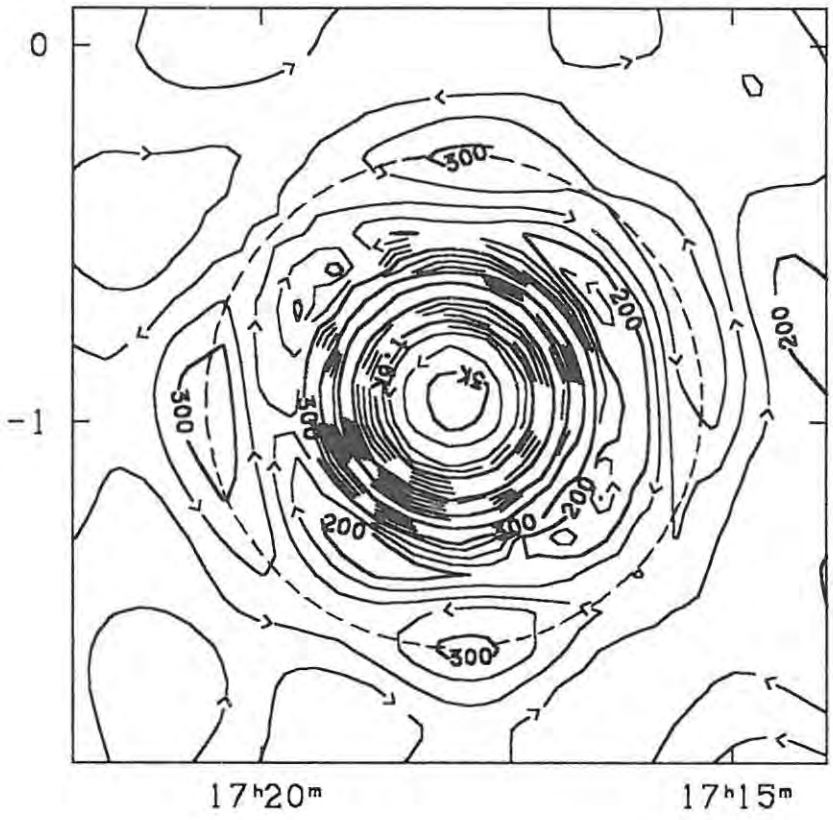

Figure 4.2 - Contour map of the radio galaxy 3C 353 showing the first set of side lobes. The dashed circle is at a radius of 40' of arc from the peak.

$$\Omega_A = \iint P_n(\theta,\phi)\, d\Omega \qquad \ldots\ldots 4.1$$

where Ω_A is the beam solid angle in steradians, $P_n(\theta,\phi)$ is the normalized antenna power pattern, $d\Omega$ is an element of solid angle and the integral is performed over 4π (note that, unless stated otherwise, all integrals in this section are performed over 4π). In order to find the solid angle of the main beam only, the integral in equation 4.1 must be performed over the main beam only. Mezger and Henderson (1967) make use of a simple formula to find the main-beam solid angle for an antenna with a circularly symmetric power pattern:

$$\Omega_M = 1.133\, \theta_{HP}^2 \qquad \ldots\ldots 4.2$$

where Ω_M is the main-beam solid angle in steradians and θ_{HP} is the half-power beam width in radians. In the case of non-circular symmetry, θ_{HP} would have to be replaced by the multiple of the half-power widths in the principle planes of the pattern. Assuming that the Hartebeesthoek antenna has a circularly symmetric, Gaussian power pattern with a half-power beam width of 20', a value of 3.8×10^{-5} steradians is obtained for Ω_M.

The beam efficiency of an antenna is given by

$$\varepsilon_M = \Omega_M / \Omega_A \qquad \ldots\ldots 4.3$$

so, in order to calculate a value for ε_M , Ω_A needs to be determined. Kraus (1966) derives the formula

$$\lambda^2 = A_p \Omega_A \qquad \ldots\ldots 4.4$$

relating the wavelength, λ, in metres, the physical antenna aperture, A_p, in m^2 and the beam solid angle in steradians. Since equation 4.4 assumes that the field be uniform over the aperture, a more realistic expression would be

$$\lambda^2 = A_{ep} \Omega_A \qquad \ldots\ldots 4.5$$

assuming no ohmic losses, where A_{ep} is the effective pattern aperture in m^2. The effective aperture, A_e, can be defined as

$$A_e = \text{total power detected by the receiver} / \text{total power density of incident radiation} \qquad \ldots\ldots 4.6$$

The effective aperture takes into account any ohmic losses in the feed system. The effective and effective pattern apertures are related by

$$A_e = R\,A_{ep} \qquad \ldots\ldots 4.7$$

where R is the ohmic loss factor. Therefore

$$\lambda^2 = (A_e / R)\,\Omega_A \qquad \ldots\ldots 4.8$$

Substituting for Ω_A in equation 4.5 from equation 4.3 yields

$$\lambda^2 = A_{ep}\,\Omega_M / \varepsilon_M \qquad \ldots\ldots 4.9$$

Therefore, using the known values for λ (0.13m) and Ω_M, the effective pattern aperture is given by

$$A_{ep} = 445\,\varepsilon_M \ \ m^2 \qquad \ldots\ldots 4.10$$

An expression for relating the effective aperture, the flux density, S, and the antenna temperature, T_a, for a point source is (see section 4.1.2)

$$S = 2\,k\,T_a / A_e \qquad \ldots\ldots 4.11$$

where k is Boltzmann's constant. Thus, if the flux density is known for a particular point source, and the antenna temperature can be measured, a value for A_e can be determined. This has been done for the source 3C 353. The antenna temperature of this source was found to be 4.15K corresponding to a value of 292 m^2 for the effective aperture, assuming a flux density of 39.29 Jy at 2.3 GHz. This results in a loss factor of

$$R = A_e / A_{ep} = 0.656 / \varepsilon_M \qquad \ldots\ldots 4.12$$

In the case of the Hartebeesthoek antenna, the loss factor is approximately unity. This leads to a beam efficiency of 65.6% and a beam solid angle of 5.8×10^{-5} steradians.

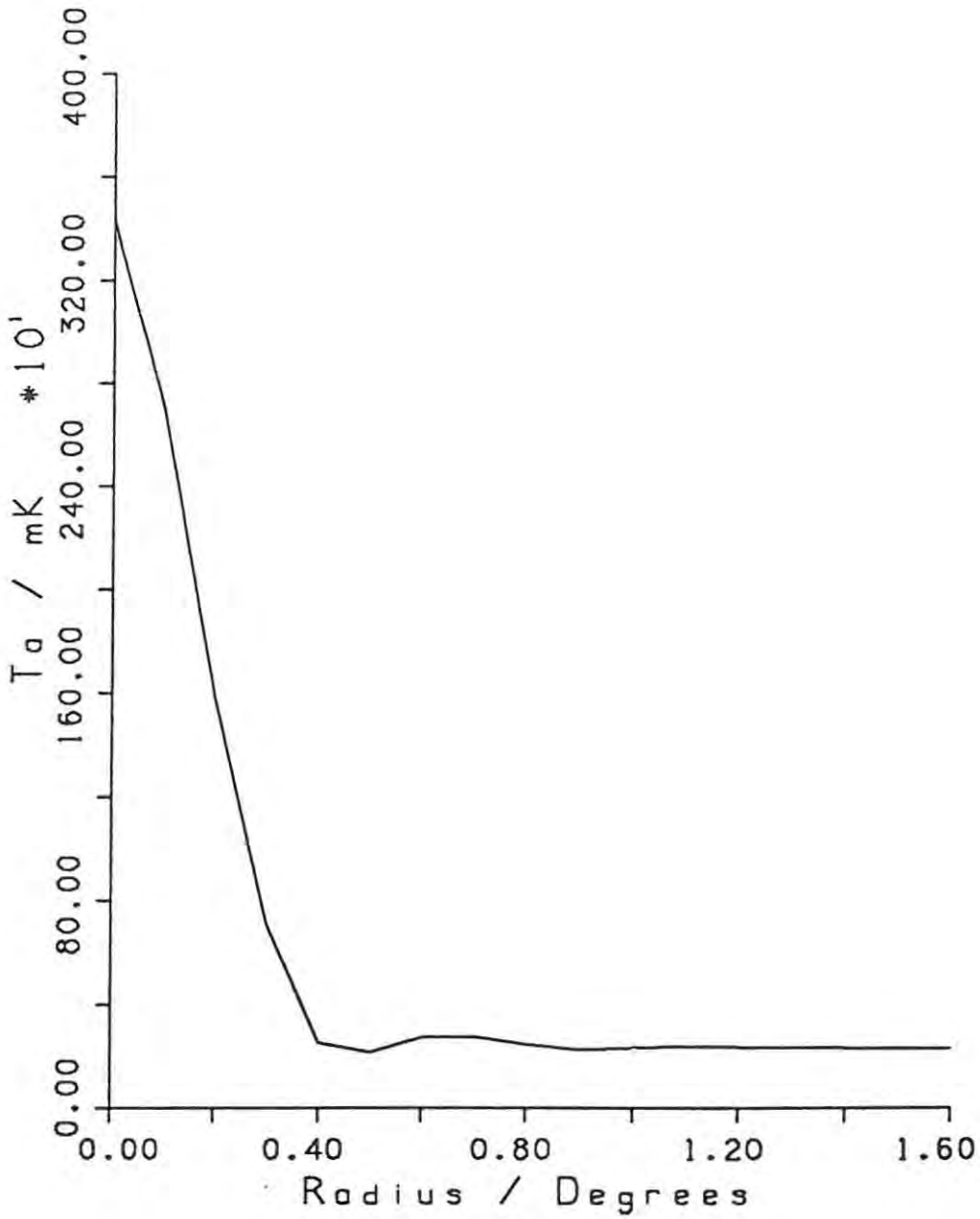

Figure 4.3 - Radial profile of the source 3C 353. At least one side lobe is present, centred at ~0.7° from the peak of the emission.

Aperture efficiency is defined by

$$\varepsilon_{ap} = A_e / A_p \qquad \ldots\ldots 4.13$$

Using the value for the effective aperture calculated above and a value of 531 m^2 for the physical aperture of the Hartebeesthoek antenna, the aperture efficiency is calculated to be 55.0%.

Appendix Five contains a table of all of the parameters calculated in this chapter and in Chapter Two and Appendix Three.

4.1.2 - Basic theory of radio astronomy

4.1.2.1 - Temperature and flux

The map of raw data obtained by the processes described in Chapter Two consists of a grid of antenna temperatures with a grid spacing of 0.1° in right ascension and declination. Antenna temperature can be defined as the convolution of the antenna pattern with the true brightness ditribution in the sky. It is related to the power per unit bandwidth received by the antenna by the relation

$$W = \tfrac{1}{2} A_e \iint B(\theta,\phi)\, P_n(\theta,\phi)\, d\Omega = k\, T_a \qquad \ldots\ldots 4.14$$

where W is the power per unit bandwidth in watts Hz^{-1}, A_e is the effective aperture in m^2, $B(\theta,\phi)$ is the brightness as a function of position over the source in watts m^{-2} Hz^{-1} $ster^{-1}$, $P_n(\theta,\phi)$ is the normalized antenna pattern of the antenna, $d\Omega$ is an element of solid angle in steradians, k is Boltzmann's constant, T_a is the antenna temperature in Kelvin, and the factor ½ is included to account for the fact that the antenna only receives one half of the power, if the radiation is unpolarized. The integral is performed over Ω_s, the solid angle subtended by the source.

For a discrete source (ie - a source which is separated from the influence of other sources), the following integral is defined as the observed flux density of the source

$$S = \iint B(\theta,\phi)\, d\Omega \qquad \ldots\ldots 4.15$$

where S is the flux density in watts m^{-2} Hz^{-1} and the integral is performed over Ω_s. The Jansky (Jy) is the accepted unit for flux density, and is equivalent to 10^{-26} watts m^{-2} Hz^{-1}.

For a point source, $P_n(\theta,\phi) \approx 1$ over Ω_s. Hence, comparing equations 4.14 and 4.15, an expression relating flux density and antenna temperature is obtained for a point source:

$$k T_a = \tfrac{1}{2} A_e \iint B(\theta,\phi)\, d\Omega = \tfrac{1}{2} A_e S \qquad \ldots\ldots 4.16$$

(This is the same as equation 4.11). Substituting equations 4.7 and 4.8 into 4.16 yields the expression

$$S = (2 k \Omega_A / R \lambda^2) T_a \qquad \ldots\ldots 4.17$$

For a point source, the antenna temperature in equations 4.16 and 4.17 would be the maximum deviation in T_a measured by means of a drift scan. Hence

$$S = (2 k \Omega_A / R \lambda^2) T_a(\max) \qquad \ldots\ldots 4.18$$

The derivation above assumes that the telescope is pointing directly at a point source. In order to take the scanning of the telescope into account, this derivation needs to be approached in a slightly different way. The brightness temperature of a source may be defined by the relation (Jonas 1982)

$$T_b(\theta,\phi) = (\lambda^2 / 2 k) B(\theta,\phi) \qquad \ldots\ldots 4.19$$

where $T_b(\theta,\phi)$ is the physical temperature distribution over the source, assuming that the frequency is low enough for the Rayleigh-Jeans law to hold (see the next sub-section for an explanation of the Rayleigh-Jeans law), which is the case at radio frequencies. Antenna temperature is related to brightness temperature by

$$T_a(\theta,\phi) = (R / \Omega_A)\ T_b(\theta,\phi) * P_n(\theta,\phi) \qquad \ldots\ldots 4.20$$

In the case of a source with angular dimensions which cannot be neglected when compared to the half-power beam width of the telescope, the result is a little more complicated since it now becomes necessary to integrate over the beam solid angle in order to determine the integrated flux density. Hence, 4.20 becomes

$$\iint T_a(\theta,\phi)\, d\Omega = (R / \Omega_A) \iint T_b(\theta,\phi) * P_n(\theta,\phi)\, d\Omega \qquad \ldots\ldots 4.21$$

This can be simplified to

$$\iint T_a(\theta,\phi)\, d\Omega = (R / \Omega_A) \iint T_b(\theta,\phi)\, d\Omega \times \iint P_n(\theta,\phi)\, d\Omega \qquad \ldots\ldots 4.22$$

which becomes, after substitution of equation 4.1,

$$\iint T_a(\theta,\phi)\, d\Omega = R \iint T_b(\theta,\phi)\, d\Omega \qquad \ldots\ldots 4.23$$

Substitution of equations 4.19 and 4.15 yields

$$\iint T_a(\theta,\phi)\, d\Omega = (R \lambda^2 / 2k)\, S \qquad \ldots\ldots 4.24$$

or, in terms of flux density,

$$S = (2k / R \lambda^2) \iint T_a(\theta,\phi)\, d\Omega \qquad \ldots\ldots 4.25$$

4.1.2.2 - Blackbody radation and optical depth

All objects at temperatures above absolute zero emit and absorb electromagnetic energy. A blackbody is defined as an object which absorbs *all* energy incident on it (ie - a perfect absorber) and, according to the well-known principle that a good absorber of electromagnetic energy is also a good radiator of electromagnetic energy, a blackbody is also a perfect radiator.

The brightness of a blackbody is given by

$$B = 2h\nu^3 / c^2 (e^{\gamma} - 1) \qquad \ldots\ldots 4.26$$

(Planck's radiation law) where B is the brightness in watts m^{-2} Hz^{-1} $ster^{-1}$, h is Planck's constant, ν is the frequency in Hz, c is the velocity of light in m s^{-1}, k is Boltzmann's constant, T is the temperature of the blackbody in Kelvin and $\gamma = h\nu / kT$. For the low frequencies in the radio region of the spectrum, γ becomes very small, and equation 4.26 becomes

$$B = 2h\nu^3 / c^2 [(1 + \gamma) - 1] \qquad \ldots\ldots 4.27$$

which reduces to

$$B = 2\nu^2 kT / c^2 \quad \text{or} \quad 2kT / \lambda^2 \qquad \ldots\ldots 4.28$$

where λ is the wavelength in metres. This is the Rayleigh-Jeans radiation law, from which the flux densities of equations 4.18 and 4.25 can be derived.

Consider now a cloud of gas through which radiation passes as it travels towards the earth. A volume element within the medium, of path length dx, will contribute towards the total intensity of radiation received by the telescope by the amount

$$dI = -I \kappa \, dx + j \, dx \qquad \ldots\ldots 4.29$$

where κ is the linear absorption coefficient and j is the linear emission coefficient in the line of sight towards the telescope. The optical depth of a medium is defined by

$$d\tau = \kappa \, dx \qquad \ldots\ldots 4.30$$

where τ is the optical depth, a dimensionless quantity. Substituting this into equation 4.29 and defining source function (S) as the ratio of the emission coefficient to the absorption coefficient, yields

$$dI / d\tau = -I + S \qquad \ldots\ldots 4.31$$

In order to determine the intensity of radiation contributed by the nebula as a whole, equation 4.31 must be integrated from the far side of the nebula to the telescope. Introducing the integrating factor e^{τ}, equation 4.31 becomes

$$I = I_0 e^{-\tau} + \int S \, e^{-(\tau - t)} \, dt \qquad \ldots\ldots 4.32$$

after integration, where I_0 is the intensity of any background sources and the integration is performed between 0 and τ. Assuming that S is a constant (that is, the absorption and emission coefficients are independent of position within the nebula), equation 4.32 becomes

$$I = I_0 e^{-\tau} + S (1 - e^{-\tau}) \qquad \ldots\ldots 4.33$$

At low frequencies, the optical depth (τ) is greater than unity for most HII regions. In this case, equation 4.33 reduces to

$$I \approx S \qquad \ldots\ldots 4.34a$$

At high frequencies, the optical depth (τ) is much less than unity for most HII regions. In this case, equation 4.33 reduces to

$$I \approx I_0 + S\tau \qquad \ldots\ldots 4.34b$$

If $\tau > 1$ at a particular frequency, the medium is said to be optically thick, or opaque, meaning that an average photon of that frequency will be absorbed before it has traversed the thickness of the medium. This explains why, in equation 4.34a, the observed intensity does not depend on the contribution of any background sources. If $\tau < 1$, the medium is said to be optically thin, or transparent, meaning that an average photon of that frequency will be able to pass through the medium without being absorbed. In the case of HII regions, the optical depth increases as the frequency decreases, resulting in an optically thin medium at high frequencies and an optically thick medium at lower frequencies. At 2.3 GHz, most of the observed HII regions are optically thin.

4.1.2.3 - Radiation mechanisms and spectral index

There are two principle mechanisms for the emission of radiation from radio sources - thermal emission from ionized gas and synchrotron emission. Both of these mechanisms involve the acceleration of free electrons to produce the radiation. Since free electrons have no specific energy levels, the radiation emitted by them is in the form of a continuous spectrum.

In thermal emission, a free electron in a region of ionized gas is accelerated as it passes near a proton and is deflected. Since the electron is in an unbound state both before and after its encouter with the proton, this type of interaction is called a free-free transition. The radiation that is emitted by the electron in a free-free transition is called bremsstrahlung, a German word meaning "braking radiation".

For HII regions, the optical depth is given by (Mezger and Henderson 1967)

$$\tau = 3.014 \times 10^{-2}\, T_e^{-1.5}\, \nu^{-2.0} \left[\ln (4.955 \times 10^{-2}\, \nu^{-1}) + 1.5 \ln T_e\right] E \qquad \ldots\ldots 4.35$$

where T_e is the electron temperature in Kelvin, ν is the frequency in GHz and E is the emission measure of the region, defined by

$$E = \int N_e^2\, dz \qquad \ldots\ldots 4.36$$

where E is measured in $cm^{-6}pc$, N_e is the free-electron density in cm^{-3}, dz is an element of distance along the line of sight and the integral is performed over the thickness of the cloud along the line of sight. (Note that one rarely sees electron density expressed in terms of m^{-3} and emission measure in terms of $m^{-6}pc$.) To simplify equation 4.35, Mezger and Henderson (1967) define a factor a by

$$a = 0.366\, T_e^{-0.15}\, \nu^{0.1} \left[\ln (4.955 \times 10^{-2}\, \nu^{-1}) + 1.5 \ln T_e\right] \qquad \ldots\ldots 4.37$$

simplifying equation 4.35 to

$$\tau = 8.235 \times 10^{-2}\, a\, T_e^{-1.35}\, \nu^{-2.1}\, E \qquad \ldots\ldots 4.38$$

The brightness temperature of an HII region is

$$T_b = T_e \left(1 - e^{-\tau}\right) \qquad \ldots\ldots 4.39$$

which, for optical depths much less than unity, simplifies to

$$T_b = T_e\, \tau \qquad \ldots\ldots 4.40$$

Hence, substituting for τ from equation 4.38, the brightness temperature becomes

$$T_b = 8.235 \times 10^{-2}\, a\, T_e^{-0.35}\, \nu^{-2.1}\, E \qquad \ldots\ldots 4.41$$

Integration of equation 4.19 over the region yields the flux density of an HII region:

$$S = (2k/\lambda^2) \iint T_b \qquad \ldots\ldots 4.42$$

Assuming a uniform surface brightness over the extent of the source (Ω_s) allows simplification of equation 4.42 to

$$S = (2k\Omega_s/\lambda^2)\, T_b \qquad \ldots\ldots 4.43$$

Hence,

$$S \propto T_b/\lambda^2 \propto \tau/\lambda^2 \qquad \ldots\ldots 4.44$$

and, by assuming E and a to be constant in equation 4.38 (a is equal to unity to within 1% at ν = 2.3 GHz and for T_e ranging from 5000K to 10000K),

$$S \propto 1/\nu^{2.1}\lambda^2 \propto \nu^{-0.1} \qquad \ldots\ldots 4.45$$

The value -0.1 is the spectral index (α) of an optically thin, thermal source.

This value was derived by assuming that the optical depth of the HII region was much less than unity. At lower frequencies, the optical depth becomes greater than unity, and equation 4.39 then becomes

$$T_b = T_e \qquad \ldots\ldots 4.46$$

yielding

$$S \propto \nu^2 \qquad \ldots\ldots 4.47$$

Hence, at lower frequencies, the spectral index becomes $\alpha = +2.0$. The term "thermal emission" arises from the fact that this spectral index is the value for a thermal blackbody radiator.

To summarize then, HII regions are typically optically thick at lower frequencies, with spectral indices of $\alpha = +2.0$, and optically thin at higher frequencies, with spectral indices of $\alpha = -0.1$.

The synchrotron mechanism involves free electrons moving at relativistic speeds through the magnetic field of a star. As the velecity, v, approaches the speed of light, c, the energy of an electron is given by

$$E = 6 \times 10^{18}\, m\, c^2 / \sqrt{1 - (v/c)^2} \qquad \ldots\ldots 4.48$$

where E is the energy in electron volts, m is the rest mass of the electron and v and c are in m s^{-1}. As the electron moves through the magnetic field of a star, it describes a circle of radius

$$R \approx {}^{c}/_{2\pi\nu} \qquad \ldots\ldots 4.49$$

where R is in metres and ν is the frequency with which the electron gyrates in the magnetic field (ie - the number of revolutions per second). This frequency is called the cyclotron frequency and is given by

$$\nu = ({}^{e B}/_{2\pi m}) \sqrt{1 - ({}^{v}/_{c})^2} \qquad \ldots\ldots 4.50$$

viewed from the reference frame of the earth, the radiation emitted by the relativistic electron is concentrated in a cone centred on the instantaneous velocity direction. Thus, if the earth is situated in the plane of orbit of the electron, pulses of radiation of length

$$\Delta t \approx ({}^{2\,m}/_{e\,B}) [1 - ({}^{v}/_{c})^2] \qquad \ldots\ldots 4.51$$

will be received, where Δt is in seconds. The peak radiation occurs at

$$\nu_{max} = {}^{1}/_{2\,\pi\,\Delta t} = {}^{e\,B}/_{4\,\pi\,m\,[\,1 - (v/c)^2\,]} \qquad \ldots\ldots 4.52$$

which simplifies to

$$\nu_{max} = 0.058\,B\,E^2 \qquad \ldots\ldots 4.53$$

Assuming that cosmic rays are responsible are responsible for the synchrotron emission, the spectrum of the radiation of a group of relativistic electrons will be a function of the energy spectrum of these cosmic rays (Kraus 1966). This is of the form

$$N(E) \propto E^{-\kappa} \qquad \ldots\ldots 4.54$$

where N(E) is the number of electrons as a function of energy and κ is the spectral index of the energy. The total power radiated is

$$W \propto \int W(E)\,N(E)\,dE \qquad \ldots\ldots 4.55$$

where W(E) is the power radiated by one electron. This power is a function of its energy squared, so equation 4.55 can be written

$$W \propto \int E^2\,E^{-\kappa}\,dE \qquad \ldots\ldots 4.56$$

So, from equation 4.53,

$$W \propto E^{3-\kappa} \propto \nu^{(3-\kappa)/2} \qquad \ldots\ldots 4.57$$

Therefore, the total power (over all frequencies) radiated by a group of relativistic electrons is given by

$$dW / d\nu \propto \nu^{(1-\kappa)/2} \propto S \qquad \ldots\ldots 4.58$$

κ is typically in the region of 2.4 for cosmic rays, resulting in a spectral index for synchrotron radiation of $\alpha = -0.7$.

As is the case with thermal radiation, the spectral index of a synchrotron source also changes at low frequencies due, in this case, to self-absorption of the emitted radiation. Thus, at lower frequencies, the spectral index is about $\alpha = +2.5$.

4.2 - The HII Region Surrounding Zeta Ophiuchi

4.2.1 - Literature Survey

The region surrounding the star Zeta Ophiuchi (ζ Ophiuchi) holds the distinction of being the most well-studied line-of-sight through a diffuse cloud. An abundance of observations, covering most of the electromagnetic spectrum, have been carried out since the region was first identified as an HII region by Sharpless and Osterbrock in 1952. All of these observations have yielded the same basic result - atomic and molecular gas occurs along the line of sight towards ζ Ophiuchi at different velocities and abundances. Naturally, many models have been produced to try and explain and/or predict the many variables associated with this region. In the following paragraphs an attempt will be made to outline the most important models (those which attempt to model the system as a whole, or at least a major part of the system) with a view to understanding the knowledge available to date on this region. Before discussing these models, however, the physical characteristics of ζ Ophiuchi and its associated HII region are given.

ζ Ophiuchi (HD 149757) is an O9.5V star (an early-type star on the main sequence) in the constellation Ophiuchus. The right ascension is $\alpha = 16^h\ 34^m\ 24^s$ and declination is $\delta = -10°\ 27'\ 58''$ (1950 coordinates), corresponding to galactic coordinates of $l_{II} = 6.2°$ and $b_{II} = 23.6°$. The reddening of the star is estimated to be about E(B-V) = 0.33 magnitudes (Savage 1975) giving an extinction of (Rieke and Lebofsky 1985)

$$A_v = 3.09\ E(B\text{-}V) = 1.0197 \qquad .....4.59$$

The apparent visual magnitude is $m_v = 2.56$ while the absolute magnitude is $M_v = -4.2$, giving a distance to ζ Ophiuchi of about 140 parsecs (Draine 1986). It is interesting to note that this distance estimate is not internationally accepted, as many authors prefer to use 170 parsecs, the distance estimate of Bohlin (1975). This, of course, will affect the calculation of many parameters (for example, electron density of the HII region), however, for this thesis, Draine's estimate of 140 parsecs will be used. The high rotational velocity of 396 kms^{-1} (Morton 1975) is responsible for broad features in the spectrum of the star. ζ Ophiuchi is approaching the sun with a radial velocity of 10.7 kms^{-1} (Lesh 1968) and its proper motion is 0.0008 seconds of time per year in right ascension and 0.023 seconds of arc per year in declination.

The HII region surrounding ζ Ophiuchi carries the designation Sharpless 27, or simply S27. According to Draine (1986), S27 covers an area 7° × 10°, giving it a mean radius of about 10.5 parsecs at 140 parsecs. According to Celnik and Weiland (1988), the most sensitive photograph of S27 yet published indicates that it extends more than 13°. Draine, using the Hα observations of Reynolds *et al* (1974), estimates a value of 460 $cm^{-6}pc$ for the emission measure of S27. Also using Hα observations, Reynolds and Ogden (1982) compute a value of 430 $cm^{-6}pc$, while Celnik and Weiland (1988) derive a value of 240 ± 26 $cm^{-6}pc$ (the high values are the result of incorrect calibration (Scherb 1981) and should be reduced by the factor 0.64). Using the 2.3 GHz data of Greybe (1984), Celnik and Weiland arrived at a value of 286 ± 59 $cm^{-6}pc$. The electron density in the HII region is $N_e = 4.7$ cm^{-3} according to Draine (1986), and 2.8 ± 1.0 cm^{-3} according to Celnik and Weiland. Draine derives a value for the hydrogen recombination rate of $10^{47.99}$ s^{-1}, which is close to

the output of Lyman continuum photons from ζ Ophiuchi of $10^{48.08}$ s^{-1} (Panagia 1973).

The two most important models used to predict and/or explain the column densities and other parameters for the molecules in S27 both involve the influence of shocks - the nonmagnetic shock model of Elitzur and Watson (1980) and the magnetohydrodynamic (MHD) shock model of Draine (1986). The occurence of shocks in the interstellar medium is an established fact, such shocks being caused by supernovae, cloud-cloud collisions, the galactic density wave, stellar winds and expansion of HII regions. The evidence of shocks can be seen in many parts of the interstellar medium as velocities in excess of the speed of sound in the local medium. It is also an established fact that such shocks do influence the production rates and column densities of a majority of the known interstellar molecular species. Over the years since the shock theory was first postulated, much alteration and re-modelling has taken place, and it is with this in mind that two different models are being discussed here.

4.2.1.1 - The Nonmagnetic Model

CH^+ was the third molecule to be detected in the interstellar medium and was first detected in 1940. It occurs widely in diffuse clouds. However, no model prior to the advent of the shock models could adequately explain its abundance (for example, the discussion of Watson (1978), in which he admits that at that time the abundance of CH^+ under the low-temperature, steady-state conditions characteristic of interstellar clouds was not understood). The problem arises due to the fact that CH^+ is rapidly destroyed through the reaction

$$CH^+ + e \Leftrightarrow C + H \qquad .....4.60$$

The model of Elitzur and Watson (1980) was proposed primarily to explain the abundance of CH^+ in diffuse interstellar clouds.

The basic idea behind the model is that CH^+ is produced in a small region of hot gas just behind the

shock front. The temperature of the gas in this region is estimated to be about 2000K to 4000K. At these temperatures, the main mechanism for the production of CH^+ is the endothermic reaction

$$C^+ + H_2 \Leftrightarrow CH^+ + H \qquad .....4.61$$

In the case of S27, observations to detect velocity shifts between CH^+ and other molecular species have been performed to a high degree of accuracy, revealing shifts of a few kms^{-1}. In the presence of any shock, three velocity components are expected - the component associated with the preshock gas, the component associated with the hot postshock gas that occupies the region immediately after the shock, and the component associated with the cold postshock gas. The dominant velocity component associated with the main cloud towards ζ Ophiuchi has a velocity of $V_{LSR} = -0.5kms^{-1}$. The main cloud towards ζ Ophiuchi consists of the cold, compressed gas that is expected in the region well behind a shock front. The distance of this region from the star (approximately 25 parsecs, according to Crutcher (1977)) suggests a shock driven by the HII region. The CH^+ line is situated at $V_{LSR} = +1.4kms^{-1}$. This component is associated with the hot postshock gas. A third velocity component, observed in optical line data and at radio wavelengths (OH observations by Crutcher (1979)), appears at $V_{LSR} = +5.5kms^{-1}$. The angular extent of this region implies that it lies beyond the HII

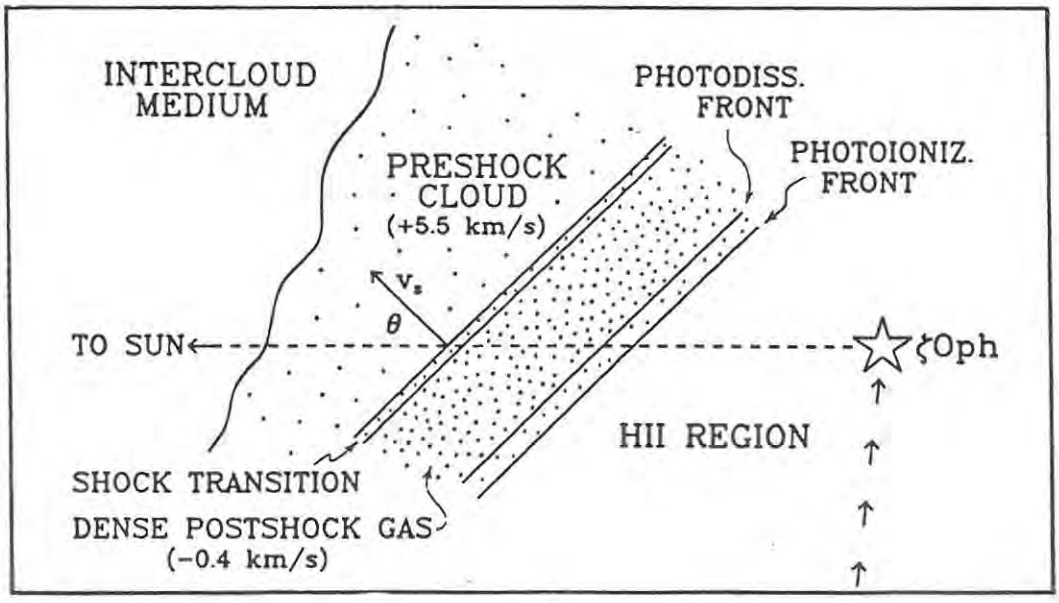

Figure 4.4 - The geometry of a shock in the ζ Ophiuchi HII region (after Draine 1986).

region, and is probably associated with Heiles Cloud 5, a dust cloud in this region. If the shock model so far presented is correct, then this component must represent the preshock gas for a shock originating at ζ Ophiuchi.

Assuming the above scenario to be correct, the shock velocity appears to be approximately 6kms^{-1}. The shock velocity produced by this model to predict the observed column density of CH^+ is approximately 12kms^{-1}. The difference between these two velocities could be explained by the introduction of an angle (approximately 60°) between the line of sight and the velocity of the shock. Figure 4.4 shows this geometry. While this geometry effectively explains the column density of CH^+, it does not produce the correct results for CH, H_2O or OH.

4.2.1.2 - The Magnetohydrodynamic Model

Although the nonmagnetic shock model of Elitzur and Watson (1980) was a great improvement on any previous models, it is by no means ideal. For example, in accounting for the observed column density of CH^+ in S27, the predicted column density of OH with the same velocity component turns out to be at least a factor of eight larger than observation. Furthermore, more recent observations of the column density of CH^+ toward ζ Ophiuchi by Hawkins, Jura and Meyer (1985) indicate that the predicted column density could also be in error by a factor of four. This discrepancy would require an increase of the already high velocity of the shock to explain.

In an attempt to improve the predictions of the model, the model of Draine (1986) takes into account the effects of magnetic fields on the shock waves, while supporting the basic idea of Elitzur and Watson - that a shock is responsible for the production of CH^+ toward ζ Ophiuchi. Figure 4.4 is also a valid geometry for Draine's model. By adjusting a number of key parameters, a number of different models were obtained and discussed by Draine. All the models assumed a preshock density of $n_H = 20$ cm^{-3} and a preshock magnetic field of $B = 4.5\mu G$ perpendicular to the direction of propogation of the shock.

Draine concludes that a shock of velocity 9 kms^{-1} propagating into difuse molecular gas, at an angle of approximately 50° to the line of sight, appears to predict the column density and velocity of CH^+ very well (an improvement of 30% on Elitzur and Watson's model), while predicting reasonable values for OH, CH and rotationally excited H_2.

4.2.1.3 - The Supernovae Origin of a Shock in S27

Both of the above two shock models assume that the origin of the shock is in the HII region surrounding ζ Ophiuchi. Earlier on it was mentioned that another cause of shocks in the interstellar medium is supernovae. Smith, Krishna Swamy and Stecher (1978) point out that the 21cm pictures of Heiles (1976) show spherical filamentary structure in the region of ζ Ophiuchi centred on $l_{II} = 0°$ and $b_{II} = 24°$. This is close to the position of a hypothetical supernova in the Scorpius OB2 association which made ζ Ophiuchi a runaway star. It is a possibility (remote as it may be) that the shock passing through the ζ Ophiuchi region is associated with this supernova event, which took place approximately 1.1 million years ago (Blaauw 1964).

4.2.2 - Results of the 2.3 GHz Survey

Figure 4.5 is a contour plot of S27 and the surrounding area of sky. The map is taken from the same data set as the maps in Appendix One, and the contour levels are the same for this map as for the maps in Appendix One. Figure 4.5 is, however, plotted in Galactic coordinates with degrees of longitude and latitude on the horizontal and vertical axes respectively. Due to the high degree of confusion in the map (due to the fact that S27 is a relatively faint source at 2.3 GHz and is swamped by the Galactic disc emission in this plot), the area between the contours at levels 225 and 250 has been shaded. This shading only affords a very rough indication of the extent of the region, and is not intended to show the true extent of S27.

Figure 4.6 is a contour plot of S27 with the Galactic disc emission removed by method four discussed in Chapter Three. The bin width was 10°. Due to the low temperatures of the residual map, it was

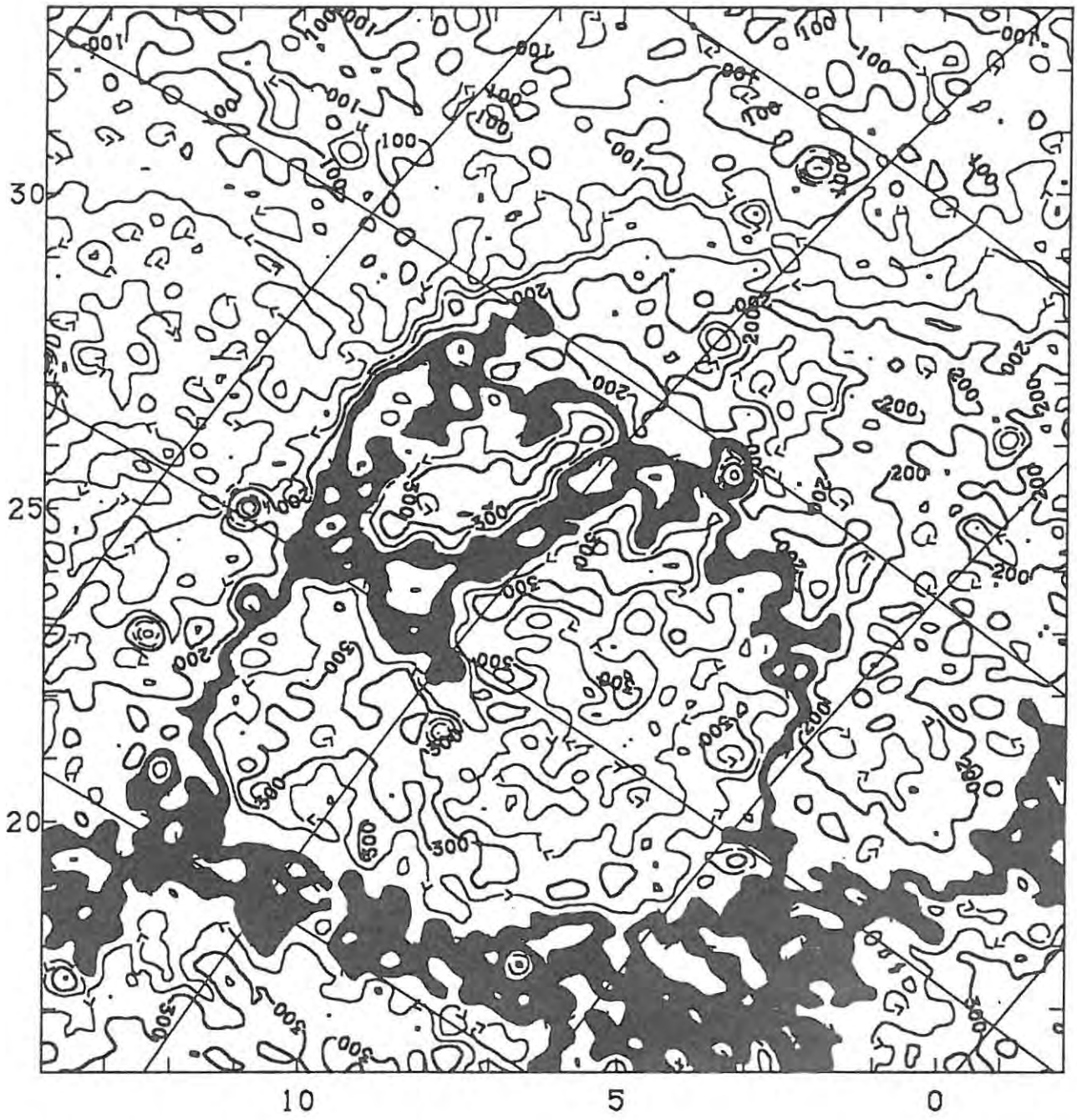

Figure 4.5 - Contour plot of S27 from the raw data. The area between contour levels 225mK and 250mK has been shaded as an indication of the position of the HII region. Contour levels are listed in Appendix One.

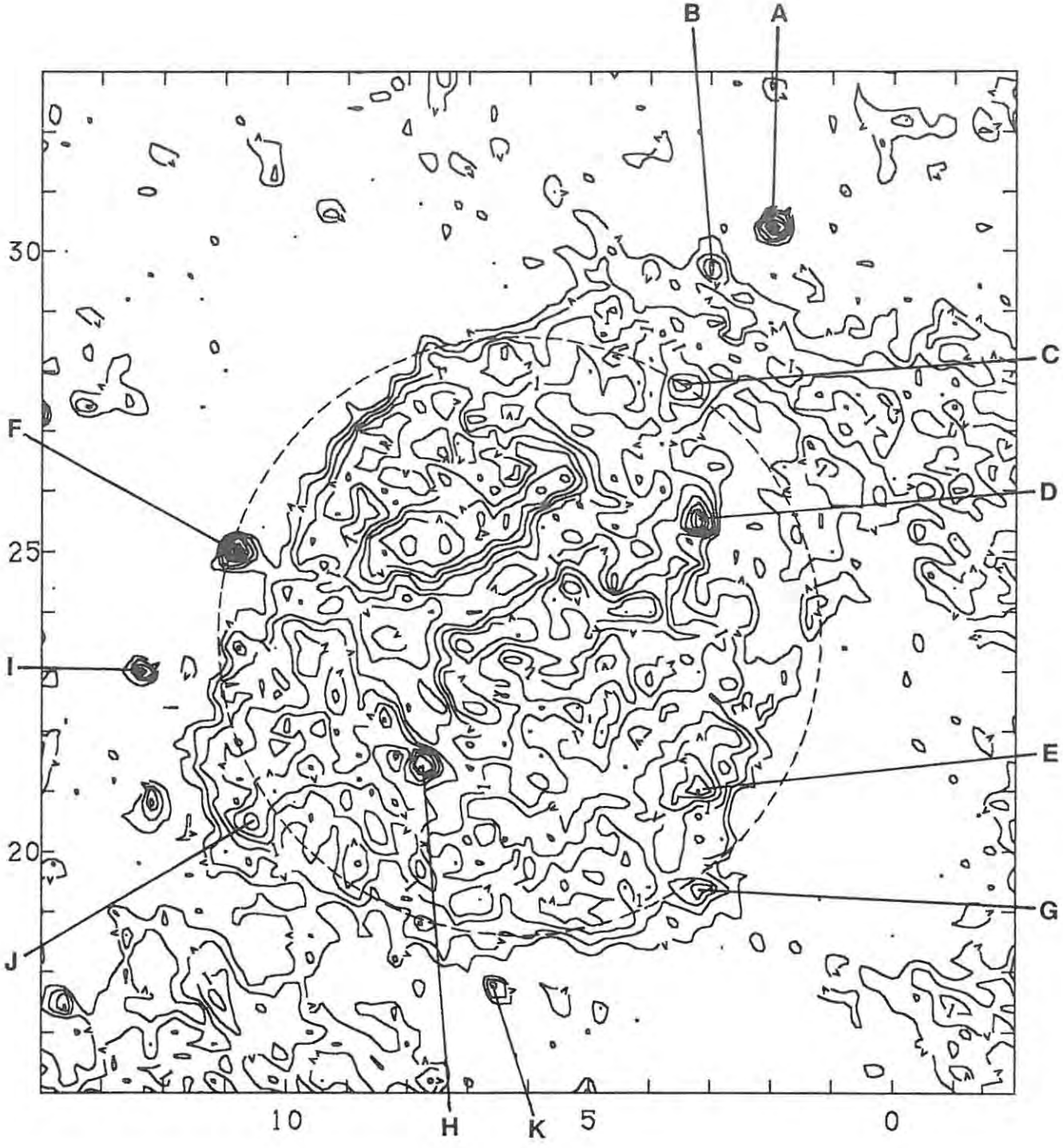

Figure 4.6 - Contour plot of S27 with the effects of the Galactic disc emission removed. The dashed circle has a radius of 5°. Contour levels for this plot are listed in table 4.1.

Table 4.1 - Contour levels for figure 4.6.

Contour Level Ta / mK	Contour Label	Contour Level Ta / mK	Contour Label
60	v	200	2
80	v	250	v
100	1	300	v
120	v	400	v
140	v	500	5
160	v	750	v
180	v	1000	v

necessary to plot this and other residual maps with a different set of contour levels. The contour levels for this plot are listed in table 4.1. In this plot, S27 appears to be almost circular with a diameter of approximately 10° - the dashed circle on the plot has a diameter of 10° and is centred on the position of ζ Ophiuchi. Towards the top right of this circular region is an extension which can be seen extending towards lower Galactic longitudes on this map and on the grey-scle images of the previous section.

A number of point sources, unrelated to S27, which were previously swamped by the Galactic disc emission are clearly seen in figure 4.6. They have been labelled according to their entry in table 4.2. The names and flux density at 408 MHz have been taken from the Molonglo reference catalogue of radio sources (Large *et al* 1981). Source types have been taken from the Parkes Master catalogue (Bolton *et al* 1979). The position, in Galactic coordinates, is the position of the peak antenna temperature at 2.3 GHz, and the flux density at 2.3 GHz was calculated by measuring the peak antenna temperatures after the subtraction of a base level (see Appendix Three) and substituting into equation 4.18. The spectral indices were calculated between the quoted 408 MHz and 2.3 GHz flux densities.

One source of interest is the source labelled "F" in table 4.2. In the column of 408 MHz flux densities, this source has the lowest value, whereas in the column of the 2.3 GHz flux densities it has the highest value, resulting in a rather high *positive* spectral index. It is possible that this is a variable source which has brightened between the time of the Molonglo survey and the current survey. Judging by the high galactic latitude of this source, it is likely to be extragalactic (ie - a galaxy or

Table 4.2 - Point sources located in the vicinity of ζ Ophiuchi.

	IAU Name	S_{408} Jy	Type	Glong °	Glat °	S_{2300} Jy	α
A	1602-093	6.08	III	2.0	30.4	2.46	-0.52
B	1607-091	4.06	III	2.9	29.7	0.81	-0.93
C	1614-099	3.36	Q	3.5	27.7	0.89	-0.77
D	1621-115	7.15	III	3.2	25.5	1.77	-0.81
E	1635-141	2.15	Q	3.2	21.1	1.03	-0.43
F	1639-062	0.72		10.8	25.0	2.54	+0.73
G	1640-153	4.40	III	3.1	19.4	0.74	-1.03
H	1644-106A	3.41	III	7.8	21.4	1.65	-0.42
I	1649-062	5.73	III	12.4	23.0	1.41	-0.81
J	1653-090	1.86	III	10.6	20.5	1.07	-0.32
K	1654-137	2.91	G	6.5	17.7	0.91	-0.67

quasar), and since there are many such objects known to to be variable, this a feasible proposition. Note that this object does not appear in the Parkes catalogue, is not seen on the 408 MHz maps of Haslam *et al* (1982) and is very weak on the 1420 MHz maps of Reich and Reich (1986). Further, no optical object is catalogued in the position of this source, according to the Master List of Nonstellar Astronomical Objects (Dixon and Sonneborn 1980). Another (more unlikely) possibility is that this source is a galactic thermal region which is optically thin at 2.3 GHz and optically thick at 408 MHz, resulting in a positive spectral index.

Shown in figure 4.7 is a grey-scale image of the same region shown in figure 4.6. The white areas on this image indicate antenna temperatures less than 60 mK, while the black areas indicate temperatures greater than 200 mK. An interesting feature which is difficult to detect on the contour maps but is clearly evident on this image, are the lanes of low antenna temperature cutting across the region. The overlying contour plot gives a clear indication of the positions of these lanes (the contours are at a level of 100 mK. Note that only the contours in the main body of the HII region have been plotted). In a recent paper by Celnik and Weiland (1988), an optical photograph and a Hα contour plot show evidence of lanes of low intensity in approximately the same positions as the lanes shown in figure 4.7. For comparison, figure 4.8 is a grey-scale image from the same residual data set of S27, except that the projection is now 1950 equatorial coordinates. The overlay is the Hα contour plot of Celnik and Weiland (the contour levels of this plot are not important here, except to note that the solid contours surround regions of *higher* intensity and the dashed contour lines

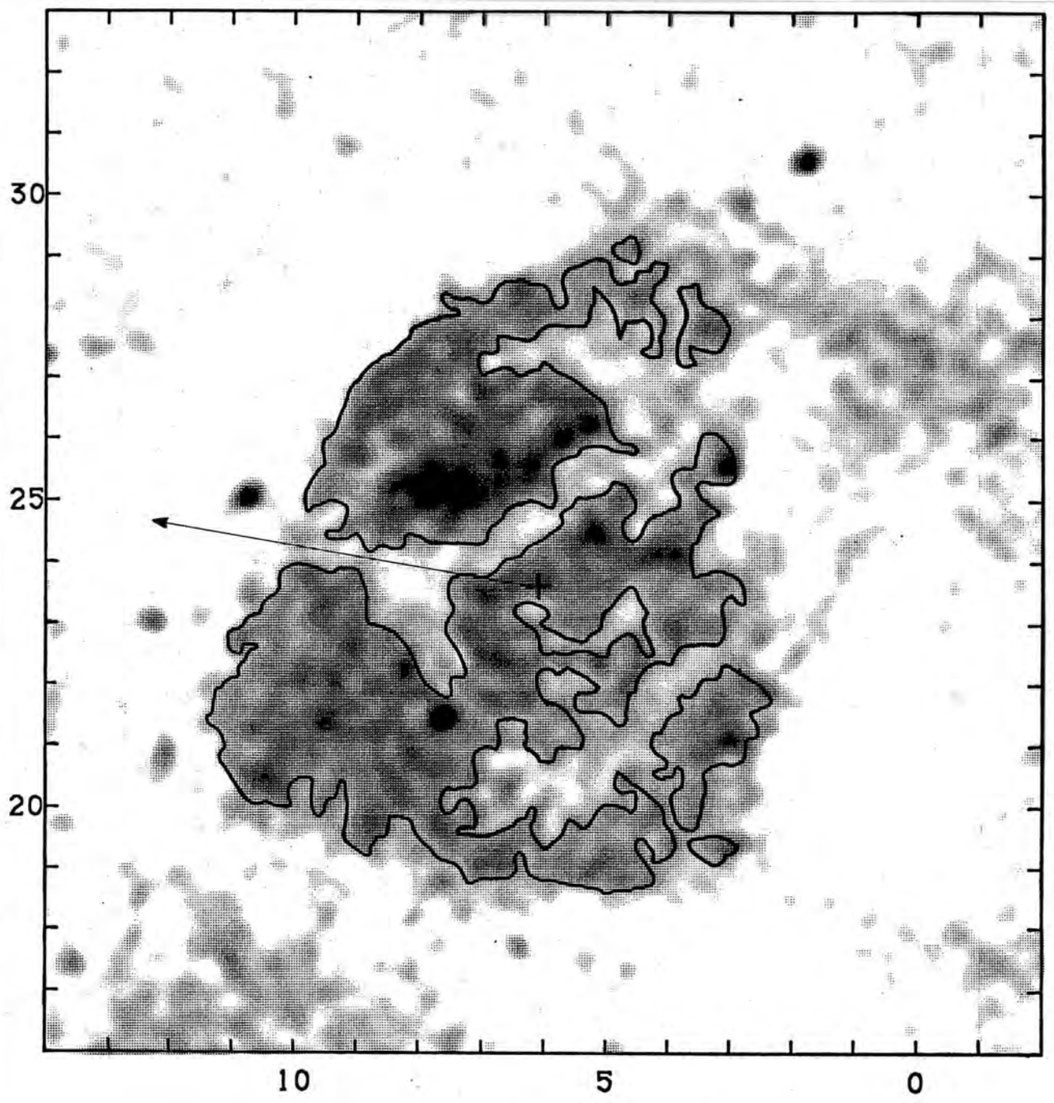

Figure 4.7 - Grey-scale image of the same region shown in figure 4.6. The contour level is 100 mK. The cross marks the position of the exciting star ζ Ophiuchi and the arrow indicates the direction of proper motion.

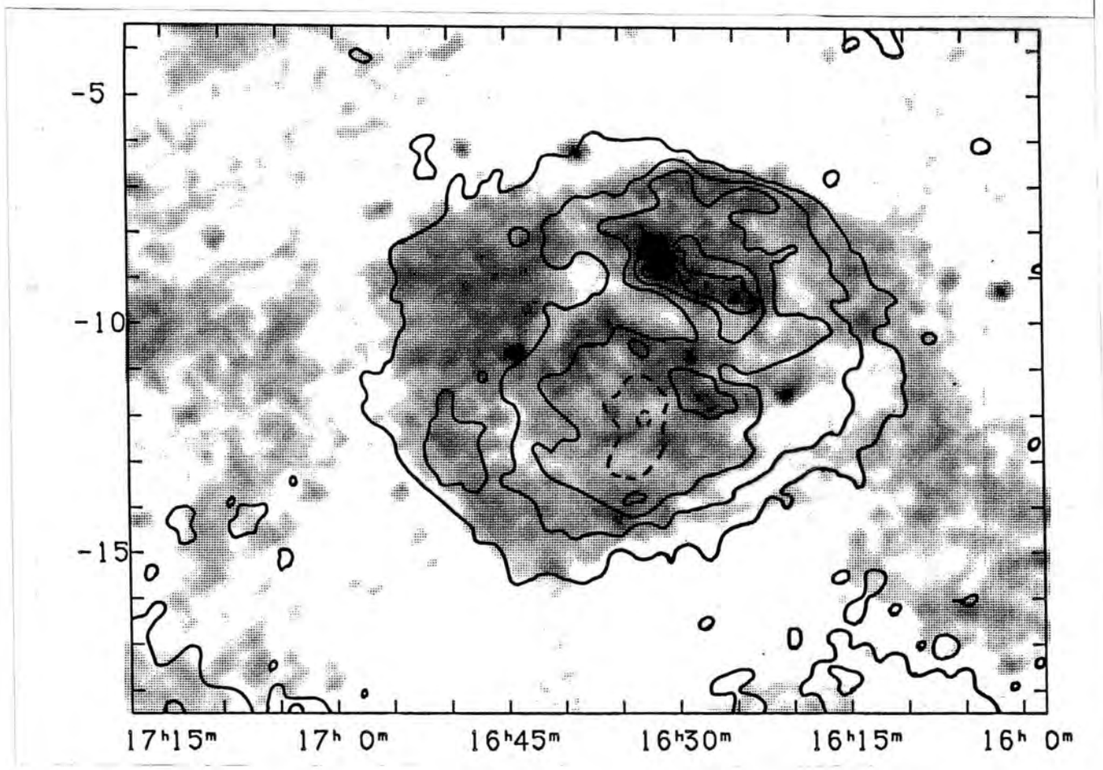

Figure 4.8 - Grey-scale image of S27 in 1950 equatorial coordinates. The contour plot is from the Hα data of Celnik and Weiland (1988). See text for details of contour levels.

surround regions of *lower* intensity than the surroundings). Note that, as should be expected, the approximate size of S27 in the Hα contour plot closely matches the size of the HII region in the 2.3 GHz data.

Two possible reasons for the existence of the lanes are a lower-than-average electron density and the presence of dust particles in these regions. The lanes cannot be caused by dust in the line of sight towards S27 since radio waves are capable of penetrating such dust. However, dust particles within the HII region itself will absorb some of the ionizing radiation from the exciting star, thus lowering the physical temperature in the region and hence lowering the rate of ionization. This would be an attractive hypothesis if it were not for the presence of a region of high intensity located on the opposite side of a lane from the exciting star, ζ Ophiuchi. The position of the exciting star is indicated on figure 4.7 by a cross and the peak emission of the HII region occurs at $l_{II} = 8°$ and $b_{II} = 25.1°$ - above and to the left of the star in figure 4.7. It would appear, therefore, that the first possibility mentioned above is the more feasible.

The arrow on figure 4.7 represents the direction of proper motion of the star ζ Ophiuchi. According to Blaauw (1964), ζ Ophiuchi is a member of the Scopius OB2 association and a runaway star. This means that ζ Ophiuchi formed in the region of this association (centred on approximately $l_{II} = 348°$ and $b_{II} = +20°$) as a secondary member of a binary or multiple star system. When the primary exploded as a supernova, the secondary was slung away from the system in such a way as to conserve the momentum of the system. The magnitude of the proper motion in the direction indicated in figure 4.7 is approximately 0.026 seconds of arc per year. If the direction of the proper motion is projected backwards, the position of the starting point of the star may be found, assuming that there is some way of determining approximately where or when the star started moving in its present direction. There are two ways of doing this - by finding out the approximate age of the OB association of which ζ Ophiuchi is a member and projecting back to this time, and by locating the point on the projected path that is closest to the centre of the association.

A program was written to calculate the position of a star at 100000 year intervals, given its right

ascension, declination, proper motion in both of these directions, radial velocity and distance. Another program calculated, also at intervals of 100000 years, the mean position of an association of stars, given the same data as above for each star. This program also calculated the standard deviation of the stars from this mean position, in parsecs. By assuming that all the stars of spectral type B3 and earlier are a representative sample of the association, an approximate age for the association can be found by determining the time of least standard deviation from the mean position of the stars. Using this method, the approximate age of the Scorpius OB2 association is 0.8 million years (somewhat less than Blaauw's (1978) estimate of 6.3 million years). This age is then an upper limit to the age of the hypothetical supernova that caused ζ Ophiuchi to become a runaway star. The second method mentioned above was also attempted, but it must be noted that this method relies on the assumption that the mean position of the association does not change with time. Since this assumption is not valid in the case of the Scorpius OB2 association (the mean position is moving in approximately the opposite direction to the motion of ζ Ophiuchi) this method is pursued no further here.

Figure 4.9 is a map of the Scorpius OB2 association. All of the stars used in the above computation are included on this diagram as filled circles. ζ Ophiuchi appears near the left edge of the diagram just below the -10° declination line. The open circles represent the positions of each of the stars (including ζ Ophiuchi) 0.8 million years ago, and the lines connecting the open and closed circles represent the path followed by each star in since this time. The large circle with the cross at 16^h 12.5^m right ascension and -16° 58′ indicates the position of the centroid of the stars, not including ζ Ophiuchi. Of interest here is the fact that ζ Ophiuchi certainly does appear to have come from the same star-forming cloud as the Scorpius OB2 association, and its proper motion, opposite in direction to the general motion of the association stars, lends support to the supernova hypothesis of Blaauw (1964). Also of interest with regards the proper motion of ζ Ophiuchi is the fact that the extension to the HII region, mentioned previously and seen in figure 4.7, appears to be parallel to the direction of motion of the star. This seems to indicate the possibility that this extension is a remnant of the star's passage through the region.

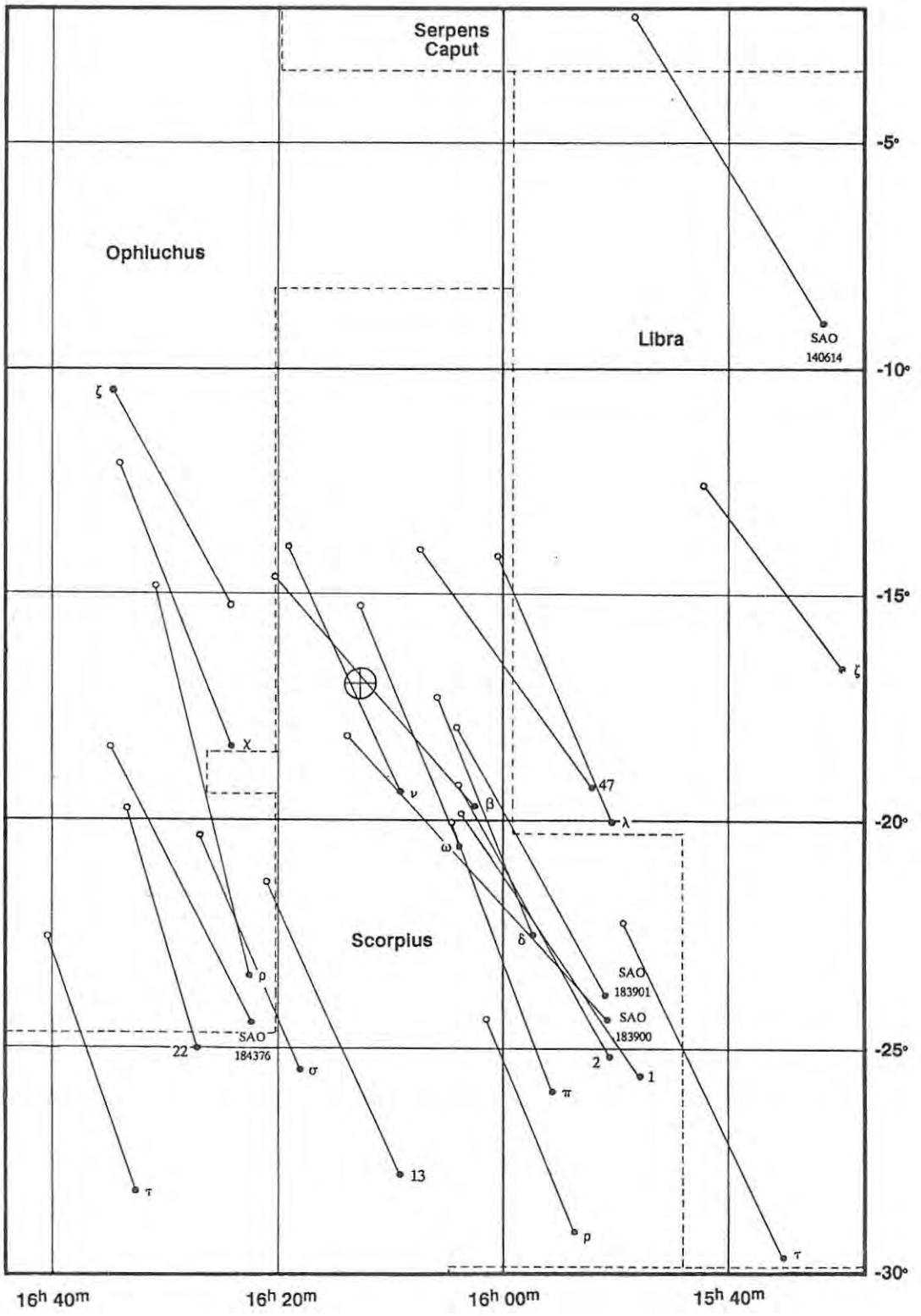

Figure 4.9 - Map of the Scorpius OB2 association. Filled circles are the current-day positions of the stars; open circles are their positions 0.8 million years ago.

A plot of the antenna temperature versus the radius of S27, averaged in annuli of width 0.2°, is presented in the top diagram of figure 4.10. The profile is centred on the position of ζ Ophiuchi. In the bottom diagram of figure 4.10 is a similar profile of the Hα intensity, from Celnik and Weiland (1988). Both profiles exhibit a sharp peak at the position of ζ Ophiuchi (ie - at r = 0) and a broad peak or flat region centred at a radius of about 2°. An average diameter for S27 can be determined from the top diagram by noting that the profile appears to level off between 5.5° and 6°. This value is in good agreement with the estimate stated previously. If, then, the average radius of the HII region is taken to be 6°, the physical radius is calculated to be approximately 14.7 parsecs, assuming a distance of 140 parsecs.

A number of physical parameters may be derived for the HII region surrounding ζ Ophiuchi. The following theory is developed specifically for the case of S27 and, therefore, may not be adequate as a model of HII regions in general.

According to equation 4.41, the brightness temperature of an HII region is given by

$$T_b = 8.235 \times 10^{-2}\, a\, T_e^{-0.35}\, \nu^{-2.1}\, E \qquad \ldots\ldots 4.41$$

where T_b is measured in Kelvin, T_e is the electron temperature in Kelvin, ν is the frequency in GHz, E is the emission measure in $cm^{-6}pc$ and the factor a is given by equation 4.37. The emission measure of an HII region is defined by equation 4.36 as

$$E = \int N_e^2\, dz \qquad \ldots\ldots 4.36$$

where N_e is the electron density in cm^{-3} and the integration is performed over the thickness of the region along the line of sight. In order to simplify the integrand it is necessary to make some assumptions about the geometry of the system. For the purpose of this calculation, it will be assumed that S27 is cylindrical, with radius r, length 2r and the axis of symmetry along the line of sight, and that the electron density of the region is constant, N_o. Equation 4.36 then becomes

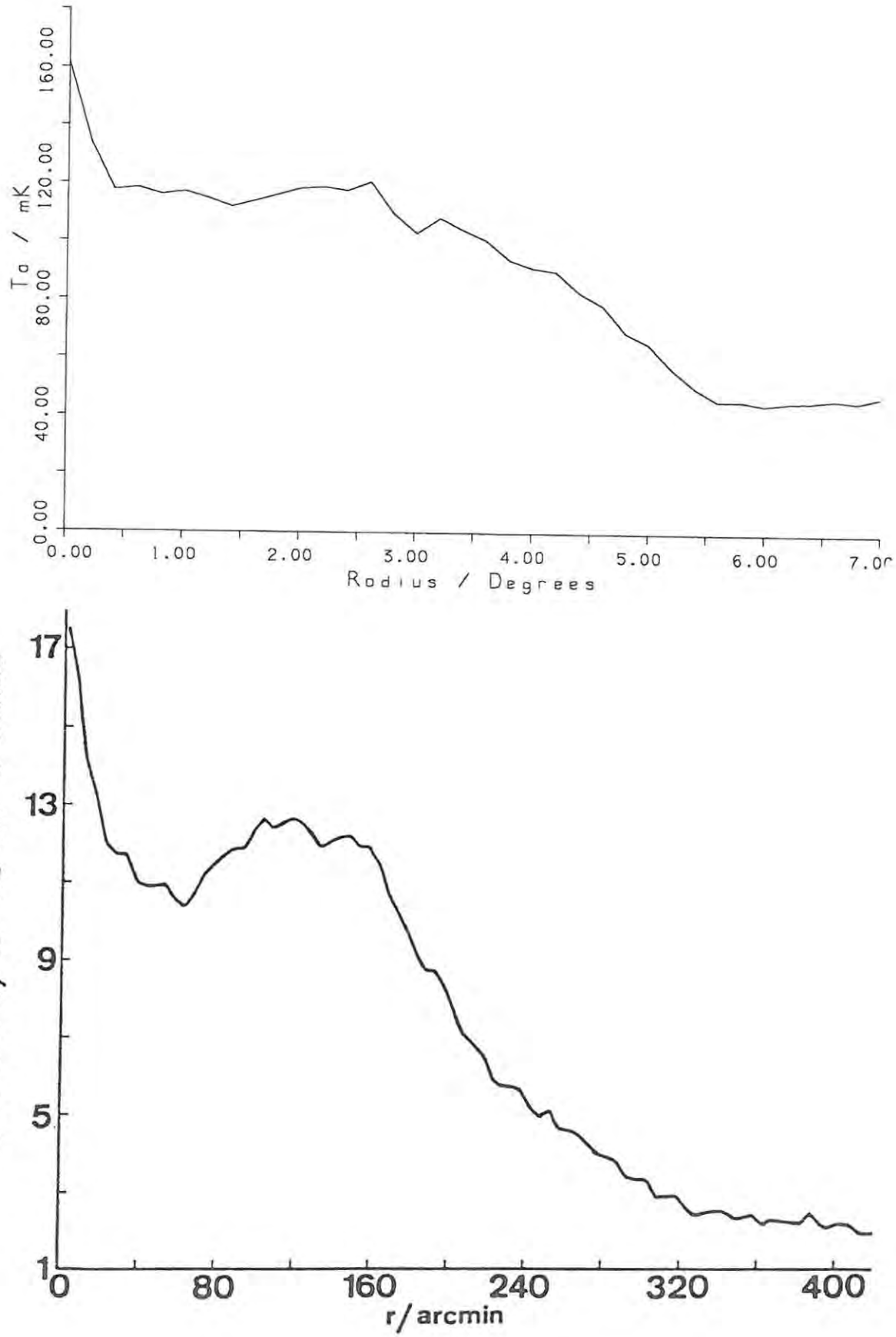

Figure 4.10 - Radial profiles of S27 from the 2.3 GHz data (top) and the Hα data of Celnik and Weiland (1988) (bottom).

$$E = N_o^2 \int_o^{2r} dz \qquad \ldots\ldots 4.62$$

yielding

$$E = 2 N_o^2 r \qquad \ldots\ldots 4.63$$

Substituting this expression into equation 4.41 yields, for the brightness temperature,

$$T_b = 0.1647\, a\, T_e^{-0.35}\, \nu^{-2.1}\, N_o^2\, r \qquad \ldots\ldots 4.64$$

A relation between brightness temperature and flux is given by equation 4.43, assuming a uniform brightness distribution:

$$T_b = S \lambda^2 / 2 k \Omega_s \qquad \ldots\ldots 4.65$$

where S is in Jy, λ is in metres, k is Boltzmann's constant and Ω_s is in steradians. So equation 4.64 becomes

$$S \lambda^2 = 454.8\, a\, T_e^{-0.35}\, \nu^{-2.1}\, N_o^2\, r\, \Omega_s \qquad \ldots\ldots 4.66$$

If the angular radius of the HII region is small, the physical radius may be approximated by

$$r \approx D \theta \qquad \ldots\ldots 4.67$$

where D is the distance of the HII region in parsecs and θ is the angular radius in radians. The source solid angle is given by

$$\Omega_s = \pi \theta^2 \qquad \ldots\ldots 4.68$$

Substituting these expressions into equation 4.66 yields

$$S\lambda^2 = 454.8\, a\, T_e^{-0.35}\, \nu^{-2.1}\, N_o^2\, D\, \pi\, \theta^3 \qquad \ldots\ldots 4.69$$

Hence, to find electron density, this equation becomes

$$N_o^2 = 2.2\times10^{-3}\, S\lambda^2\, T_e^{0.35}\, \nu^{2.1} / D\, \pi\, \theta^3\, a \qquad \ldots\ldots 4.70$$

Now, $\lambda = {}^{c}/_{\nu}$. So, with λ in metres and ν in GHz, c is 0.299793, and equation 4.70 becomes

$$N_o^2 = 6.29\times10^{-5}\, S\, T_e^{0.35}\, \nu^{0.1} / D\, \theta^3\, a \qquad \ldots\ldots 4.71$$

and

$$N_o = 7.93\times10^{-3}\, S^{0.5}\, T_e^{0.175}\, \nu^{0.05} / D^{0.5}\, \theta^{1.5}\, a^{0.5} \qquad \ldots\ldots 4.72$$

The integrated flux density of S27 from the 2.3 GHz data is approximately 392 Jy. Assuming an electron temperature of 7000K, the factor a becomes 0.9954. The distance of S27 is 140pc and the angular radius is 0.096 radians. In order to compensate for the fact the S27 does not have a cylindrical geometry or uniform surface brightness, the radius at half-power (0.078 radians) is used. Substituting these values in to equation 4.72 yields a value for the electron density of $N_o = 3.0\ cm^{-3}$.

The mass of ionized hydrogen in an HII region can be obtained by multiplying N_o by the volume of the region, V, and the mass of a hydrogen atom, m_H ($= 1.67333 \times 10^{-27}$ kg). The volume is given by

$$V = 1.23\times10^{56}\, r^3 \qquad \ldots\ldots 4.73$$

where V is in cm^3 and r is the radius in parsecs. Hence, substituting for r from equation 4.67 and multiplying by m_H,

$$M = 2.056 \times 10^{29} N_o D^3 \theta^3 \quad \ldots\ldots 4.74$$

where M is in kg. To find M in terms of solar masses, divide this equation by the mass of the sun ($M_\odot = 1.991 \times 10^{30}$ kg) to get

$$M = 0.103 N_o D^3 \theta^3 \quad \ldots\ldots 4.75$$

Hence, substituting for N_o, D and θ from above, the mass of S27 is $M = 400 M_\odot$.

Emission measure was defined by equation 4.63 for a uniform density, spherical HII region. Writing r in terms of D and θ,

$$E = 2 N_o^2 D \theta \quad \ldots\ldots 4.76$$

and the emission measure for S27 is calculated to be $E = 197$ cm^{-6}pc. It is now possible to calculate a value for the optical depth of S27. Using equation 4.38, $\tau = 1.8 \times 10^{-5}$.

The excitation parameter of an HII region is given by (Churchwell and Walmsley 1973)

$$U_{rad} = 0.044 \nu^{0.03} T_e^{0.12} D^{0.67} S^{0.33} \quad \ldots\ldots 4.77$$

where U_{rad} is in cm^{-2}pc. Therefore, for S27, the excitation parameter is $U_{rad} = 25.8$ cm^{-2}pc. For an O9.5V star, the excitation parameter is (Panagia 1973) $U_* = 30.5 \pm 6.0$ cm^{-2}pc. If the value of U_{rad} is less than the value of U_* then the HII region is said to be density-bounded, meaning that the flux of ionizing photons from the exciting star is more than sufficient to explain the excitation of the region. If U_{rad} is equal to U_*, the region is ionization-bounded, meaning that all of the ionizing photons emitted by the star are absorbed by the HII region. Thus, from the above calculation, it can be concluded that, since U_{rad} is within the limits of uncertainty quoted by Panagia (1973) for U_*, S27 is ionization-bounded. This conclusion is supported by the presence of pre-shock gas in the

model of Draine (1986), illustrated in figure 4.4.

The flux of continuum Lyman photons from the star required to maintain an HII region is given by (Jonas 1982)

$$L_c = 4.7613 \times 10^{42} S D^2 T_e^{-0.45} \nu^{0.1} \quad \ldots\ldots 4.78$$

For S27, this yields a value of $L_c = 10^{47.87}$ s^{-1}.

According to Stromgren (1936), if re-radiation from ionized hydrogen is neglected, a star of effective temperature T_s and radius R_s will be capable of supporting an HII region of radius r, where r is given by

$$\log (r N_e^{0.67}) = -0.44 - (22730 / T_s) + \log T_s^{0.5} + \log R_s^{0.67} \quad \ldots\ldots 4.79$$

where r is in parsecs, N_e is the electron density in cm^{-3}, T_s is in Kelvin and R_s is in solar radii. Panagia (1973) gives T_s to be 33000K and R_s to be 7.94 $R_\odot$ for a typical O9.5V star. Assuming these values to be correct for ζ Ophiuchi and using the previously determined value for N_e, yields a Stromgren radius of r = 26 pc.

One parameter which has so far been neglected is the spectral index. In order to obtain an estimate of the spectral index of S27, longitude scans at $b_{II} = 25°$ were taken through the 408 MHz map of the region and the 2.3 GHz data. The 2.3 GHz data was smoothed by the application of a Gaussian filter to the resolution of the 408 MHz data. Figure 4.11 shows these longitude scans (note that the vertical axis on the 408 MHz longitude scan represents brightness temperature, while on the 2.3 GHz scan it represents antenna temperature - the conversion factor from antenna temperature to brightness temperature is 1.51). The temperature at $l_{II} = 12°$ was taken as the base level for each of the scans. The brightness temperatures relative to this base level were measured from the scans at 1° intervals in longitude. These temperatures are recorded in columns 2 and 3 of table 4.3, with the respective

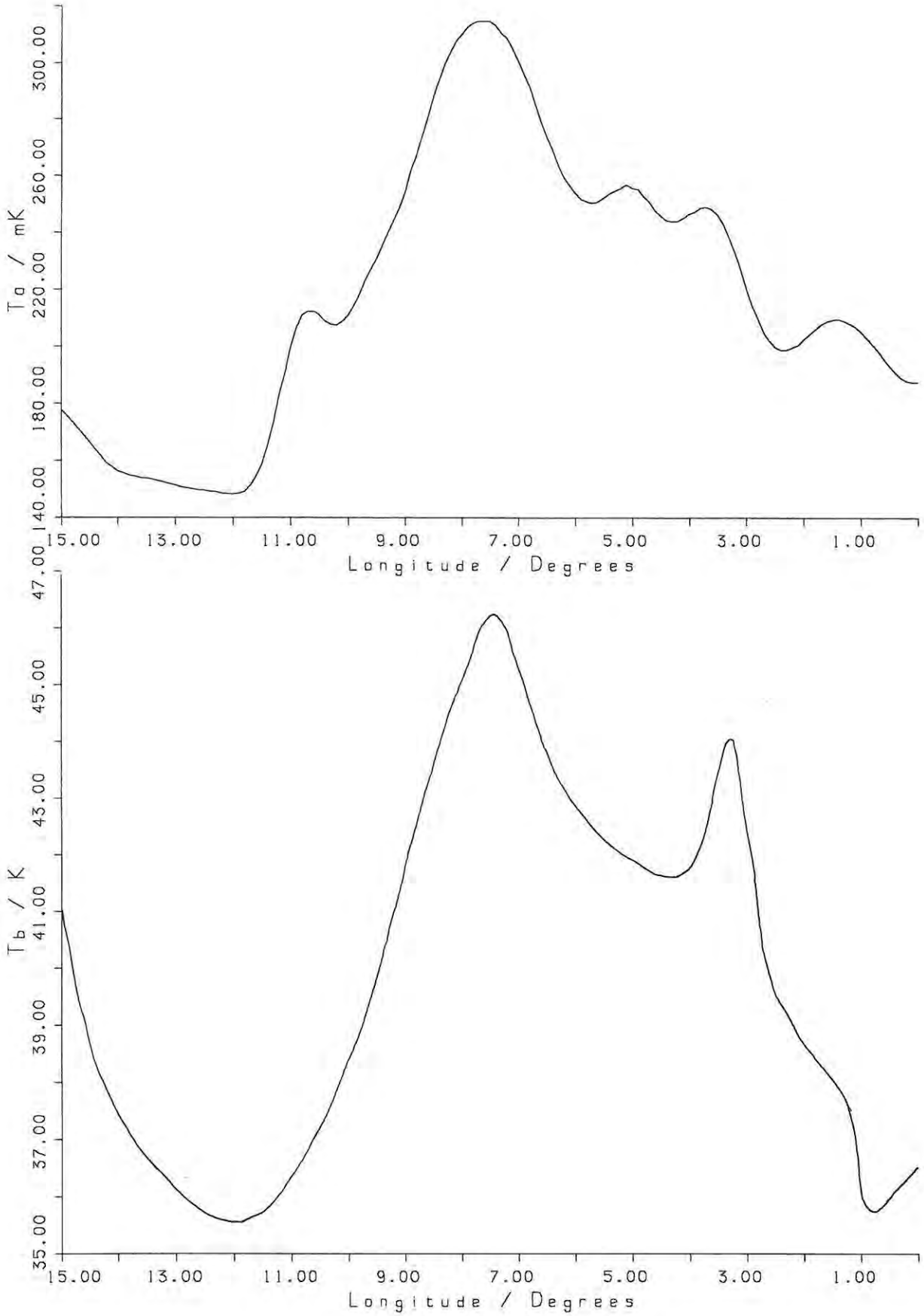

Figure 4.11 - Longitude scans ($b_{II} = 25°$)

through the 2.3 GHz (top) and 408 MHz

(bottom) data.

longitudes in column 1. Column 4 contains the spectral index calculated from these two brightness temperatures using the relation

$$T_{b1} / T_{b2} = (\nu_1 / \nu_2)^{\alpha - 2} \qquad \ldots\ldots 4.80$$

where T_{b1} is the brightness temperature at ν_1 (=408 MHz), T_{b2} is the brightness temperature at ν_2 (=2.3 GHz) and α is the spectral index.

Table 4.3 - Spectral index of S27 calculated at 1° intervals along a scan at b_{II} = 25°.

Longitude	T_b(408)	T_b(2300)	α
2°	3.20K	0.083K	-0.11
3°	6.80K	0.109K	-0.39
4°	6.20K	0.149K	-0.16
5°	6.35K	0.164K	-0.11
6°	7.30K	0.162K	-0.20
7°	9.70K	0.232K	-0.16
8°	9.60K	0.247K	-0.12
9°	6.20K	0.160K	-0.11
10°	2.80K	0.096K	+0.05
11°	0.85K	0.079K	+0.70

The spectral index for longitudes 10° and 11° have obviously been affected by the unusual source ("F" in table 4.2) with a positive spectral index. The spectral index at 3° has been affected by the presence of source "D" (table 4.2). The remaining seven spectral indices can be taken as representative of the HII region, averaging to α = -0.14, the spectral index of a thermal region. In order to get a more reliable estimate of the spectral index from this method, the above procedure should be carried out over a two-dimensional grid of temperatures covering the entire HII region.

Table 4.4 is a summary of the physical parameters of the HII region surrounding ζ Ophiuchi, as calculated from the 2.3 GHz data. Since a number of assumptions have been made throughout these calculations, it is difficult to assign a limit to the accuracy of these values. A conservative estimate, based mainly on the uncertainty in the integrated flux measurement, is 25% on all calculated values.

Table 4.4 - Physical parameters of the HII region surrounding ζ Ophiuchi (S27).

Distance	=	140 pc (Draine 1986)
Stromgren radius	=	26 pc
Actual radius	=	14.7 pc
Integrated flux density	=	392 Jy
Electron temperature	=	7000 K (estimated)
Electron density	=	3.0 cm^{-3}
Mass of ionized hydrogen	=	400 $M_\odot$
Emission measure	=	192 $cm^{-6}pc$
Optical depth	=	1.8×10^{-5}
Excitation parameter	=	25.8 $cm^{-2}pc$
Lyman continuum flux	=	$10^{47.87}$ s^{-1}
Spectral index	=	-0.14

4.3 - The North Polar Spur

4.3.1 - Literature Survey

As with ζ Ophiuchi and its associated HII region, the north polar spur (NPS) is the most well-studied object of its type in the sky. It is by far the largest member of a group of radio continuum spurs which extend into intermediate Galactic latitudes. The existence of this structure was noted in the very early days of radio astronomy, at the time when radio telescopes were incapable of producing high quality, high resolution maps of the sky. Figure 4.12 is one of the earliest large-scale maps clearly indicating the presence of the NPS. It is a map of brightness temperature at 200 MHz published by Oort (1959) and shows the NPS extending out of the top of the Galactic plane towards the north Galactic pole. The origin of this object has been cause for much speculation and debate over the years and many models have been produced in an attempt to explain what we see. Thus, although some basic observational facts of the NPS are presented, this section deals mainly with these models in an attempt to understand the present knowledge of the origin and nature of the NPS.

The NPS is a section (approximately 60° long) of a much larger structure called Loop I. Loop I forms a small circle on the sky centred on l_{II} = 329° and b_{II} = 17.5° and having a radius of

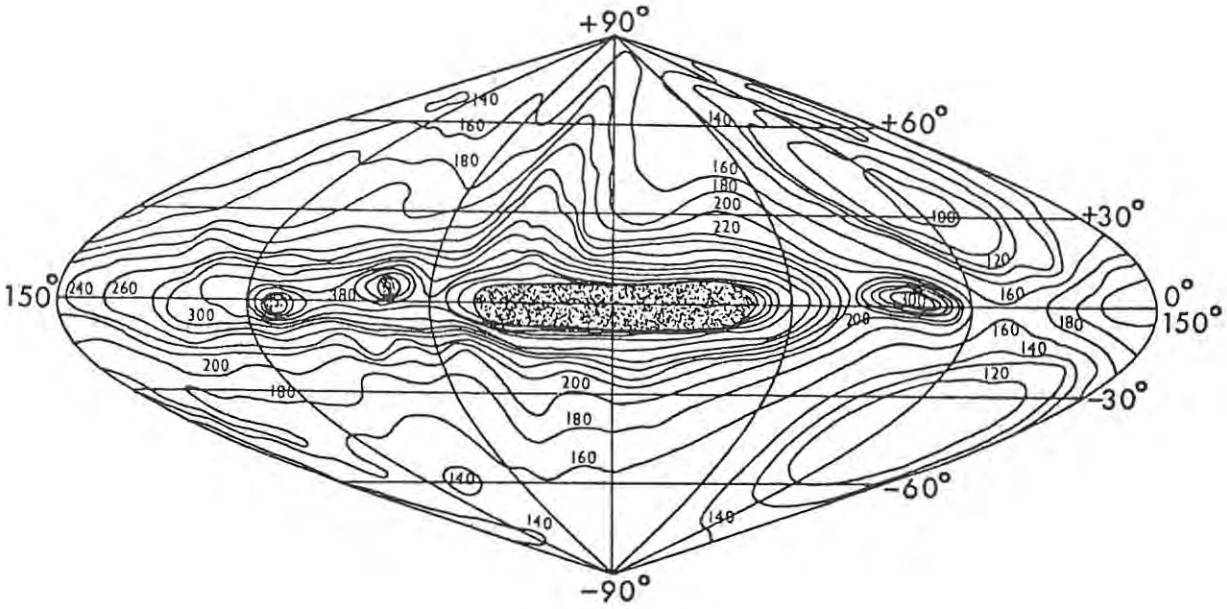

Figure 4.12 - A radio map of the sky at a frequency of 200 MHz (in old galactic coordinates) clearly revealing the presence of the north polar spur (after Oort 1959).

approximately 116° (Salter 1970). Distance estimates are many and varied, ranging from 100 pc to 8 kpc, depending on the model adopted. The most commonly quoted distance, however, is 130 pc, the distance of the centre of Loop I adopted by Berkhuijsen (1973). At this distance, the angular radius of 58° corresponds to a physical radius of 110 pc and a distance of approximately 70 pc for the NPS (if the NPS is assumed to be part of a shell viewed tangentially). The distance of the centre of Loop I above the Galactic plane is approximately 40 pc.

Observations of the NPS have indicated that it extends approximately from l_{II} = 26° and b_{II} = 10° towards the north Galactic pole, reaching latitudes greater than b_{II} = 70°. Salter (1970) has indicated the possible presence of an extension of the NPS to the far side of Loop I (b_{II} = 270°). Most of the observations to date have been unable to resolve the narrowest parts of the NPS, indicating a shell thickness in these regions of less than 0.7 pc. Sofue and Reich (1979) have studied an extension of the NPS towards the Galactic plane (b_{II} < 10°), but up to the present time, no observations have convincingly indicated the presence of a negative latitude extension of the spur. Observations of soft

X-rays and neutral hydrogen have shown a concentric shell structure associated with the NPS, and most obervations suggest a small-scale ridge structure superimposed on a structure with a larger spatial scale.

Berkhuijsen (1973) has made measurements of the average surface brightness of the NPS by dividing the region up into several segments and combining the estimates for each section, after a background level was subtracted. She found an average surface brightness at 1 GHz of $\Sigma = 2.1 \times 10^{-22}$ W m^{-2} Hz^{-1} $ster^{-1}$. Her brightness temperatures of 0.70K at 1 GHz and 1.2K at 820 MHz yields a spectral index of $\alpha = -0.72$, indicating the involvement of a synchrotron mechanism in the production of the emission.

Of all the models suggested over the years for the nature and origin of the NPS, only one has received acceptance from radio astronomers - the model of a supernova outburst occuring in the region of the Scorpius-Centaurus OB association. However, in order to obtain a comparison between models, two further models will be described - a model involving the propogation of magnetohydrodynamic waves from the Galactic centre and a model relating the NPS to spiral arms in the Galaxy.

4.3.1.1 - The NPS as a wave front propogating from the Galactic centre

Sofue (1977) has proposed that an explosion at the Galactic centre could radiate isotropic, magnetohydrodynamic waves which would propogate through the Galactic halo until being eventually reflected back towards the Galactic disc again. The percentage of the original waves reflected would depend on the assumptions made, but in general, more than 80% of the waves will be reflected. Most of these reflected waves will be focused onto a ring in the Galactic plane, but some of them will continue to expand forming a large, near-spherical shell structure in the halo of the Galaxy. Figure 4.13 shows two views of a wave front expanding into the halo of the Galaxy - the top diagram as seen from a Galactocentric latitude of 30° and the bottom diagram as seen from the position of the sun. The bottom diagram has a Galactic coordinate grid for easy comparison with observations.

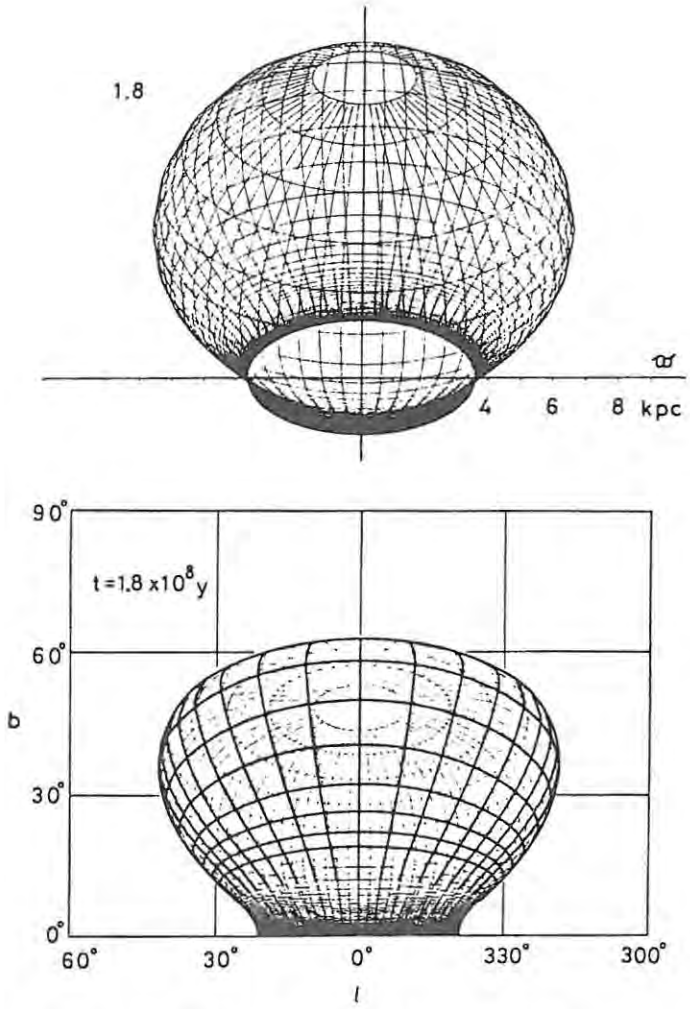

Figure 4.13 - Two views of a magnetohydrodynamic wave front propogating from the Galactic centre as seen from a galactocentric latitude of 30° (top) and from the sun (bottom) (after Sofue 1977).

This model was originally suggested to explain the origin of the arm of the Galaxy located at a Galactocentric radius of 3.5 kpc. As can be seen from figure 4.13 (which is for a time 180 million years after the explosion at the Galactic centre), the majority of waves have been focused onto a ring with a radius of approximately 3.5 kpc. In reproducing this ring, however, a shell structure analagous to the shell structure of Loop I and the NPS is produced. Figure 4.14 compares the wave front produced by this model, for times between 170 and 200 million years, with the radio structure of the Galaxy at 150 MHz. The fit to the NPS is rather poor, but of interest is the fact that a number of

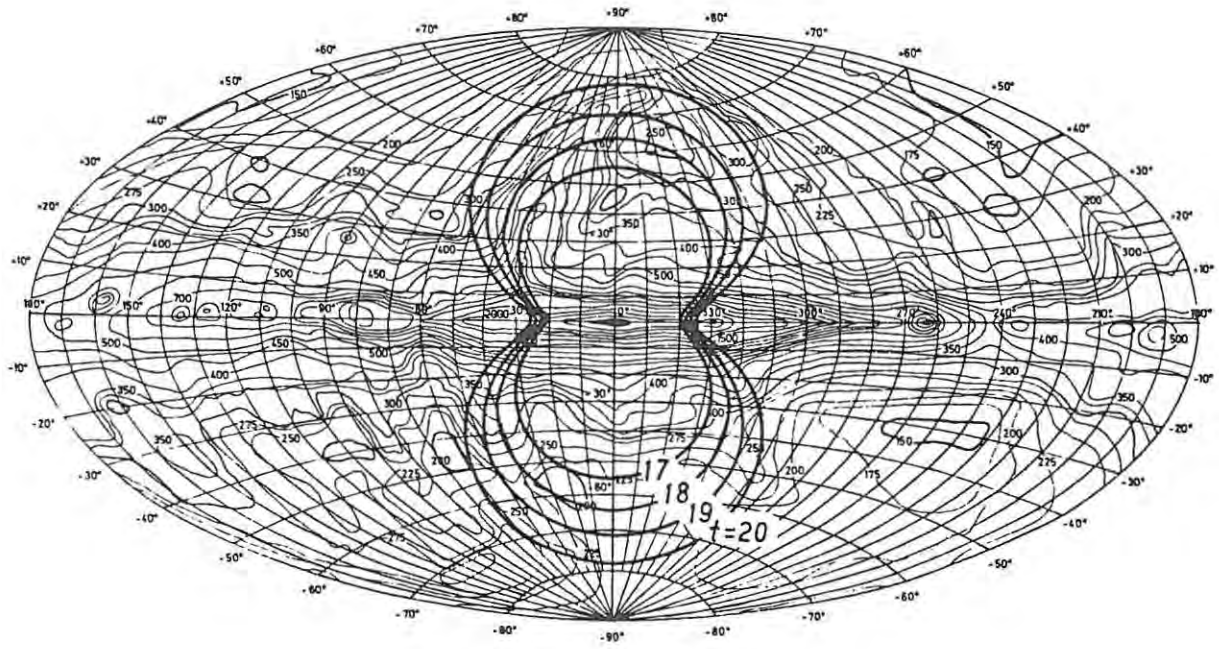

Figure 4.14 - A comparison of the results of the Sofue (1977) model with observation. The radio map is the 150 MHz map of Landecker and Wielebinski (1970) (after Sofue 1977).

other spurs appear to fit the wave front (for example, a spur at l_{II} = 330° and b_{II} = -20°). If this model were correct, it would imply a distance of approximately 8 kpc for the NPS

4.3.1.2 - The association of the NPS with spiral arms

This model, also proposed by Sofue (1973), suggests that the NPS is a bank-shaped, radio-emitting region located on a link between the local and Sagittarius arms of the Galaxy. This bank, which emits non-thermal radiation, is produced by the interaction of shock waves with the gaseous arms of the Galaxy, producing inflation of the the magnetic field and cosmic rays above the arms. The model assumes that the bank extends vertically upward from the plane to a height of about 1 kpc and that the radio emissivity is constant up to this height and proportional to the density of the gas in the Galactic plane at that Galactocentric radius. At heights greater than 1 kpc above the plane, the radio emissivity is assumed to be zero. Figure 4.15 shows this geometry for a line of sight towards the

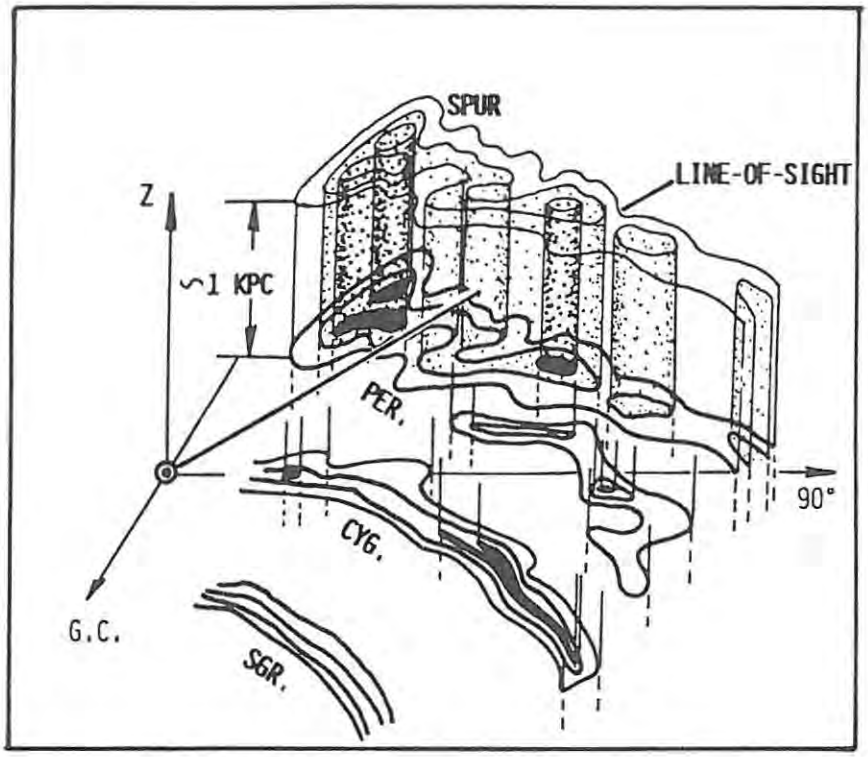

Figure 4.15 - The geometry of the non-thermal banks proposed as an explanation for the origin of the radio spurs (after Sofue 1976).

Perseus arm. A further assumption is that the NPS is located, not directly above an arm, but above a link with a length of between 1 pc and 2 pc stretching from the region of the sun towards the Sagittarius arm.

4.3.1.3 - The NPS as a supernova remnant

Observational evidence is overwhelmingly in favour of a supernova event being the origin of Loop I and the NPS. This idea was first suggested by Hanbury Brown *et al* in 1960, and since then, the model has developed, with the aid of improved theory and observational results, to the stage where it satisfactorily explains most of characteristics of the NPS.

The basic idea behind the model is that a very massive star explodes and creates an expanding shell of gas known as a supernova remnant. The evolution of such a remnant can be divided into four

parts - the free-expansion, adiabatic-expansion, isothermal-expansion and extinction phases. In the first phase, the physics of the remnant is dominated by the properties of the explosion itself. The expansion velocity of the remnant at this stage is in the region of 10000 kms^{-1} and the duration is about 100 years. This is a very short time on astronomical time scales and is therefore not considered further here. As the remnant expands into the local interstellar medium of the star, it begins to sweep up gas and dust in its path. In the second phase, the remnant is dominated by this swept-up material and very little energy radiation takes place (hence the name of this phase). This phase lasts for tens of thousands of years, during which time the remnant expands to a diameter in the region of 10 pc and the velocity of the remnant drops to about 200 kms^{-1}. As the velocity of the shell drops, radiative losses become more significant, and begin to dominate the remnant as the velocity drops below 200 kms^{-1}. This is the beginning of the third phase, a phase which is destined to last for many hundreds of thousands of years. It is during this phase of evolution that a dense shell of neutral hydrogen forms on the leading edge of the remnant. The third phase ends when the expansion velocity of the remnant has dropped to the value of the random motions of the interstellar medium (approximately 10 kms^{-1}). At this stage, the remnant has a radius of the order of 30 pc and is beginning to merge into the interstellar medium.

The number of known supernova remnants in the Galaxy is fast approaching the two hundred limit, indicating that supernova events are not particularly unusual (Clark and Caswell (1976) estimate that one supernova capable of producing an observable remnant occurs every 150 years). What is unusual, however, is the large angular size of the NPS - most of the known supernova remnants have angular diameters in the region of half a degree, whereas the NPS (or more specifically, Loop I) has an angular diameter of 116°. How is it possible that the NPS could have such a large diameter? The answer to this question lies in the fact that the above theory for the evolution of a supernova remnant makes the assumption that the supernova occured close the the plane of the Galaxy where the density of the interstellar medium is highest, on average. No account is taken of the possibility that a supernova could occur at a high Galactic latitude, where the average density of the interstellar medium is far below that of the plane. This fact leads to the first correlation between the observations and the model - the centre of Loop I, and hence of the NPS, is located at a Galactic

latitude of b_{II} = 17.5°. Another piece of observational evidence which supports the supernova remnant hypothesis is the fact that Loop I and the NPS trace out an almost perfect small circle on the sky. Figure 4.16 shows the four major loop structures modelled by small circles (Loop I is the largest of these loops), clearly showing the goodness of fit of the small circle to the observed structure of the NPS.

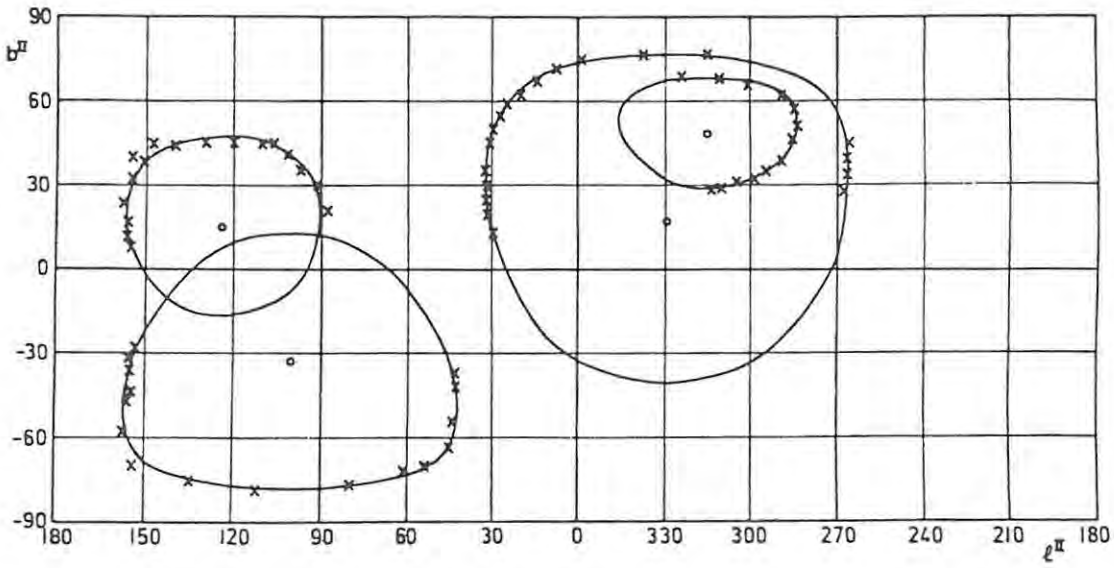

Figure 4.16 - Small circles fitted to the observations of the peak emission (X) for each of the four major loop structures (after Salter 1970).

Further evidence in support of this model comes from the apparent relationship between the NPS and the observed distribution of neutral hydrogen in the vicinity of the spur, and between the NPS and observations of soft X-ray emission. Assuming that the NPS is a very old supernova remnant, well into the radiative phase of its evolution, it is to be expected that a shell of neutral hydrogen should be associated with the spur, due to the fact that, as the remnant expands, it sweeps up neutral hydrogen in its path. Thus, it is also to be expected that such a shell should be located on the outside of the small circle defining the approximate extent of Loop I. Much work has been carried out in this area, and the conclusion reached is always in support of this association. Figure 4.17 illustrates the association well on a map of McGee *et al* (1959) giving the distribution of the peak brightness

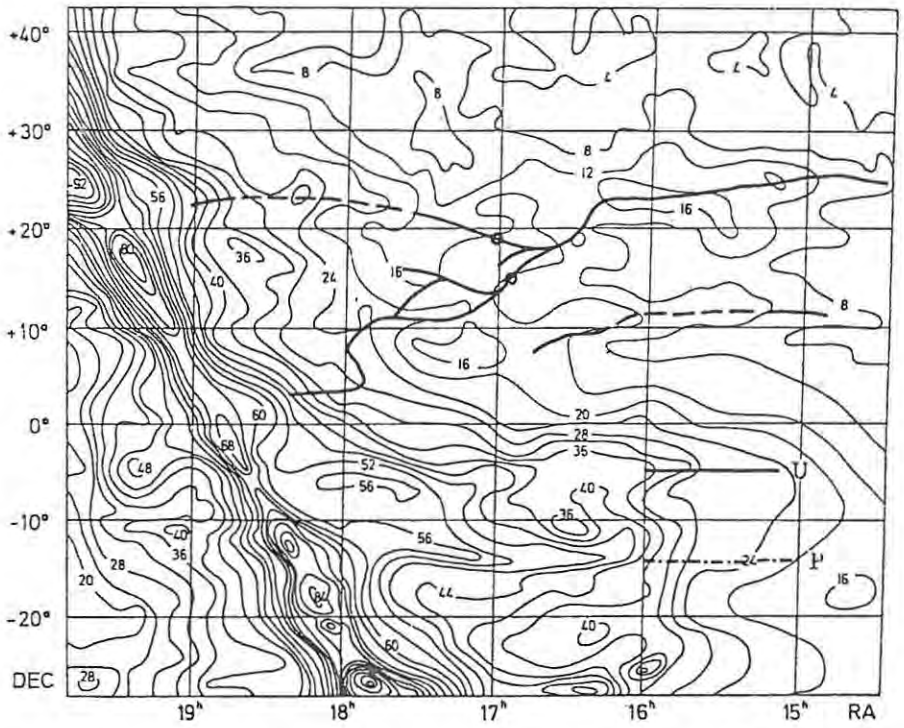

Figure 4.17 - A map of the brightness temperature distribution profiles of neutral hydrogen (McGee et al 1959) with superimposed lines indicating the positions of the steep gradients at the edges of the NPS (after Berkhuijsen et al 1971). Note the coincidence of these (bold) lines with the spurs observed in the neutral hydrogen distribution.

temperature of hydrogen profiles. It is of interest to note that Berkhuijsen *et al* (1971) report that the position of the maximum density of neutral hydrogen lies approximately 5° on the outside of the radio continuum maximum, as expected.

The association of soft X-rays with the NPS is rather more difficult to explain, and it was for this reason that Borken and Iwan (1977) proposed a slight revision to the basic supernova remnant model. The problem arises in the fact that, for a supernova remnant of the assumed age and size of the NPS, there should not be any observable X-ray emission. Seward *et al* (1976) have determined

that, for remnants with diameters greater than 25 to 50 pc, the emission of X-rays falls to very low values, and so, for the immense diameter of the NPS, any X-rays associated with the intitial explosive event should have dissipated a long time ago. Cruddace *et al* (1976) have suggested that these X-rays are, in fact, due to the original supernova event, assuming that the supernova was extremely energetic. While the energy of an average supernova is in the region of 10^{43} J, the model of Cruddace *et al* (1976) requires the released energy to be of the order of 10^{46} J. Hayakawa *et al* (1977) have suggested that the density of the interstellar medium local to the star prior to explosion was smaller than average (in the region of 10^{-2} cm^{-3}), allowing an average energy for the supernova explosion. The model of Borken and Iwan (1977), however, is probably the most convincing. They suggest that the NPS is a very old supernova remnant which has been reheated by the intersection of another, younger supernova remnant. They also suggest that Loop IV is the remnant responsible for

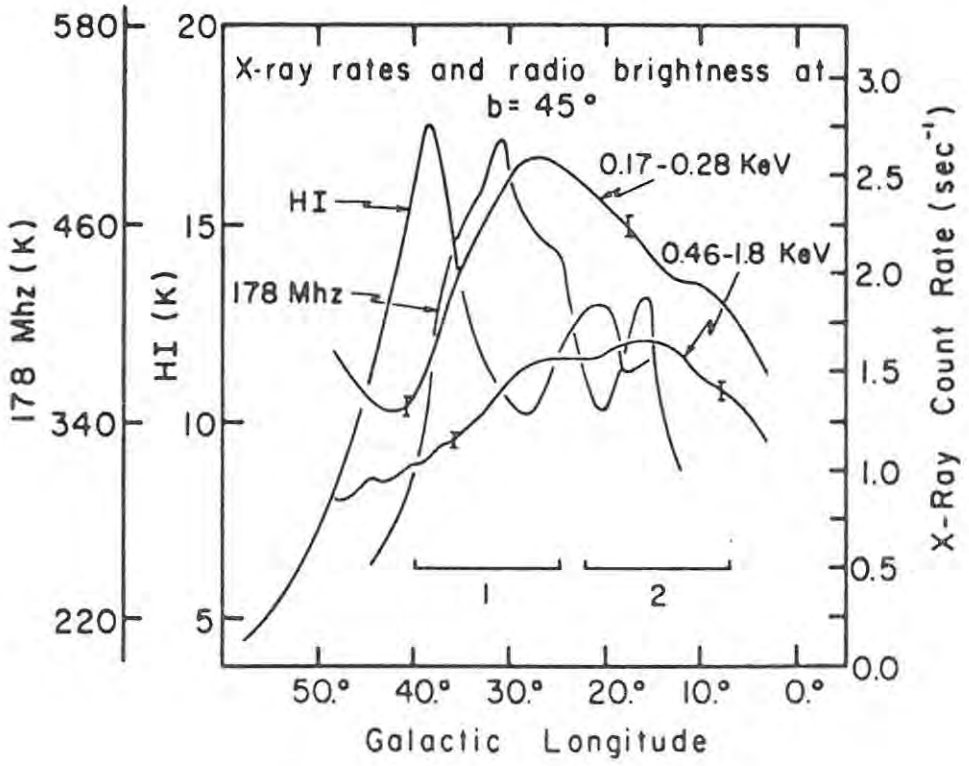

Figure 4.18 - Relationship between the neutral hydrogen distribution, the radio continuum emission at 178 MHz and the soft X-ray emission for $b_{II} = 45°$ *(after Borken and Iwan 1977).*

the reheating of Loop I and the NPS, and that some of the radio continuum brightness is due to this reheating event. It is of interest to note that the soft X-ray emission comes from a region just inside the small circle defining the maximum in the radio continuum emission, as should be expected. Figure 4.18 illustrates the relationship between the X-ray emission, the radio continuum emission and the neutral hydrogen at a latitude of $b_{II} = 45°$.

If the NPS is the result of a supernova explosion, there is the possibility that a runaway star might be associated with the event. Berkhuijsen *et al* (1971) have suggested that the runaway star ζ Ophiuchi, which was discussed in the preceeding section, is a candidate for this association. This would mean that the star did not originate in the Scorpius OB2 association, as suggested by Blaauw (1964), but rather in the Scorpius-Centaurus association. Berkhuijsen *et al* (1971) find that ζ Ophiuchi would have been close to the centre of Loop I approximately 3 million years ago.

A final piece of evidence supporting the supernova remnant hypothesis is the fact that a variable X-ray source is situated within five degrees of the central position of Loop I (Conner *et al* 1969).

4.3.2 - Results of the 2.3 GHz Survey

The NPS is a very prominent feature in the 2.3 GHz map presented in this thesis. The grey-scale image of the raw data shown in figure 2.2 clearly shows the NPS extending from the Galactic plane emission at $l_{II} = 18^h\ 05^m$ and $b_{II} = 0°$ towards the top right-hand corner of the image. In the maps of Appendix One, the NPS can be seen in map E3 and maps C4 to E4. The problem with these maps and with the grey-scale image is that the NPS appears to be swamped by the overwhelming Galactic disc emission, as has been mentioned before. Very little small-scale structure associated with the NPS is evident and it appears evident that an extension of the spur towards the plane exists but is being overpowered by the disc emission. One of the primary reasons for the development of the disc emission removal procedures was to enhance both the small-scale structure and the low latitude extension of the NPS.

Figure 4.19 is a contour map of the raw data centred (in galactic longitude) on the NPS. The contour levels for this plot and the following two plots are listed in table 4.5 (the contour spacing has been deliberately increased in these plots for the sake of clarity). Figure 4.20 is a contour map of the Galactic disc emission for the same area of sky as the previous plot. This map was produced by method four (the cubic spline method) described in Chapter Three using a bin width of 10°. From this plot it is clear to see that the NPS has not affected the production of the disc emission model to a very great extent - a desirable feature of the disc modelling procedure. Figure 4.21 is a contour plot of the residual data remaining after the subtraction of the disc emission model of the previous plot from the raw map. Comparison of this plot with the plot of figure 4.20 shows that an definite improvement has been obtained. In the raw map, an antenna temperature of 100 mK is plotted between latitudes 30° and 50° (the maximum latitude of the NPS down to a temperature of 100 mK). In the map of the residual data, the maximum extent in latitude of the NPS is unaffected, but now the 100 mK contour level comes to within 2° of the plane. A great deal of small-scale structure close to the plane has become evident. Of particular interest in this regard is the secondary spur extending from the plane at l_{II} = 18.5° and running parallel to the NPS for nearly 15° and the apparent extension of the NPS below the plane at $l_{II} \approx 20°$. These features will be discussed in greater detail in due course. The residual data plotted in a simplified form in figure 4.21 appears in more detail in Appendix Two.

Table 4.5 - Contour levels for figures 4.19, 4.20, 4.21 and 4.23.

Contour Level Ta / mK	Contour Label	Contour Level Ta / mK	Contour Label
100	100	2500	-
200	-	5000	-
300	-	10000	-
500	500	20000	-
1000	1K		

Assuming that the supernova remnant hypothesis for the origin of the NPS is correct, it is to be expected that the spur follows a small circle, even down to and beyond the plane of the Galaxy. Salter (1970) made use of the positions of the peaks in the spur at various latitudes to determine his small circle fit of Loop I and the NPS (see figure 4.16). Both his method and the fit he produced for the data at hand were good. However, his data points were all located further than about 12° from

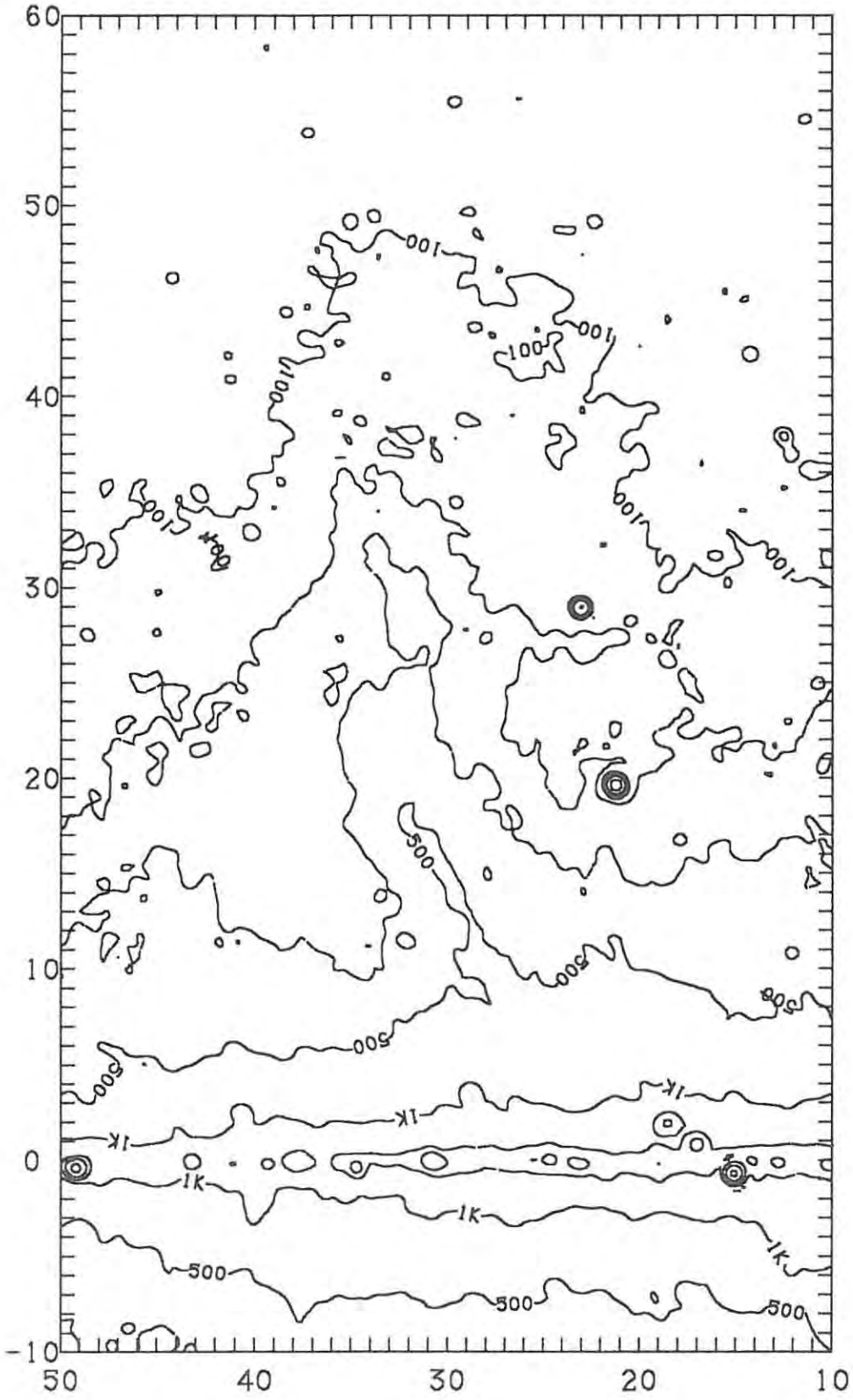

Figure 4.19 - Contour map of the NPS from the raw data. Contour levels are listed in table 4.5.

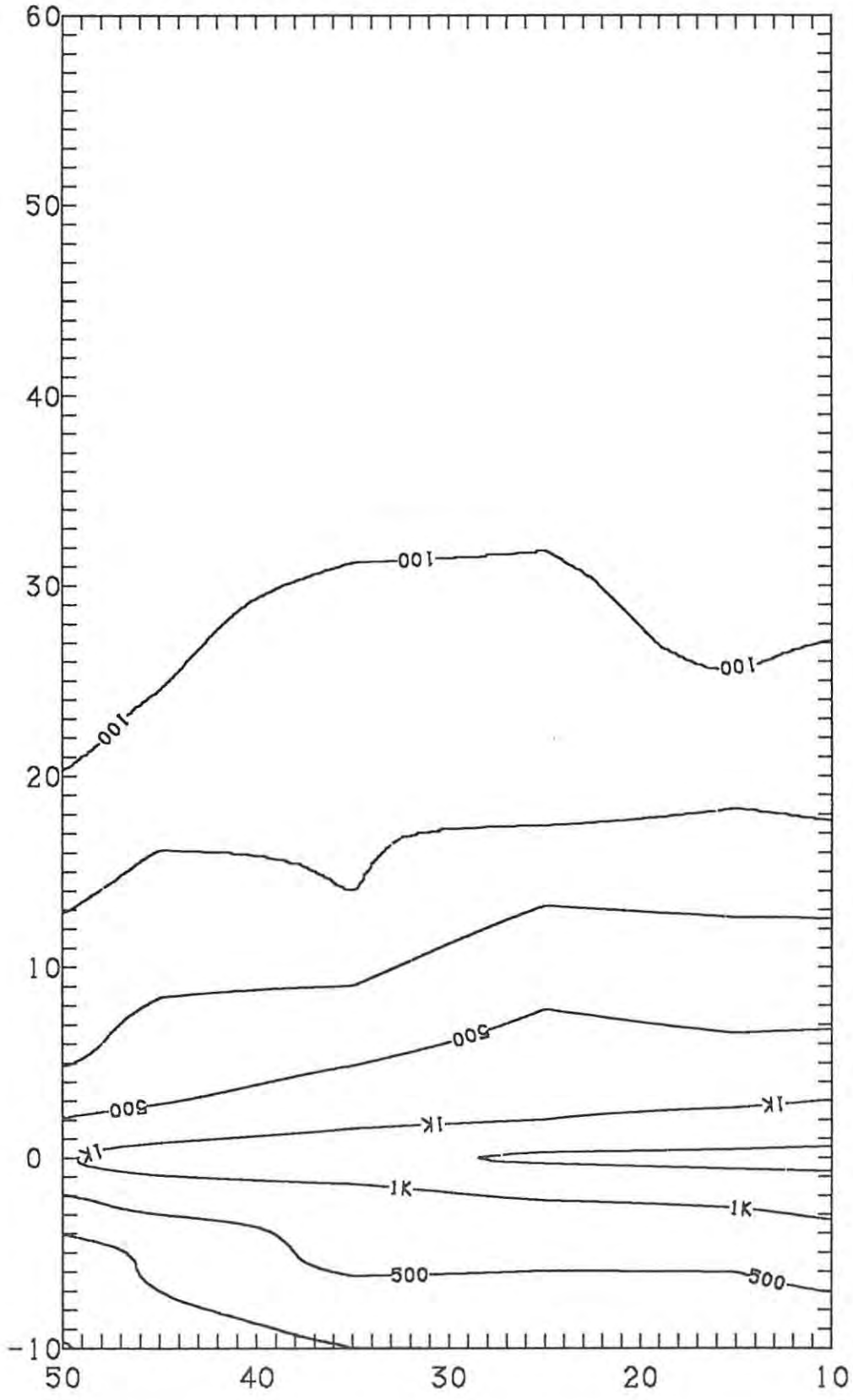

Figure 4.20 - Contour map of the Galactic disc emission in the region of the NPS.

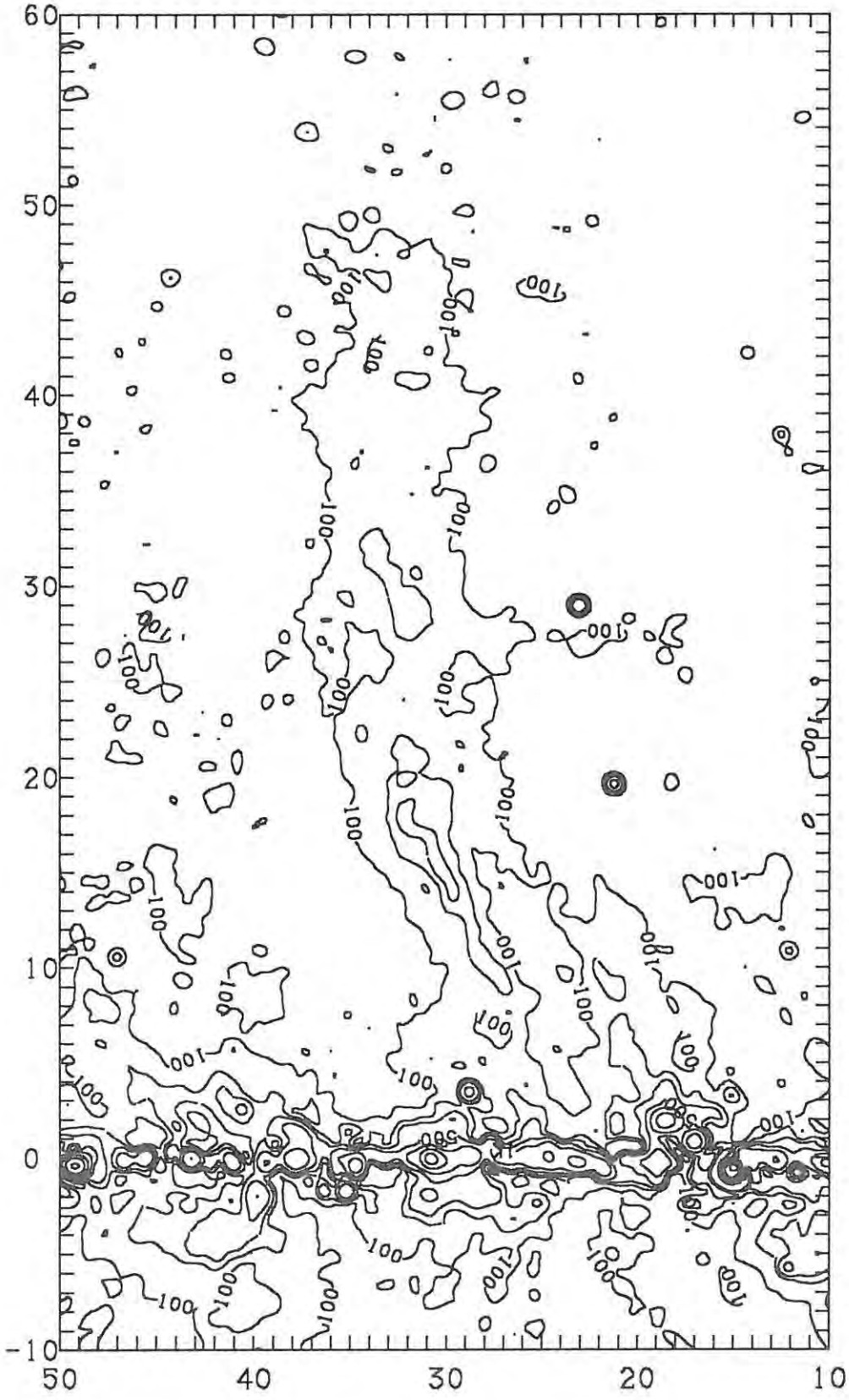

Figure 4.21 - Contour map of the NPS after subtraction of the plane model.

the plane of the Galaxy. Upon attempting to fit a small circle, with Salter's (1970) values for the position of the centre and the radius, to the residual data plotted in figure 4.21 and Appendix Two, the peaks in the data were found to deviate more and more from the position of the small circle as the latitude tended towards zero. Two possible causes for this discrepancy are that the small circle fitted by Salter (1970) is not the best possible circle and that, as the remnant approaches the plane, it no longer expands spherically.

The second explanation is easily justified by the fact that the average density of the interstellar medium decreases as the latitude increases. If a supernova occurs high above (or below) the plane of the Galaxy, the expanding remnant will encounter differing densities in its path, depending on which direction is taken. Thus, that part of the remnant moving vertically away from the plane of the Galaxy will expand into a medium with a decreasing density gradient, while that part of the remnant moving perpendicularly towards the plane will expand into a medium with a positive density gradient. Therefore, it can be expected that the remnant will not expand spherically as it approaches the Galactic plane.

In order to explore the first explanation mentioned above, a program was written which fits the best small circle to a set of points supplied to it, by a least-squares method (the same method used by Salter (1970)). By supplying the program with the positions of a number of the peaks in the profile of the NPS at various latitudes, a good fit was found for the low latitude structure evident in figure 4.21. This circle is centred on $l_{II} = 332.4°$ and $b_{II} = 20.9°$ and has a radius of 54.0° with an r.m.s. deviation of 0.5°. Figure 4.22 shows this small circle plotted on a rectangular grid with galactic coordinates (hence the non-circular appearance) with the data points of Salter (1970) marked by crosses and the data points taken from the 2.3 GHZ survey data marked by filled circles. The double lines indicate the limits of the r.m.s. deviation - the best fit small circle is actually midway between these two lines. It is interesting to note that the only place where this small circle deviates from the data of Salter to any great extent is on the far side of Loop I ($l_{II} \approx 270°$). Note also that, in producing this small circle fit, two points at *negative* latitudes were used. These points coincide with the small extension seen in figures 4.19 and 4.21 between $l_{II} = 17°$ and $l_{II} = 23°$.

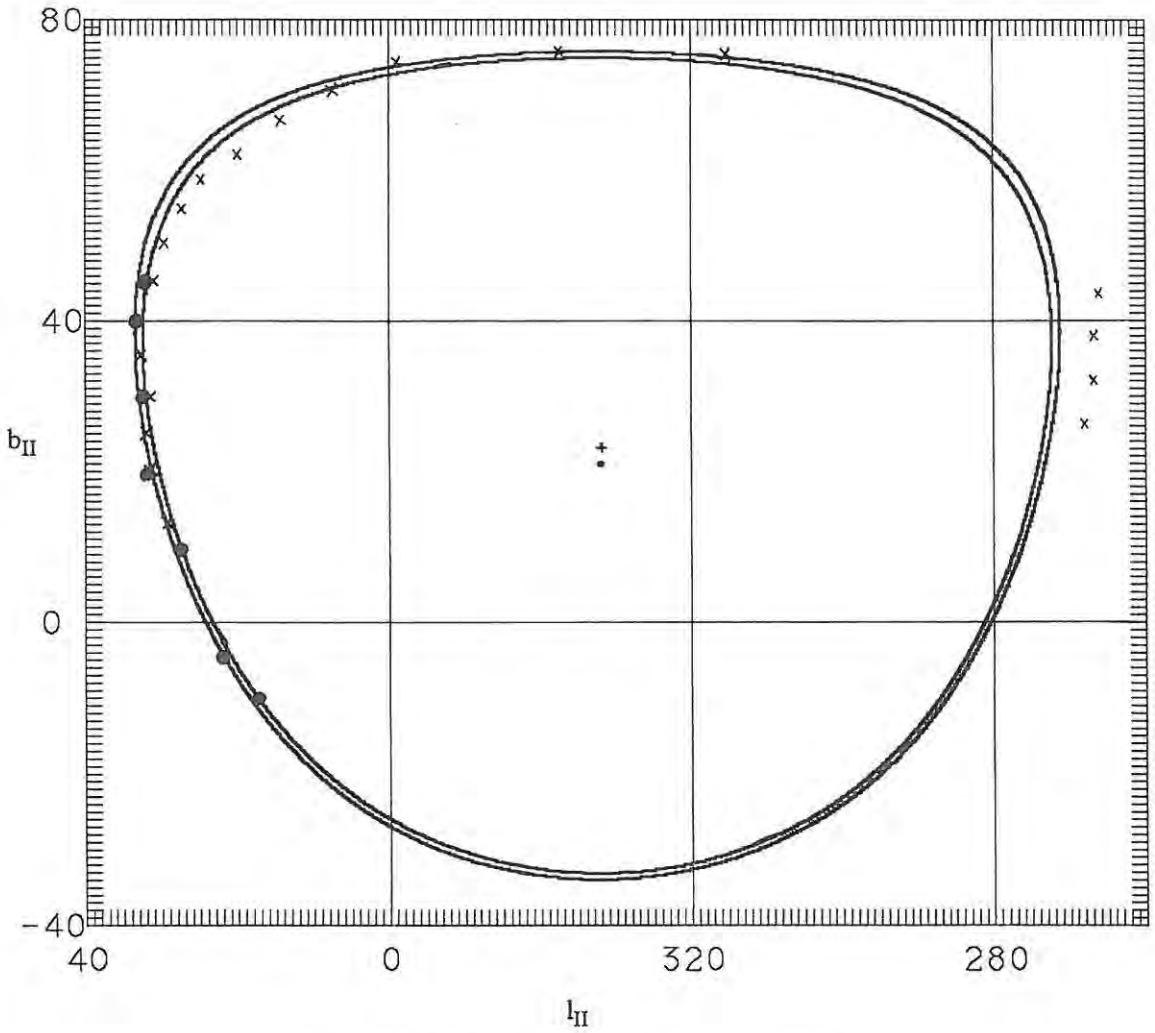

Figure 4.22 - Small circle fit to the data points of the 2.3 GHz data (filled circles). The data points of Salter (1970) are marked by crosses. The centre of the small circle is indicated by a small dot and the position of the X-ray source of Conner et al (1969) is marked by a plus.

Figure 4.23 shows the small circle derived above superimposed onto a similar contour plot to that in figure 4.21. The small circle is indicated by a pair of concentric, solid lines (similar to figure 4.22). The small circle appears to fit the curve of the NPS extremely accurately in this region, including the extension below the plane. To the right of the NPS appears the spur mentioned previously in this section. Also evident in this map (but not in the previous maps) is another spur extending from the

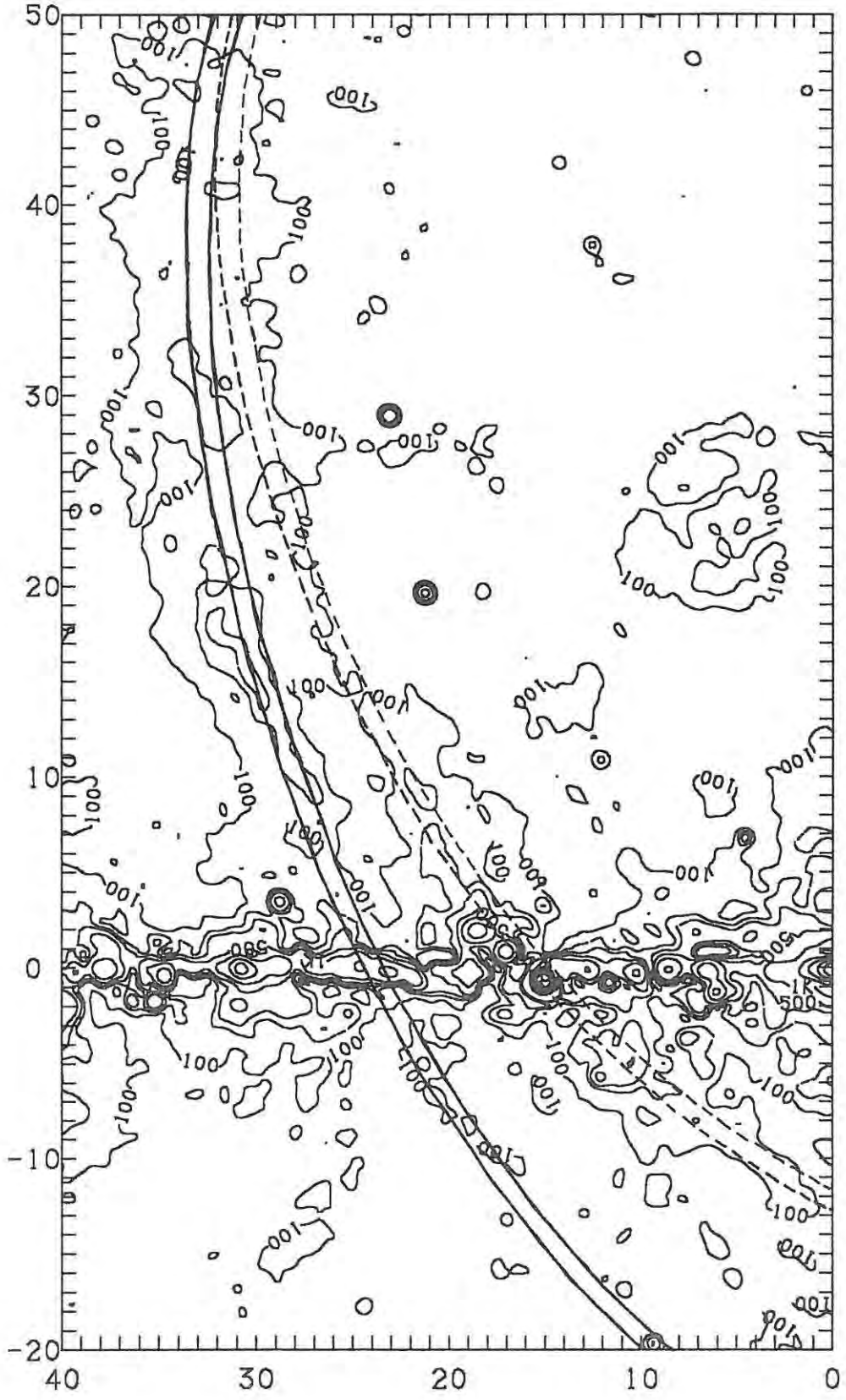

Figure 4.23 - Small circles, discussed in the text,

superimposed on the NPS and adjacent spurs.

bottom of the plane at $l_{II} \approx 10°$ towards $l_{II} = 0°$ and $b_{II} = -12°$. It is clearly evident from the contour plot that there is a strong possibility that these two spurs are related. The dashed lines indicate the position of a small circle best fitting these two spurs. This circle is centred on $l_{II} = 337.8°$ and $b_{II} = 27.8°$ and has a radius of 45.0° with an r.m.s. deviation of 0.3° (although the deviation indicated by the two dashed lines in figure 4.23 is still 0.5°). Not only does this small circle accurately fit the two spurs, but it also appears to fit a number of small extensions on the inside edge of the NPS (for example, at $l_{II} = 28°$ and $b_{II} = 24°$).

There are a number of possible explanations for this pair of spurs. Firstly, it is possible that the spurs are actually part of the NPS that have become dislocated from the rest of the NPS by interaction with the high-density interstellar medium in the Galactic plane. If this is the case, then neither of the small circles plotted in figure 4.23 represents the true location of the NPS. However, the fact that the small circles so accurately fit the data in this region seems to indicate another explanation for the presence of the spurs. The second possible explanation, then, is that the spurs are totally unrelated to the NPS (and possibly to each other), merely being chance alignments as seen from the sun. The third (and possibly the most interesting) explanation is that the spurs indicate the presence of a second shock front moving through the same region of space. This is an attractive possibility in view of the hypothesis made by Borken and Iwan (1977) - that the NPS is an old supernova remnant that is being reheated by the intersection of a younger remnant (although, judging by the apparent size of this "loop", it cannot be very much younger than the NPS).

It has been suggested by Berkhuijsen *et al* (1971) that the runaway star ζ Ophiuchi could be associated with the event that produced the NPS (see the previous section). Since the position of the centre of Loop I and the NPS is in the region of the constellations Lupus and Centaurus, they proposed that ζ Ophiuchi was once a member of the large OB association stretching from Centaurus to Scorpius (of which the Scorpius OB2 association is a part), and more specifically of the association referred to by Blaauw (1964) as the Upper Centaurus-Lupus OB association. There are two major problems connected with this proposal. Firstly, if the proper motion of ζ Ophiuchi is projected back in time (in a similar way to the method discussed in section 4.2) its closest approach to the centre of

the NPS (the centre of the small circle in figure 4.22)is found to have occured 7.8 $\times$ 10^6 years ago. While this is not a problem as far as the star is concerned (ζ Ophiuchi would still be on the main sequence), it is a problem as far as the theory of remnant evolution is concerned, since this time is an order of magnitude larger than the average theoretical time required for a remnant to lose its identity (ie - to reach the extinction phase). The second problem, with regard to ζ Ophiuchi being a member of the Centaurus-Lupus association, is the fact that, 7.8 million years ago, the stars of the association were not located where they are now, but were located in the region of the boundary between the constellations Ophiuchus and Hercules, approximately sixty degrees away. Thus, if ζ Ophiuchi did come from an OB association in the region of Centaurus, there must have been another OB association there at the time which has since moved to another part of the sky.

If the proper motion of ζ Ophiuchi is projected back to its closest approach to the centre of Salter's (1970) small circle (figure 4.16), a time just over 1 $\times$ 10^7 years is derived. Note that, in these calculations, the "closest approach" was taken as the smallest angular distance projected onto the sky. At the two times mentioned above, ζ Ophiuchi was actually between 250 and 300 pc away from the present position of the sun, which places it well over 150 pc from the centre of Loop I at closest approach. This is clearly inadequate, and good reason for rejecting the hypothesis that ζ Ophiuchi is associated with the NPS.

Conner *et al* (1969) reported the discovery of a variable X-ray source near the position of the centre of Loop I, at l_{II} = 332° and b_{II} = 23°. As was stated in the literature survey, this source lies within 5° of the centre of Loop I, as determined by Salter (1970). Taking the centre of the small circle determined from the 2.3 GHz data as the centre of Loop I, it is found that this X-ray source is only 2.3° away from the centre of Loop I. The X-ray source is indicated on figure 4.22 by a plus sign just above the centre of the small circle. Thus, there is a good chance that this X-ray source is associated with the NPS.

The method developed by Sofue and Reich (1979) to remove the effects of the Galactic disc emission (method three discussed in Chapter Three) was developed specifically to enhance the small-scale

structure and the low latitude extension of the NPS. Figure 4.24 shows the result of their method on their 1420 MHz survey of the NPS in the form of a grey-scale image. The resolution of this survey was 10′ of arc, allowing much more detail to be seen than in the present 2.3 GHz survey. However, in order to obtain a comparison between the 1420 MHz data and the 2.3 GHz data, method three was applied to the 2.3 GHz data of the NPS. A Gaussian,of half-power width 2°, was convolved with the data, and figure 4.25 presents the result after two iterations of the procedure and subtraction of the plane model from the raw data. The contour levels are listed in table 4.6 and are unlabelled for clarity. All of the structure evident in figure 4.24 can be seen in figure 4.25, even though the resolution of the latter is poorer. Also seen in figure 4.25 are a number of spur-like structures parallel to the NPS. These features are associated with the secondary spur to the right of the NPS mentioned previously. The small circles superimposed on this map are the same as those superimposed on the map of figure 4.23.

Table 4.6 - Contour levels for figure 4.25.

Contour Level Ta / mK	Contour Label	Contour Level Ta / mK	Contour Label
20	-	4000	-
40	-	7000	-
60	-	10000	-
80	-	14000	-
100	-	18000	-
500	-	24000	-
1000	-	30000	-
2000	-		

In order to determine a value for the spectral index of the NPS, a method similar to that used for S27 was used. Longitude scans were taken through the 408 MHz data of Haslam *et al* (1982) at latitudes of $b_{II} = 15°$, $b_{II} = 20°$ and $b_{II} = 25°$. The 2.3 GHz data set was smoothed to the same resolution as the 408 MHz map, and similar longitude scans were taken. For each latitude, the longitude limits of the NPS and the base level were found by inspection. The brightness temperature was measured at intervals of 1° along each longitude scan between the above longitude limits. These measurements are tabulated in table 4.7, along with the spectral index, calculated for each point using equation 4.80. From these measurements, the average spectral index of the NPS (assuming

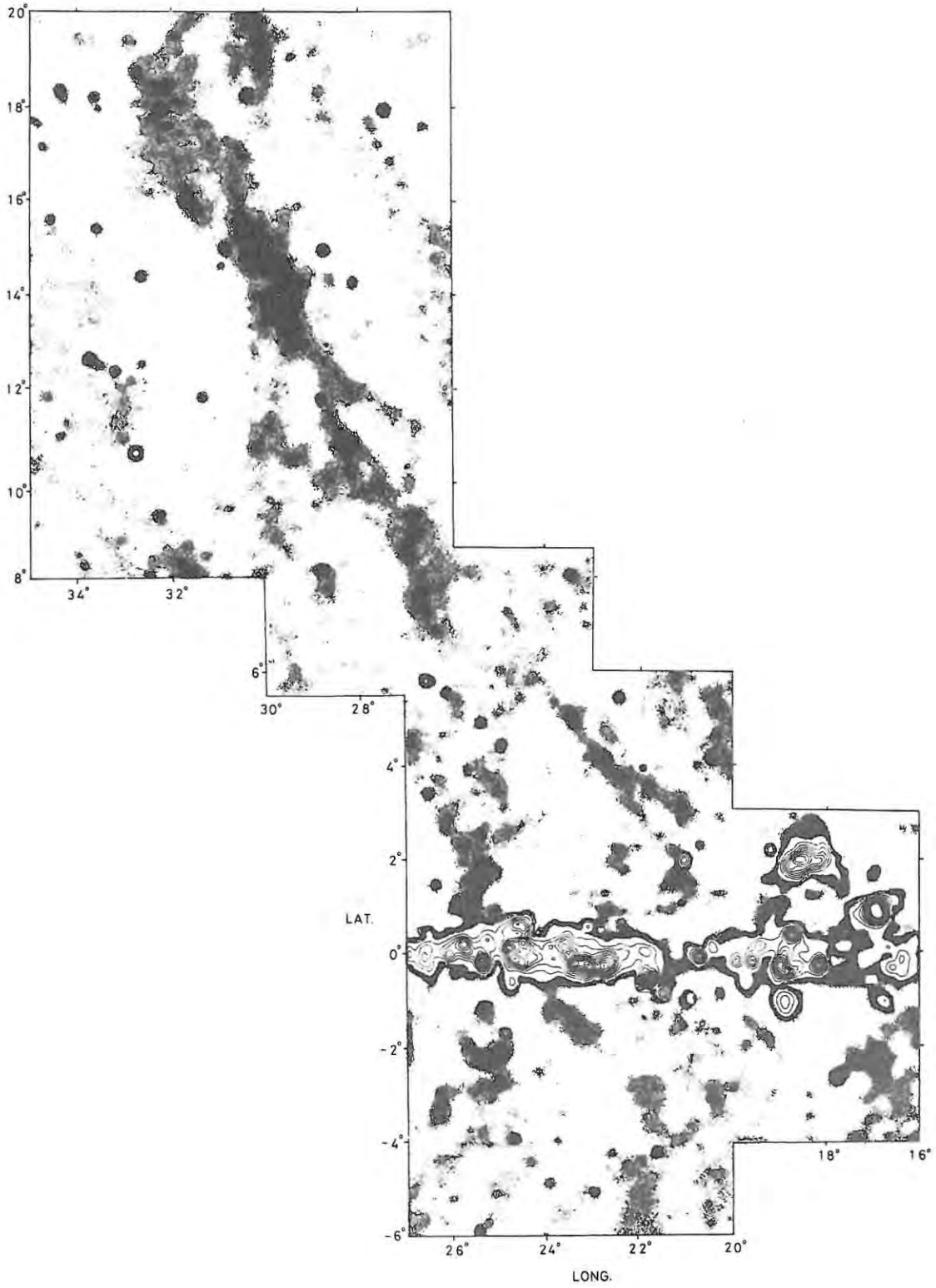

Figure 4.24 - Grey-scale image of the NPS at 1420 MHz (after Sofue and Reich 1979).

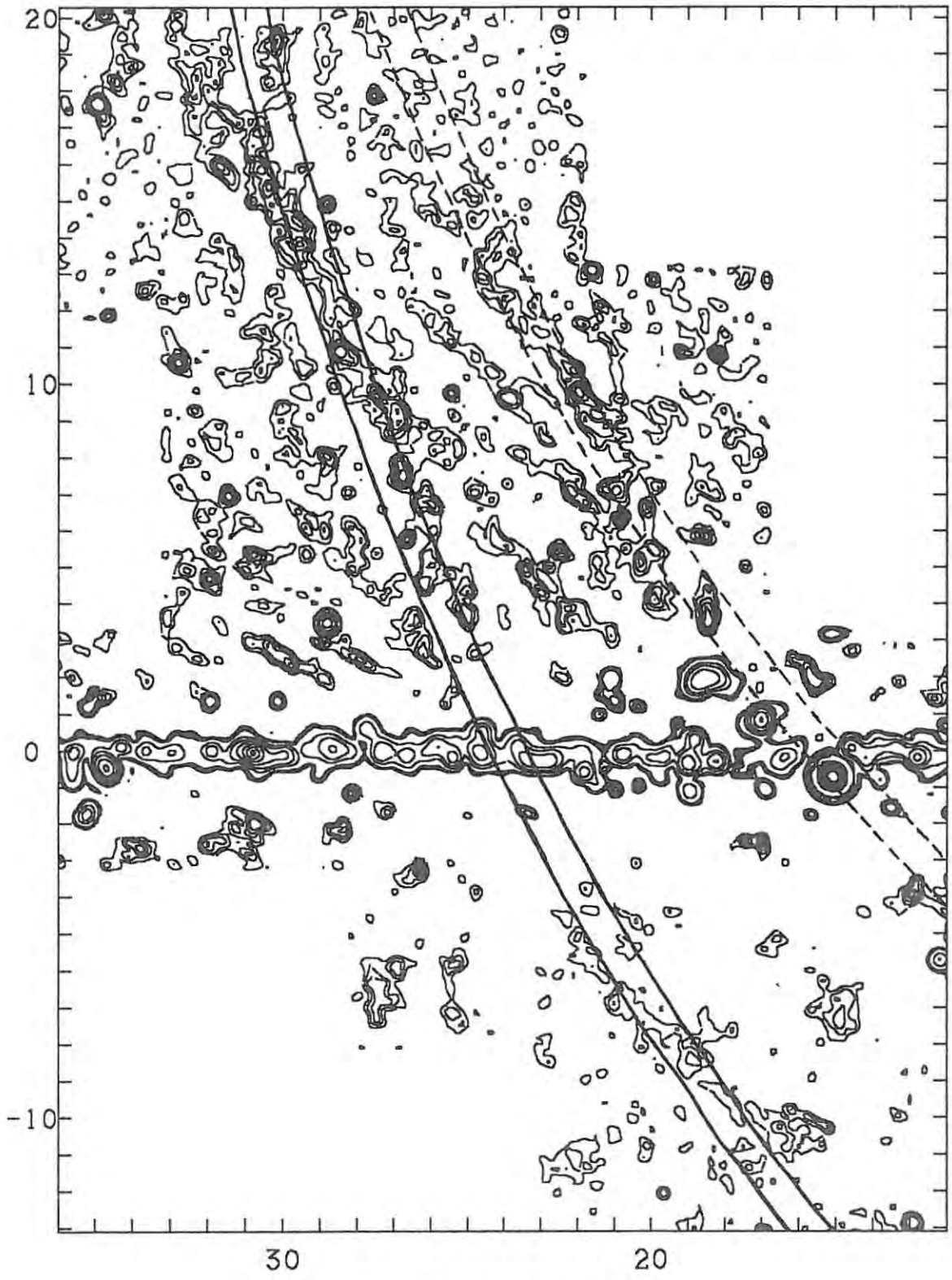

Figure 4.25 - Contour map of the NPS after subtraction of a plane model produced by method three. Small circles are as for figure 4.23. Contour levels are listed in table 4.6.

Table 4.7 - Spectral index of the NPS calculated at 1° intervals along scans at b_{II} = 15°, b_{II} = 20° and b_{II} = 25°.

Latitude	Longitude	T_b(408)	T_b(2300)	α
15°	27°	8.8K	0.142K	-0.39
15°	28°	6.2K	0.102K	-0.38
15°	29°	17.8K	0.249K	-0.47
15°	30°	33.8K	0.432K	-0.52
15°	31°	26.2K	0.279K	-0.63
15°	32°	11.8K	0.145K	-0.54
15°	33°	9.6K	0.122K	-0.52
15°	34°	5.6K	0.057K	-0.65
15°	35°	1.4K	0.018K	-0.52
20°	25°	4.0K	0.042K	-0.63
20°	26°	11.3K	0.090K	-0.79
20°	27°	17.2K	0.134K	-0.81
20°	28°	22.4K	0.196K	-0.74
20°	29°	25.0K	0.191K	-0.82
20°	30°	37.6K	0.265K	-0.87
20°	31°	42.0K	0.305K	-0.85
20°	32°	40.8K	0.304K	-0.83
20°	33°	30.8K	0.293K	-0.69
20°	34°	28.8K	0.261K	-0.72
20°	35°	28.3K	0.218K	-0.81
20°	36°	12.4K	0.113K	-0.72
25°	26°	10.0K	0.071K	-0.86
25°	27°	13.2K	0.128K	-0.68
25°	28°	17.2K	0.172K	-0.66
25°	29°	16.6K	0.156K	-0.70
25°	30°	21.4K	0.185K	-0.75
25°	31°	27.8K	0.272K	-0.68
25°	32°	34.2K	0.312K	-0.72
25°	33°	24.8K	0.260K	-0.63
25°	34°	20.2K	0.247K	-0.55
25°	35°	17.2K	0.229K	-0.50
25°	36°	14.6K	0.246K	-0.36

the measurements to be representative of the whole spur) is $\alpha = -0.65 \pm 0.14$, the spectral index of a non-thermal (synchrotron) source.

From the observational evidence presented above for the 2.3 GHz survey, it can be concluded that the model of Borken and Iwan (1977) is best suited to the results obtained. Judging from the spectral index and the geometry of the spur, it is evident that the NPS is the remnant of a supernova which occurred some million years ago at the approximate galactic coordinates of l_{II} = 332.4° and b_{II} = 20.9°. This remnant is in the process of being reheated by the intersection of a younger remnant,

possibly associated with the spurs located on a small circle centred on l_{II} = 337.8° and b_{II} = 27.8°.

4.4 - The Thermal Spur Associated With the HII Region S54

The HII region S54 is situated in the constellation Serpens Cauda (just north of Sagittarius) 18.6° from the Galactic centre at l_{II} = 18.5° and b_{II} = 2°. It is a well studied object, being bright in both the radio and optical wavelengths, and carries numerous other designations - NGC 6604, W35, RCW 167 and Gum 84, to name a few. Optically, it is a well-defined emission nebula (ie - clearly identifiable in the rich star fields of the Sagittarius region) with an associated cluster (Messier 16, NGC 6611) of bright, early-type stars. Due to the presence of numerous dark globules within the nebula, it is a confirmed fact that S54 is an active star forming region (the cluster of O and B stars within its boundaries also confirms this fact).

In the map of the fourth part of the Skymap program, S54 features as one of the most intense sources. It can be clearly seen on map E2 in Appendix One at $\alpha \approx 18_h\ 15_m$ and δ = -12° and in Appendix Two at the position noted above (in Galactic coordinates). Figure 4.26 is a contour map centred on S54 from the 2.3 GHz data. The contour levels are the same as for the plots in Appendix One. It is evident from this plot that S54 is an extended source with no apparent fine detail (due to the fact that the resolution of the beam was not high enough to detect such structure, and not because such structure does not exist). What is of interest, however, is the apparent extension of S54 on its high-latitude boundary. On this map, this feature appears to extend almost vertically away from the plane of the Galaxy to a latitude of about b_{II} = 4.5° (the edge of the map - an examination of map E2 in Appendix One shows that it does not appear to extend much further than this).

This feature was described in some detail by Muller *et al* (1987), who refer to it as a thermal spur. Since this is the only paper available which describes this feature in detail, results from this paper are used extensively throughout this section. The spur was first detected by Muller (1985) in a survey of the Galaxy at 2720 MHz, and was subsequently investigated by Muller *et al* (1987) in an attempt to

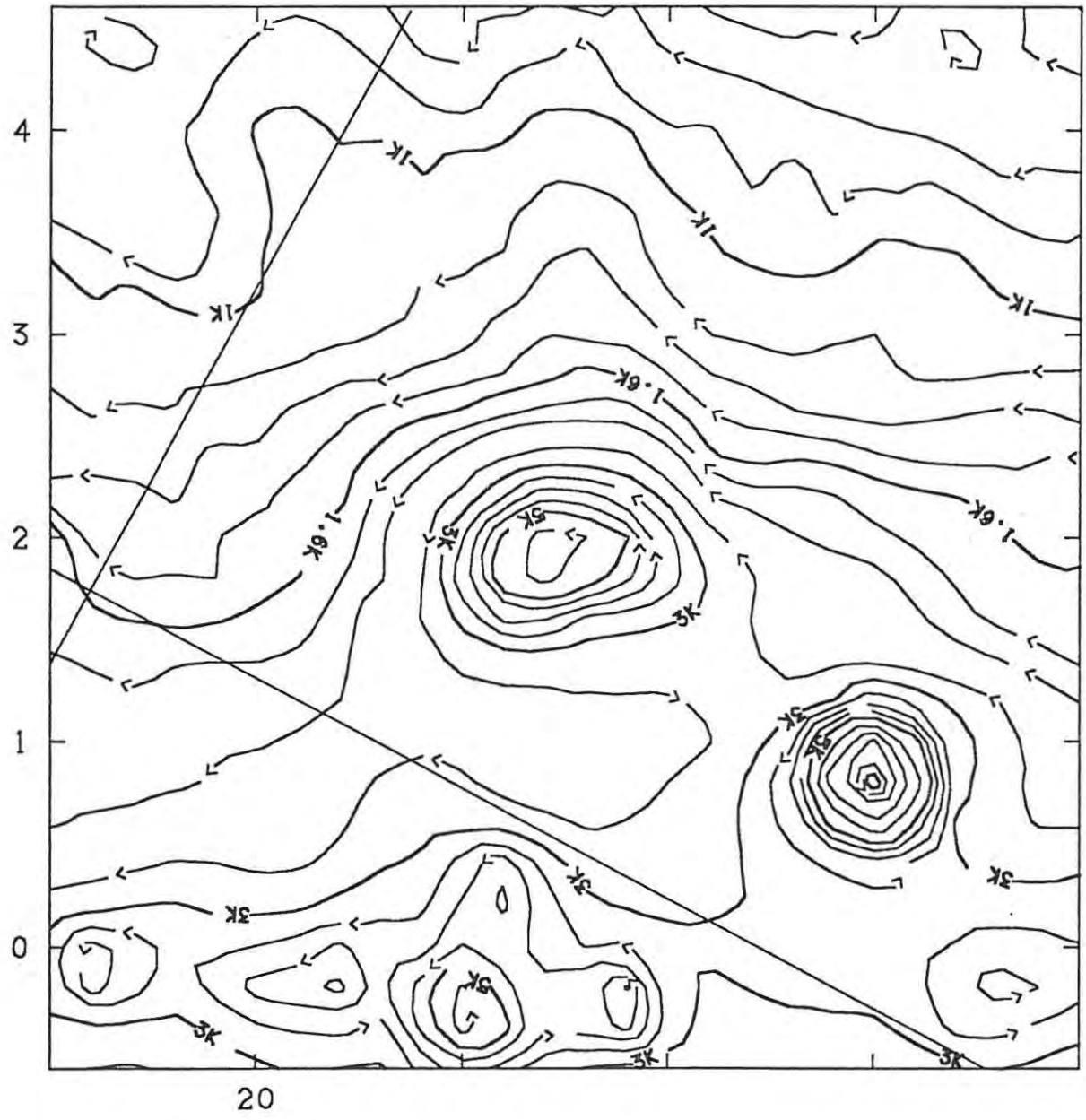

Figure 4.26 - Contour map of S54 from the raw data. Contour levels are listed in Appendix One.

ascertain the nature of this object. They were alerted to the possibility of a thermal nature by the fact that the spur is not seen in the 408 MHz maps of Haslam *et al* (1982) and is barely seen in the 1420 MHz maps of Reich and Reich (1986).

Figures 4.26, 4.27, 4.28 and 4.29 show the HII region S54 and its associated spur at the frequencies used by Muller *et al* (1987) - 1420 MHz, 2695 MHz, 2720 MHz and 4750 MHz respectively. The resolution of each of these maps is 9.4′, 5′, 21′ and 3′ respectively. These maps show the spur in varying amounts of detail (depending on the resolution of the map), and indicate an extension from $b_{II} \approx 2.5°$ to $b_{II} \approx 8°$ and a width of between 0.5° and 1°. Note that the maps at 2695 MHz and 4750 MHz do not cover the entire extent of the spur. Upon moving away from S54 along the length of the spur, the temperature gradient is initially quite steep, decreasing by about 80% in the first two degrees, followed by a more gradual decrease to the limit of the spur.

From studies of the H110α recombination line, Muller *et al* (1987) derive a distance to S54 of 2.9 ± 0.4 kpc. Assuming a diameter for S54 of 1°, this distance leads to a linear diameter of 50 pc. The galactic latitude of S54 corresponds to a height of 100 pc above the Galactic plane and the dimensions of the spur indicate a linear extent of 300 pc by 25 pc (assuming the width to be 0.5° and the spur to extend perpendicularly away from the plane of the Galaxy). The recombination line study of Muller *et al* (1987) indicates conclusively that the spur is related to S54 by the fact that the radial velocities of the recombination lines in the spur match those of S54.

Figure 4.30 shows the result, obtained from the 2.3 GHz data, after subtraction of a model of the Galactic disc emission in this region. The model was produced by method four (Chapter Three) with a bin width of 1.5°. The contour levels for this map are the same as for the maps in Appendix One. The spur is now clearly evident to galactic latitude $b_{II} \approx 9°$, and has been separated from adjacent structure for most of its length. There is a very clear comparison between this map and the map at 1420 MHz plotted in figure 4.26 - note in particular the two "sources" situated in the spur at $b_{II} \approx 3.4°$ and $b_{II} \approx 5.85°$.

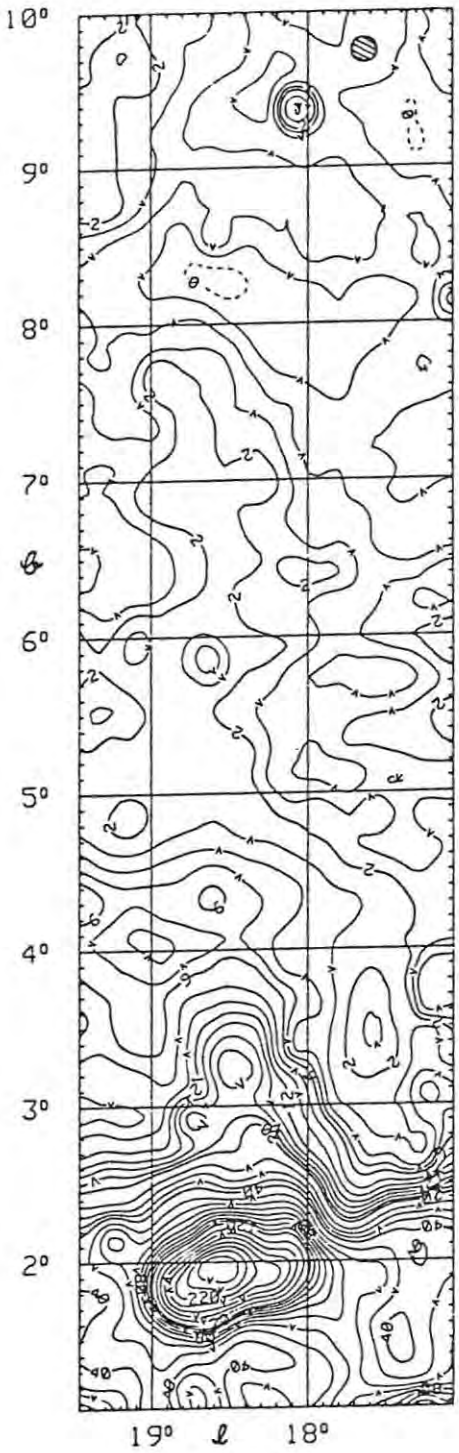

Figure 4.27 - Map of S54 and the thermal spur at 1420 MHz (after Muller et al 1987).

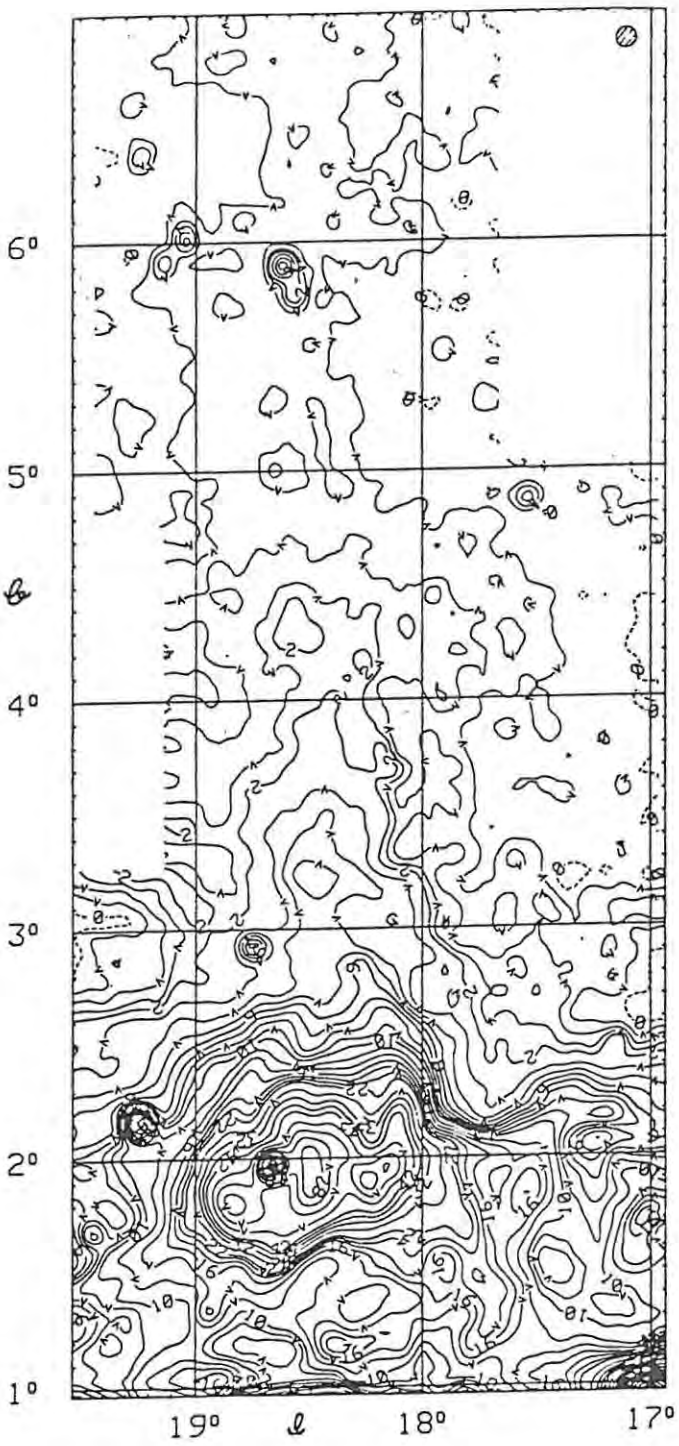

Figure 4.28 - Map of S54 and the thermal spur at 2695 MHz (after Muller et al 1987).

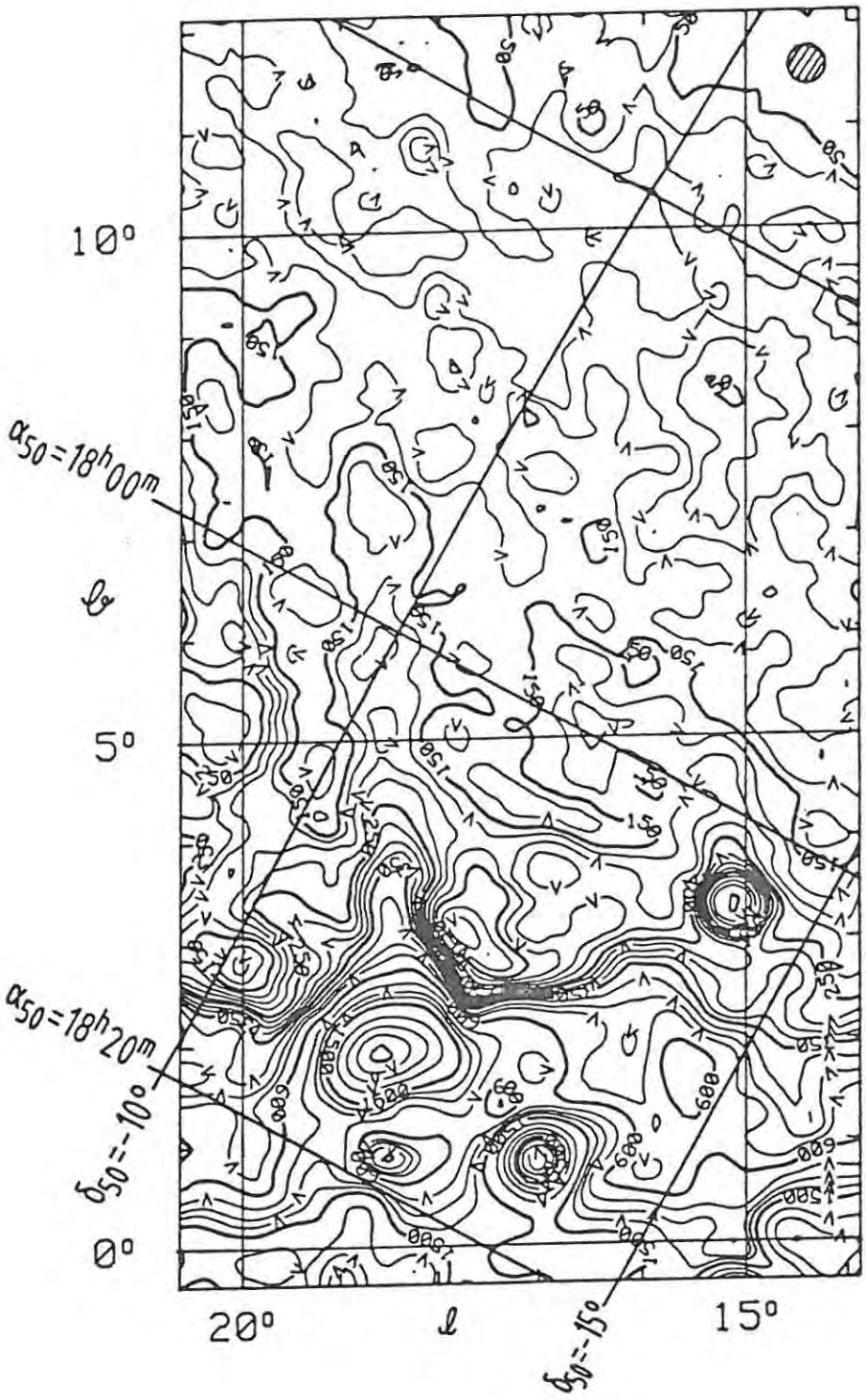

Figure 4.29 - Map of S54 and the thermal spur

at 2720 MHz (after Muller et al 1987).

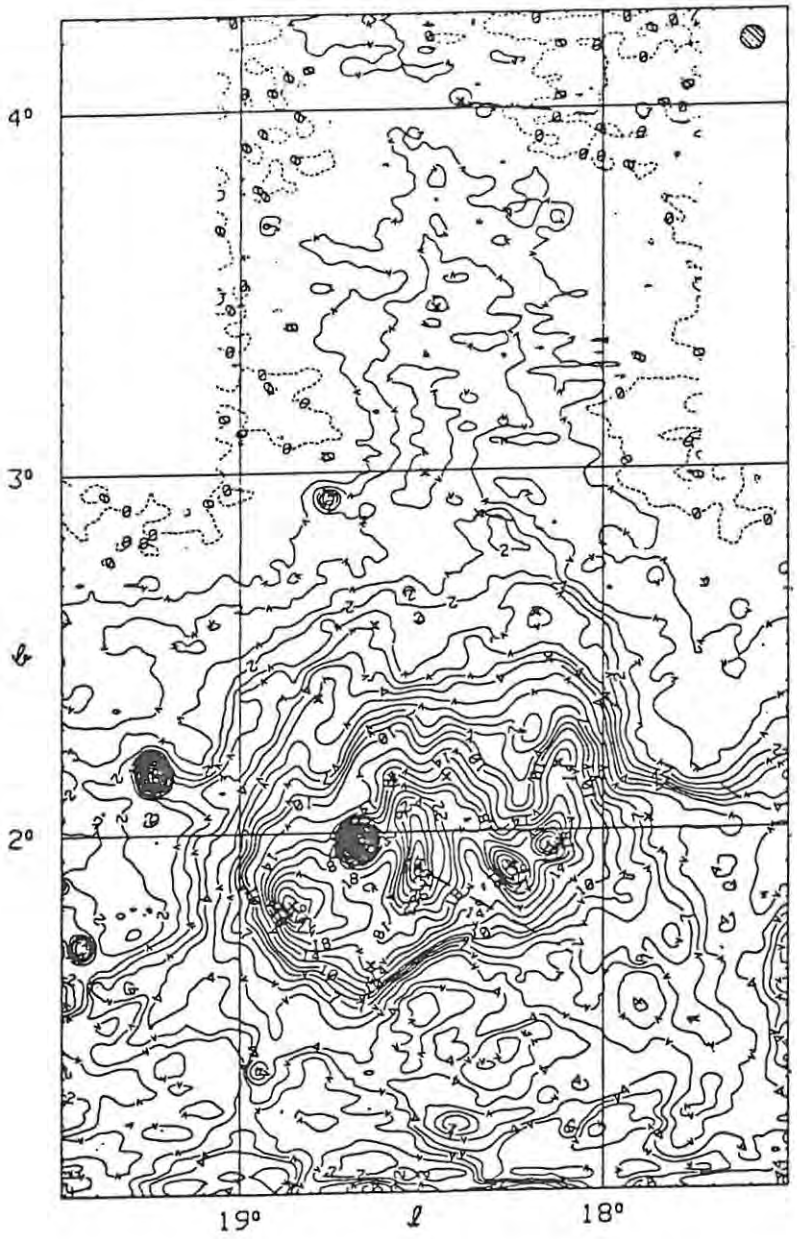

Figure 4.30 - Map of S54 and the thermal spur

at 4750 MHz (after Muller et al 1987).

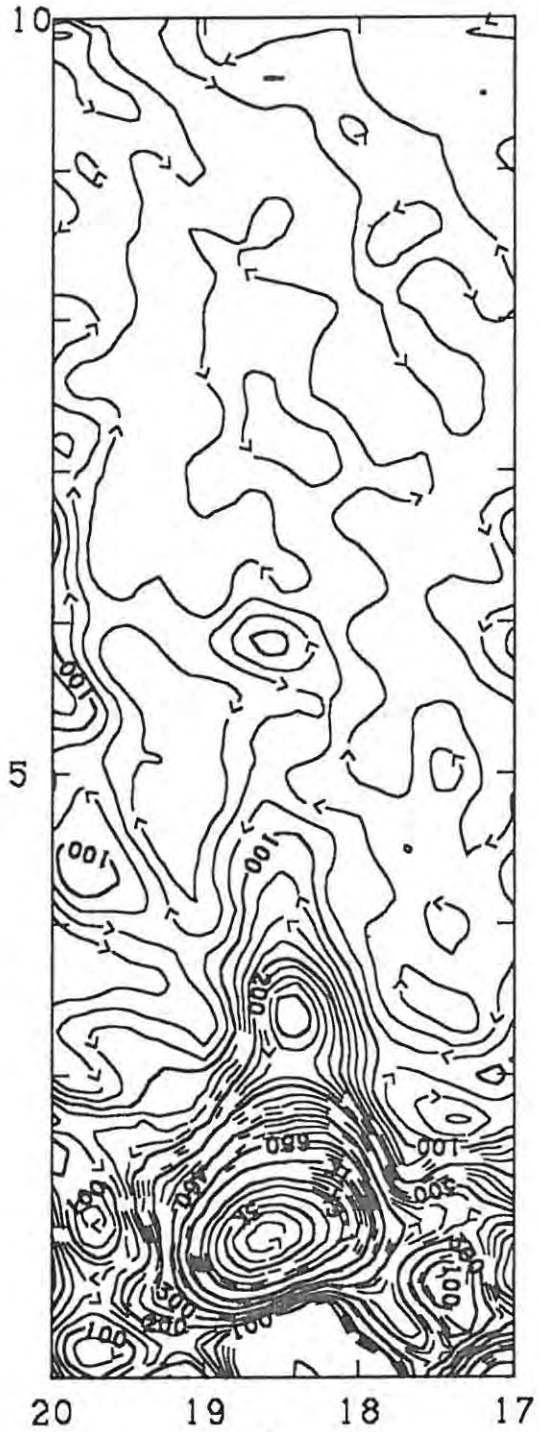

Figure 4.31 - Map of S54 and the thermal spur at 2.3 GHz. Contour levels are listed in Appendix One.

Muller *et al* (1987) derived values for the spectral indices of S54 and the spur using their data at 1420 MHz and 2695 MHz. Their values were α = -0.1 for the HII region and α = -0.1 for the spur, indicating that the spur is indeed an optically thin, thermal source. In attempting to derive spectral indices for S54 and the spur using the 2.3 GHz data and the data of Muller *et al* (1987), physically unrealistic values were obtained. This is probably due to the fact that base levels were subtracted from the data of Muller *et al* (1987) in order to reduce the Galactic disc emission, and this had an adverse effect on the calculations of spectral index. Figure 4.31 are latitude scans through S54 and the spur at l_{II} = 18.5° for the 2.3 GHz data (solid line) and the 2720 MHz data (dashed line). The vertical axis represents brightness temperature, and the scales on both axes are the same for both frequencies. A comparison of the two plots shows that the 2720 MHz profile appears to have a sloping base level for the region between b_{II} = 5° and b_{II} = 10°, whereas the 2.3 GHz profile appears to have a flat base level over this same region. This is an indication that the disc emission removal process of Muller *et al* (1987) differed from that used on the 2.3 GHz data.

Using the equations derived in section 4.2, a number of physical parameters can be derived for the HII region S54. Assuming that the flux density quoted in Appendix Four for S54 (1815-119) is correct (S = 43.91 Jy) and assuming an electron temperature of 7000K, the electron density of S54 is calculated to be N_e = 2.2 cm^{-3}, using equation 4.72. This is very much less than the value of 16 cm^{-3} derived by Muller *et al* (1987), probably partly due to the fact that S54 is an extended source making the measured value of the flux density incorrect. For this calculation, the values of Muller *et al* (1987) for distance and angular diameter were used. From equation 4.75, the mass of ionized hydrogen in the HII region is M = 27000 $M_\odot$. Using equation 4.76, the emission measure of S54 is calculated to be 477 $cm^{-6}pc$ and the optical depth is found to be 4.4 $\times$ 10^{-5} using equation 4.38. From equation 4.77, the excitation parameter is U_{rad} = 93.6 $cm^{-2}pc$ and from equation 4.78, the flux of Lyman continuum photons required to maintain the HII region is L_c = $10^{49.55}$ s^{-1}. According to Humphreys (1978), at least 10 members of the Serpens OB2 association belong to S54. The total Lyman continuum flux of these stars is $10^{49.95}$, making S54 a density bounded HII region.

In conclusion, it can be stated that, although no parameters (such as spectral index) could be

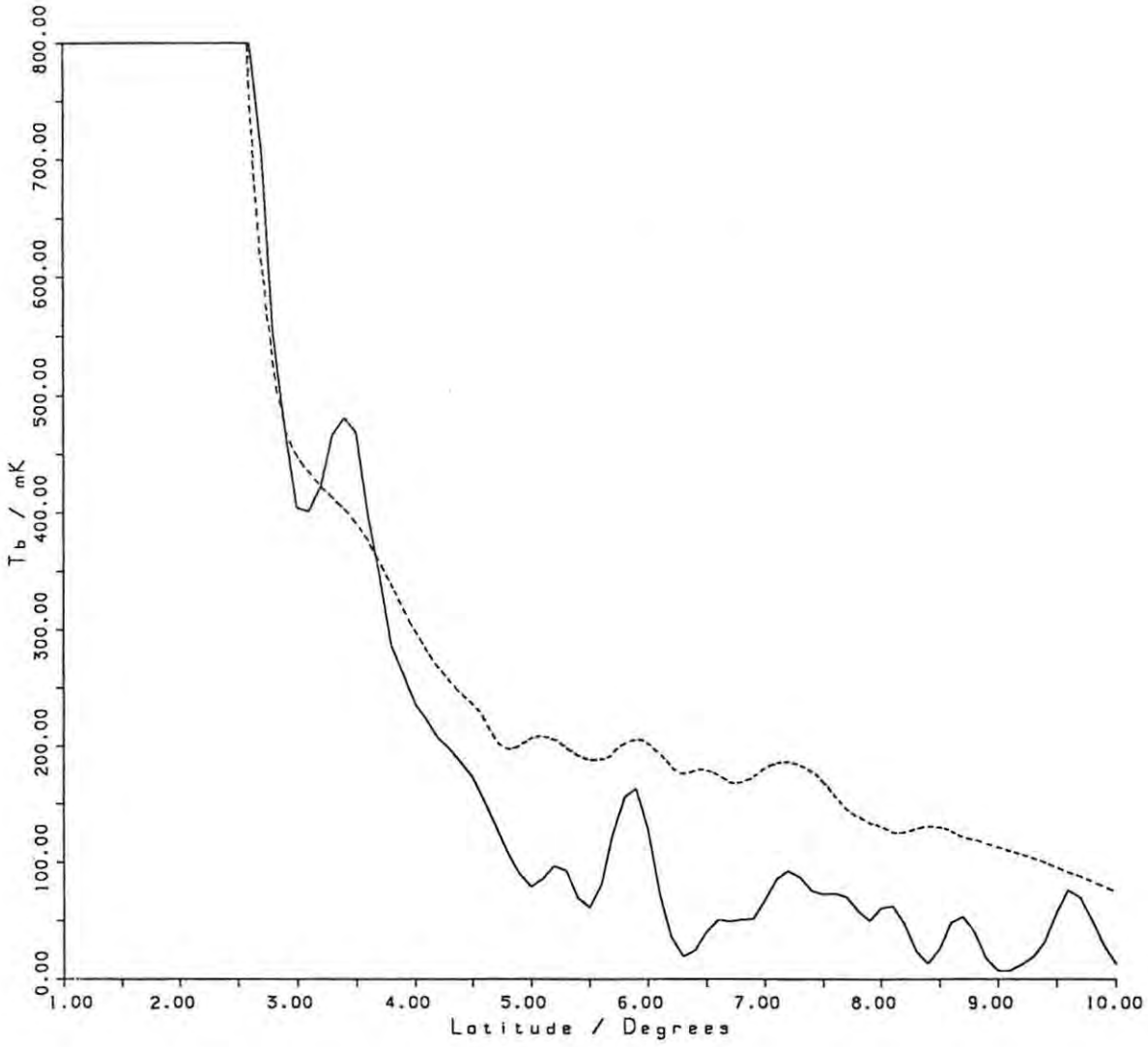

Figure 4.32 - Latitude scans of S54 and the thermal spur at 2.3 GHz and 2720 MHz.

calculated for the spur structure extending from S54, its presence in the maps of the 2.3 GHz survey is undeniable. The fact that this structure is visible at 2.3 GHz and invisible at 408 MHz is good indication that the spur is thermal in nature, as proposed by Muller *et al* (1987).

4.5 - Other Objects of Interest

This section is intended to be a brief summary of some of the objects contained within the region of the fourth part of the Skymap program that are not discussed in detail in this thesis. This summary is not intended to be complete, but rather to give an overview of possible future study in this region of the sky.

4.5.1 - Supernova remnants

Mention has already been made of such objects in connection with the north polar spur, discussed in section 4.3. There it was stated that the NPS is an old, but reheated supernova remnant well into the radiative phase of its evolution. Classified as one of the largest structures in the sky, in angular extent, it also necessarily classifies as the largest supernova remnant, as seen from the sun. A vast majority of the known supernova remnants are a great deal smaller than this structure, averaging less than 1° in diameter. It is, therefore, not surprising that such remnants get overlooked in a large-scale survey such as the present one.

Table 4.8 lists all of the known supernova remnants, the centres of which fall within the boundaries of the fourth part of the Skymap survey. This table is in all probability not complete since new supernova remnants are being discovered constantly. The first column lists the recognized name of the remnant, indicating the position of the source in Galactic coordinates. Columns 2 and 3 list the position of the source in 1950 equatorial coordinates. Column 4 lists the mean angular size of the source in minutes of arc, column 5 lists the flux density of the source at 408 MHz and column 6 lists the spectral index of the source. No attempt has been made to determine flux densities or spectral

Table 4.8 - Catalogue of supernova remnants.

Name	RA h m s	Dec ° ′	Ang size	S_{1GHz} Jy	α	Other Names
G4.5+6.8	17 27 42	-21 27	3	19	-0.64	Kepler's SN
G5.4-1.2	17 59 00	-24 55	35	35	-0.2	Milne 56
G5.9+3.1	17 44 20	-22 15	20	3.3	-0.4	
G6.4-0.1	17 57 30	-23 25	42	310	varies	W28
G6.4+4.0	17 42 10	-21 20	31	1.3	-0.4	
G7.7-3.7	18 14 20	-24 05	18	10	-0.32	1814-24
G8.7-0.1	18 02 35	-21 25	45	90	-0.25	(W30)
G9.8+0.6	18 02 10	-20 14	12	3.9	-0.5	
G10.0-0.3	18 05 40	-20 26	8	2.9	-0.8	
G11.2-0.3	18 08 30	-19 26	4	22	-0.49	
G11.4-0.1	18 07 50	-19 06	8	6	-0.5	
G12.0-0.1	18 09 15	-18 38	5	3.5	-0.7	
G15.9+0.2	18 16 00	-15 03	7x5	4.5	-0.7	
G16.8-1.1	18 22 30	-14 48	30x24	2	?	
G18.8+0.3	18 21 10	-12 25	18x13	27	-0.4	Kes 67
G18.9-1.1	18 27 00	-13 00	33	37	varies	
G20.0-0.2	18 25 20	-11 37	10	10	0.0	
G21.5-0.9	18 30 37	-10 37	1.2	6	0.0	
G21.8-0.6	18 30 00	-10 10	20	69	-0.5	Kes 69
G22.7-0.2	18 30 30	-09 15	26	33	-0.6	
G23.3-0.3	18 32 00	-08 50	27	70	-0.5	W41
G23.6+0.3	18 30 20	-08 15	10	8	-0.3	
G24.7+0.6	18 31 30	-07 07	30x15	20	-0.2	
G24.7-0.6	18 36 00	-07 35	15	8	-0.5	
G27.4+0.0	18 38 40	-04 59	4	6	-0.68	Kes 73
G27.8+0.6	18 37 06	-04 28	50x30	30	varies	
G29.7-0.3	18 43 48	-03 02	3	10	-0.7	Kes 75
G30.7+1.0	18 42 10	-01 35	24x18	6	-0.4	
G31.5-0.6	18 48 35	-01 35	18	2	?	
G31.9+0.0	18 46 50	-00 59	5	24	-0.55	3C 391
G32.0-4.9	19 03 00	-03 00	60	22	-0.5	3C 396.1
G32.8-0.1	18 48 50	-00 12	17	11	-0.2	Kes 78
G33.2-0.6	18 51 12	-00 05	18	5	varies	
G33.6+0.1	18 50 15	+00 37	10	22	-0.5	Kes 79
G34.7-0.4	18 53 30	+01 18	35x27	230	-0.30	W44, 3C 392
G36.6-0.7	18 58 05	+02 52	25	?	?	
G39.2-0.3	19 01 40	+05 23	8x6	18	-0.6	3C 396
G39.7-2.0	19 10 00	+04 50	120x60	85	-0.7	W50, SS 433
G40.4-7.1	19 27 39	+03 08	300			
G40.5-0.5	19 04 45	+06 26	22	11	-0.5	
G41.1-0.3	19 05 08	+07 03	4.5x2.5	22	-0.48	3C 397
G42.8+0.6	19 04 55	+09 00	24	3	-0.5	
G43.3-0.2	19 08 44	+09 01	4x3	38	-0.48	W49B
G45.7-0.4	19 14 05	+11 04	22	4.2	-0.4	
G46.8-0.3	19 15 50	+12 04	17x13	14	-0.42	

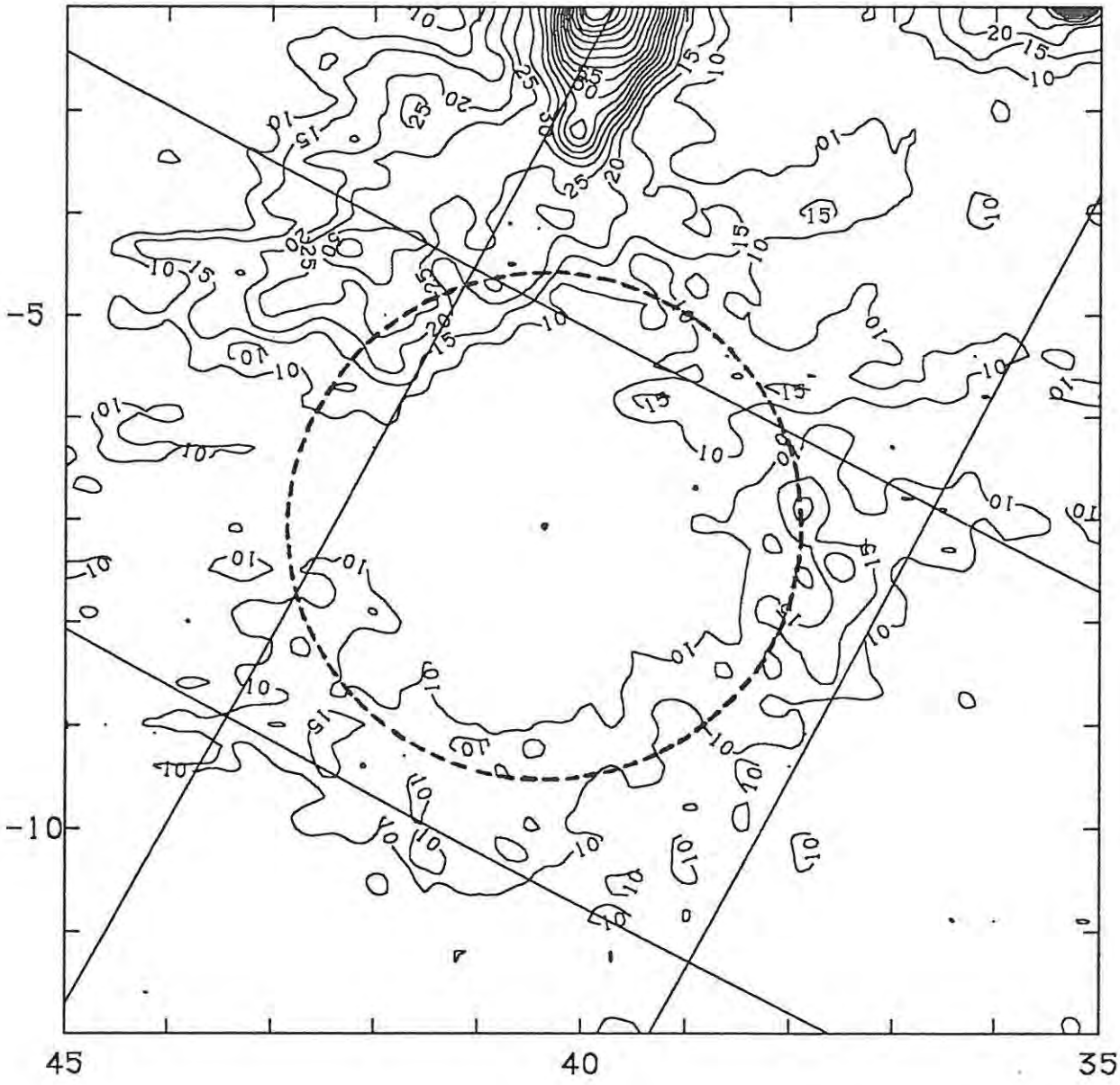

Figure 4.33 - Contour plot of the supernova remnant G40.4-7.1. Contour levels are listed in table 4.9.

indices for these sources, although most of them should appear in the source listing in Appendix Four. The source for table 4.8 is Green (1988).

It will be noted that the source G40.4-7.1 has no values listed for the flux density at 408 MHz or the spectral index. This source is rather more unusual than the rest of the sources due to its large angular size of 5°. It is easily seen on the grey-scale image of figure 3.14 as a loop-shaped structure just below the plane of the Galaxy on the left hand side of the image. Figure 4.32 is a contour map of this loop after subtraction of a plane model produced by method four with a bin width of 4°. The contour levels are listed in table 4.9. The dashed circle has a diamter of 5° and is centred on l_{II} = 40.34° and b_{II} = -7.07°. This structure is clearly seen on the 408 MHz data of Haslam *et al* (1982) and the 1420 MHz data of Reich and Reich (1986).

Table 4.9 - Contour levels for figure 4.32.

Contour Level Ta / mK	Contour Label	Contour Level Ta / mK	Contour Label
100	10	550	55
150	15	600	60
200	20	650	65
250	25	700	70
300	30	750	75
350	35	800	80
400	40	850	85
450	45	900	90
500	50	950	95

4.5.2 - HII regions

Up to this point, two HII regions have been discussed in some detail. In the discussion on the HII region surrounding the star ζ Ophiuchi, the formulae for the physical parameters of an HII region were derived. These formulae could be applied to any HII region, but no attempt was made to do this for the ±40 HII regions in the fourth part of the Skymap survey. These HII regions are listed in table 4.10 in order of increasing Galactic longitude. Column 1 contains the name of the source, again derived from the Galactic coordinates of the source, columns 2 and 3 contain the positions of the

Table 4.10 - Catalogue of HII regions.

Name	RA h m s	Dec ° ′ ″	S_{408} Jy	Other Names
G5.9-0.4	17 57 38	-24 04 52	12	
G6.0-1.2	18 00 38	-24 22 50	185	RCW 146, W29, M8
G6.2+23.6	16 34 24	-10 27 58		S27
G6.3-0.2	17 57 41	-23 38 47	460	W28
G7.0-0.3	17 59 19	-23 02 29	6	RCW 147, M20
G9.9-0.7	18 07 27	-20 42 43	13	
G10.2-0.3	18 06 26	-20 19 36	30	W31
G10.3-0.2	18 06 00	-20 06 00	12	
G10.6-0.4	18 07 30	-19 57 44	6	
G12.7-0.2	18 11 00	-17 58 48	33	W33
G16.9+0.7	18 16 07	-13 51 51	193	RCW 165, M16, W37, S54
G18.5+1.9	18 14 52	-11 55 07	7	RCW 167, W35
G22.8-0.5	18 31 43	-09 18 32	236	W41
G23.1+0.6	18 28 40	-08 30 50	6	RCW 171
G23.9-0.1	18 32 31	-08 09 25	4	
G24.0+0.2	18 31 40	-07 56 15		
G24.4+0.1	18 32 49	-07 35 52	2	
G24.5+0.5	18 31 27	-07 20 09	3	
G24.5-0.2	18 34 07	-07 37 13	4	RCW 172
G24.7-0.2	18 34 09	-07 26 55	11	
G24.8+0.1	18 33 29	-07 13 07	12	W42
G25.3+0.3	18 33 35	-06 41 38	6	RCW 173 ?
G25.4-0.2	18 35 33	-06 50 12	12	
G25.4+0.0	18 34 50	-06 42 20	2	
G28.8+3.5	18 28 49	-02 07 35	25	RCW 174, W40
G29.9-0.0	18 43 30	-02 45 26	15	
G30.2-0.1	18 44 23	-02 32 18	3	
G30.4-0.2	18 45 01	-02 23 36	4	
G30.6+0.0	18 44 26	-02 09 43		
G30.7-0.3	18 45 43	-02 10 09	5	
G30.8-0.0	18 45 02	-01 59 36	51	W43
G35.1-1.5	18 58 13	+01 08 42	5	
G35.2-1.8	18 59 15	+01 08 14	9	W48
G35.4-1.8	18 59 46	+01 15 28	7	
G37.5-0.1	18 57 47	+03 58 12	20	
G37.7+0.1	18 57 11	+04 11 57	5	
G37.8-0.2	18 59 32	+04 08 04	11	W47
G39.3-0.0	19 00 43	+05 31 49	2	
G45.1+0.1	19 11 05	+10 48 35	6	
G45.5+0.1	19 11 59	+11 03 58	13	

sources in 1950 equatorial coordinates and column 4 lists the 408 MHz flux densities. As with the table of supernova remnants, this table is not intended to represent the complete list of HII regions.

The source for table 4.10 is Shaver and Goss (1970).

4.5.3 - Extragalactic objects

There are primarily two types of extragalactic radio source - radio galaxies and quasi-stellar sources or quasars. Even though these objects are many orders of magnitude larger than the average HII region or supernova remnant, they appear essentially as point sources on most radio maps. This can be explained by the fact that, due to the immense distances involved, these sources subtend very small solid angles when viewed from the sun - in general, a great deal smaller than the beam width of the telescope.

Contrary to the HII regions and supernova remnants, which tend to cluster towards the plane of the Galaxy, extragalactic objects, in general, have no connection with the Galaxy and can therefore be situated in any part of the sky. However, due to overpowering effect of the Galactic disc emission, very few extragalactic objects are observed close to the Galactic plane - this effect is more readily noticable in optical astronomy, but the effect is still evident at radio frequencies. Therefore, it appears that a majority of Galactic objects are clustered near the plane while a majority of extragalactic objects are observed away from the plane.

The two facts stated in the above paragraphs can be used to good effect when considering the source listing in Appendix Four. As is stated in the preliminary explanation to that Appendix, the source listing was compiled by considering all peaks, isolated by 0.5°, to be point sources. The flux densities listed in column 5 of Appendix Four were calculated on this assumption. Therefore, it is clear that most of the listed sources that are situated more than about 5° from the plane are extragalactic sources. The flux densities listed in column 5 can therefore be taken as accurate to within a few percent for these sources.

Since the Skymap survey is aimed at observing large-scale structure, these small-scale, extragalactic sources are considered no further in this thesis.

Chapter Five - Discussion of Method and Results

Throughout the course of this dissertation, sections have been written on the various methods used and results obtained during the fourth part of the Rhodes University Skymap program. These sections are complete in themselves, presenting all the relevent facts, whether derived from the 2.3 GHz data or not, in a sequential manner followed by a brief discussion of the methods used and/or the results obtained. Thus, in Chapter Three, which dealt with the procedures for the removal of the Galactic disc emission, the pros and cons for each method were presented and discussed within the chapter itself, along with the results obtained for each method. This method of presentation allows this final chapter to be brief since it is only necessary to include a summary of the methods and results discussed in the previous chapters.

5.1 - The Observations and Data Processing

The observations for the fourth part of the Skymap survey were made at Hartebeesthoek Radio Astronomy Observatory, using software developed initially by Pete Mountfort and discussed in great detail by Jonas (1982). Since none of the software for these observations was written, or even modified, by the author, it is not necessary to discuss this further.

In the same light, most of the initial data processing was performed using software developed primarily by Justin Jonas and discussed in his thesis (Jonas 1982). All the processing from the raw data on magnetic tape to the raw map presented in Appendix One was performed using this software and, therefore, this is not discussed here.

The Galactic disc emission removal procedures discussed in Chapter Three represent the primary data processing technique used in this thesis. The aim of the exercise was to remove the overpowering effect that the emission from the Galactic disc has on the data in such a way as to leave unaltered *all* structure (whether small- or large-scale) not directly associated with this emission.

The obvious assumption that is made is that the disc emission is a smoothly varying function of both longitude and latitude and that no structure smaller than a few degrees is present in this emission. Therefore, in effect, the disc emission removal procedures involve the *separation* of the observed temperature distribution into a low spatial frequency part, representing the disc emission, and a high spatial frequency part, representing the structure due to discrete sources superimposed on top of the disc emission.

The four methods discussed in Chapter Three all have their pros and cons, as noted in that chapter. It is apparent that method four, the method by which the plane is modelled by cubic splines fitted to cross-sections of the plane, is the most effective in performing its task. A criterion for the accuracy of a particular method is whether cross-sections at constant longitude of the resulting residual data map have a flat base level. If the base level of a cross-section still decreases with increasing latitude, then the procedure has been unsuccessful in subtracting away all of the emission due to the disc emission. If, on the other hand, the cross-section becomes negative as the plane is approached, the procedure has produced a model with temperatures greater than the recorded temperature for that part of the sky. Of the four methods discussed, the method of Flanagan (1981) was unsuccessful in subtracting away all of the disc emission, the method of Sofue and Reich (1979) oversubtracted in the region near the plane, and method four apparently produced a flat background (see, for example, figure 3.7). Due to the fact that the method of Wright (1985) works only in localized boxes around discrete sources, it is not considered here.

It is important to note that all of the methods discussed in Chapter Three have their uses, depending on what the desired result is. Thus, if one wishes to model the Galactic disc emission in such a way as to produce *two* models - one for the thick component of the disc and one for the thin component, as described by Beuermann *et al* (1985) - the method of Flanagan (1981) would be the most useful. Figure 4.25 demonstrates a useful aspect of the method of Sofue and Reich (1979). Due to the fact that this method smoothes the observed temperature distribution, it has the effect of subtracting away part of any source with an angular diameter greater than the half power width of the Gaussian beam used in the method. The result is that, for such sources, only the peaks of the

small-scale structure remain. This is the case with the north polar spur, as can be seen by comparing figure 4.25 with, for instance, figure 4.23. In figure 4.23, most of the emission from the NPS is evident, whereas in figure 4.25 only the peak ridges of of the NPS remain. This, in fact, is not necessarily an undesirable effect, as a great deal of useful information can be obtained from such a picture (for instance, the peak ridges of the NPS represent more clearly the true position of the remnant).

Improvements are possible in all of the methods discussed in Chapter Three, and there are no doubt other methods which are effective in removing the disc emission which could be compared with those discussed here. A possible improvement to method four would be to attempt to model the variation of the disc emission with longitude, rather than use linear interpolation between the cross-sections obtained. The possibility of using a number of the methods together also warrants investigation. However, from the results presented in this thesis, it can be said that, of the four methods described and discussed in Chapter Three, method four is generally the most effective in subtracting away the contribution due to the Galactic disc emission.

5.2 - Results of the 2.3 GHz survey

In Chapter Four, a number of results are obtained for various objects contained within the limits of the fourth part of the Skymap survey. The calculation of these results relied on the assumption that a model of the disc emission had been subtracted from the raw data. In this section, the aim is not to restate the values calculated or recompare them with the literature, but rather to present a broad outline summarizing the most important of the observed parameters for each object.

5.2.1 - The HII region surrounding Zeta Ophiuchi

From the results obtained from the 2.3 GHz data, it is concluded that the HII region surrounding the early-type, main-sequence star ζ Ophiuchi is a density-bounded region with a rather lower than average electron density. There appears to be only one exciting star in this region, ζ Ophiuchi, which

is a runaway star from the Scorpius OB2 association. The spectral index of the HII region is α = -0.14, the spectrum of an optically thin, thermal region, as expected. In explaining the shock models of Draine (1986) and Elitzur and Watson (1980) for the line of sight towards ζ Ophiuchi, it can be said that the most likely source for the shock is this HII region. The space velocity of ζ Ophiuchi is in the region of 21 kms^{-1} indicating that, if this velocity is the result of a supernova which occured about a million years ago, the shock is unlikely to be associated with this event (Draine (1986) predicts a shock velocity of 9 kms^{-1}).

5.2.2 - The North Polar Spur

The conclusion reached from examination of the observations of the NPS indicates that this structure is most likely the remnant of a very old supernova (many millions of years old), well into the radiative phase of its evolution, which is in the process of being reheated by some external influence. The most likely source of this reheating is the interaction of a younger supernova remnant with the NPS. Possible candidates for this young, "reheating" remnant are Loop IV, suggested by Borken and Iwan (1977) and the "loop" suggested in figure 4.23 as a dashed small circle. The spectral index of the spur, calculated by averaging the values calculated at a number of points in the NPS, is α = -0.65, the spectrum of a synchrotron source. This confirms the suggestion that the NPS is a supernova remnant.

5.2.3 - The thermal spur associated with the HII region S54

This object is clearly seen in the 2.3 GHz data after removal of the Galactic disc emission. A comparison of the structure and extent of the spur at 2.3 GHz with the maps of Muller *et al* (1987) shows an appreciable amount of correlation. Although a spectral index determination proved to be unsuccessful, there is every reason to support the result of Muller *et al* (1987) that the spur is associated with the HII region and that it has the spectrum of an optically thin, thermal source.

5.3 - Conclusion

From the overall results obtained from the data of the fourth part of the Rhodes University Skymap program, it can be concluded that the primary method used for the removal of the Galactic disc emission is a valid and useful method, yielding results which are acceptable and directly comparable with results quoted in the literature and with theory. The results of this part of the Skymap program are valid proof that medium-resolution, large-scale surveys are important in the overall understanding of the Galaxy in which we live.

References

Berkhuijsen, E.M., Haslam, C.G.T., Salter, C.J.: 1971, *Astron. Astrophys.* **14**, 252

Berkhuijsen, E.M.: 1973, *Astron. Astrophys.* **24**, 143

Beuermann, K., Kanbach, G., Berkhuijsen, E.M.: 1985, *Astron. Astrophys.* **153**, 17

Blaauw, A.: 1964, *Ann. Rev. Astron. Astrophys.* **2**, 213

Blaauw, A.: 1978, Internal Motions and Age of the Sub-association Upper Scorpio in *Problems of Physics and Evolution of the Universe*, ed. V.L. Mirzoyan, American Academy of Sciences, Yerevah, p. 101

Bohlin, R.: 1975, *Astrophys. J.* **200**, 402

Bolton, J.G., Wright, A.E., Savage, A.: 1979, *Aust. J. Phys. Astrophys. Suppl.* **46**, 1

Borken, R.J., Iwan, D.C.: 1977, *Astrophys. J.* **218**, 511

Celnik, W.E., Weiland, H.: 1988, *Astron. Astrophys.* **192**, 316

Churchwell, E., Walmsley, C.M.: 1973, *Astron. Astrophys.* **23**, 117

Clark, D.H., Caswell, J.L.: 1976, *Mon. Not. R. Astron. Soc.* **174**, 267

Conner, J.P., Evans, W.D., Belian, R.D.: 1969, *Astrophys. J.* **157**, L157

Cruddace, R.G., Friedman, H., Fritz, G., Shulman, S.: 1976, *Astrophys. J.* **207**, 888

Crutcher, R.M.: 1977, *Astrophys. J.* **217**, L109

Crutcher, R.M.: 1979, *Astrophys. J.* **231**, L151

Dixon, R.S., Sonneborn, G.: 1980, *A Master List of Nonstellar Optical Astronomical Objects*, Ohio State University Press

Draine, B.T.: 1986, *Astrophys. J.* **310**, 408

Elitzur, M., Watson, W.D.: 1980, *Astrophys. J.* **236**, 172

Flanagan, C.S.: 1981, *Honours Project*, Rhodes University

Green, D.A.: 1988, *Astrophysics and Space Science* **148**, 3

Hanbury Brown, R., Davis, R.D., Hazard, C.: 1960, *Observatory*, **80**, 191

Haslam, C.G.T., Salter, C.J., Stoffel, H., Wilson, W.E.: 1982, *Astron. Astrophys. Suppl.* **47**, 1

Hawkins, I., Jura, M., Meyer, D.M.: 1985, *Astrophys. J.* **294**, L131

Hayakawa, S., Kato, T., Nagase, F., Yamashita, K., Murakami, T., Tanaka, Y.: 1977, *Astrophys. J.* **213**, L109

Heiles, C.: 1979, *Astrophys. J.* **208**, L137

Humphreys, R.M.: 1978, *Astrophys. J. Suppl.* **38**, 309

Jonas, J.L.: 1982, *Master of Science Thesis*, Rhodes University

Jonas, J.L., de Jager, G., Baart, E.E.: 1985, *Astron. Astrophys. Suppl.* **62**, 105

Kraus, J.D.: 1966, *Radio Astronomy*, McGraw-Hill Book Company

Landecker, T.L., Wielebinski, R.: 1970, *Aust. J. Phys.* **16**, 1

Large, M.I., Mills, B.Y., Little, A.G., Crawford, D.F., Sutton, J.M.: 1981, *Mon. Not. R. Astron. Soc.* **194**, 693

Lesh, J.R.: 1968, *Astrophys. J.* **152**, 905

McGee, R.X., Murray, J.D., Milton, J.A.: 1959, *Aust. J. Phys.* **12**, 127

Mezger, P.G., Henderson, A.P.: 1967, *Astrophys. J.* **147**, 471

Morton, D.C.: 1975, *Astrophys. J.* **197**, 85

Mountfort, P.I., Jonas, J.L., de Jager, G., Baart, E.E.: 1987, *Mon. Not. R. Astron. Soc.* **226**, 917

Muller, P., Rief, K., Reich, W.: 1987, *Astron. Astrophys.* **183**, 327

Muller, P.: 1985, *Diploma thesis*, Bonn University

Nicolson, G.D.: 1970, *IEEE T.M.T.T.* **18**, 169

Oort, J.H.: 1959, *Handbuch der Physik*, **211**, 124

Pacholczyk, A.G.: 1978, *A Handbook of Radio Sources - Part One*, Pachart Publishing House, P.O.Box 42963, Tucson, Arizona 85733

Panagia, N.: 1973, *Astron. J.* **78**, 929

Phillipps, S., Kearsey, S., Osborne, J.L., Haslam, C.G.T., Stoffel, H.: 1981, *Astron. Astrophys.* **98**, 286

Reich, P., Reich, W.: 1986, *Astron. Astrophys. Suppl.* **63**, 205

Reynolds, R.J., Roessler, F.L., Scherb, F.: 1974, *Astrophys. J.* **192**, L53

Reynolds, R.J., Ogden, P.M.: 1982, *Astron. J.* **87**, 306

Rieke, G.H., Lebofsky, M.J.: 1985, *Astrophys. J.* **288**, 613

Salter, C.J.: 1970, *PhD thesis*, Manchester University

Savage, B.D.: 1975, *Astrophys. J.* **199**, 92

Scherb, F.: 1981, *Astrophys. J.* **243**, 644

Seward, F., Burginyon, G., Grader, R., Hill, R., Palmieri, T., Stoering, P., Toor, A.: 1976, *Astrophys. J.* **205**, 238

Shaver, P.A., Goss, W.M.: 1970b, *Aust. J. Phys. Astrophys. Suppl.* **14**, 133

Smith, A.M., Krishna Swamy, K.S., Stetcher, T.P.: 1978, *Astrophys. J.* **220**, 138

Sofue, Y.: 1976, *Astron. Astrophys,* **48**, 1

Sofue, Y.: 1977, *Astron. Astrophys.* **60**, 327

Sofue, Y., Reich, W.: 1979, *Astron. Astrophys. Suppl.* **38**, 251

Stromgren, B.: 1936, *Astrophys. J.* **89**, 526

Watson, W.D.: 1978, *Ann. Rev. Astron. Astrophys.* **16**, 585

Woermann, B.: 1988, *Master of Science Thesis*, Rhodes University, in preparation

Wright, M.R.: 1985, *Honours Project*, Rhodes University

Appendix One - Contour Maps

Presented in this appendix are contour maps covering the entire area of sky discussed in this thesis. The contour levels are tabulated below in table A1.1, and the limits of each map (the whole area is divided into 56 sections) and the lowest and highest contours plotted on each map are tabulated in table A1.2. The horizontal contour line(s) appearing at the bottom of maps A1 to I1 and at the top of maps B4 to N4 is an effect of the coordinate transform program and the contour plotting program, and should be ignored.

The resolution of these maps (the half power beam width) is 0.38°, and the beam sensitivity is 12.26 Jy/K. The rms noise level is 10.8mK. Note that 1K antenna temperature corresponds to 1.51K full beam brightness temperature.

These maps are plotted in equatorial coordinates, with hours and minutes of right ascension labelled along the horizontal axes and degrees of declination labelled along the vertical axes. The epoch for these maps is 1950.0. The grid lines on the maps represent Galactic longitude and Galactic latitude at a spacing of five degrees. Note that, in table A1.2, the left and right limits of the maps are given in degrees (one hour of right ascension corresponds to fifteen degrees).

Table A1.1 - Contour levels.

Contour Level Ta / mK	Contour Label	Contour Level Ta / mK	Contour Label
25	>	1450	>
50	>	1600	1.6K
75	>	1800	>
100	100	2000	>
125	>	2500	>
150	>	3000	3K
175	>	3500	>
200	200	4000	>
225	>	4500	>
250	>	5000	5K
275	>	6000	>
300	300	7000	>
340	>	8000	>
380	>	9000	>

Table A1.1 - Contour levels continued.

Contour Level Ta / mK	Contour Label	Contour Level Ta / mK	Contour Label
420	>	10000	10K
460	460	12000	>
500	>	14000	>
550	>	16000	>
600	>	18000	>
680	680	20000	20K
760	>	25000	>
840	>	30000	>
920	>	40000	>
1000	1K	50000	50K
1150	>	55000	>
1300	>	60000	>

Table A1.2 - Map limits and lowest/highest contour levels plotted.

MAP NUMBER	LEFT LIMIT deg	RIGHT LIMIT deg	BOTTOM LIMIT deg	TOP LIMIT deg	LOWEST CONTOUR mK	HIGHEST CONTOUR mK
A1	223.55	209.20	-26.2	-15.6	25	175
B1	236.90	222.55	-26.2	-15.6	25	380
C1	250.25	235.90	-26.2	-15.6	25	680
D1	263.60	249.25	-26.2	-15.6	25	1300
E1	276.95	262.60	-26.2	-15.6	25	50000
F1	290.30	275.95	-26.2	-15.6	25	1600
G1	303.65	289.30	-26.2	-15.6	25	500
H1	317.00	302.65	-26.2	-15.6	25	760
I1	330.35	316.00	-26.2	-15.6	25	760
J1	343.70	329.35	-26.2	-15.6	50	550
K1	357.05	342.70	-26.2	-15.6	25	225
L1	10.40	356.05	-26.2	-15.6	25	300
M1	23.75	9.40	-26.2	-15.6	25	340
N1	37.10	22.75	-26.2	-15.6	25	125
A2	223.55	209.20	-16.6	-6.0	25	275
B2	236.90	222.55	-16.6	-6.0	50	340
C2	250.25	235.90	-16.6	-6.0	75	340
D2	263.60	249.25	-16.6	-6.0	150	840
E2	276.95	262.60	-16.6	-6.0	340	50000
F2	290.30	275.95	-16.6	-6.0	200	6000
G2	303.65	289.30	-16.6	-6.0	100	550
H2	317.00	302.65	-16.6	-6.0	75	225
I2	330.35	316.00	-16.6	-6.0	75	300
J2	343.70	329.35	-16.6	-6.0	25	225
K2	357.05	342.70	-16.6	-6.0	25	200
L2	10.40	356.05	-16.6	-6.0	25	150
M2	23.75	9.40	-16.6	-6.0	25	275
N2	37.10	22.75	-16.6	-6.0	25	275
A3	223.55	209.20	-7.0	3.6	25	225
B3	236.90	222.55	-7.0	3.6	25	275

Table A1.2 - Map limits and lowest/highest contour levels plotted continued.

MAP NUMBER	LEFT LIMIT deg	RIGHT LIMIT deg	BOTTOM LIMIT deg	TOP LIMIT deg	LOWEST CONTOUR mK	HIGHEST CONTOUR mK
C3	250.25	235.90	-7.0	3.6	50	500
D3	263.60	249.25	-7.0	3.6	100	3000
E3	276.95	262.60	-7.0	3.6	250	1300
F3	290.30	275.95	-7.0	3.6	340	14000
G3	303.65	289.30	-7.0	3.6	125	680
H3	317.00	302.65	-7.0	3.6	75	250
I3	330.35	316.00	-7.0	3.6	50	600
J3	343.70	329.35	-7.0	3.6	25	500
K3	357.05	342.70	-7.0	3.6	25	340
L3	10.40	356.05	-7.0	3.6	25	340
M3	23.75	9.40	-7.0	3.6	25	420
N3	37.10	22.75	-7.0	3.6	25	175
A4	223.55	209.20	2.6	13.2	25	275
B4	236.90	222.55	2.6	13.2	25	275
C4	250.25	235.90	2.6	13.2	25	300
D4	263.60	249.25	2.6	13.2	25	2000
E4	276.95	262.60	2.6	13.2	25	600
F4	290.30	275.95	2.6	13.2	25	7000
G4	303.65	289.30	2.6	13.2	25	1300
H4	317.00	302.65	2.6	13.2	25	300
I4	330.35	316.00	2.6	13.2	25	340
J4	343.70	329.35	2.6	13.2	25	460
K4	357.05	342.70	2.6	13.2	25	250
L4	10.40	356.05	2.6	13.2	25	275
M4	23.75	9.40	2.6	13.2	25	275
N4	37.10	22.75	2.6	13.2	25	150

Figure A1.1 - Rhodes 2.3 Ghz Sky Survey (Map A1).

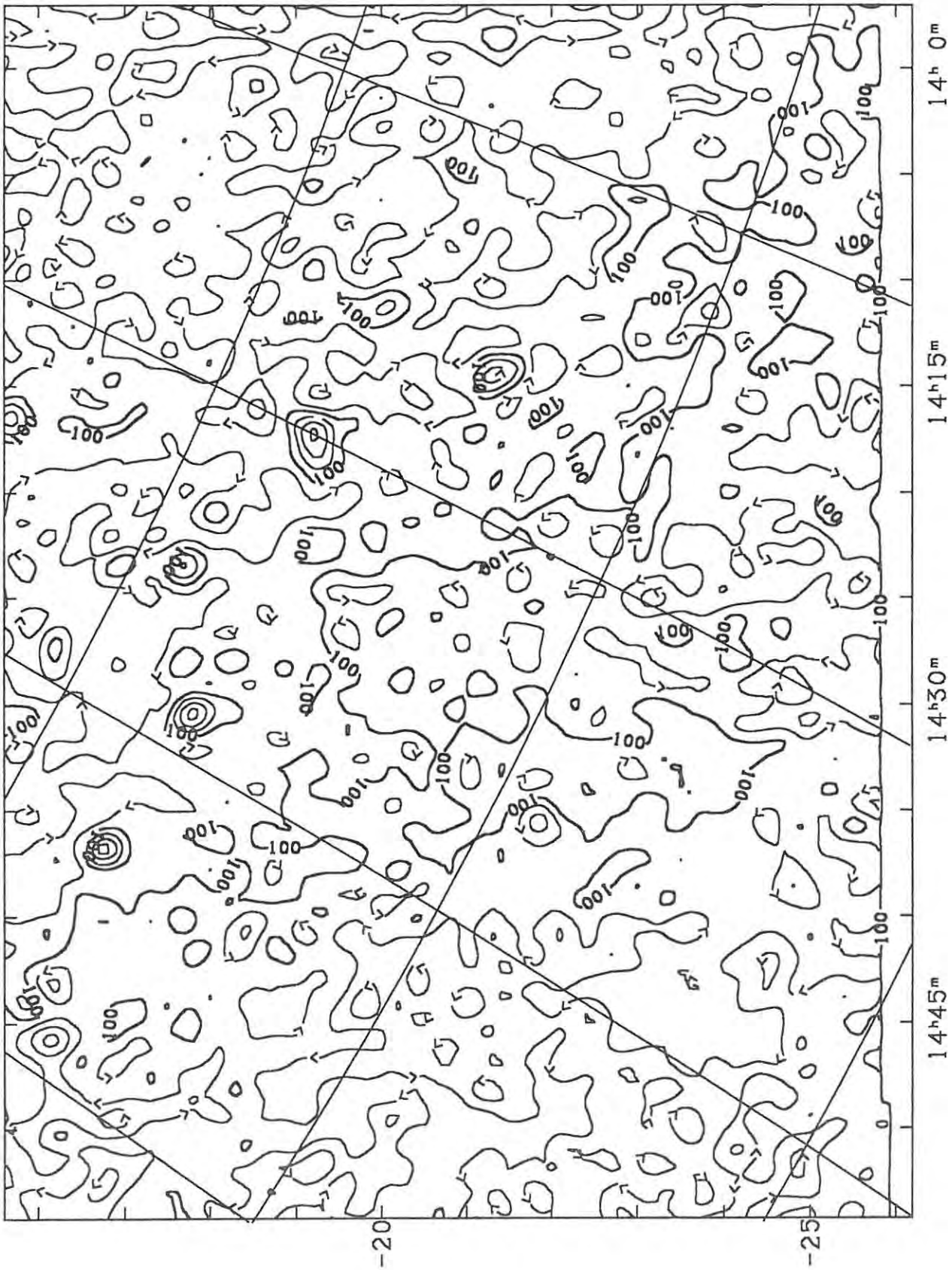

Figure A1.2 - Rhodes 2.3 Ghz Sky Survey (Map B1).

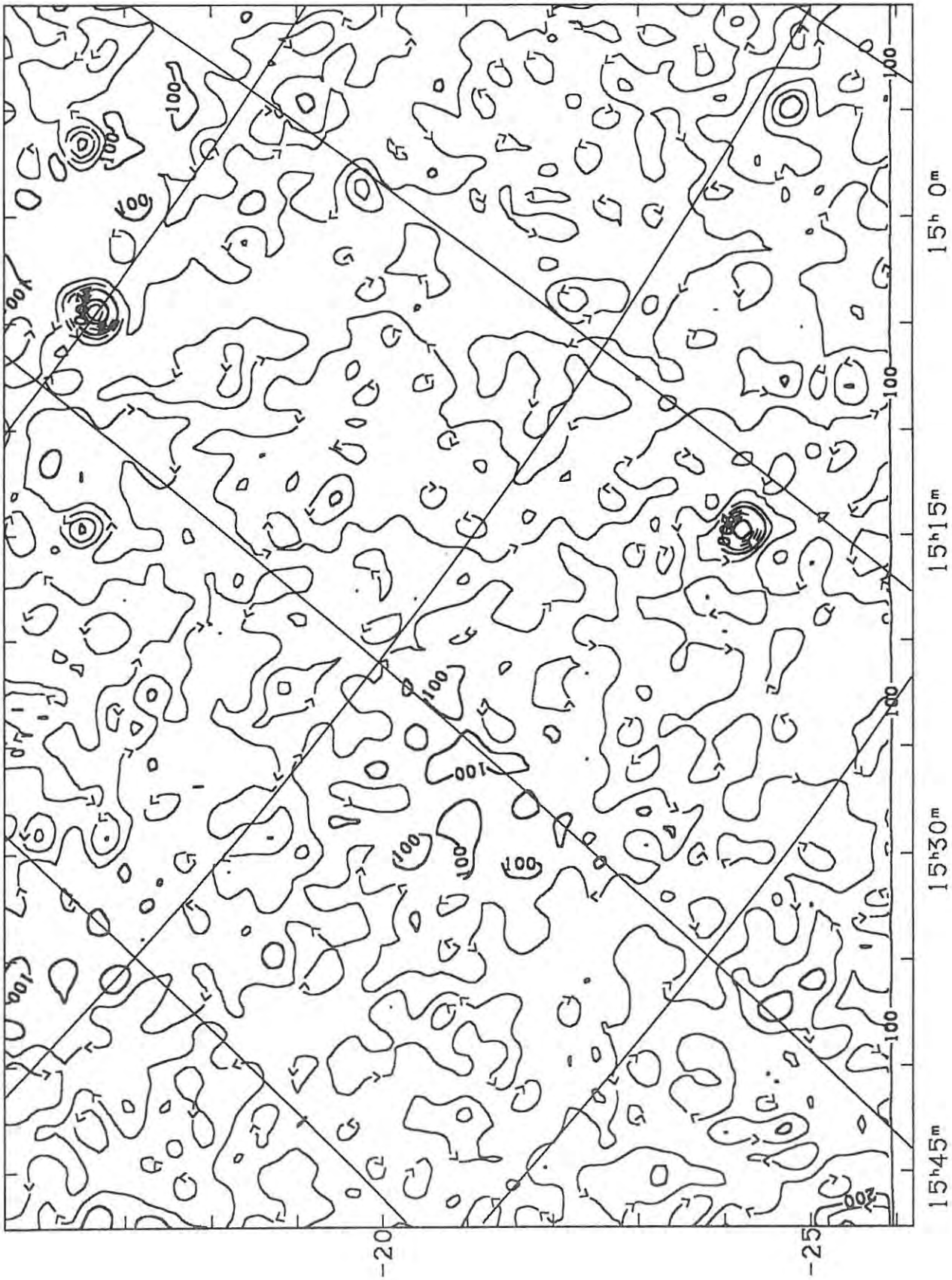

Figure A1.3 - Rhodes 2.3 Ghz Sky Survey (Map C1).

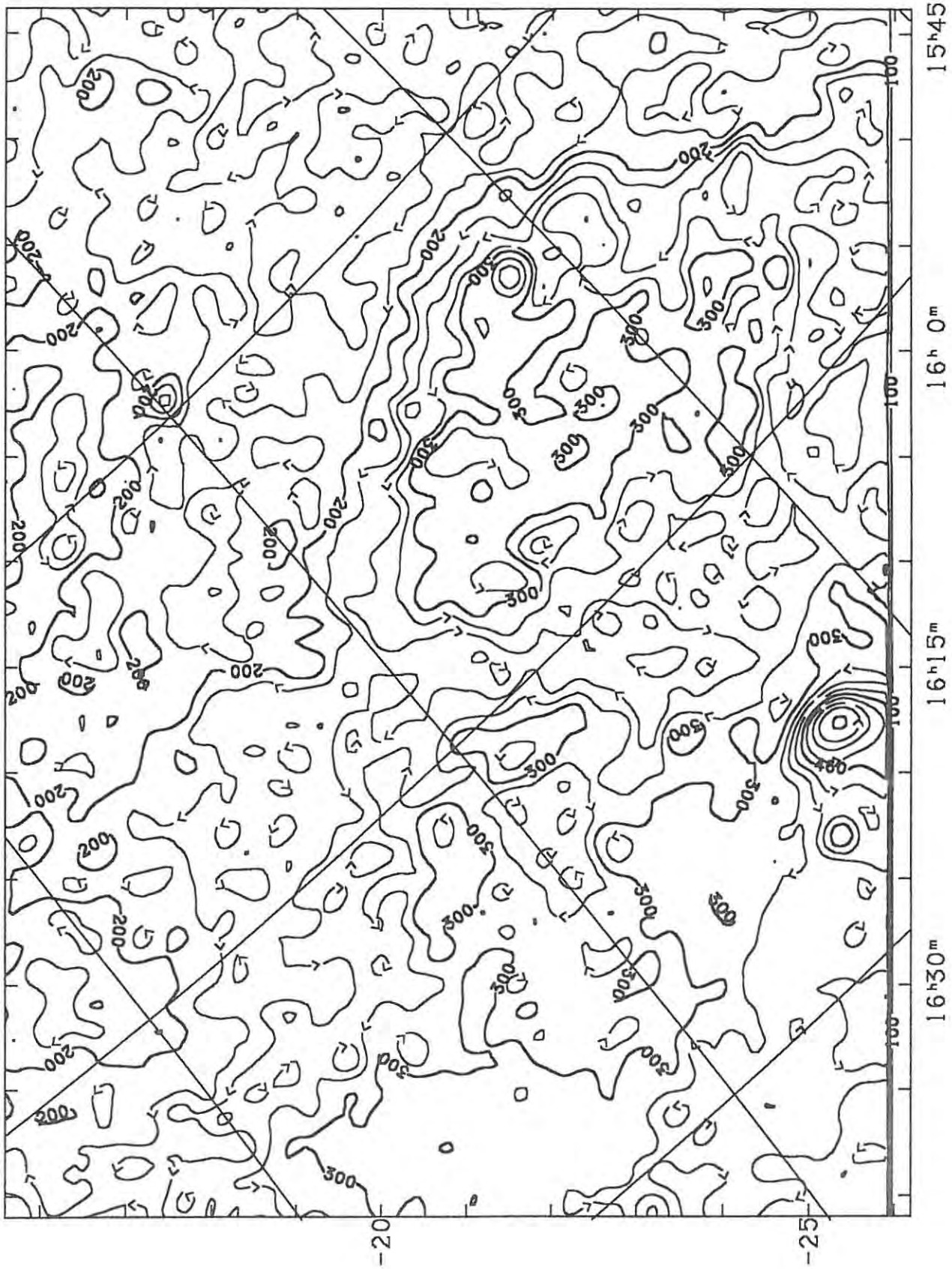

Figure A1.4 - Rhodes 2.3 Ghz Sky Survey (Map D1).

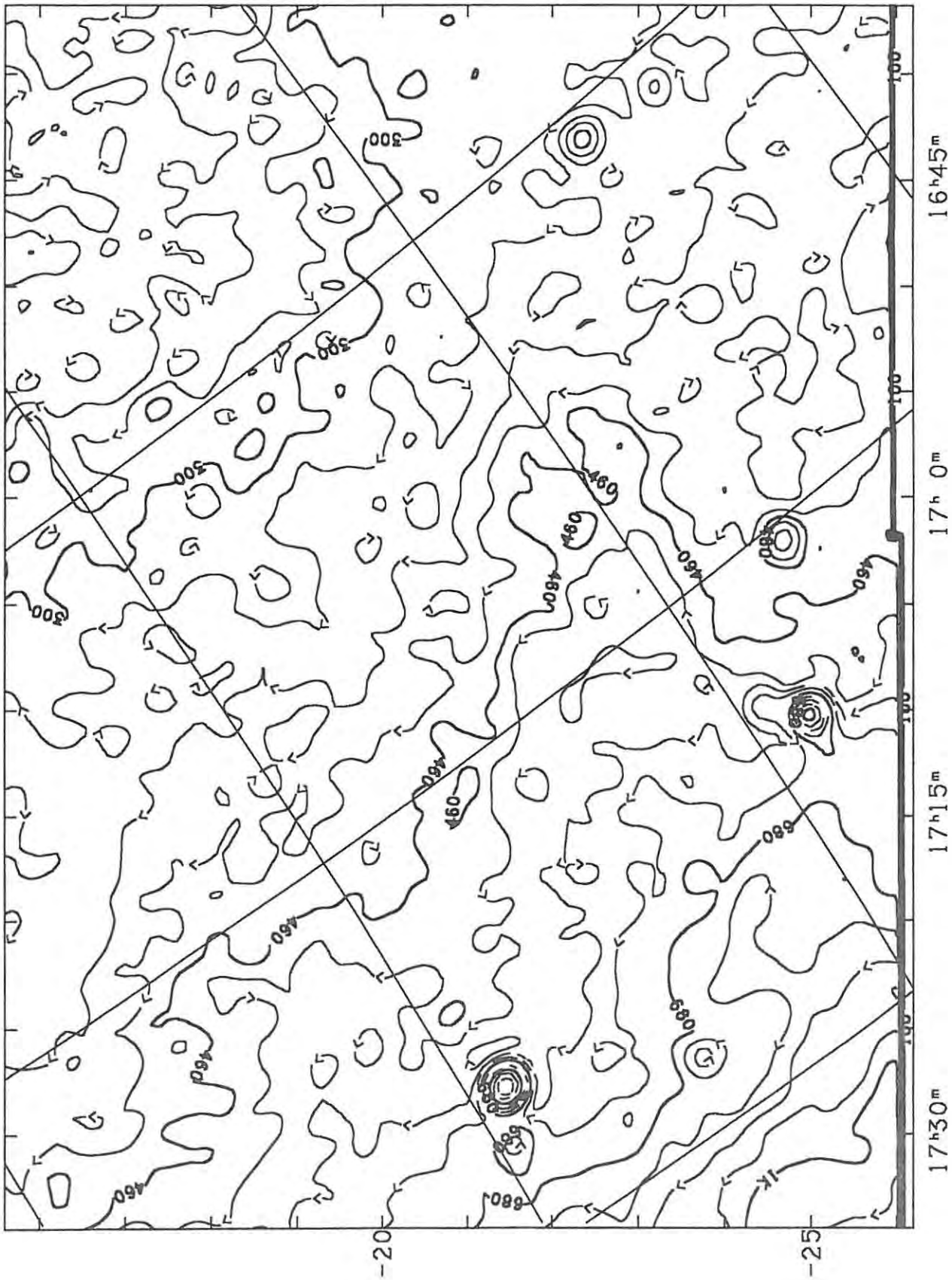

Figure A1.5 - Rhodes 2.3 Ghz Sky Survey (Map E1).

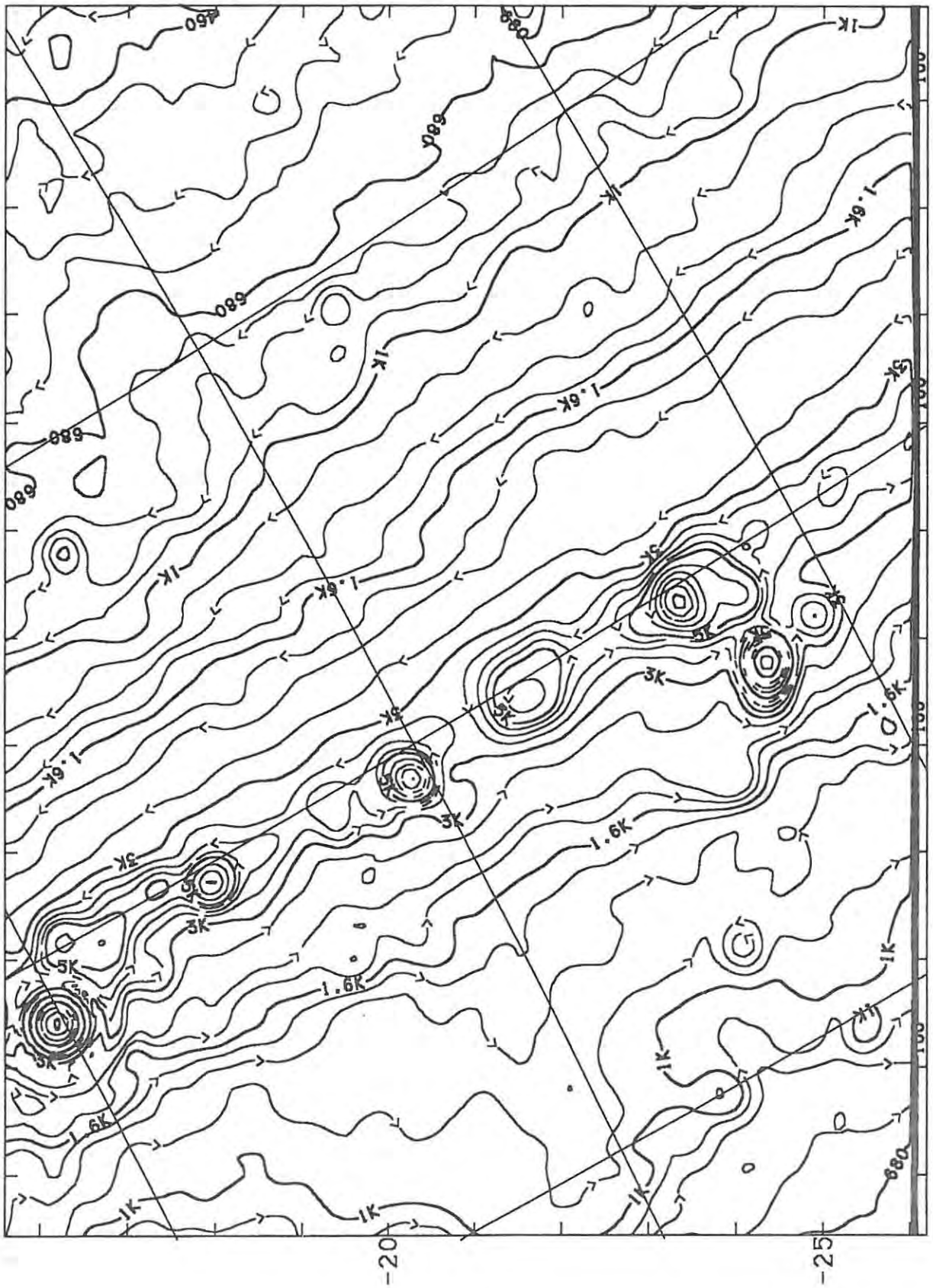

Figure A1.6 - Rhodes 2.3 Ghz Sky Survey (Map F1).

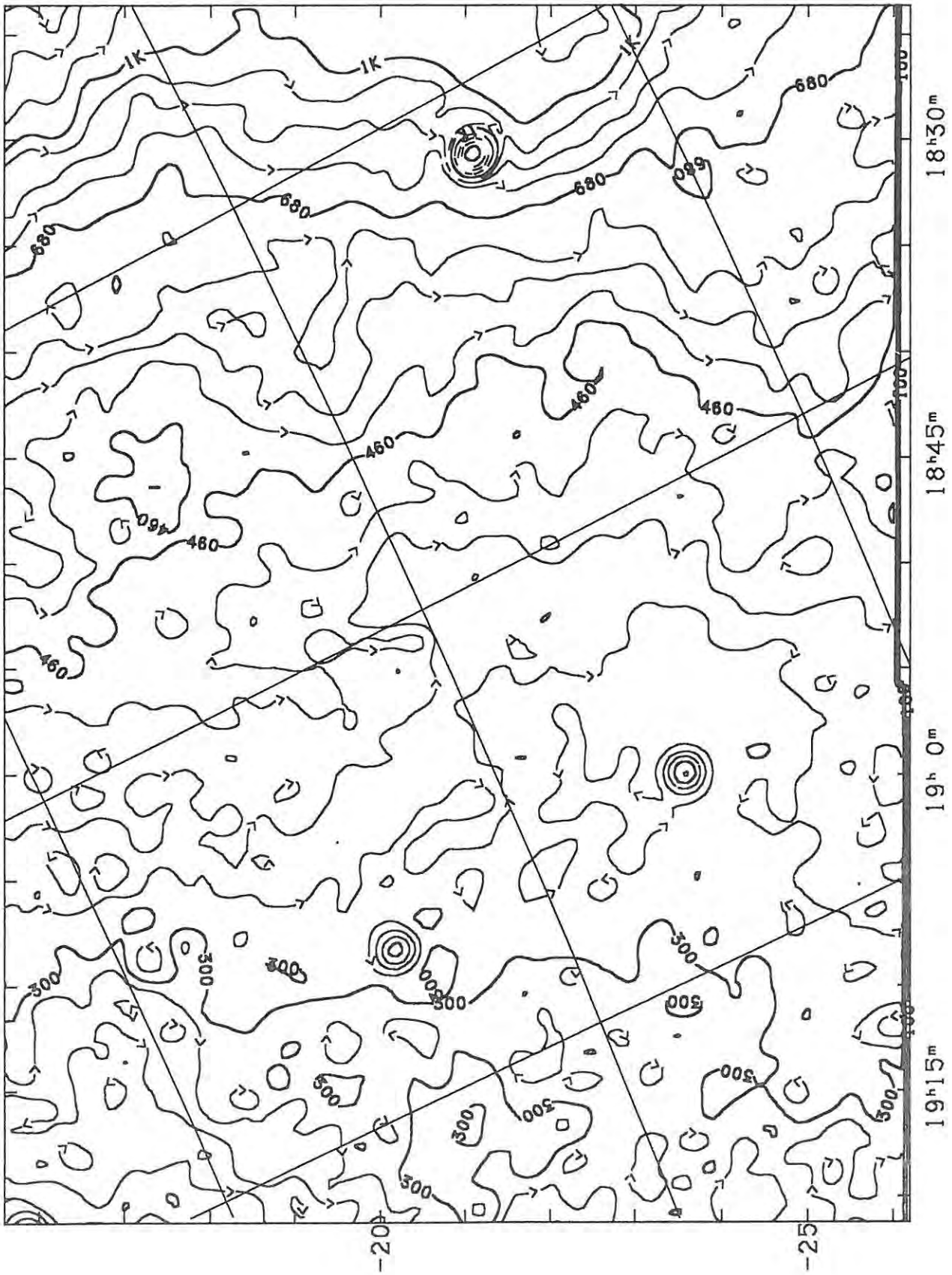

Figure A1.7 - Rhodes 2.3 Ghz Sky Survey (Map G1).

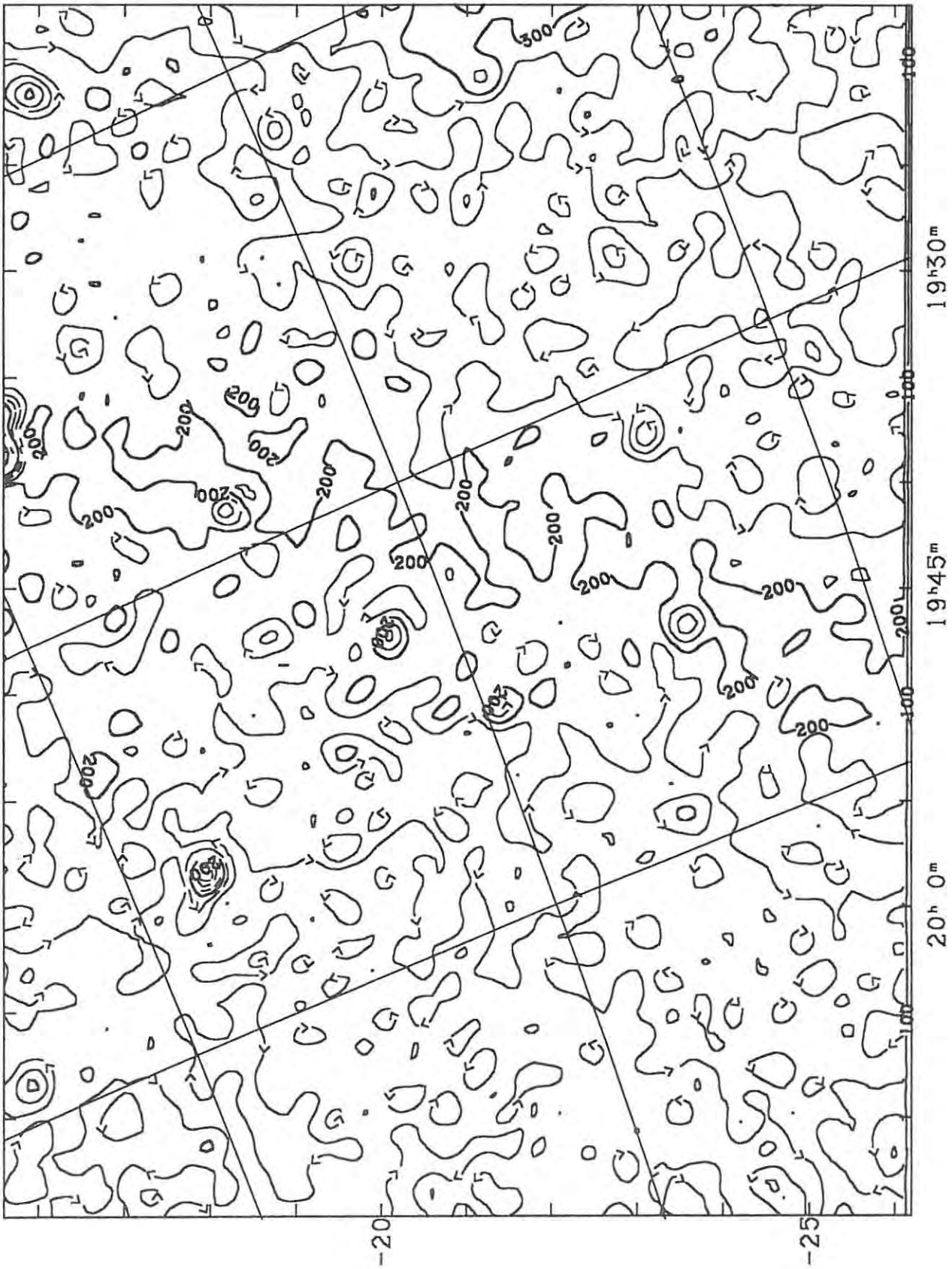

Figure A1.8 - Rhodes 2.3 Ghz Sky Survey (Map H1).

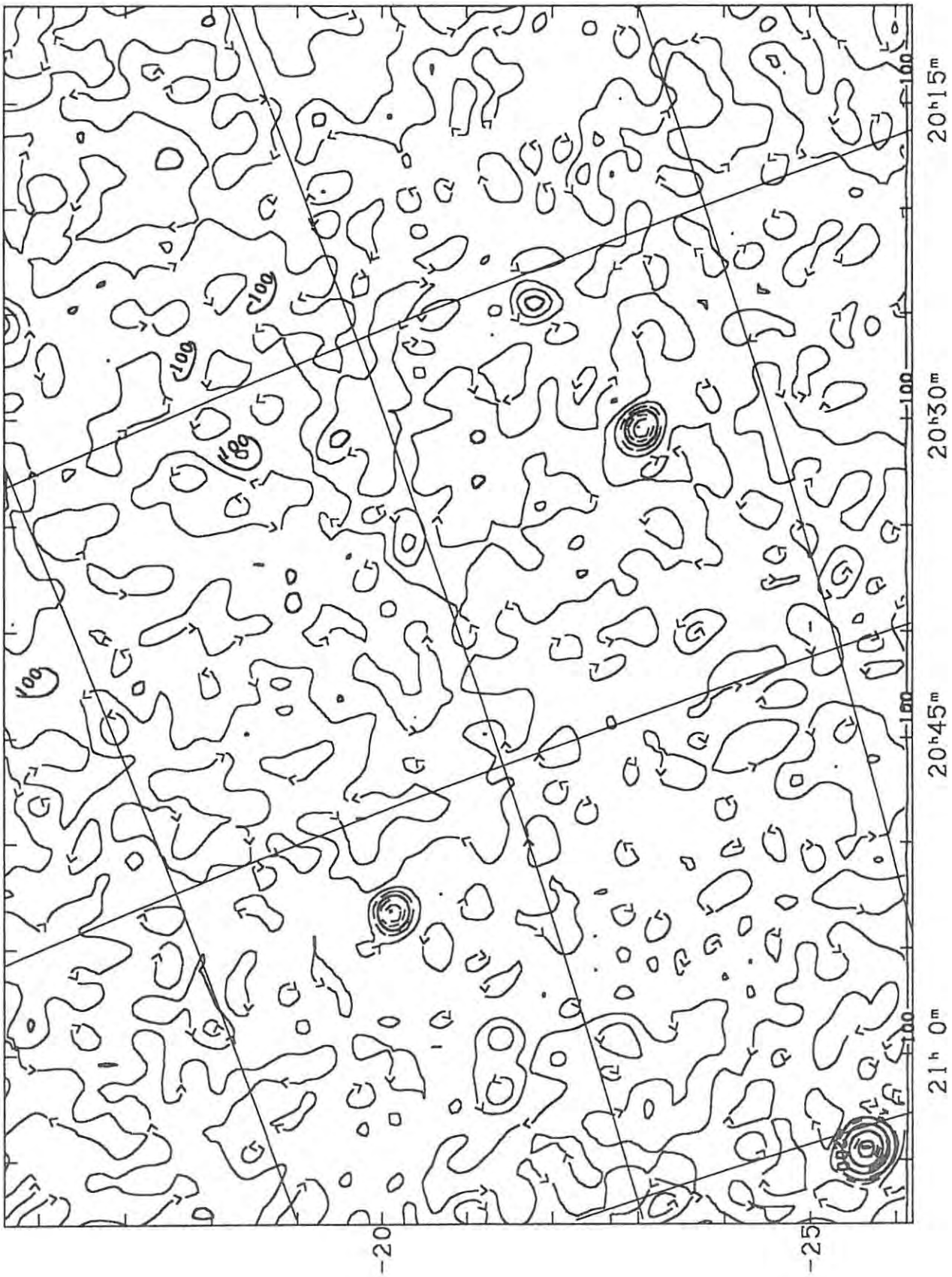

Figure A1.9 - Rhodes 2.3 Ghz Sky Survey (Map I1).

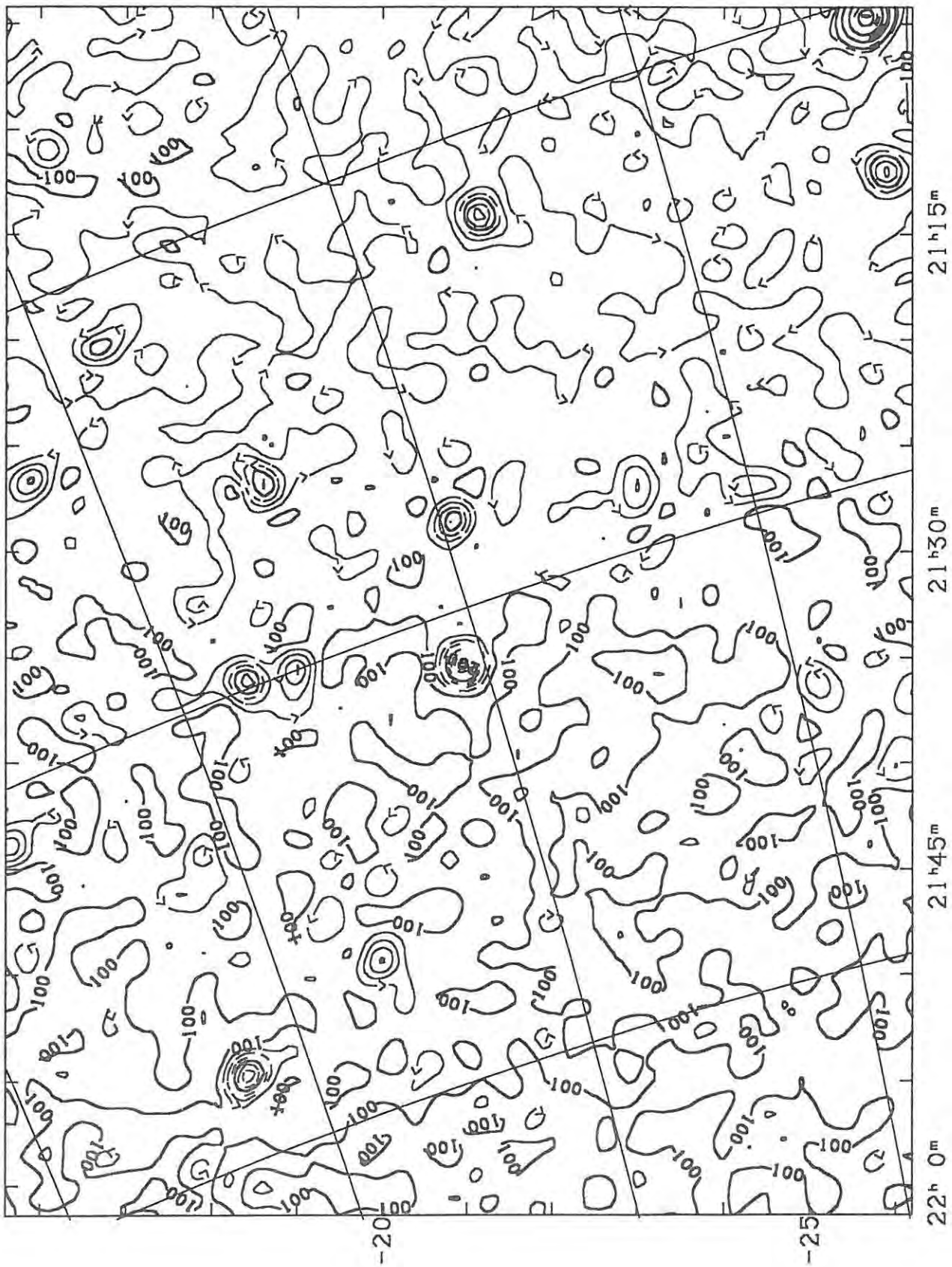

Figure A1.10 - Rhodes 2.3 Ghz Sky Survey (Map J1).

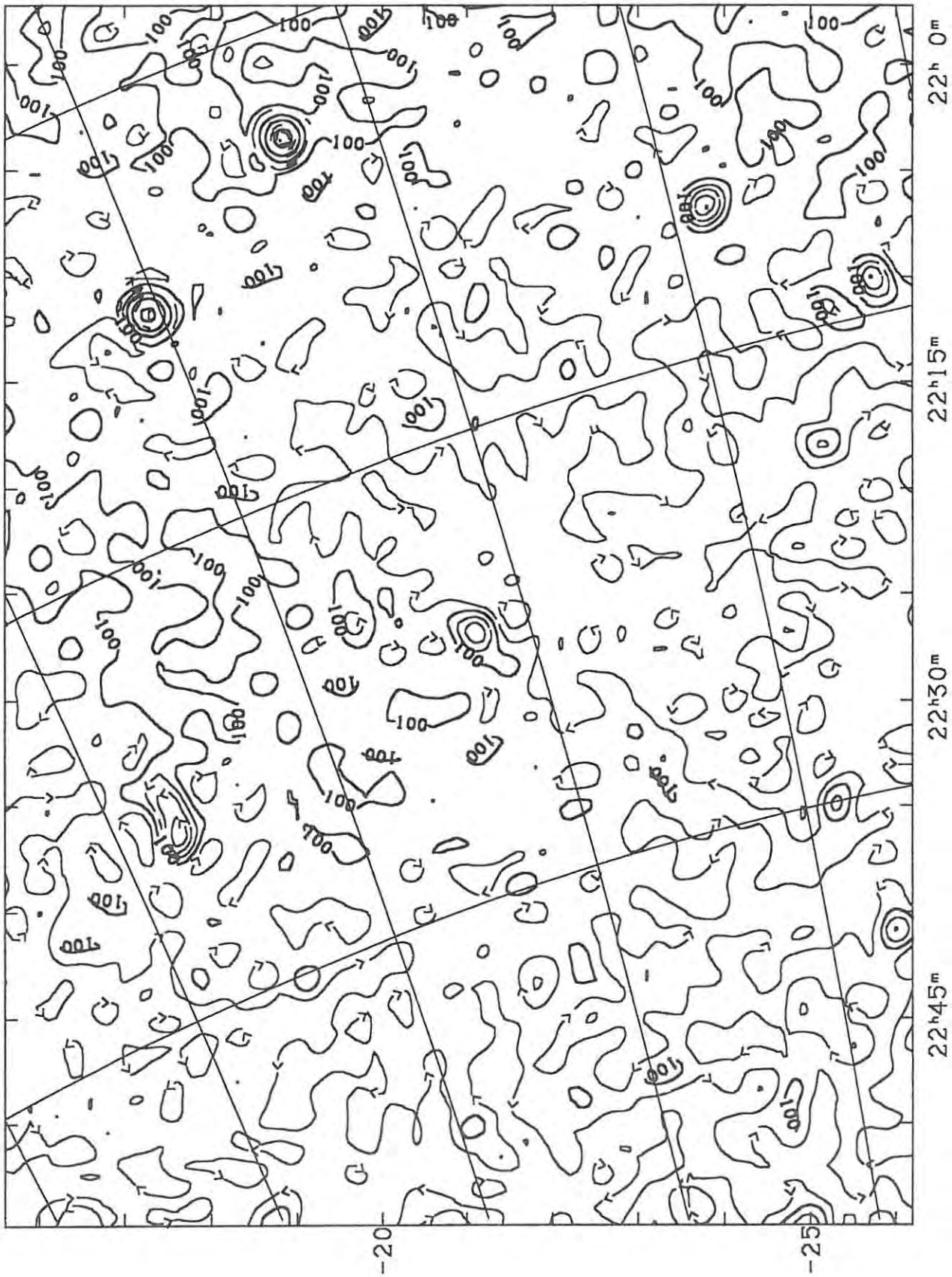

Figure A1.11 - Rhodes 2.3 Ghz Sky Survey (Map K1).

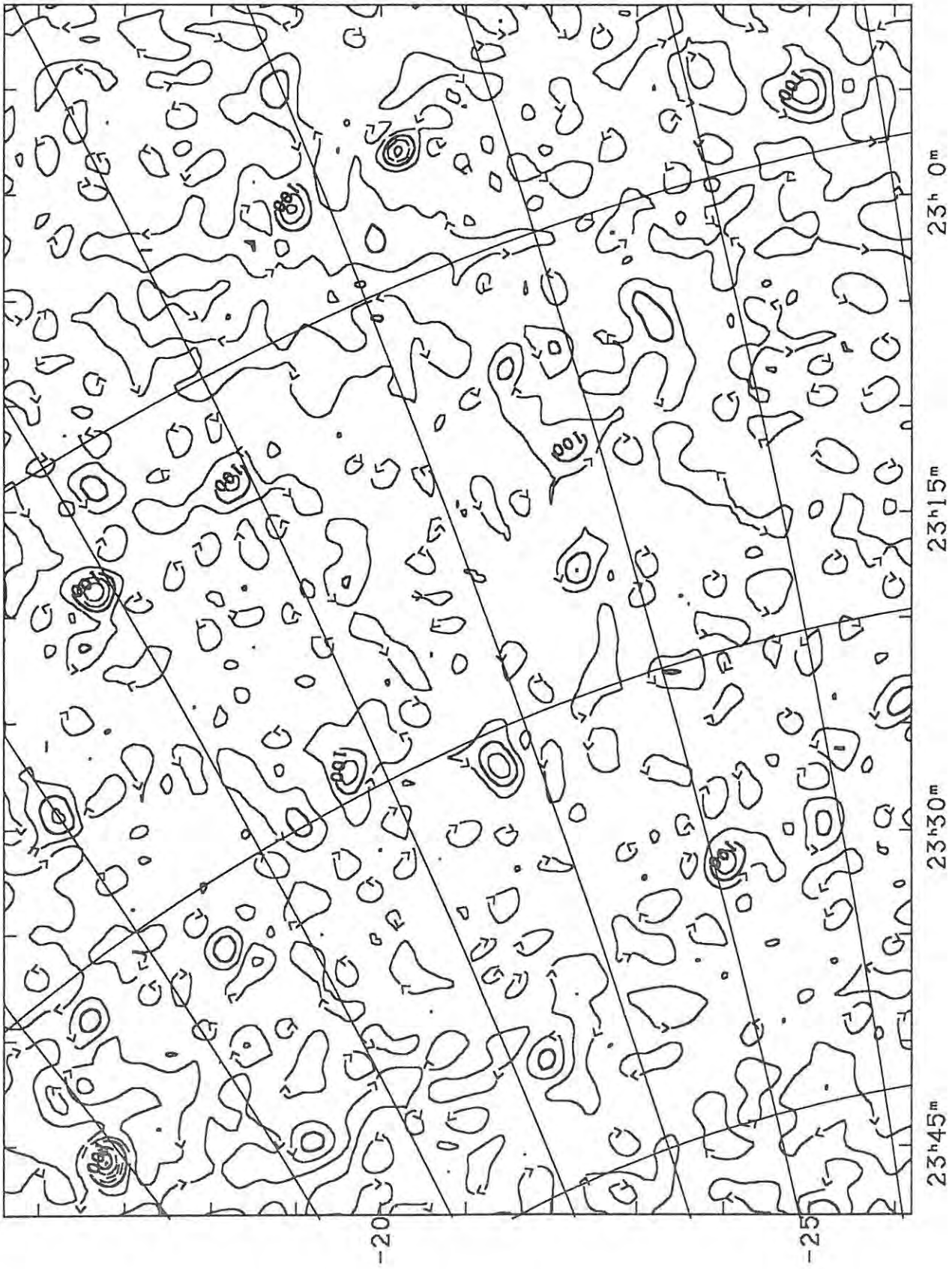

Figure A1.12 - Rhodes 2.3 Ghz Sky Survey (Map L1).

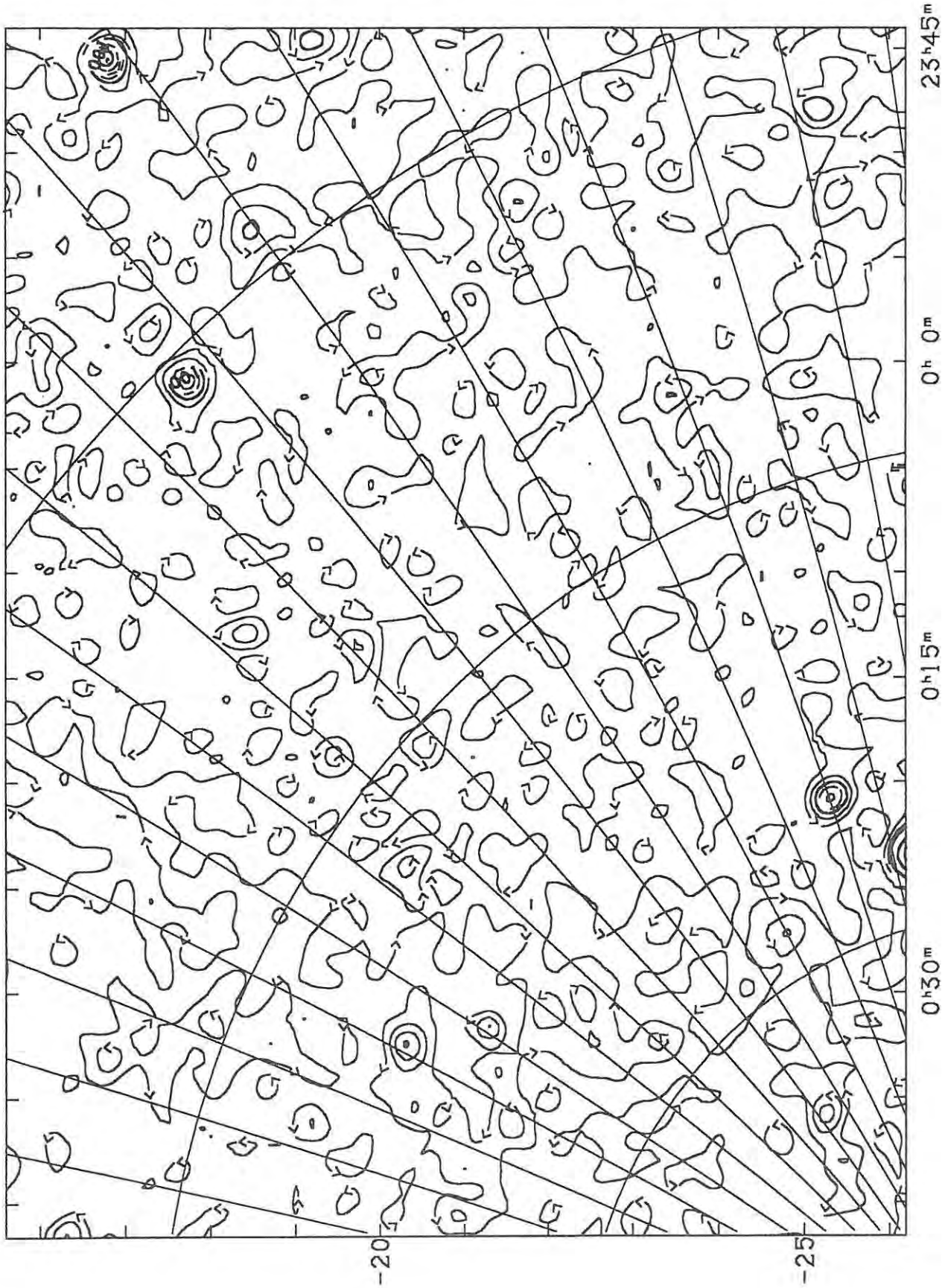

Figure A1.13 - Rhodes 2.3 Ghz Sky Survey (Map M1).

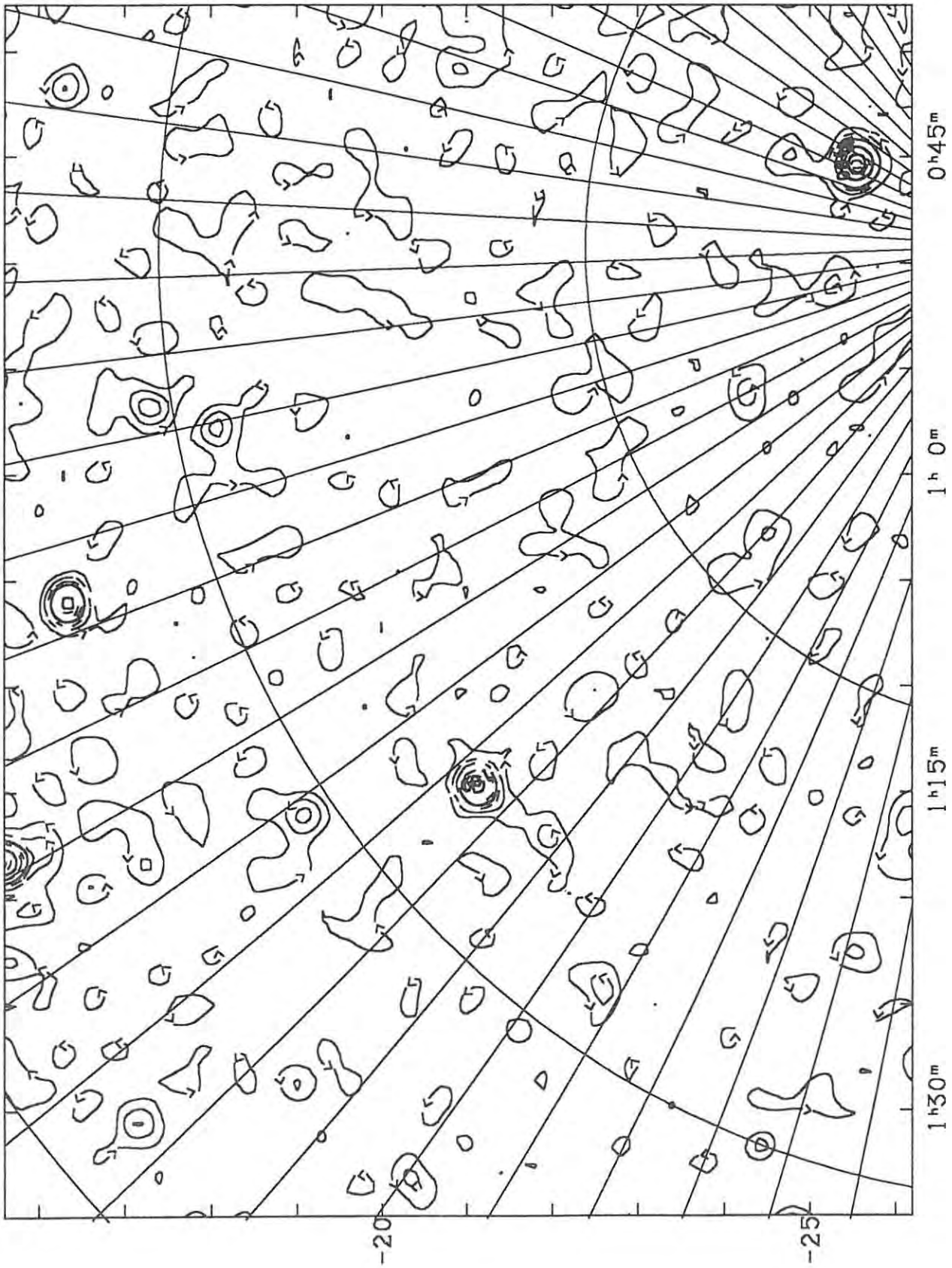

Figure A1.14 - Rhodes 2.3 Ghz Sky Survey (Map N1).

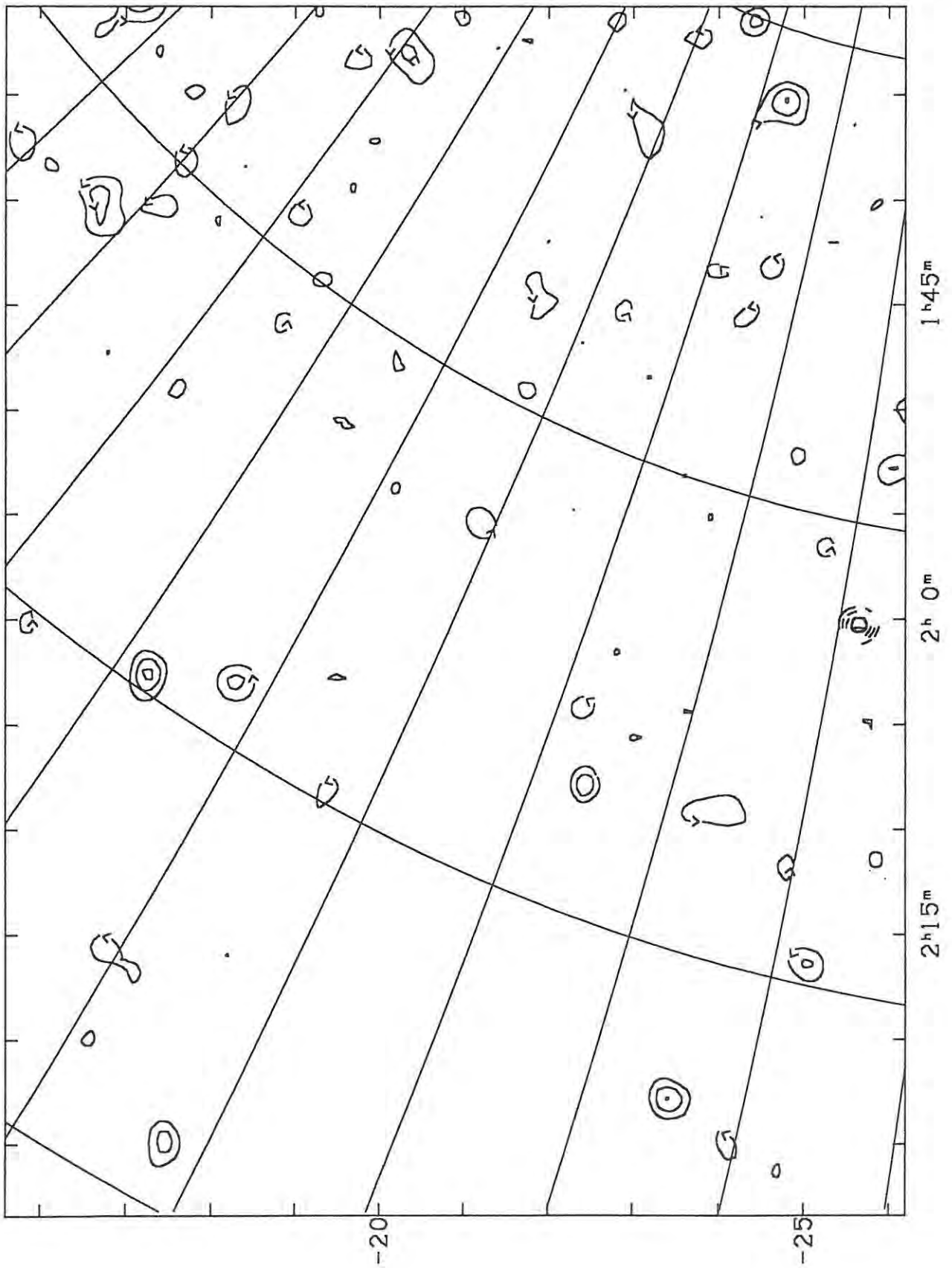

Figure A1.15 - Rhodes 2.3 Ghz Sky Survey (Map A2).

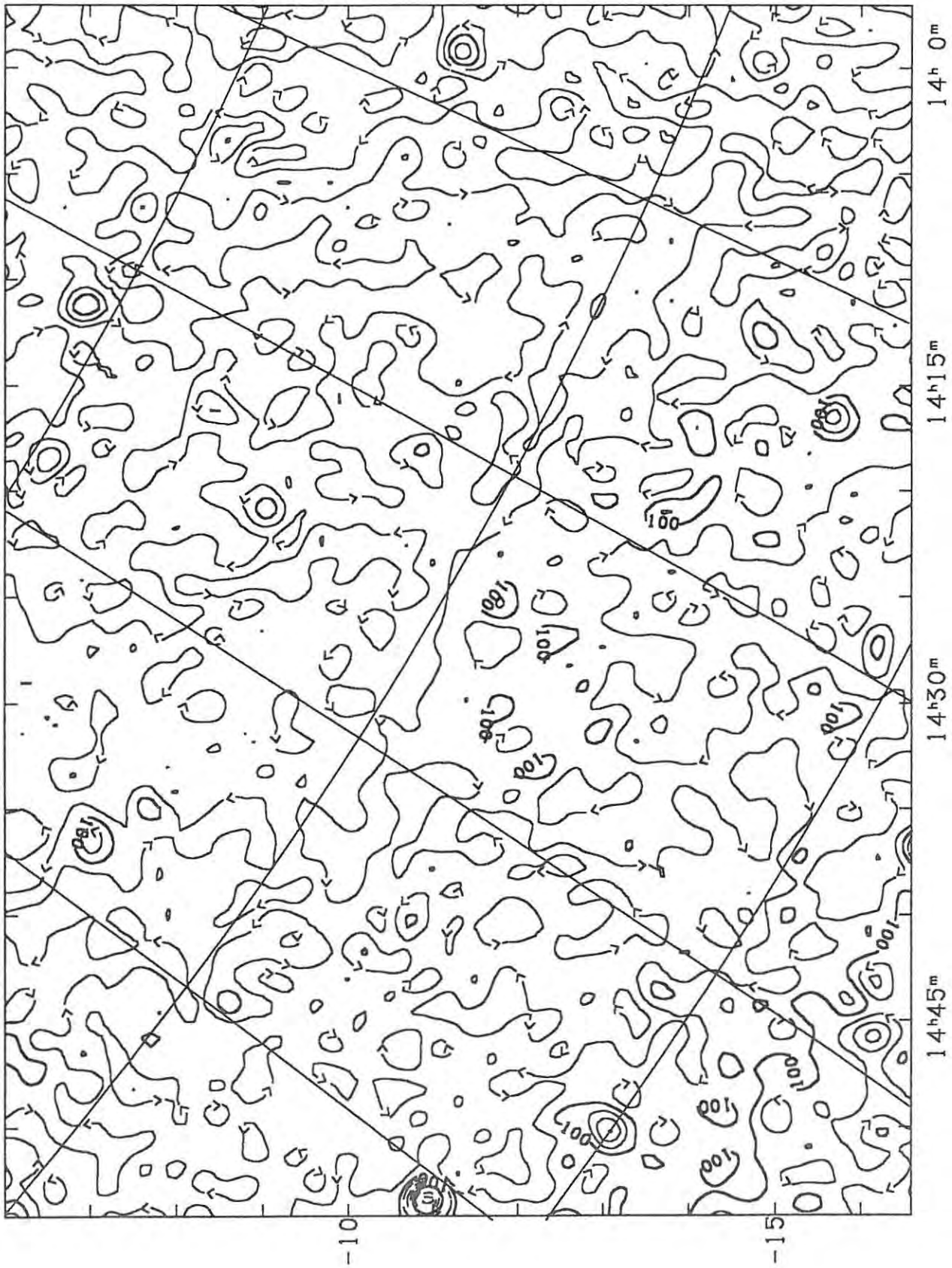

Figure A1.16 - Rhodes 2.3 Ghz Sky Survey (Map B2).

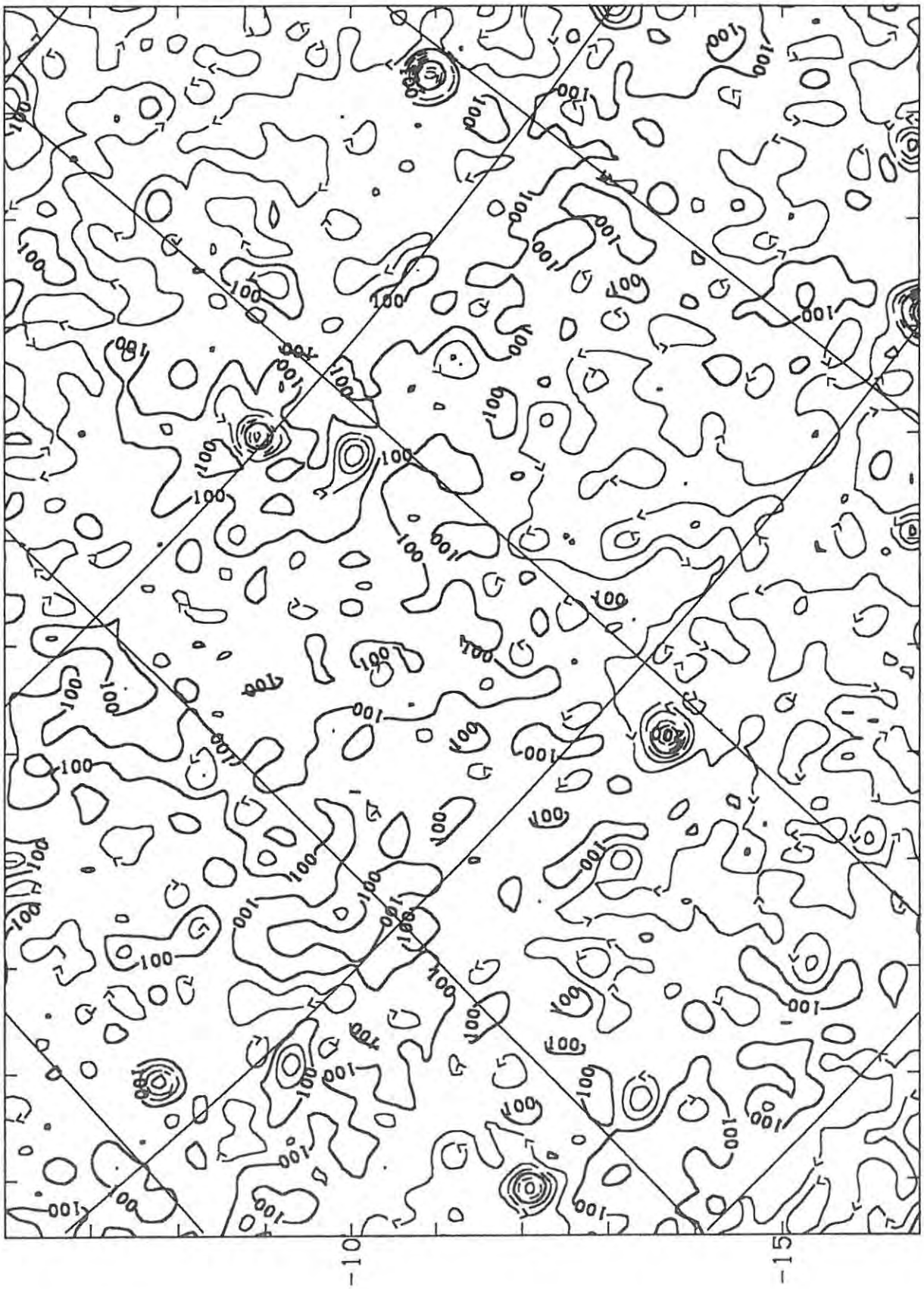

Figure A1.17 - Rhodes 2.3 Ghz Sky Survey (Map C2).

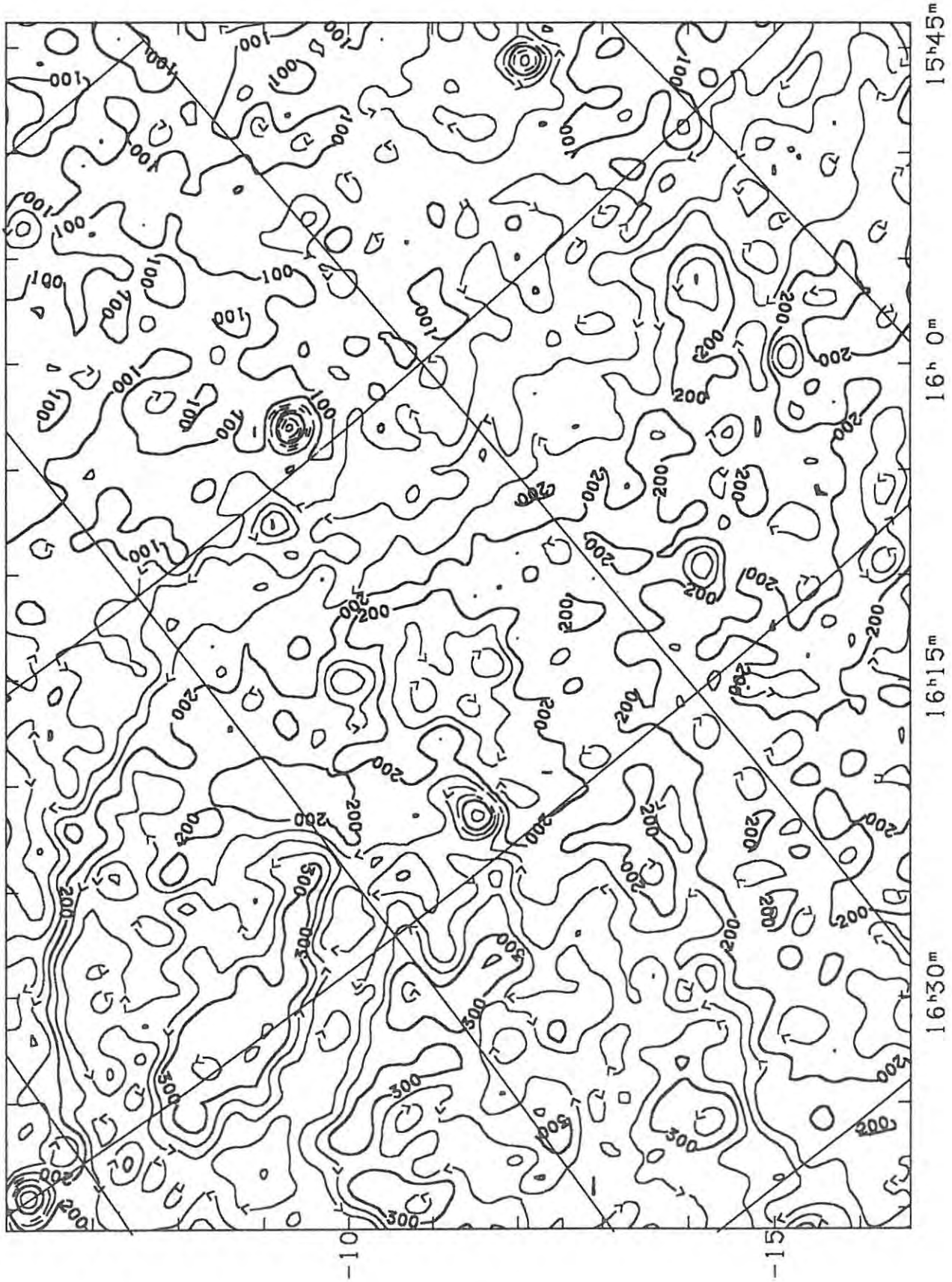

Figure A1.18 - Rhodes 2.3 Ghz Sky Survey (Map D2).

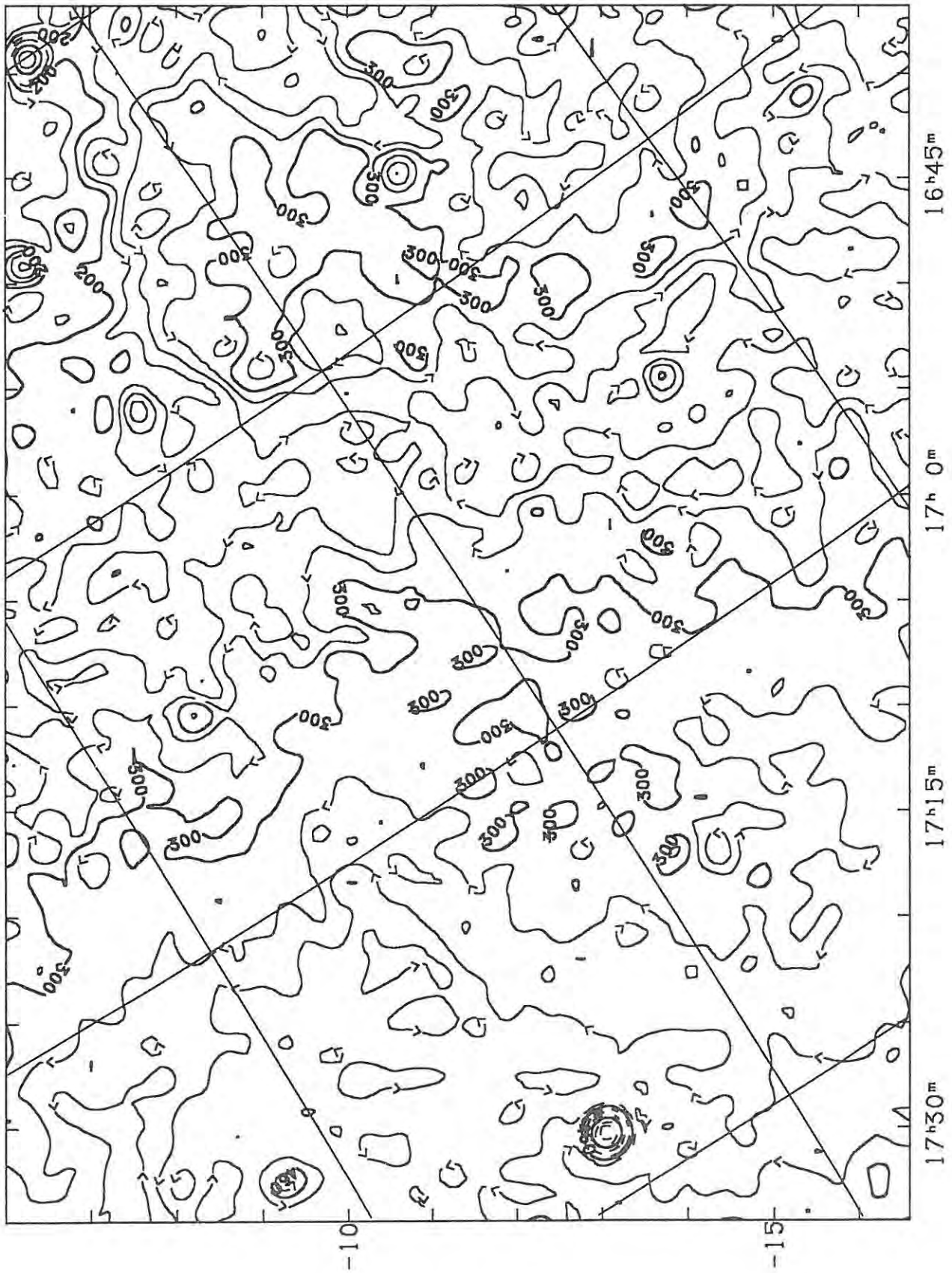

Figure A1.19 - Rhodes 2.3 Ghz Sky Survey (Map E2).

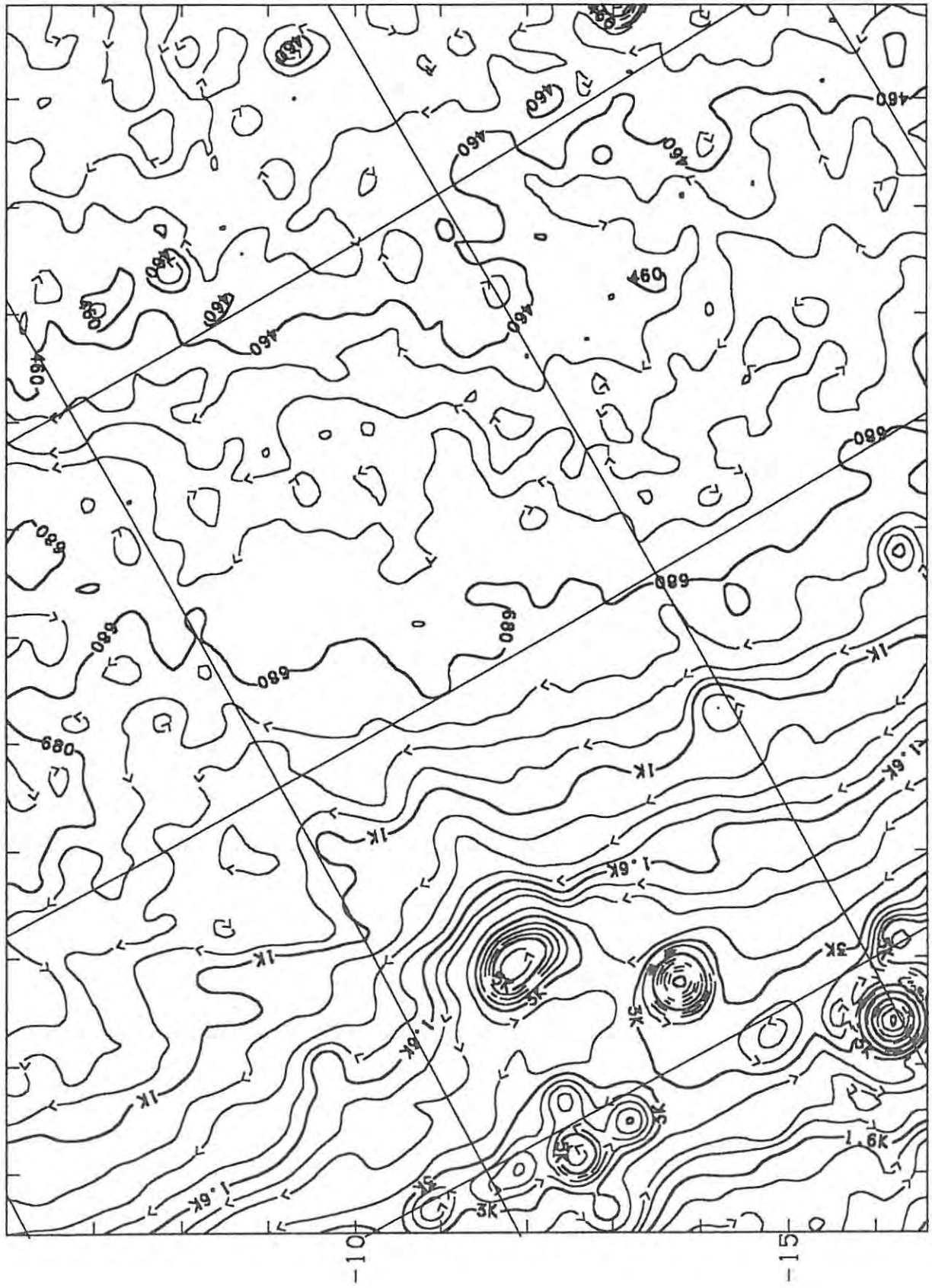

Figure A1.20 - Rhodes 2.3 Ghz Sky Survey (Map F2).

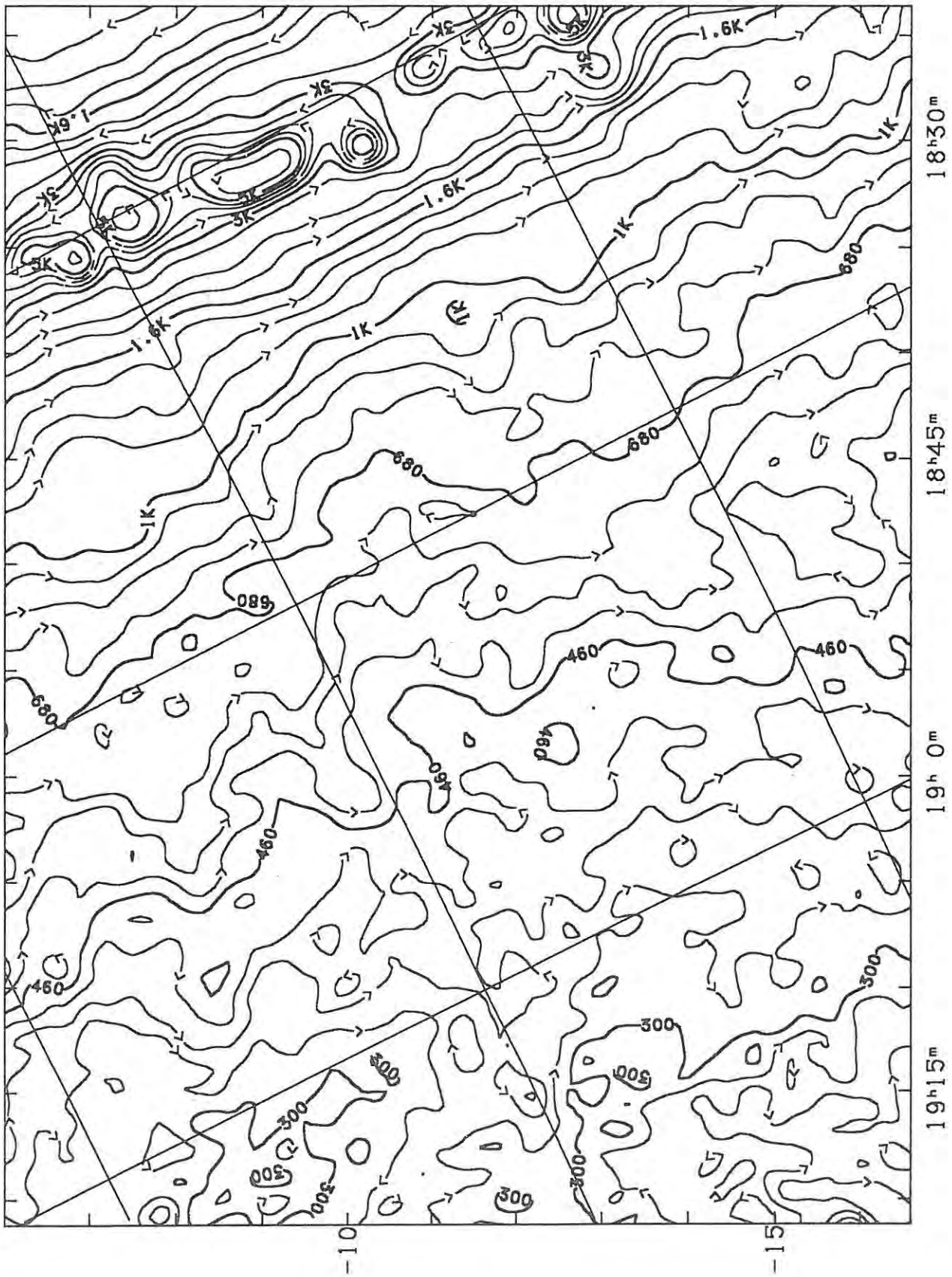

Figure A1.21 - Rhodes 2.3 Ghz Sky Survey (Map G2).

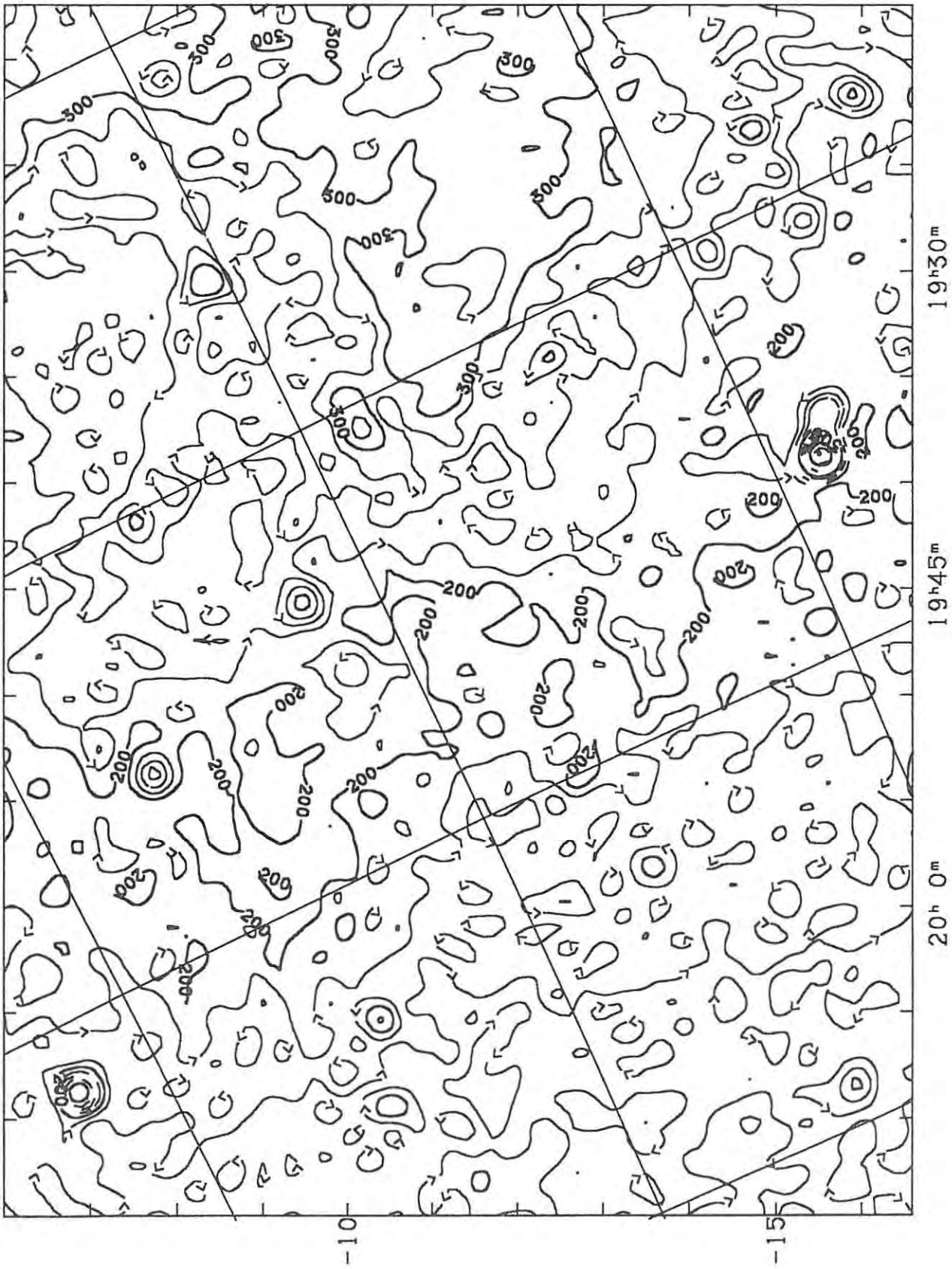

Figure A1.22 - Rhodes 2.3 Ghz Sky Survey (Map H2).

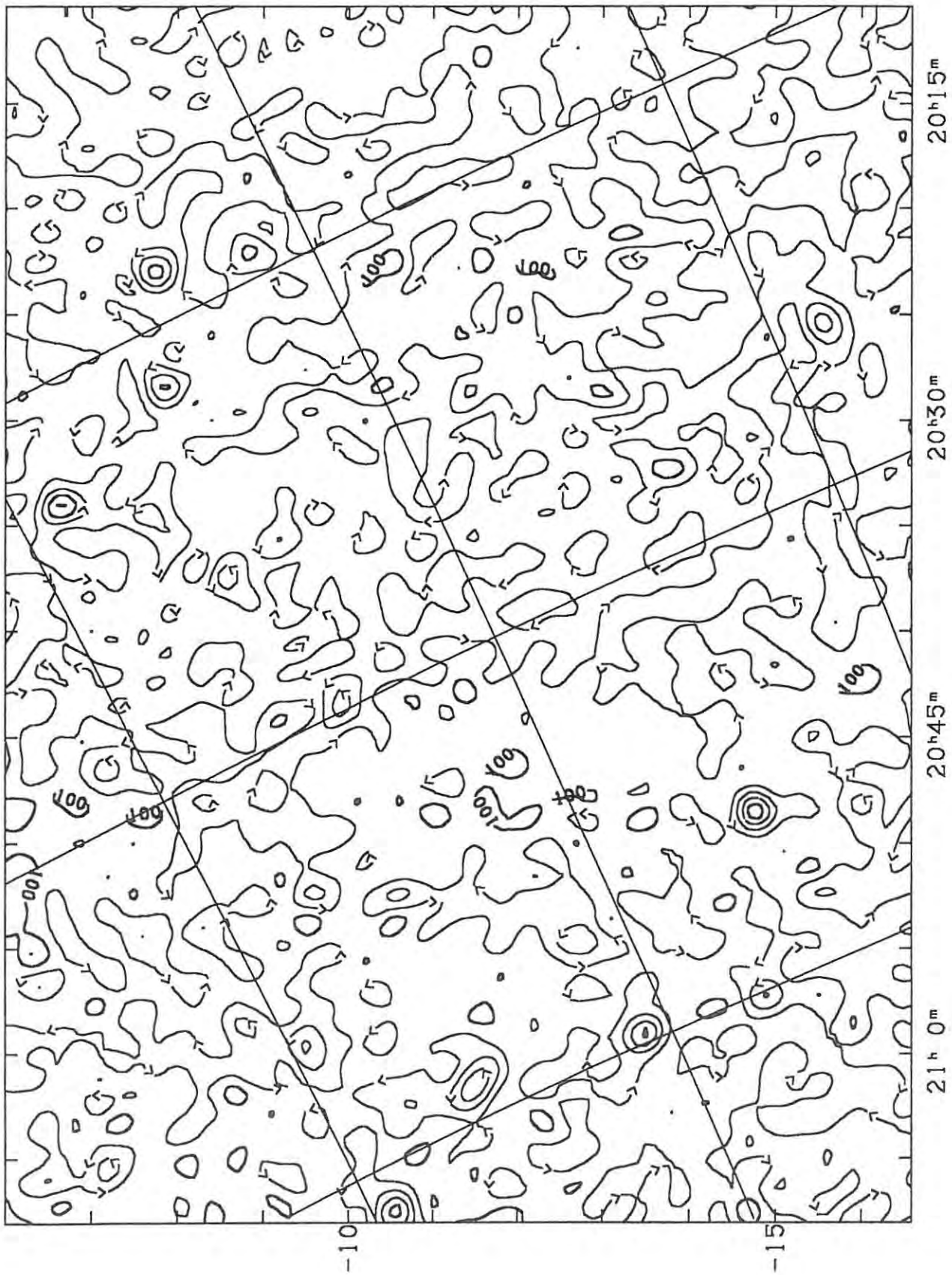

Figure A1.23 - Rhodes 2.3 Ghz Sky Survey (Map I2).

Figure A1.24 - Rhodes 2.3 Ghz Sky Survey (Map J2).

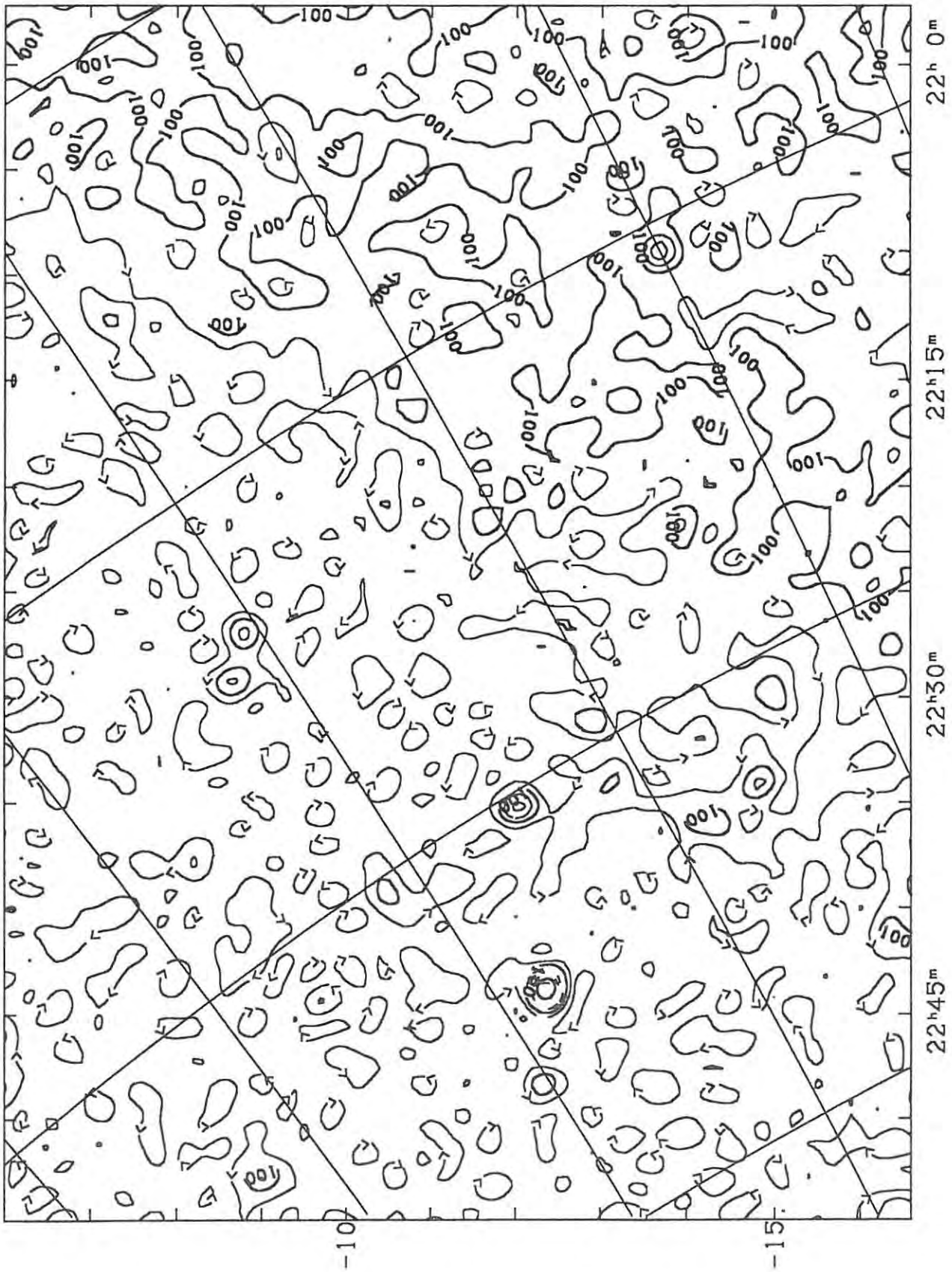

Figure A1.25 - Rhodes 2.3 Ghz Sky Survey (Map K2).

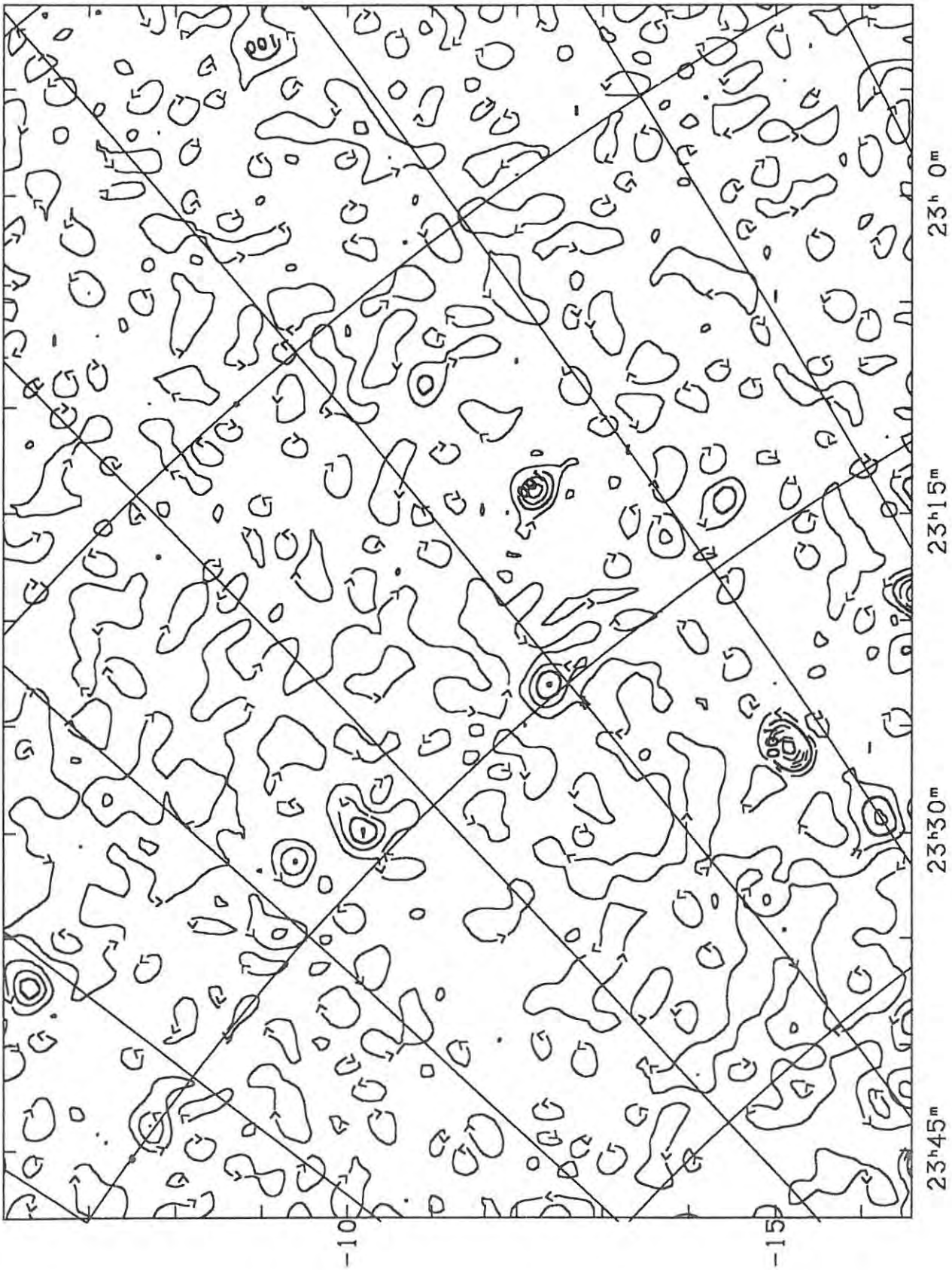

Figure A1.26 - Rhodes 2.3 Ghz Sky Survey (Map L2).

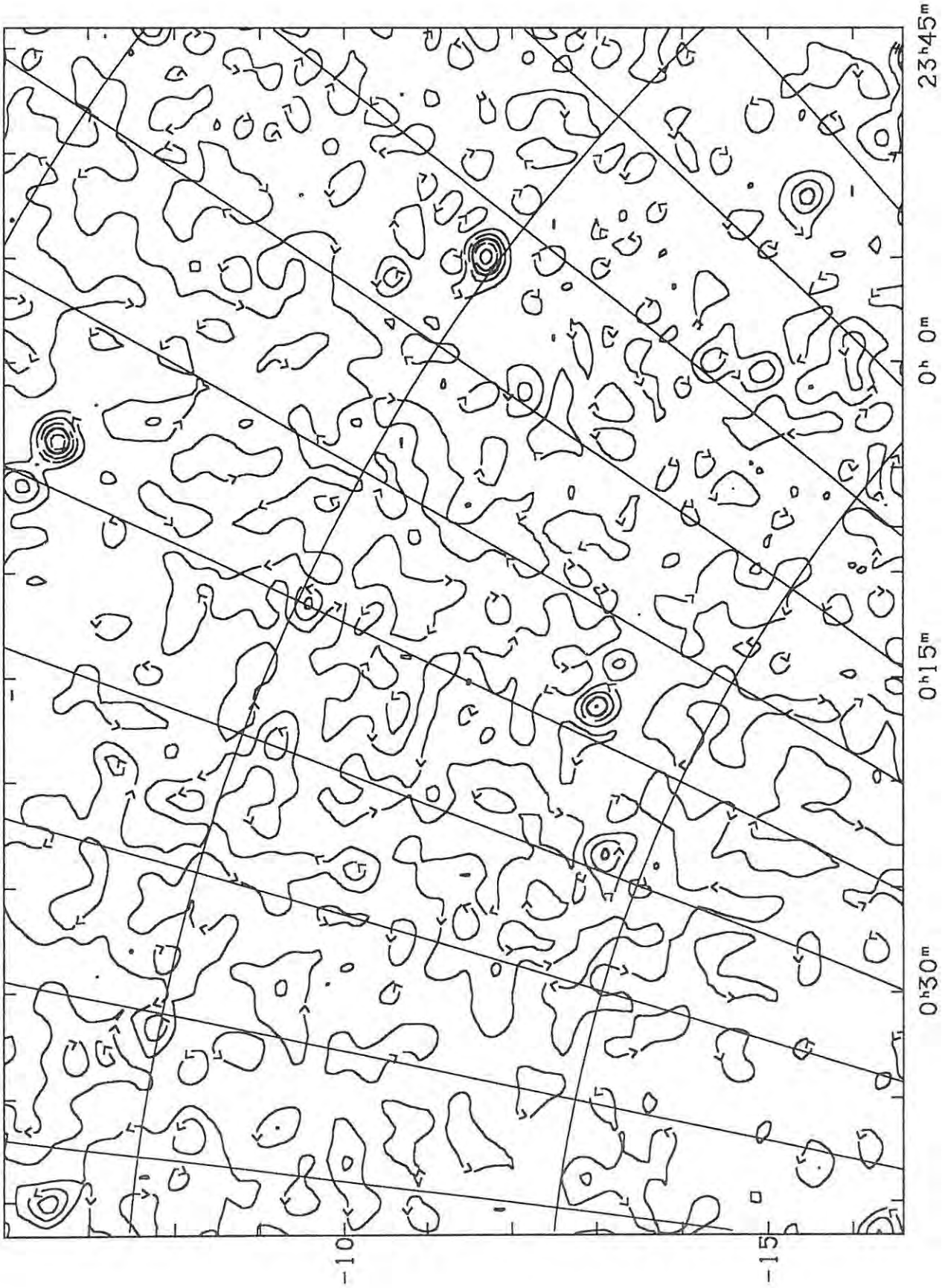

Figure A1.27 - Rhodes 2.3 Ghz Sky Survey (Map M2).

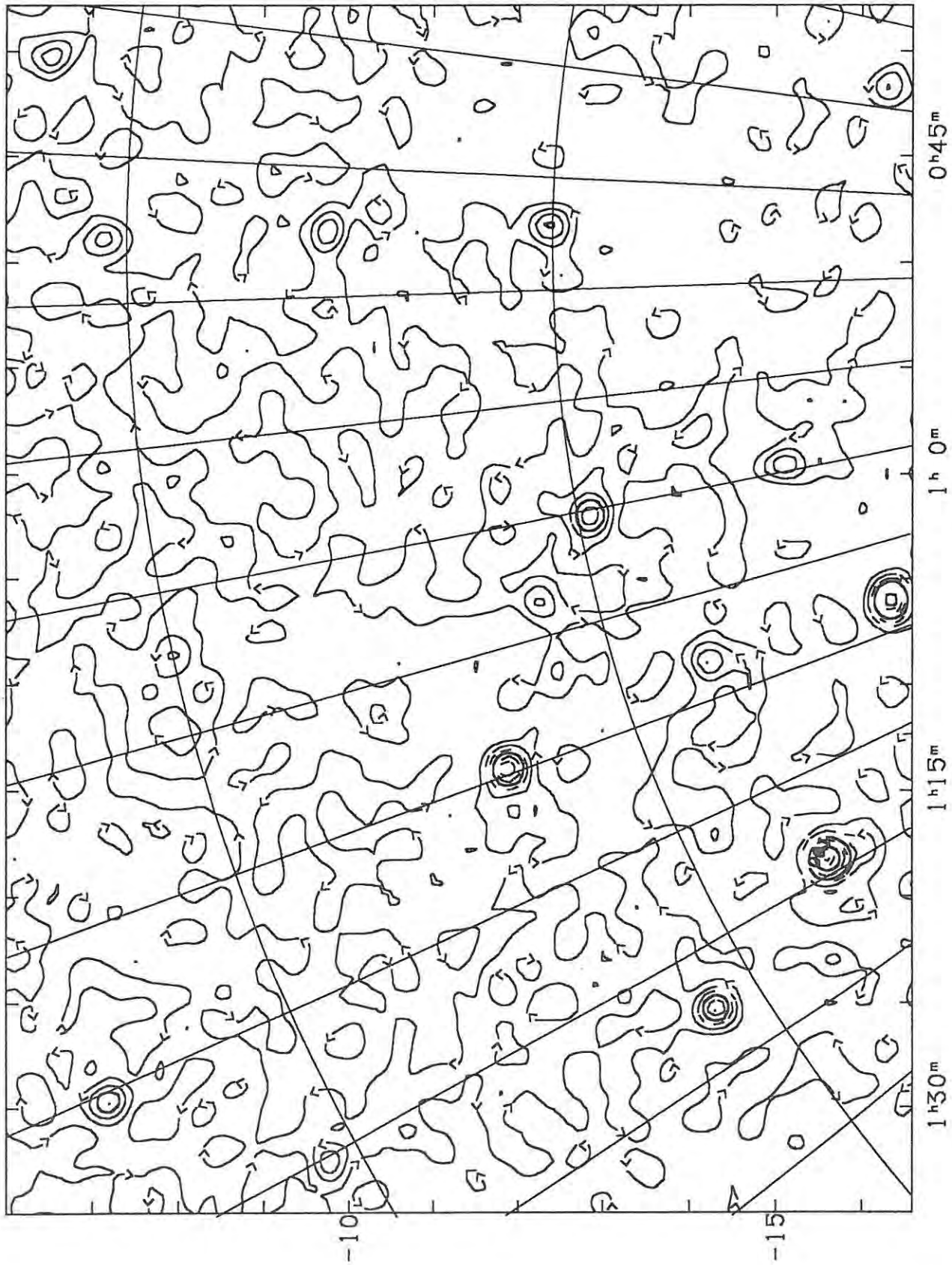

Figure A1.28 - Rhodes 2.3 Ghz Sky Survey (Map N2).

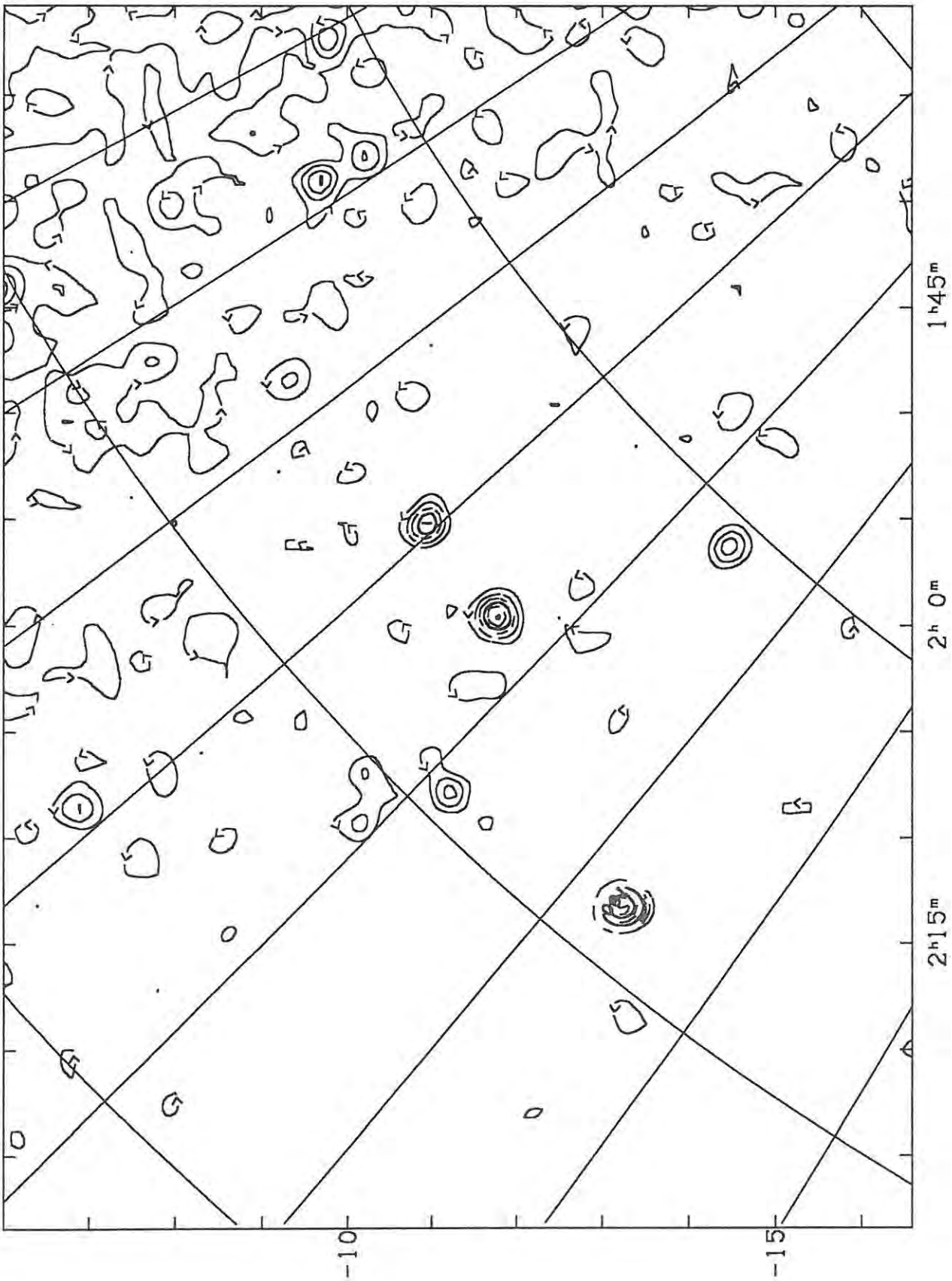

Figure A1.29 - Rhodes 2.3 Ghz Sky Survey (Map A3).

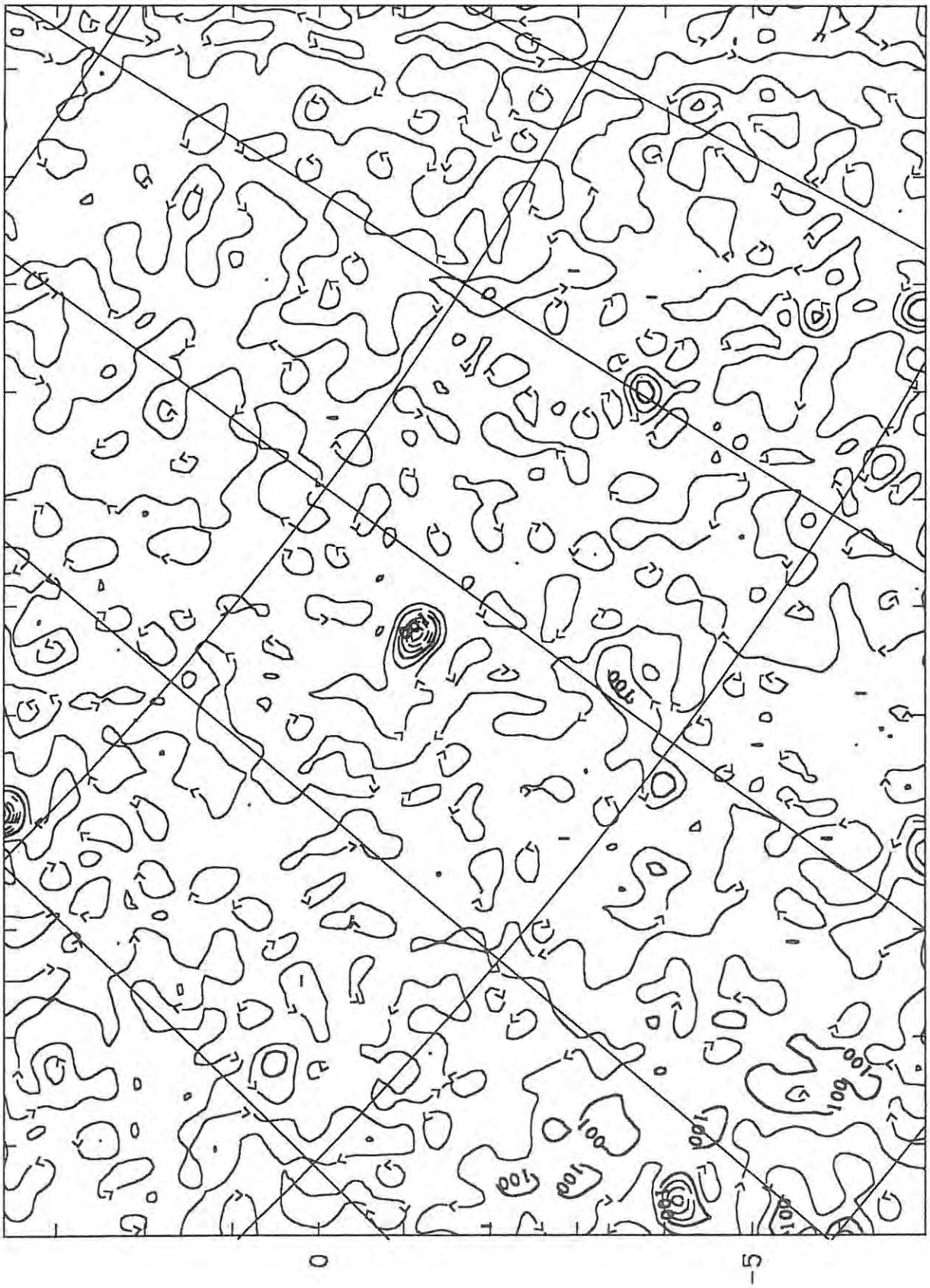

Figure A1.30 - Rhodes 2.3 Ghz Sky Survey (Map B3).

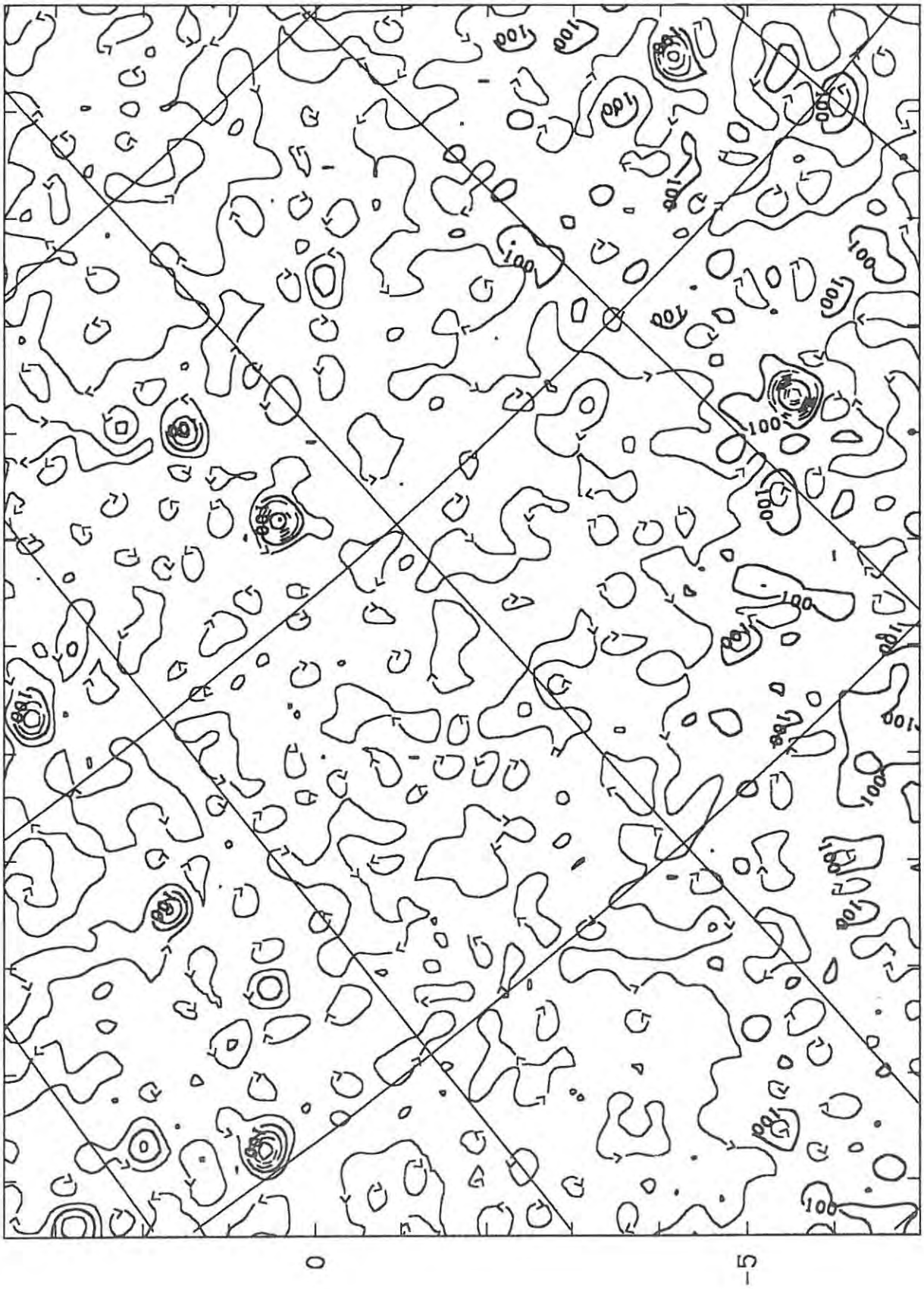

Figure A1.31 - Rhodes 2.3 Ghz Sky Survey (Map C3).

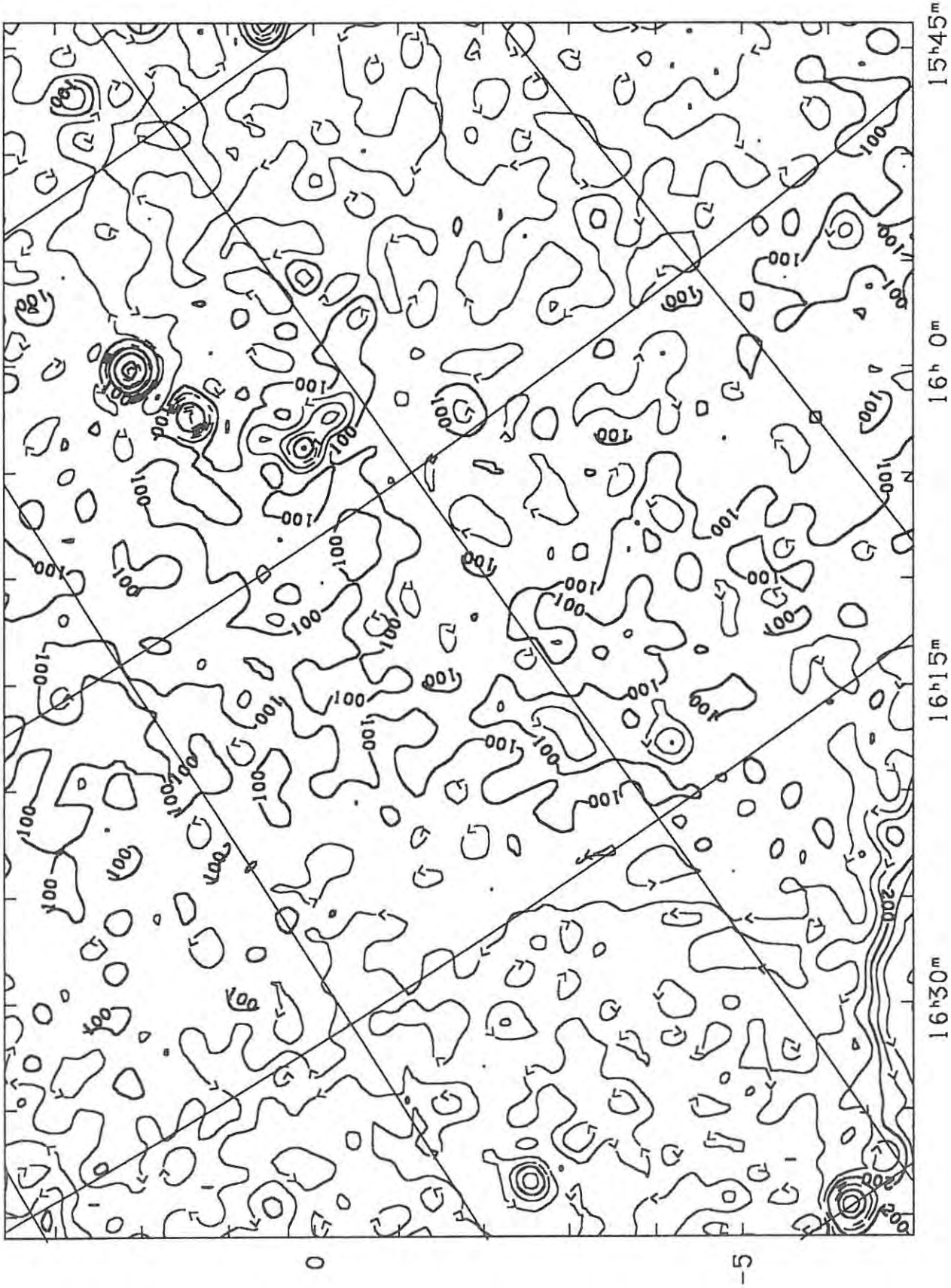

Figure A1.32 - Rhodes 2.3 Ghz Sky Survey (Map D3).

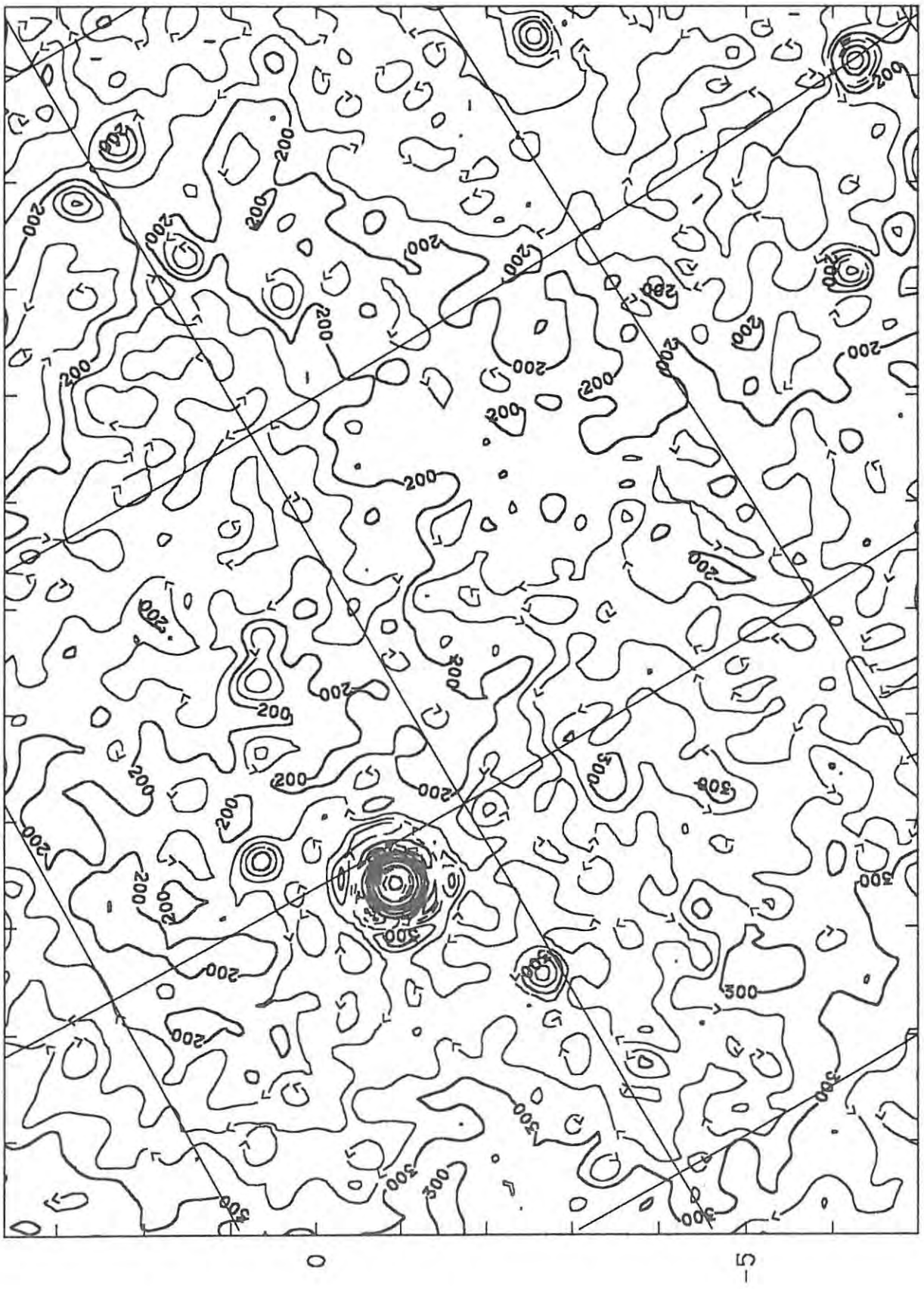

Figure A1.33 - Rhodes 2.3 Ghz Sky Survey (Map E3).

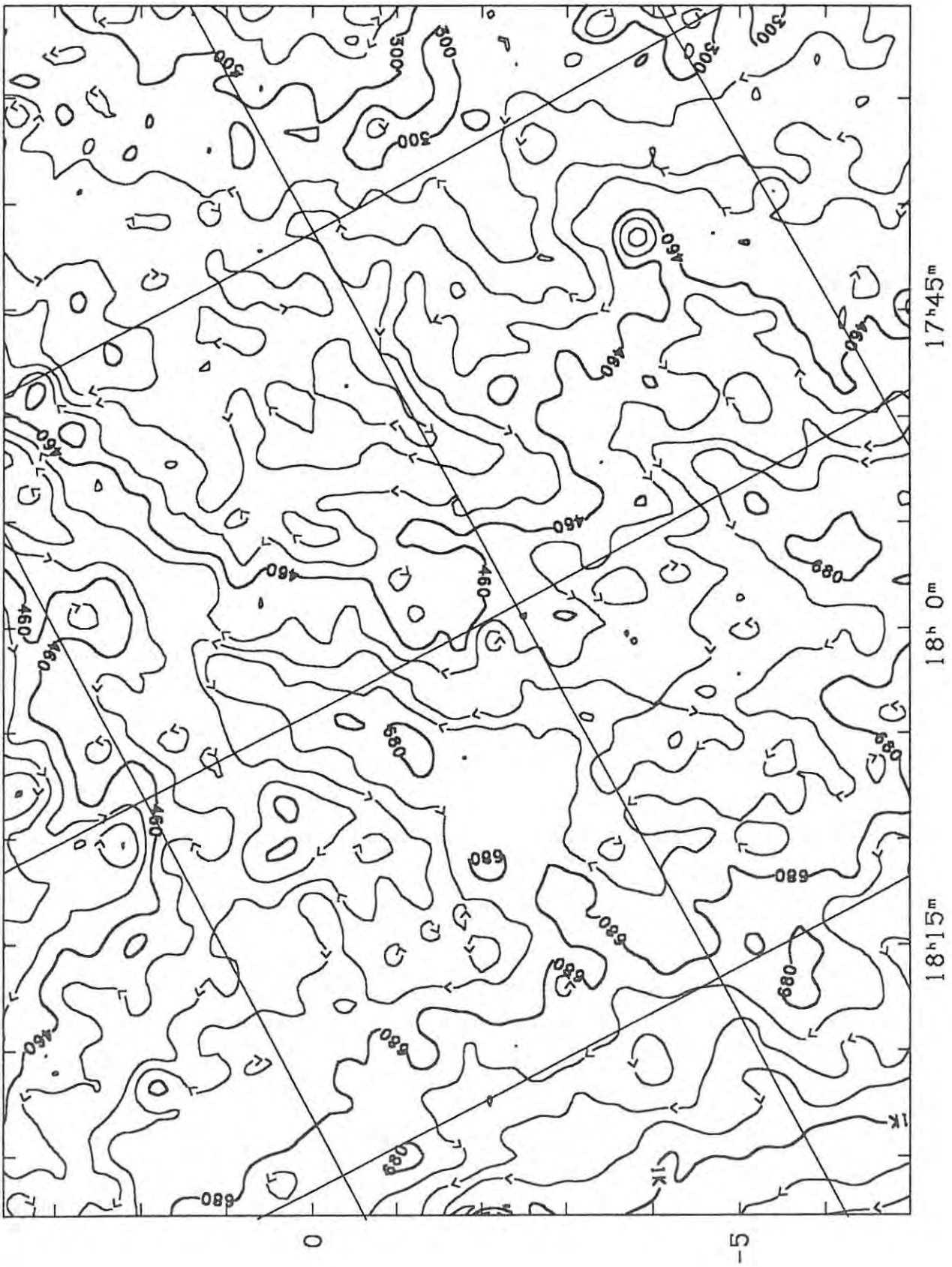

Figure A1.34 - Rhodes 2.3 Ghz Sky Survey (Map F3).

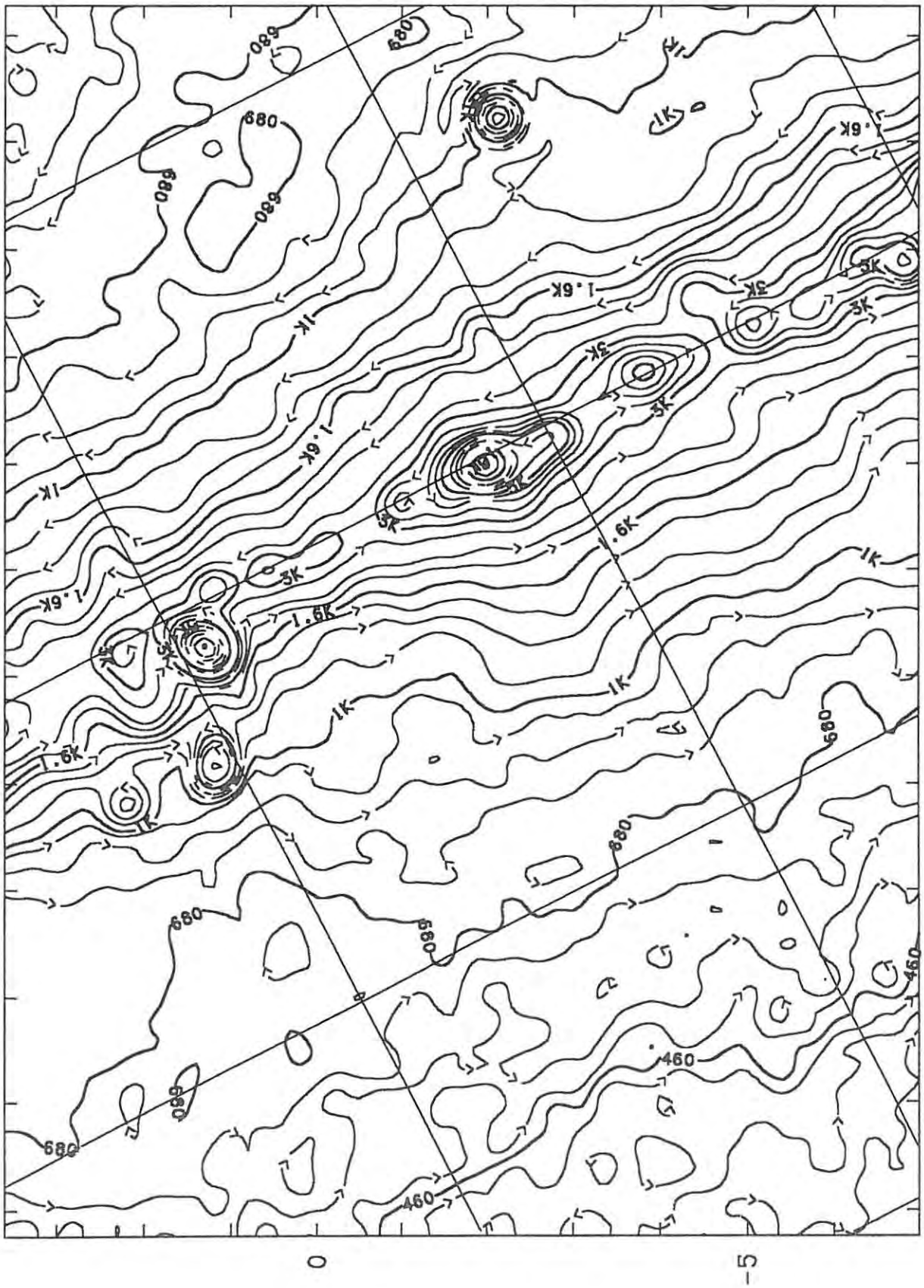

Figure A1.35 - Rhodes 2.3 Ghz Sky Survey (Map G3).

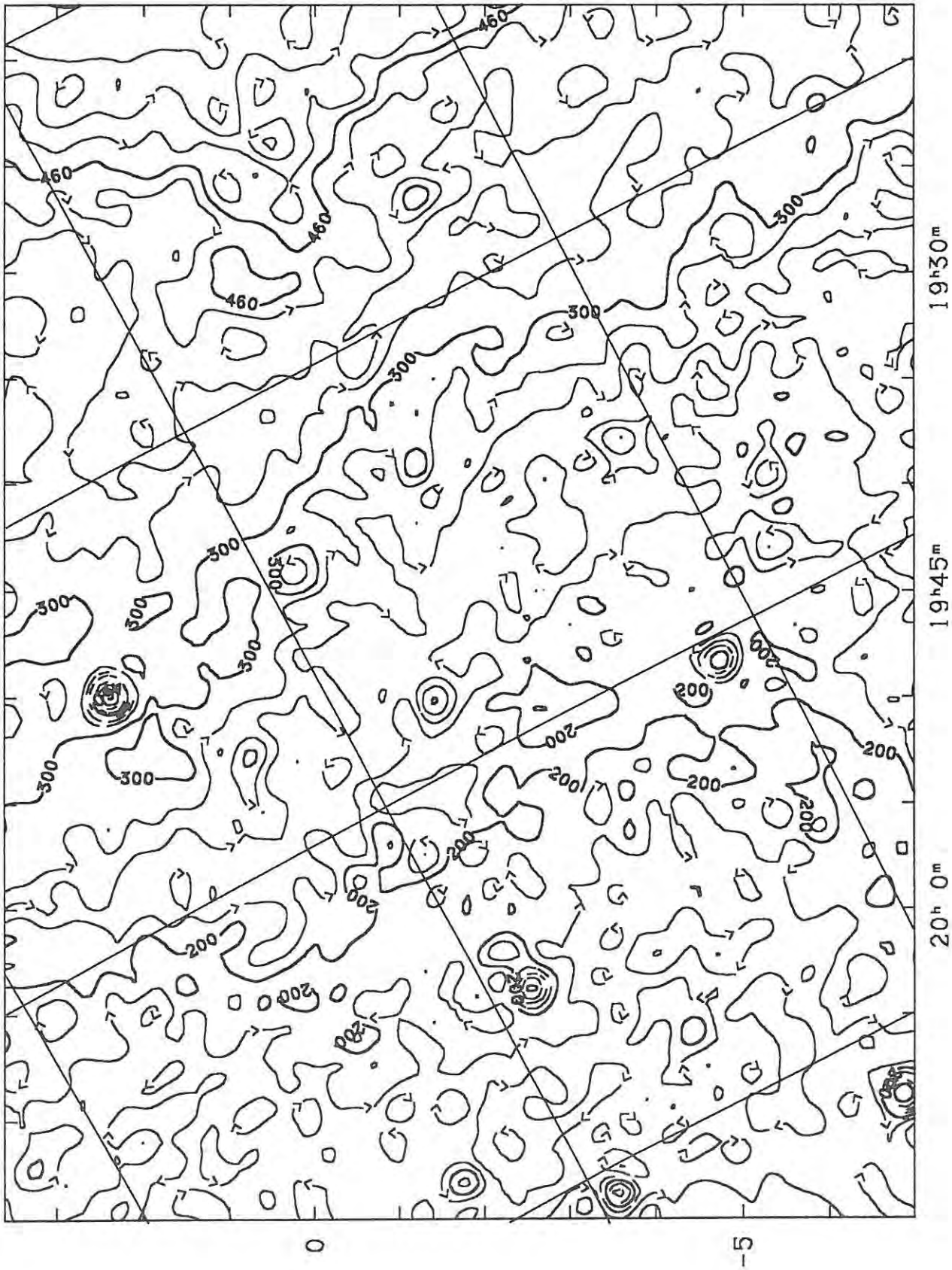

Figure A1.36 - Rhodes 2.3 Ghz Sky Survey (Map H3).

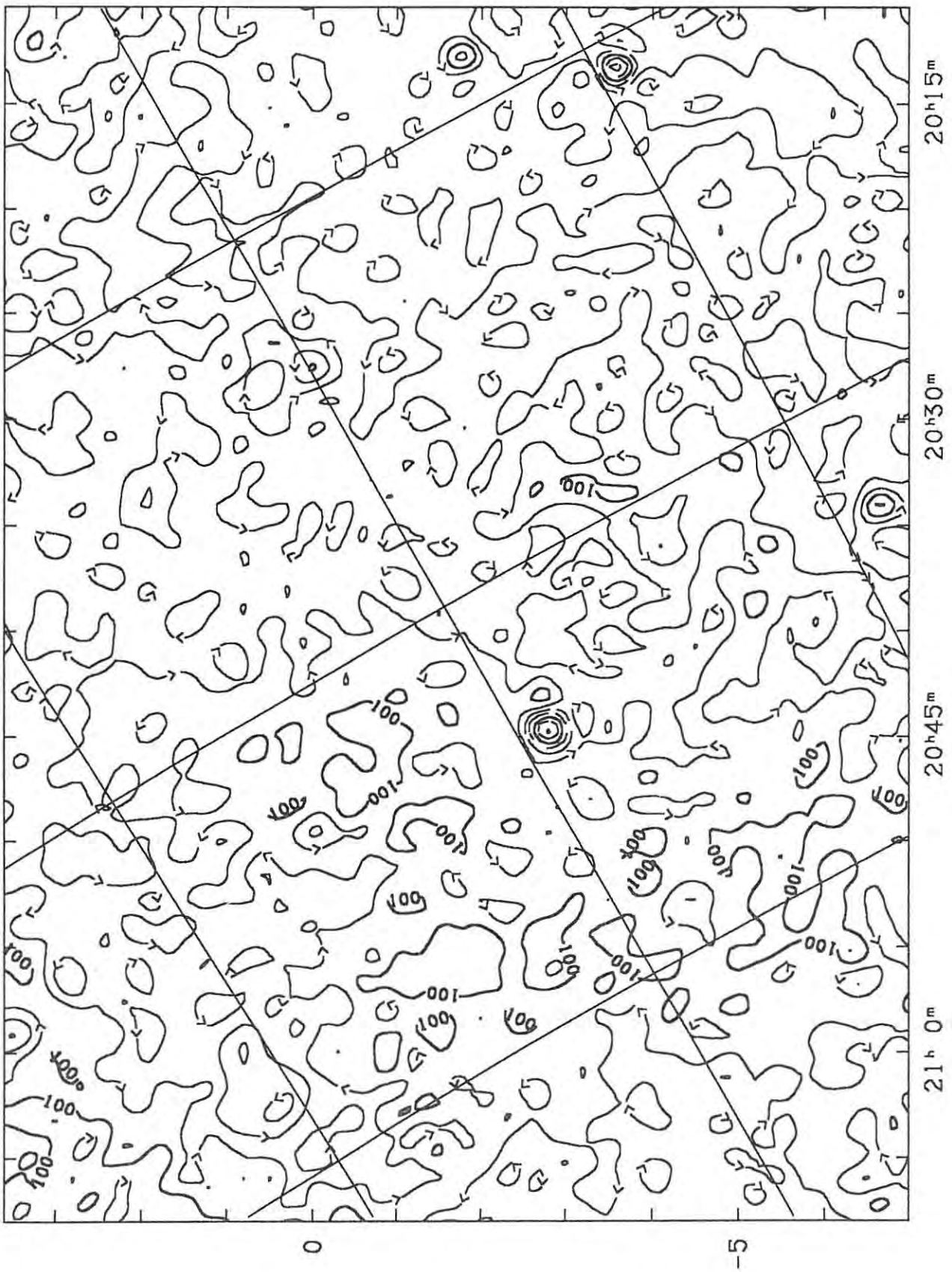

Figure A1.37 - Rhodes 2.3 Ghz Sky Survey (Map I3).

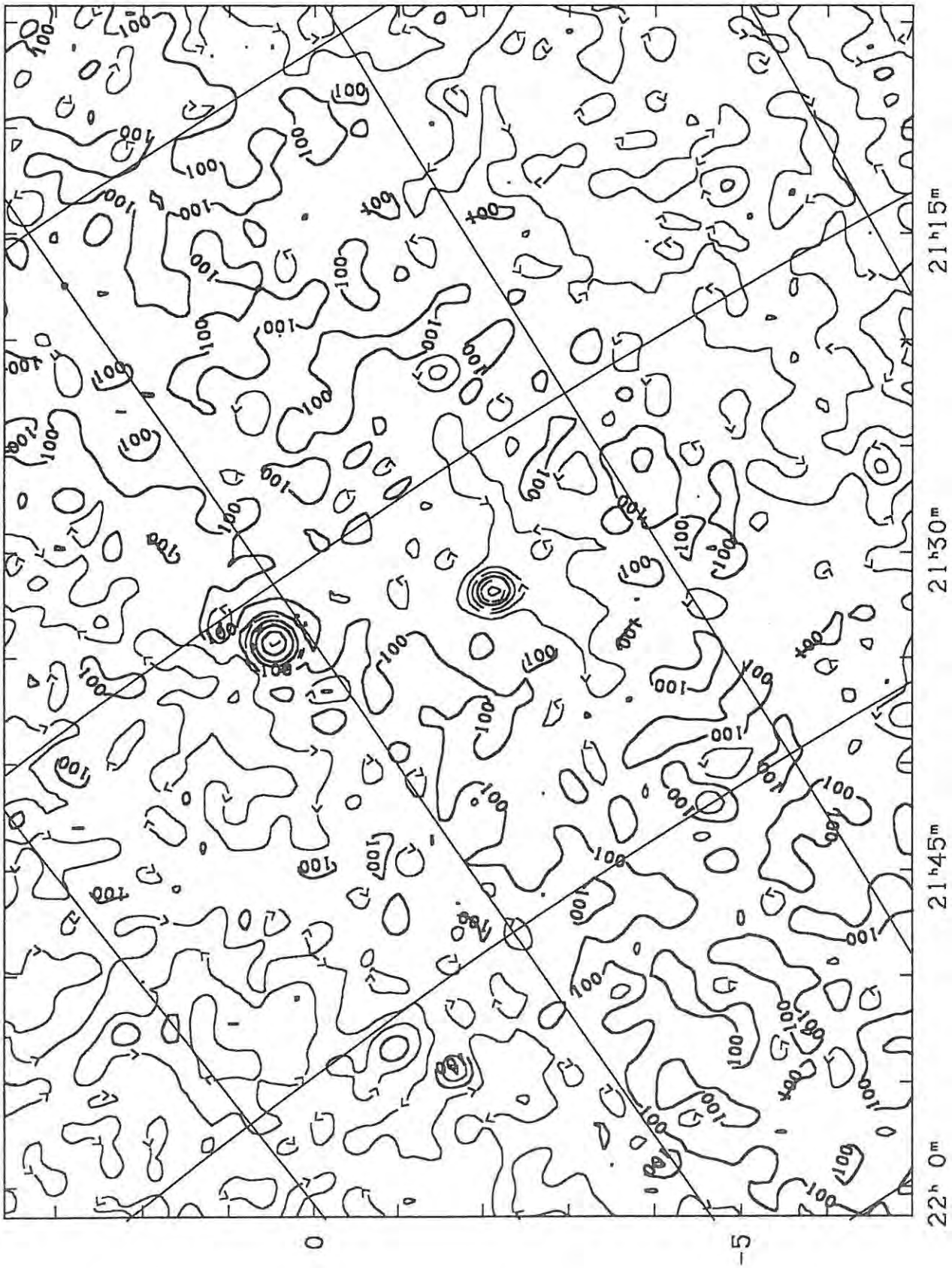

Figure A1.38 - Rhodes 2.3 Ghz Sky Survey (Map J3).

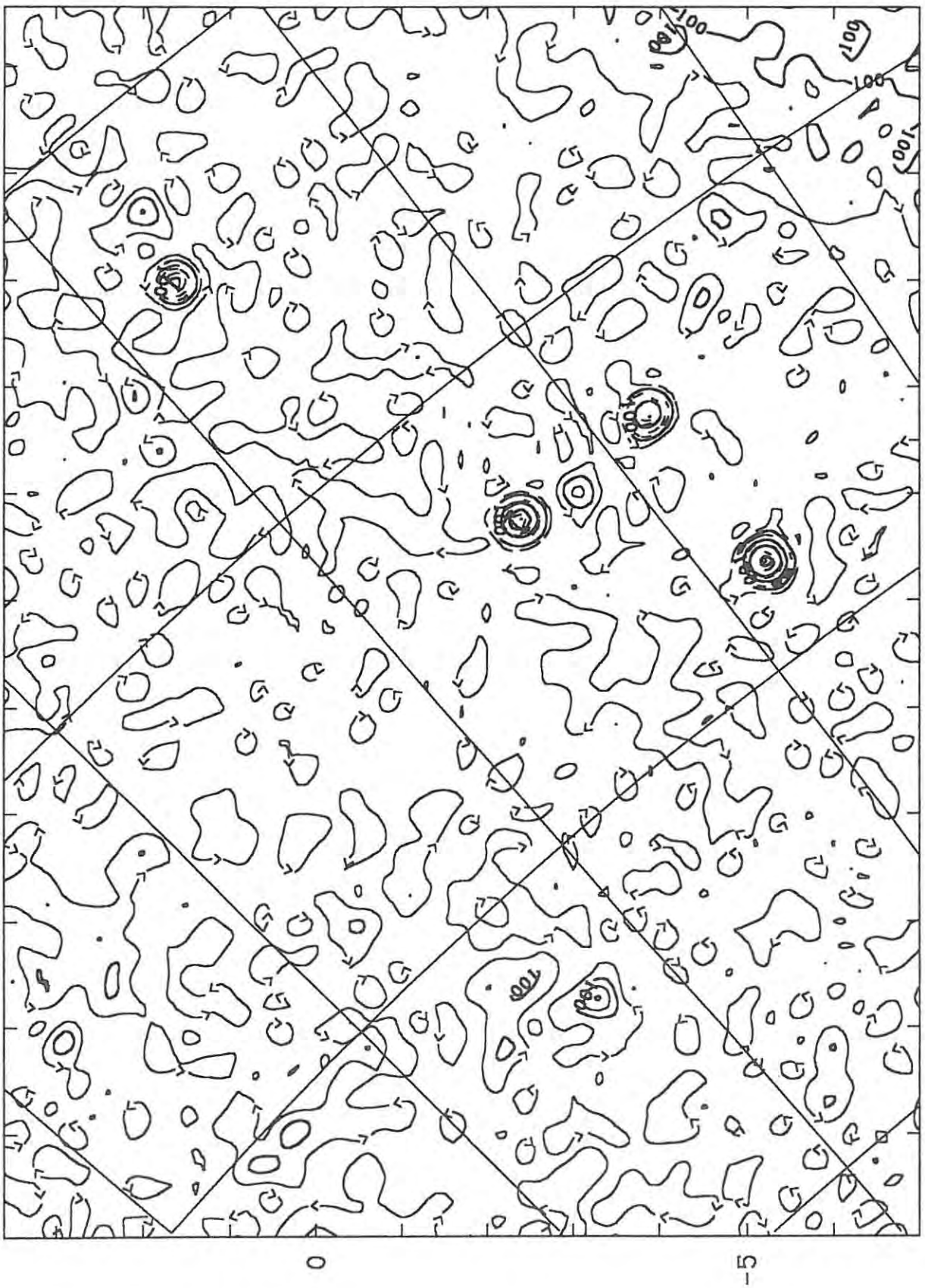

Figure A1.39 - Rhodes 2.3 Ghz Sky Survey (Map K3).

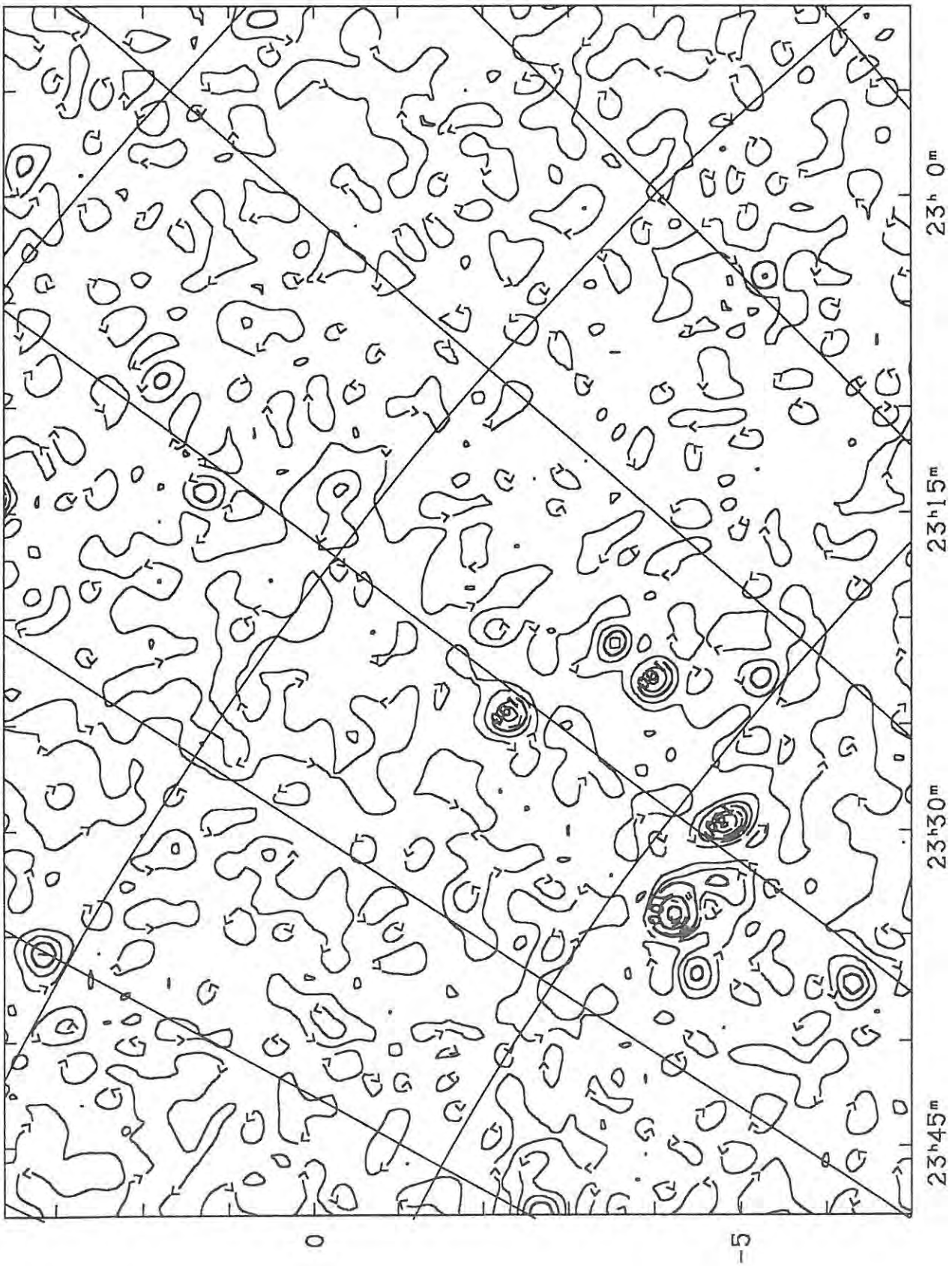

Figure A1.40 - Rhodes 2.3 Ghz Sky Survey (Map L3).

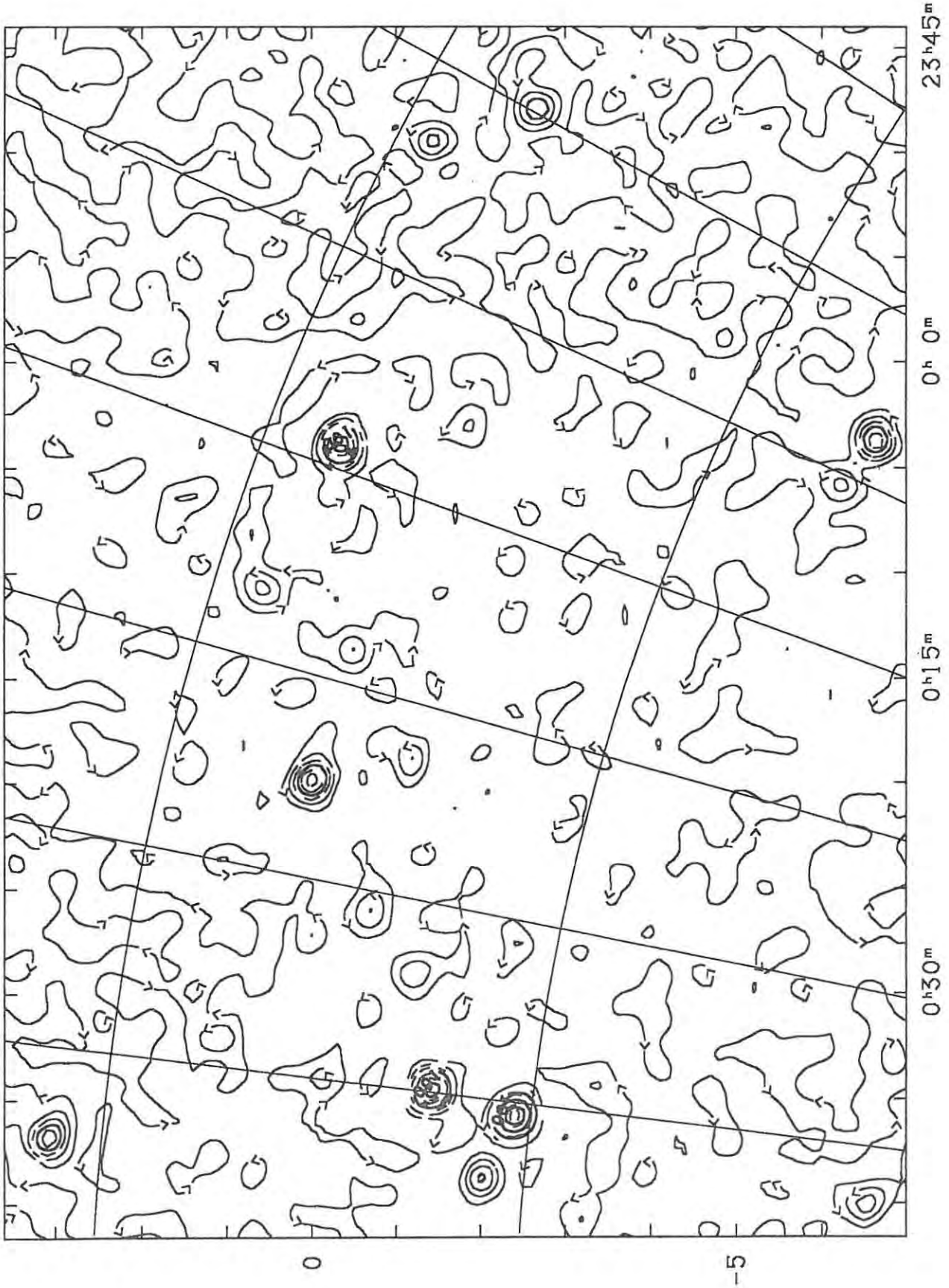

Figure A1.41 - Rhodes 2.3 Ghz Sky Survey (Map M3).

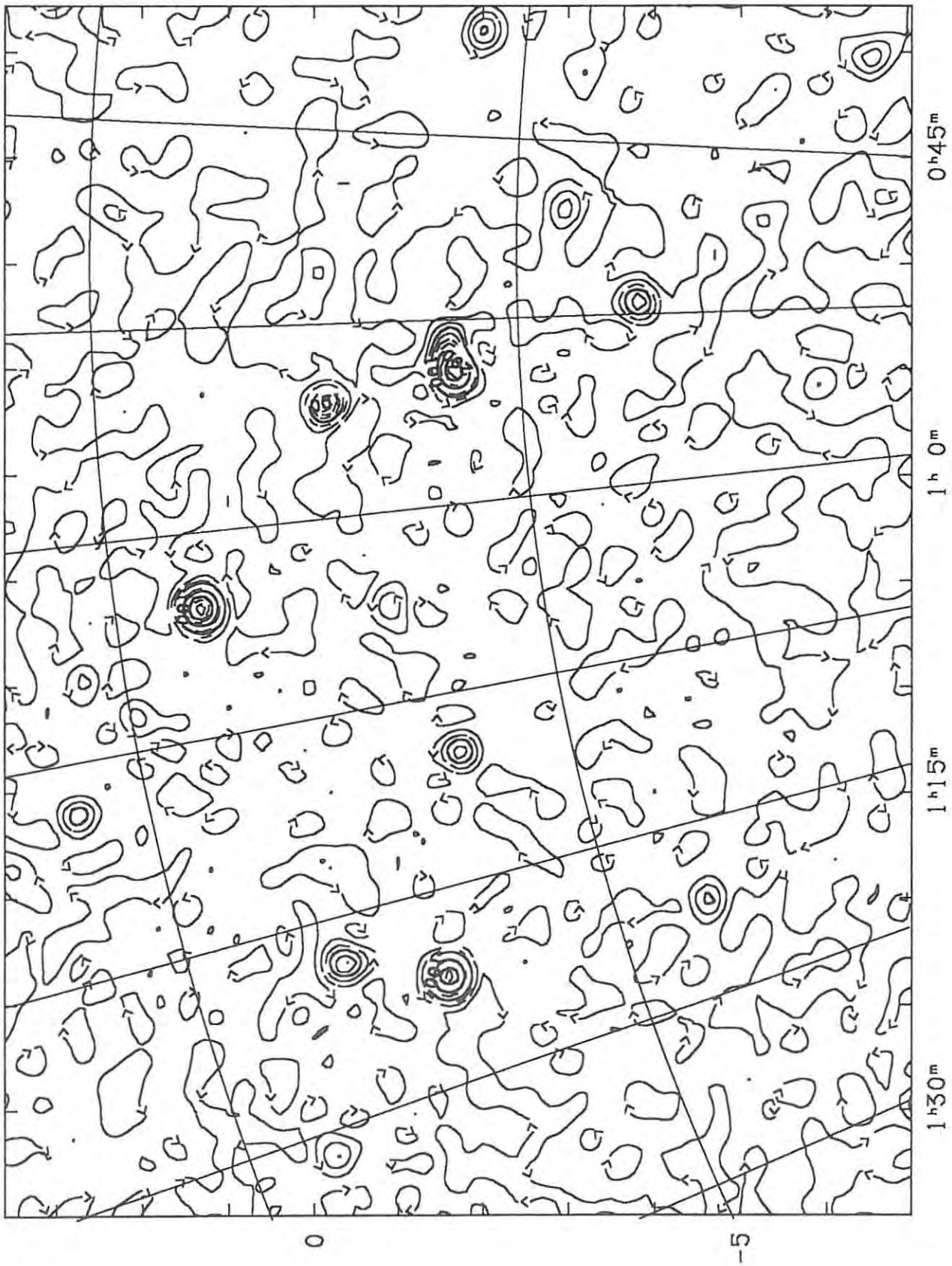

Figure A1.42 - Rhodes 2.3 Ghz Sky Survey (Map N3).

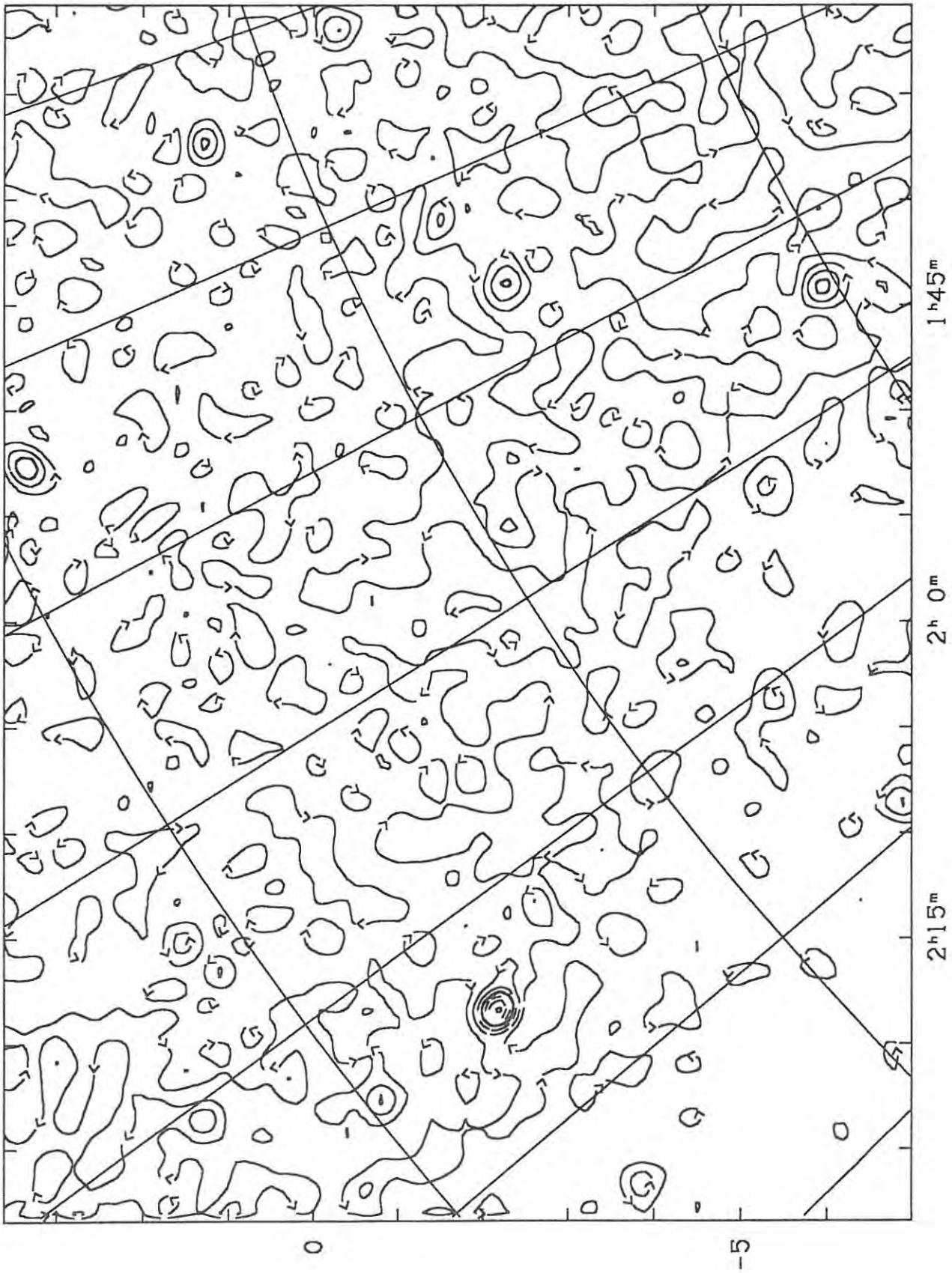

Figure A1.43 - Rhodes 2.3 Ghz Sky Survey (Map A4).

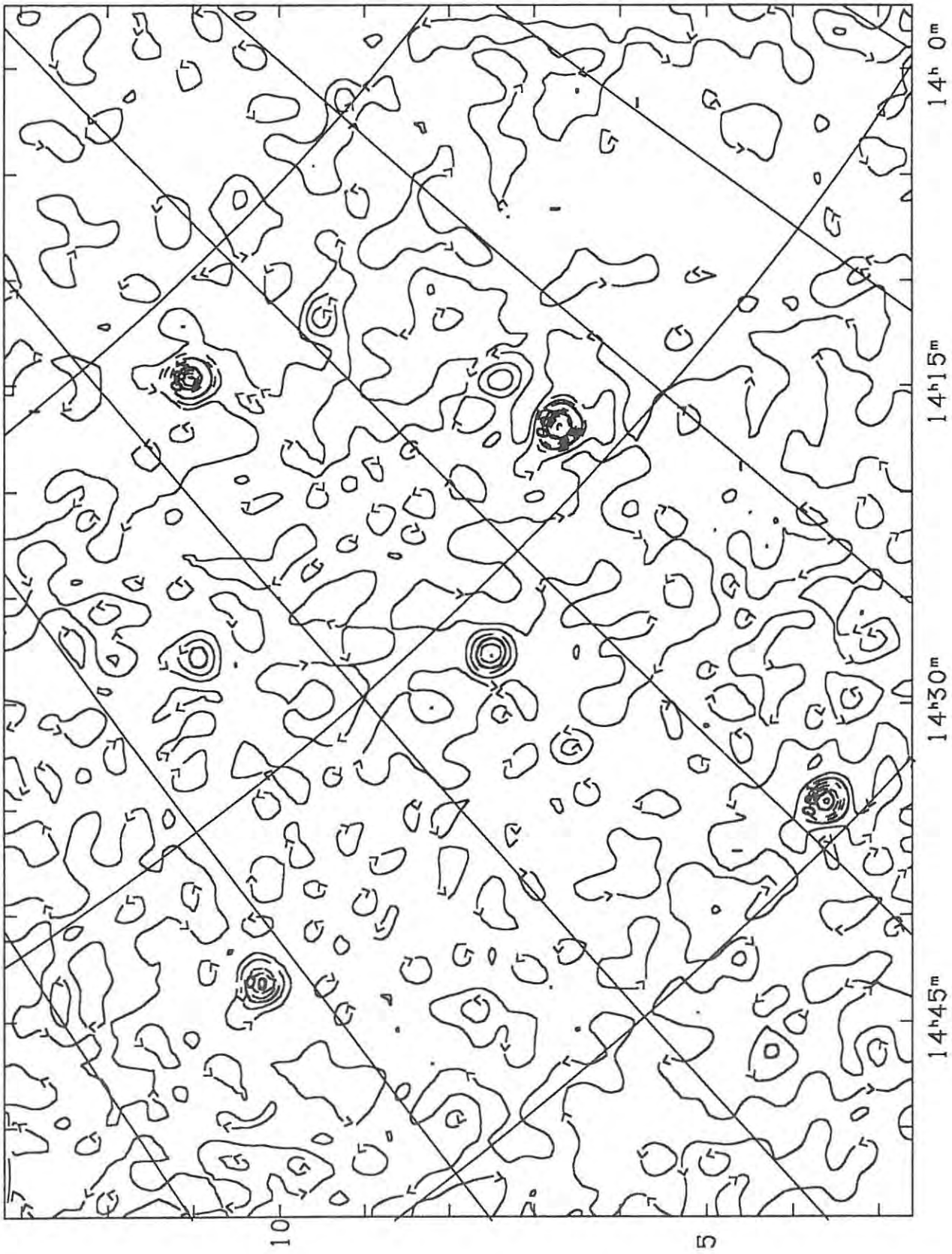

Figure A1.44 - Rhodes 2.3 Ghz Sky Survey (Map B4).

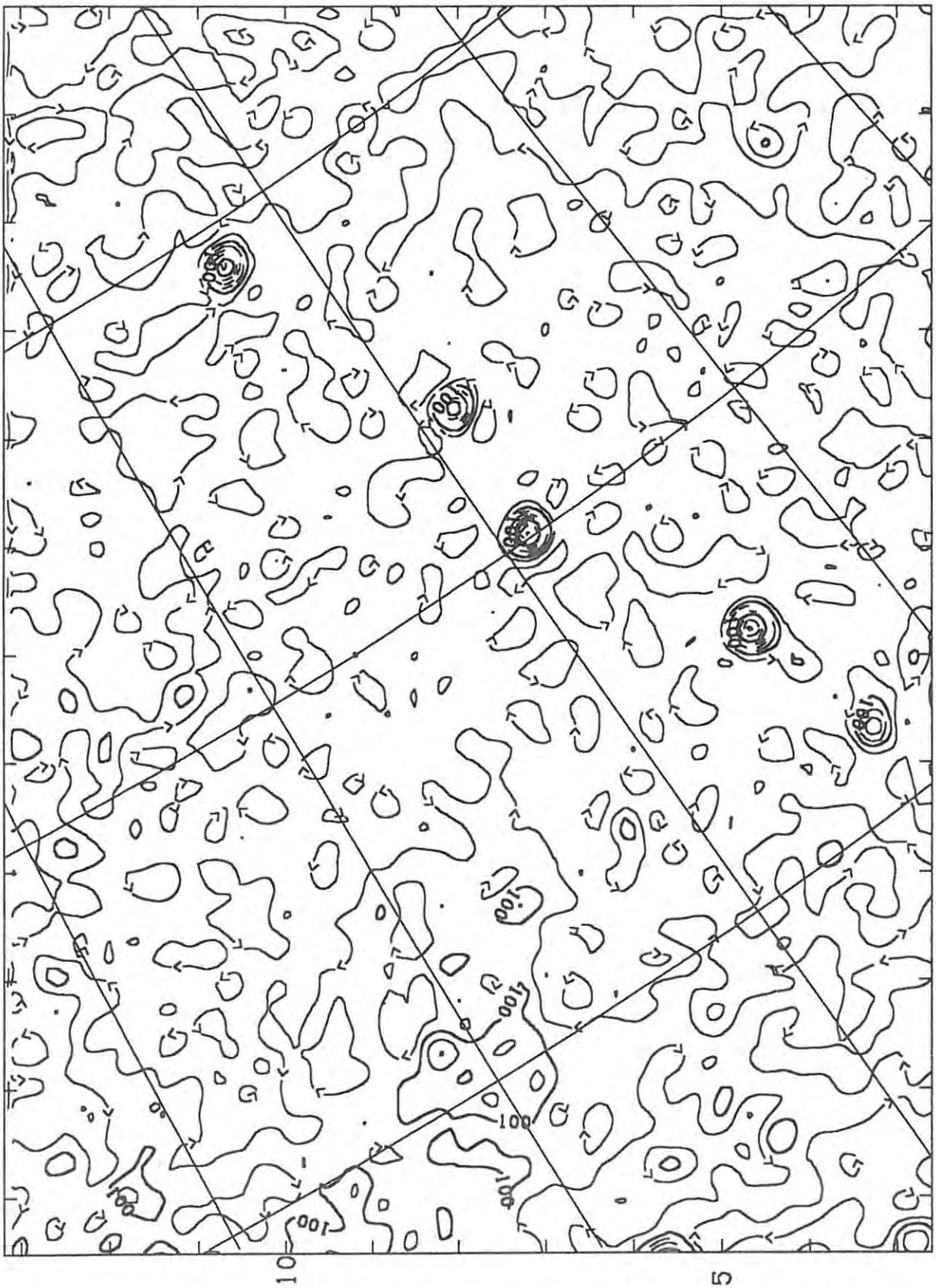

Figure A1.45 - Rhodes 2.3 Ghz Sky Survey (Map C4).

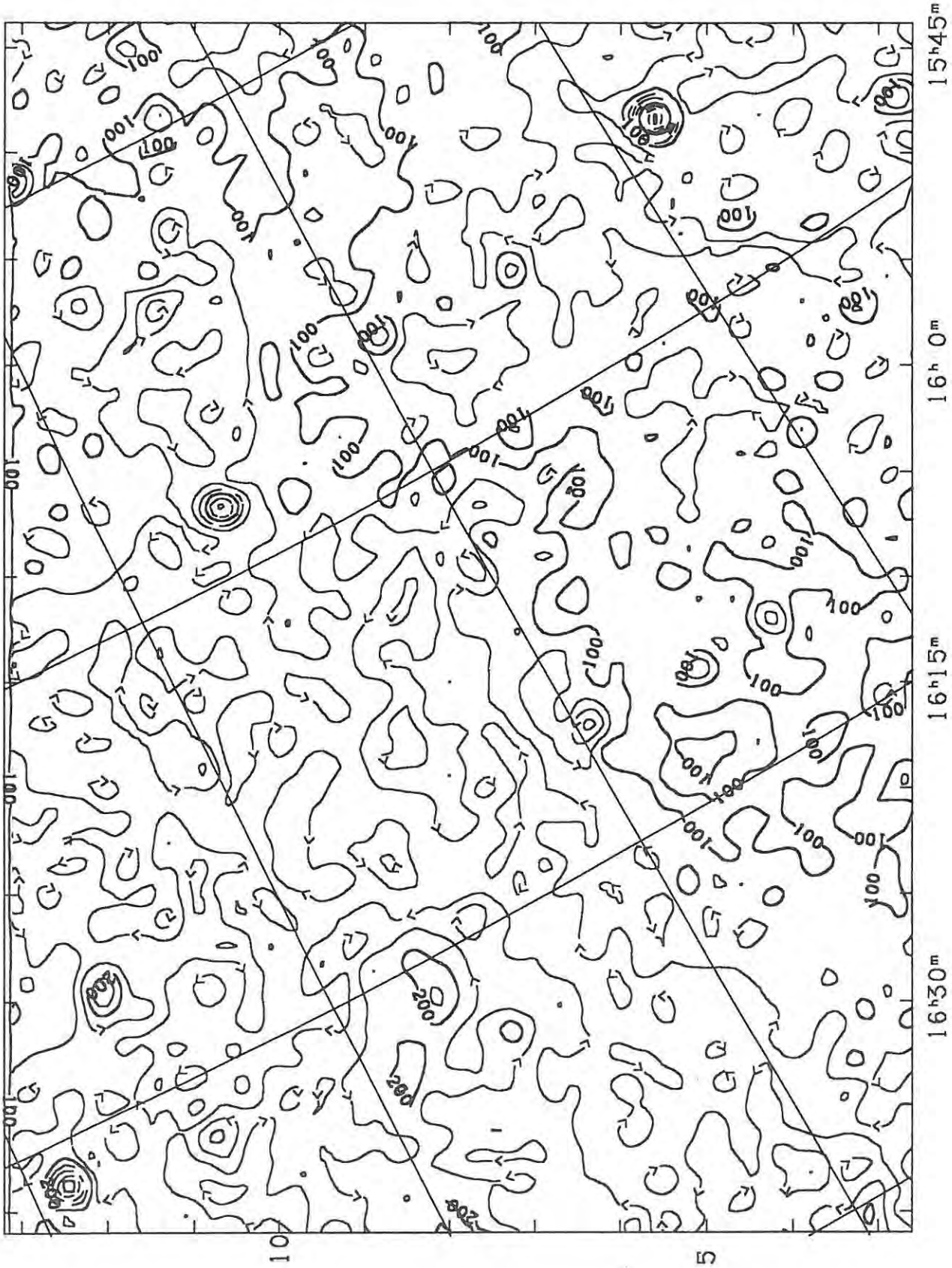

Figure A1.46 - Rhodes 2.3 Ghz Sky Survey (Map D4).

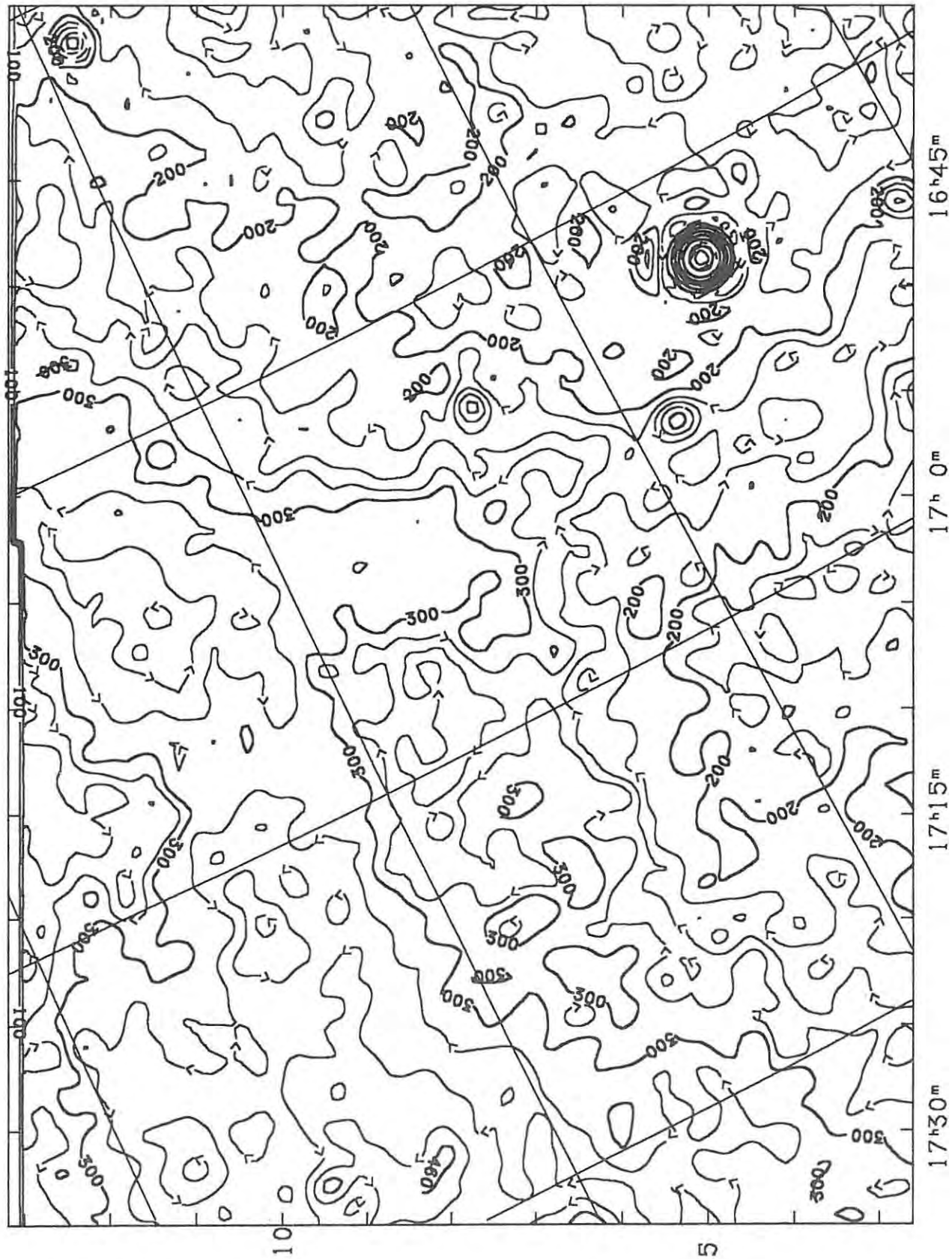

Figure A1.47 - Rhodes 2.3 Ghz Sky Survey (Map E4).

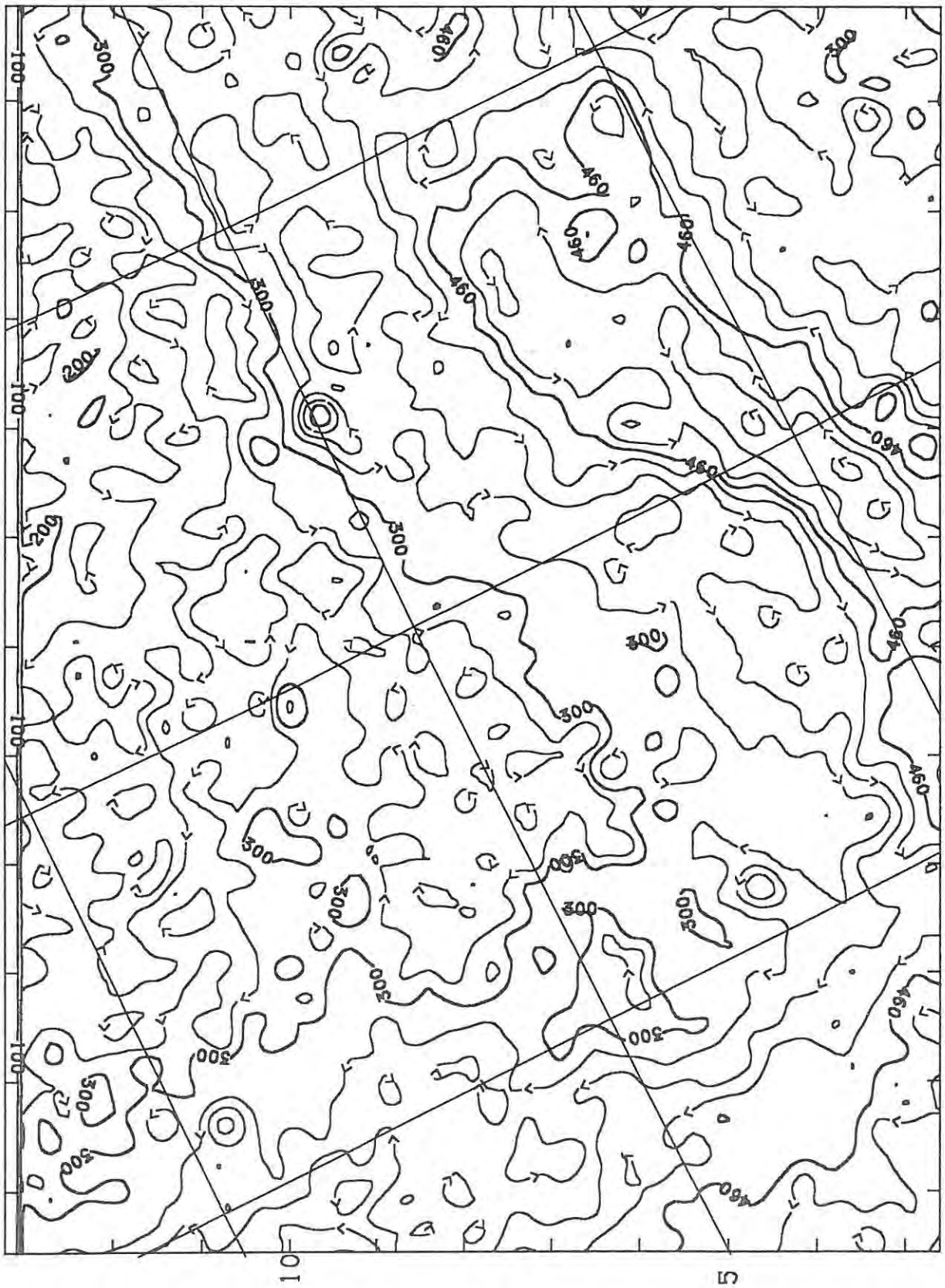

Figure A1.48 - Rhodes 2.3 Ghz Sky Survey (Map F4).

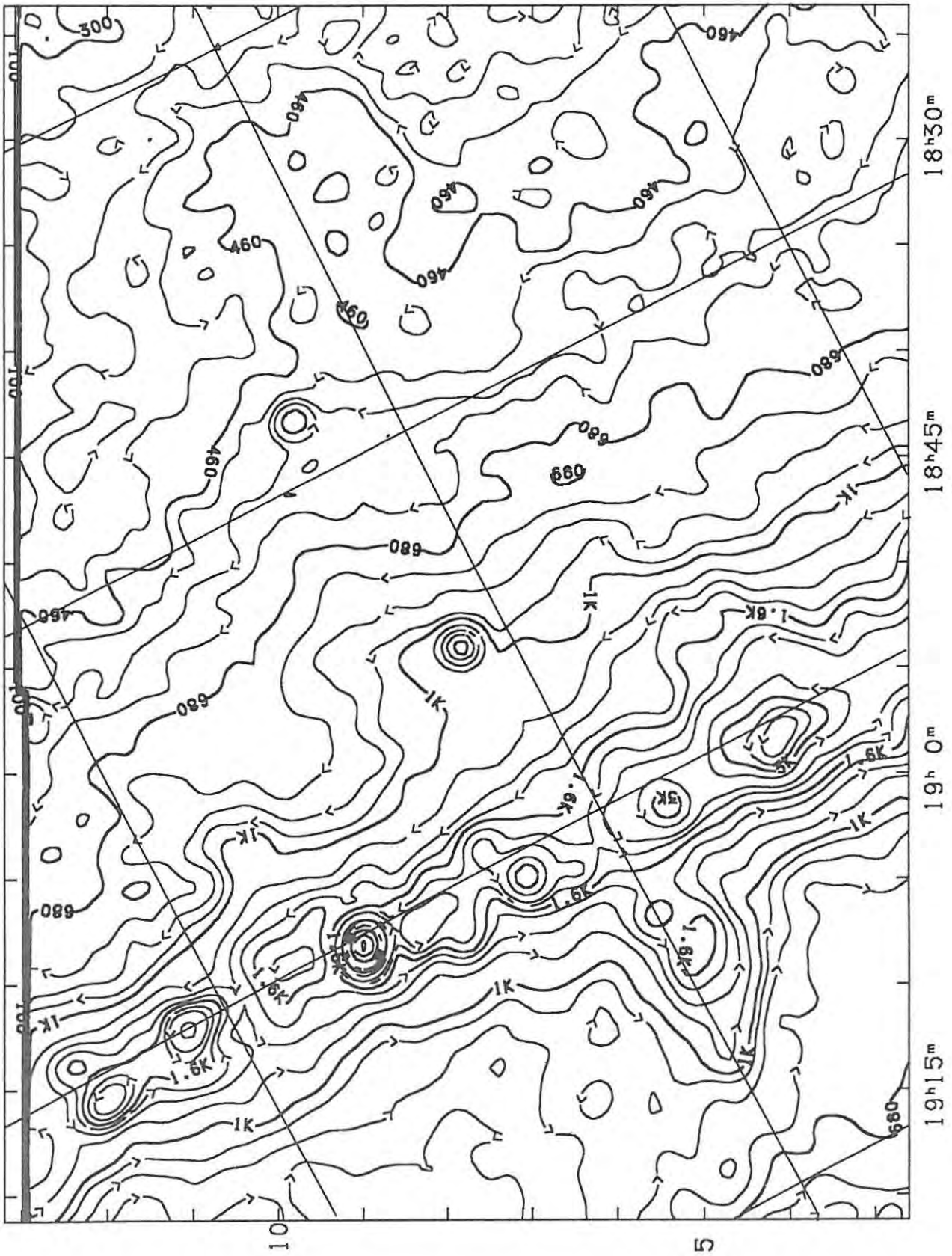

Figure A1.49 - Rhodes 2.3 Ghz Sky Survey (Map G4).

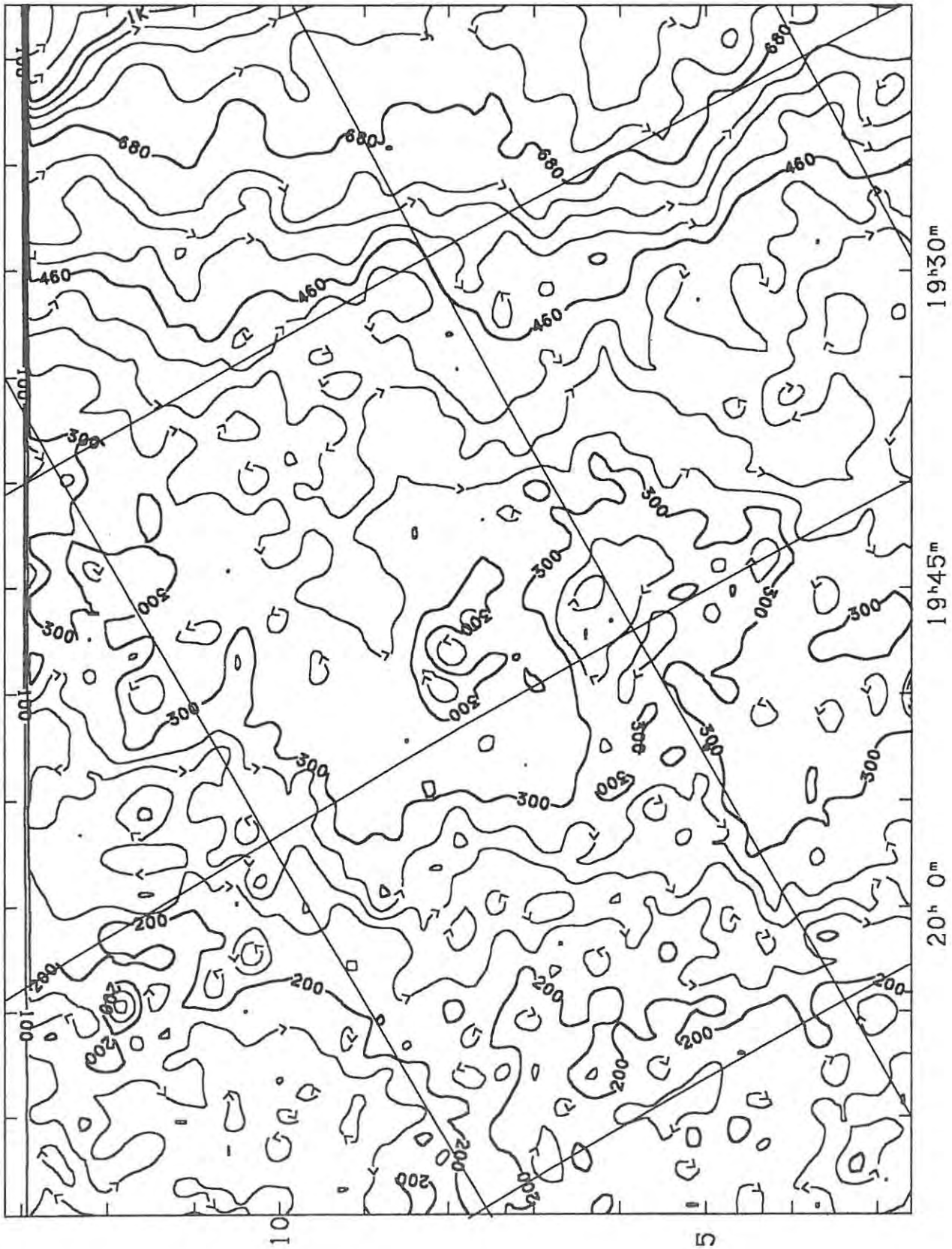

Figure A1.50 - Rhodes 2.3 Ghz Sky Survey (Map H4).

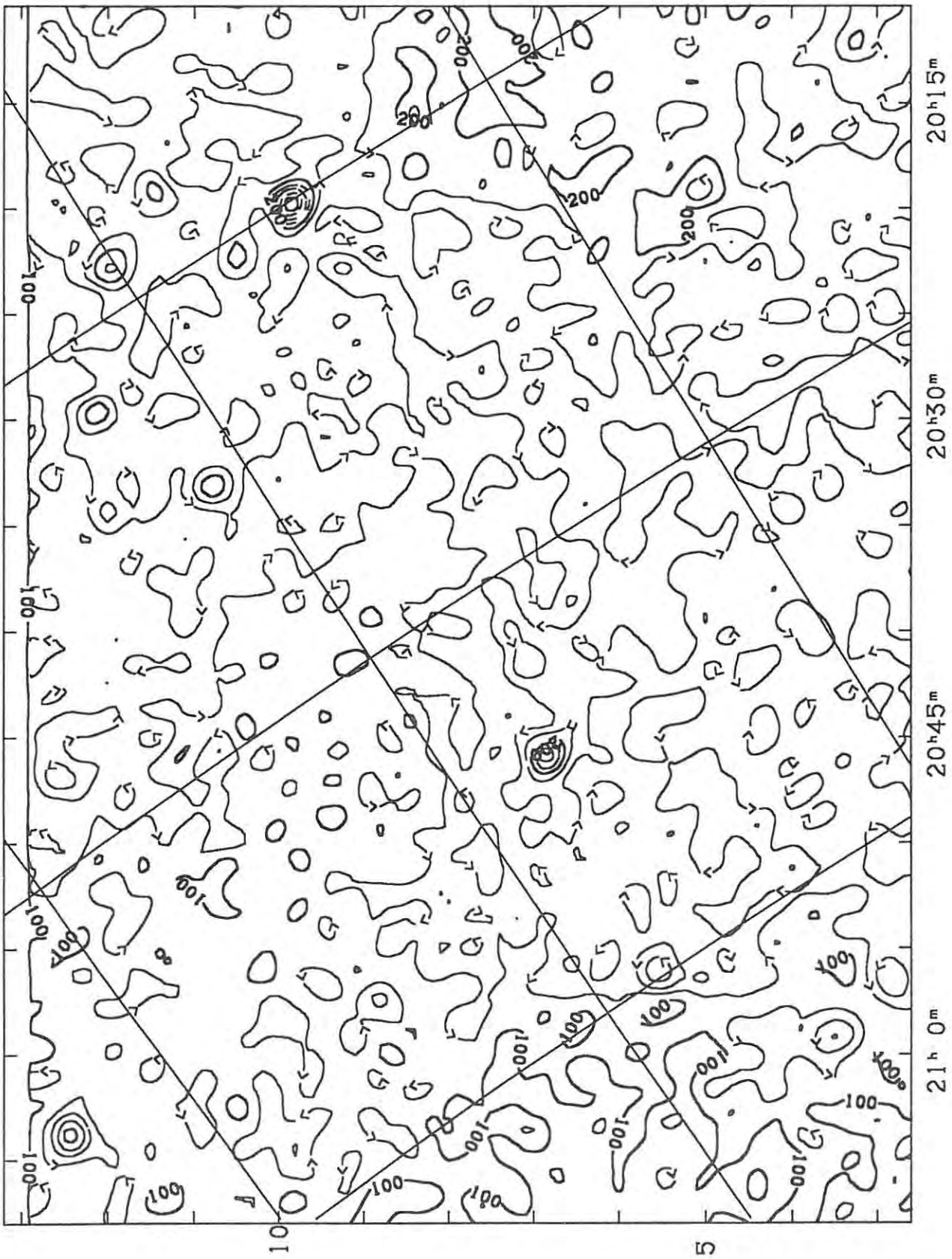

Figure A1.51 - Rhodes 2.3 Ghz Sky Survey (Map I4).

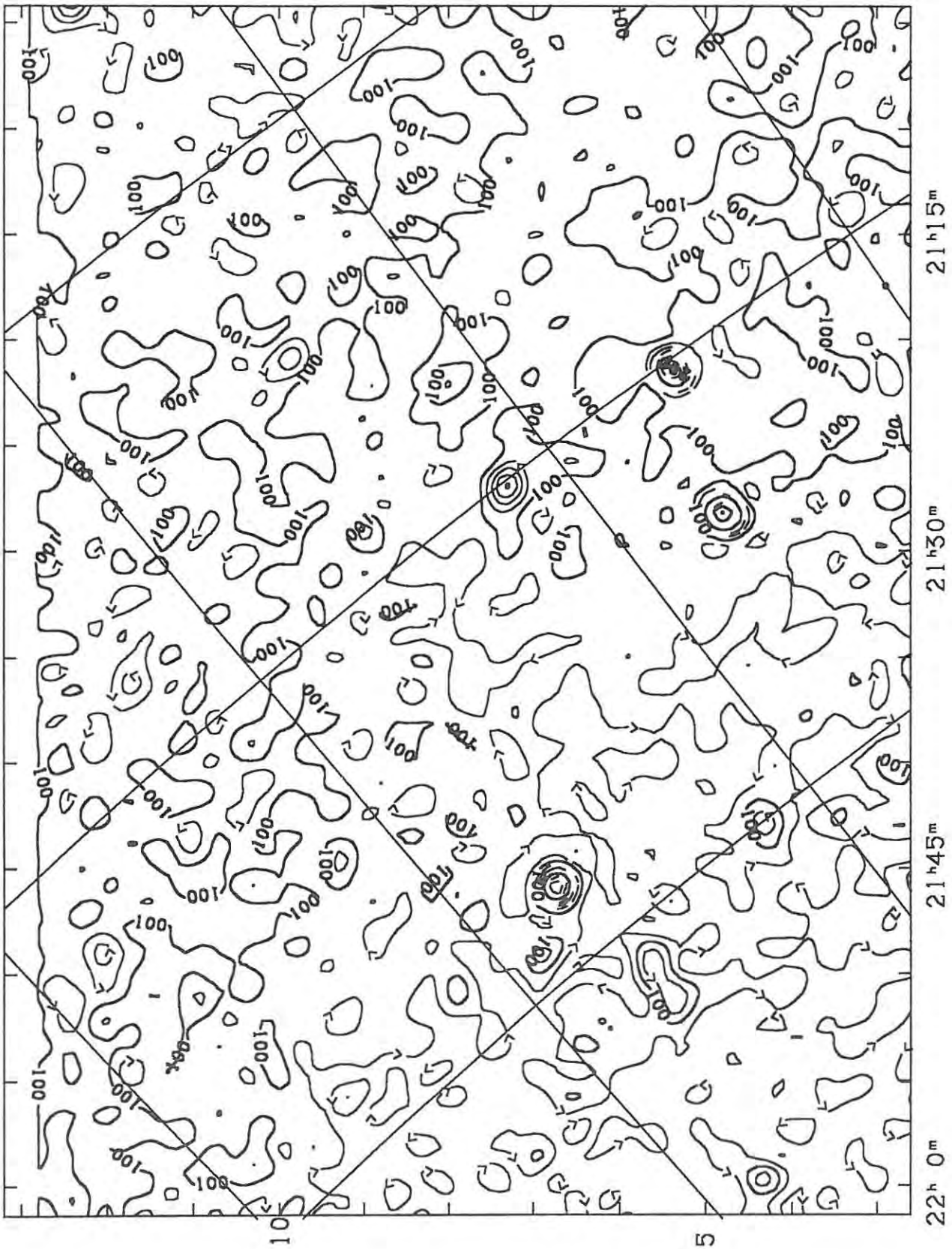

Figure A1.52 - Rhodes 2.3 Ghz Sky Survey (Map J4).

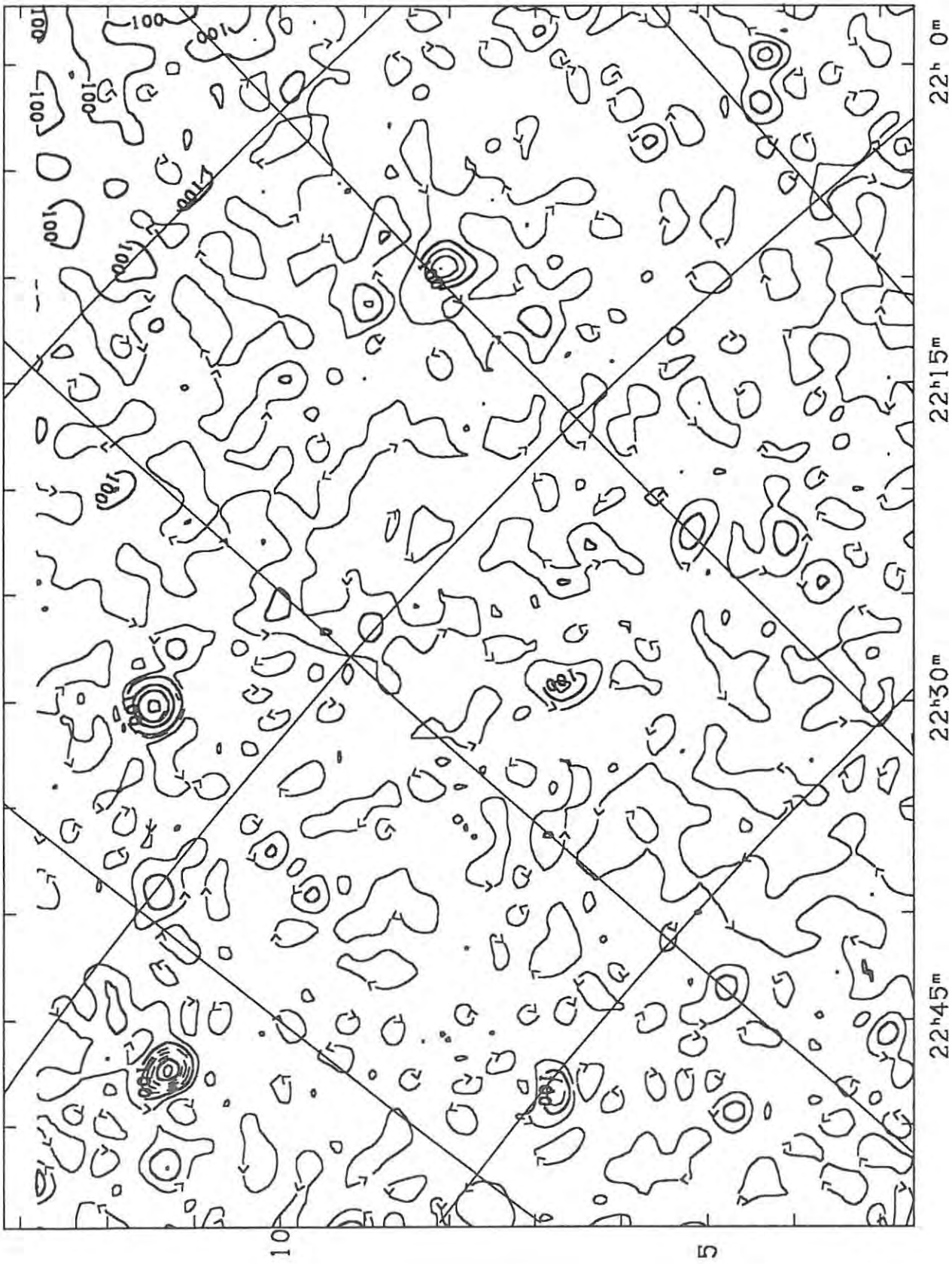

Figure A1.53 - Rhodes 2.3 Ghz Sky Survey (Map K4).

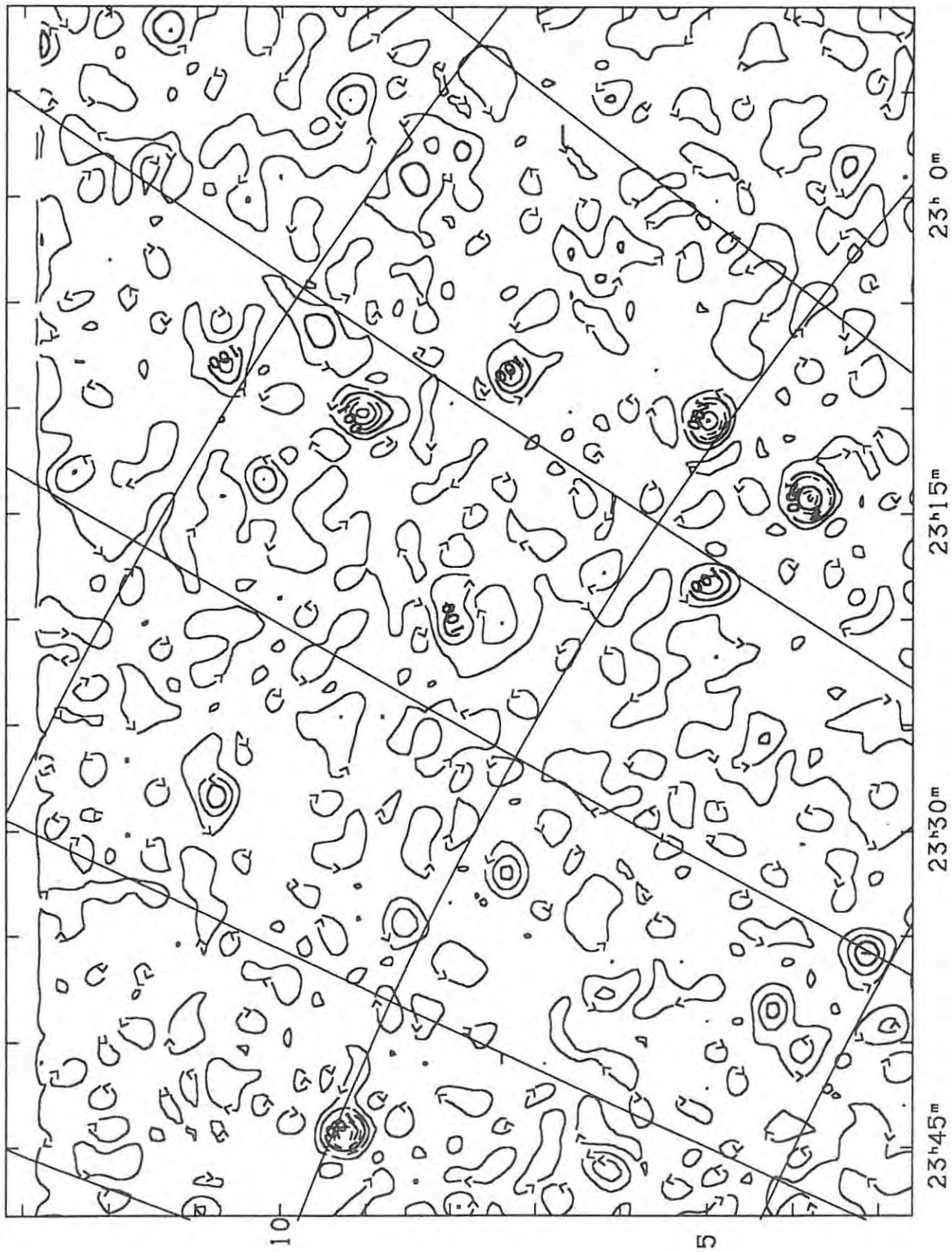

Figure A1.54 - Rhodes 2.3 Ghz Sky Survey (Map L4).

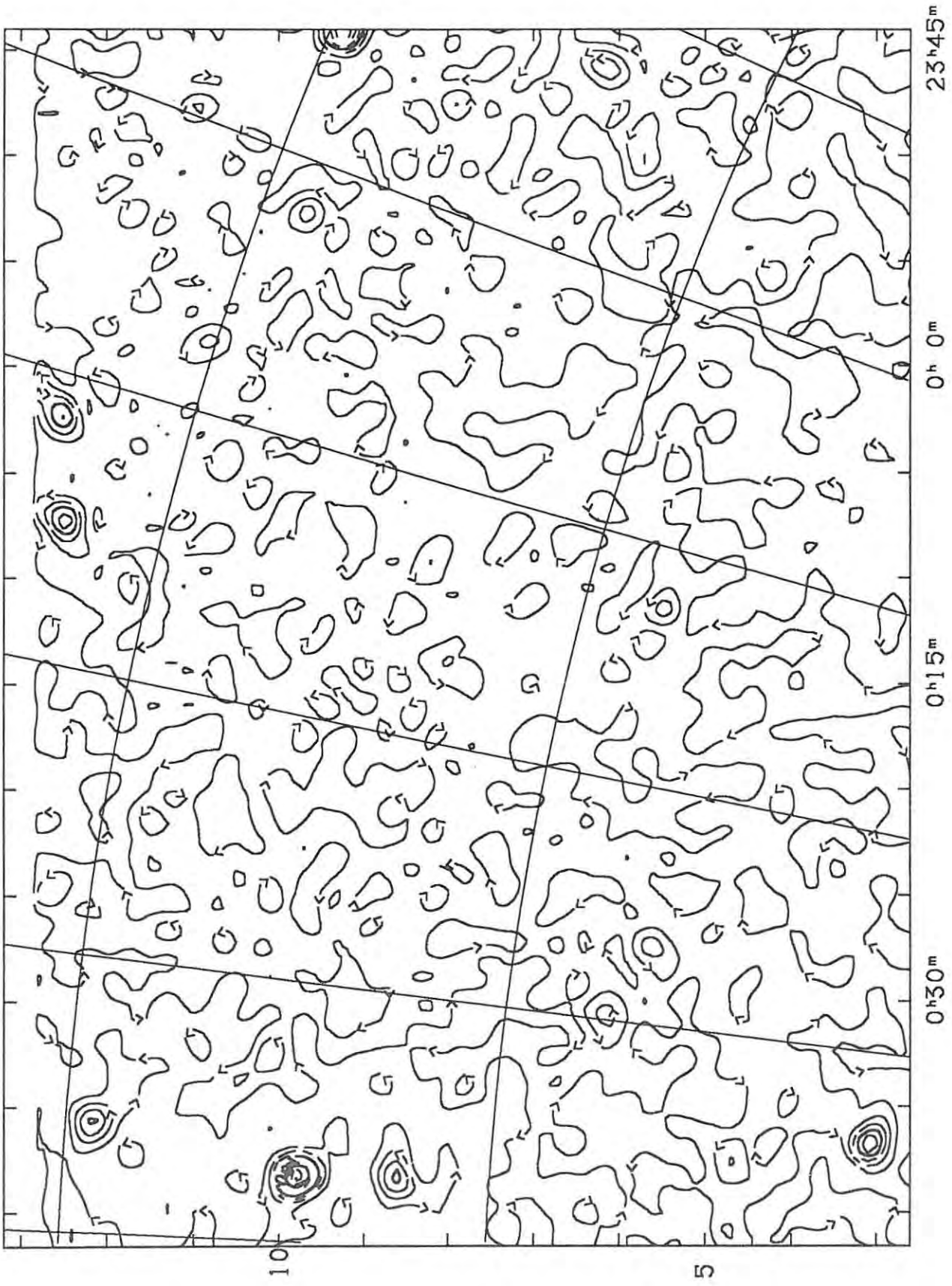

Figure A1.55 - Rhodes 2.3 Ghz Sky Survey (Map M4).

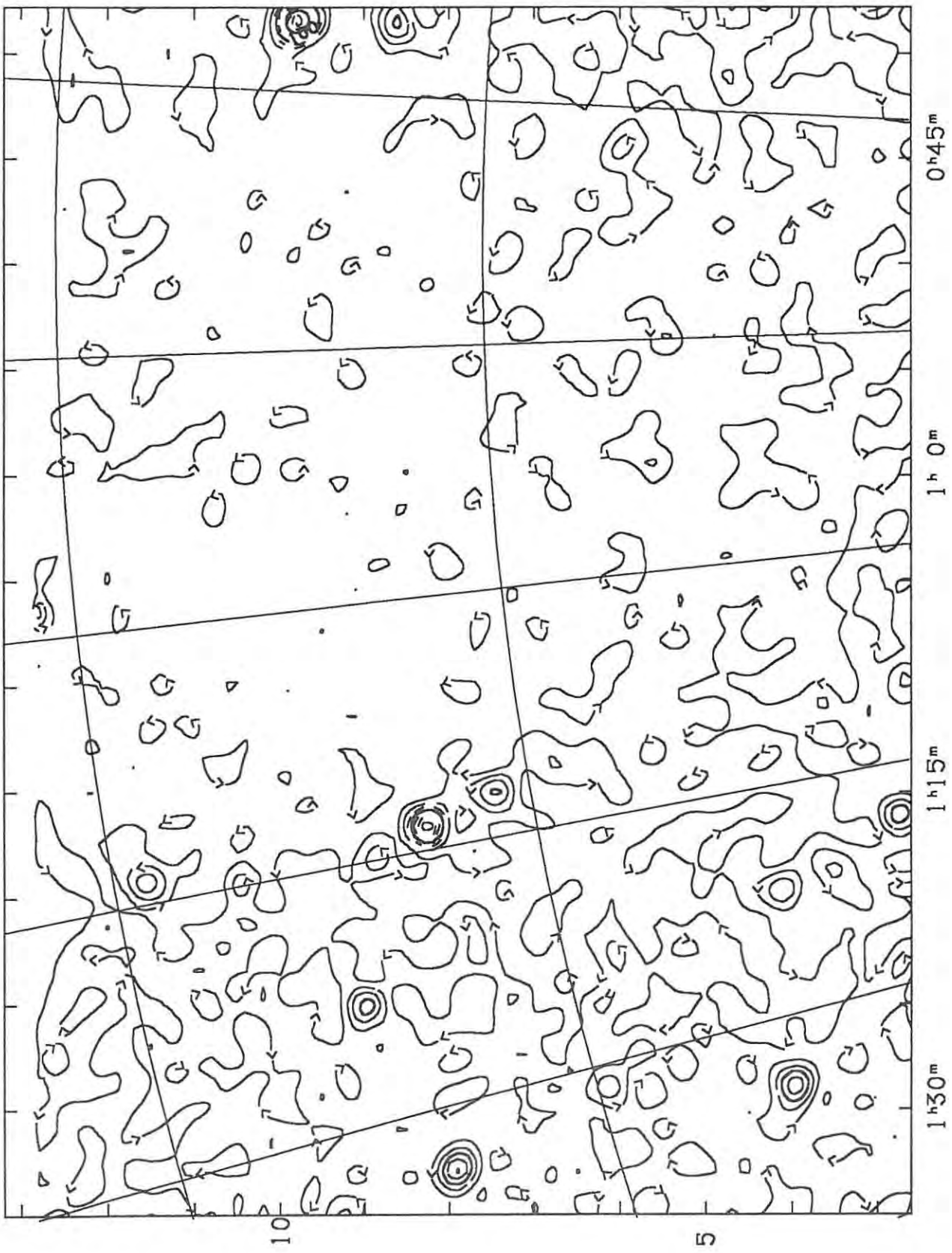

Figure A1.56 - Rhodes 2.3 Ghz Sky Survey (Map N4).

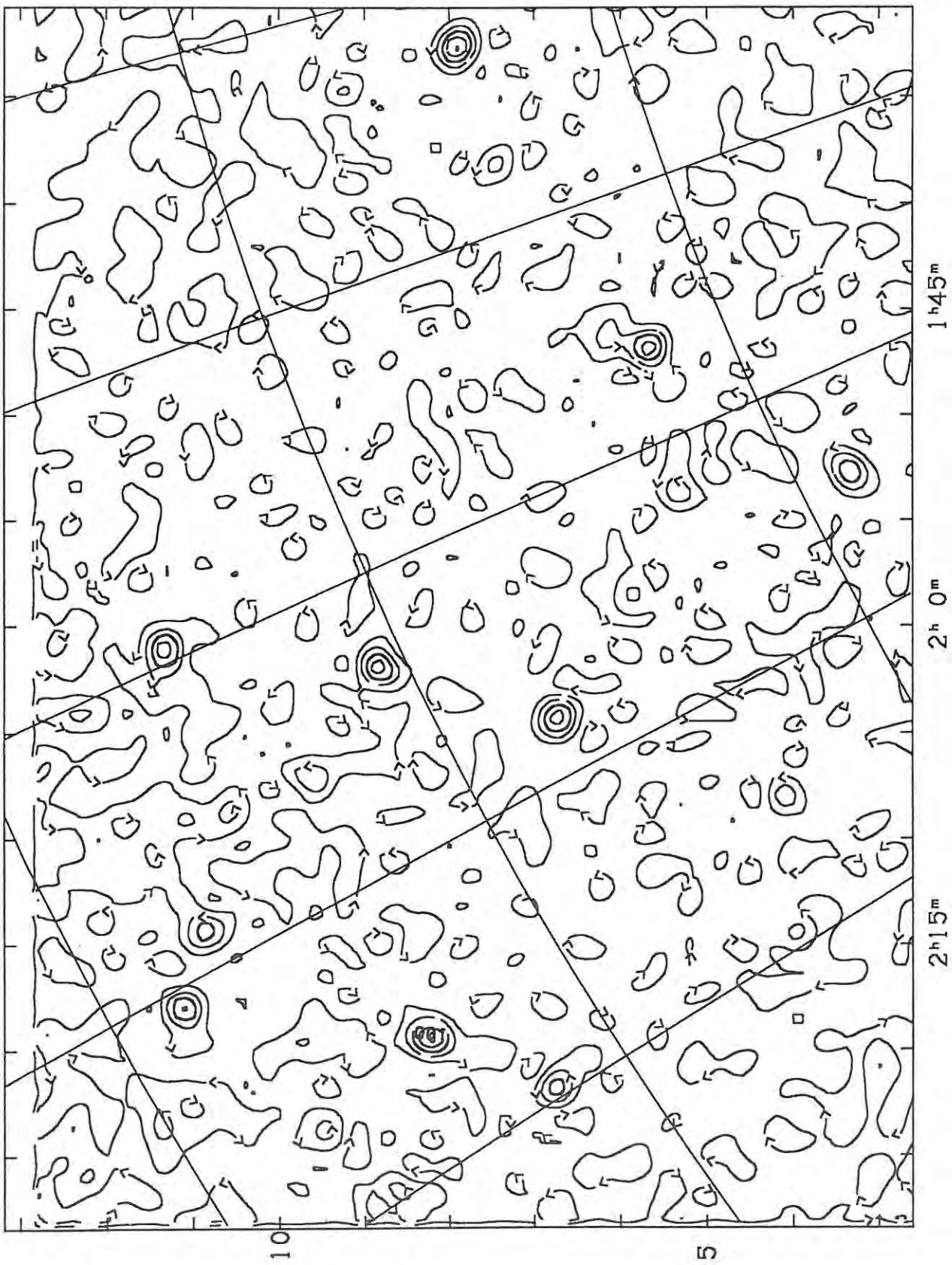

Appendix Two - Contour Maps of the North Polar Spur

Presented in this appendix are contour maps covering the area of sky containing the North Polar Spur. The contour levels are tabulated below in table A2.1, and the limits of each map (the whole area is divided into 27 sections) and the lowest and highest contours plotted on each map are tabulated in table A2.2. Note that these maps are plotted in new Galactic coordinates, and not in equatorial coordinates as the maps in Appendix One are plotted. Degrees of Galactic longitude are labelled along the horizontal axes and degrees of Galactic latitude are labelled along the vertical axes.

The grid lines on the maps represent right ascension and declination at a spacing of five degrees. Note that 1K antenna temperature corresponds to 1.51K full beam brightness temperature.

Table A2.1 - Contour levels.

Contour Level Ta / mK	Contour Label	Contour Level Ta / mK	Contour Label
50	>	1200	>
100	100	1500	1.5K
150	>	2000	>
200	200	2500	>
250	>	3000	3K
300	300	4000	>
400	>	5000	5K
500	500	7000	>
650	>	10000	10K
800	>	14000	>
1000	1K	20000	20K

Table A2.2 - Map limits and lowest/highest contour levels plotted.

MAP NUMBER	LEFT LIMIT deg	RIGHT LIMIT deg	BOTTOM LIMIT deg	TOP LIMIT deg	LOWEST CONTOUR mK	HIGHEST CONTOUR mK
A1	24.0	10.0	-10.0	-2.1	50	500
B1	37.0	23.0	-10.0	-2.1	50	650
C1	50.0	36.0	-10.0	-2.1	50	1000
A2	24.0	10.0	-3.1	4.8	50	14000
B2	37.0	23.0	-3.1	4.8	50	7000
C2	50.0	36.0	-3.1	4.8	50	10000
A3	24.0	10.0	3.8	11.7	50	300
B3	37.0	23.0	3.8	11.7	50	800
C3	50.0	36.0	3.8	11.7	50	250
A4	24.0	10.0	10.7	18.6	50	200
B4	37.0	23.0	10.7	18.6	50	300
C4	50.0	36.0	10.7	18.6	50	200
A5	24.0	10.0	17.6	25.5	50	1200
B5	37.0	23.0	17.6	25.5	50	300
C5	50.0	36.0	17.6	25.5	50	100
A6	24.0	10.0	24.5	32.4	50	800
B6	37.0	23.0	24.5	32.4	50	800
C6	50.0	36.0	24.5	32.4	50	100
A7	24.0	10.0	31.4	39.3	50	200
B7	37.0	23.0	31.4	39.3	50	200
C7	50.0	36.0	31.4	39.3	50	150
A8	24.0	10.0	38.3	46.2	50	150
B8	37.0	23.0	38.3	46.2	50	150
C8	50.0	36.0	38.3	46.2	50	200
A9	24.0	10.0	45.2	53.1	50	100
B9	37.0	23.0	45.2	53.1	50	200
C9	50.0	36.0	45.2	53.1	50	200

Figure A2.1 - North Polar Spur (Map A1)

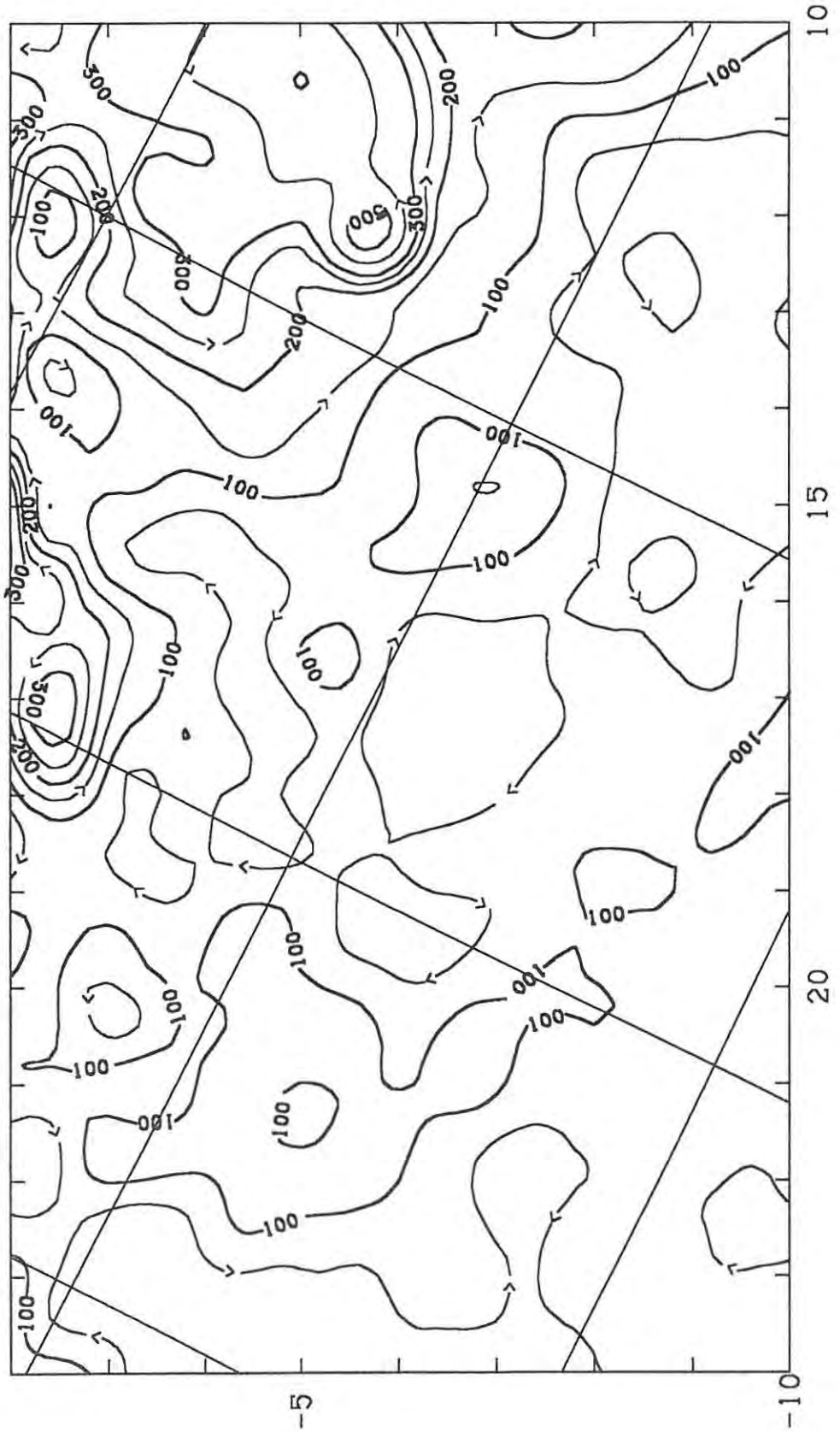

Figure A2.2 - North Polar Spur (Map B1)

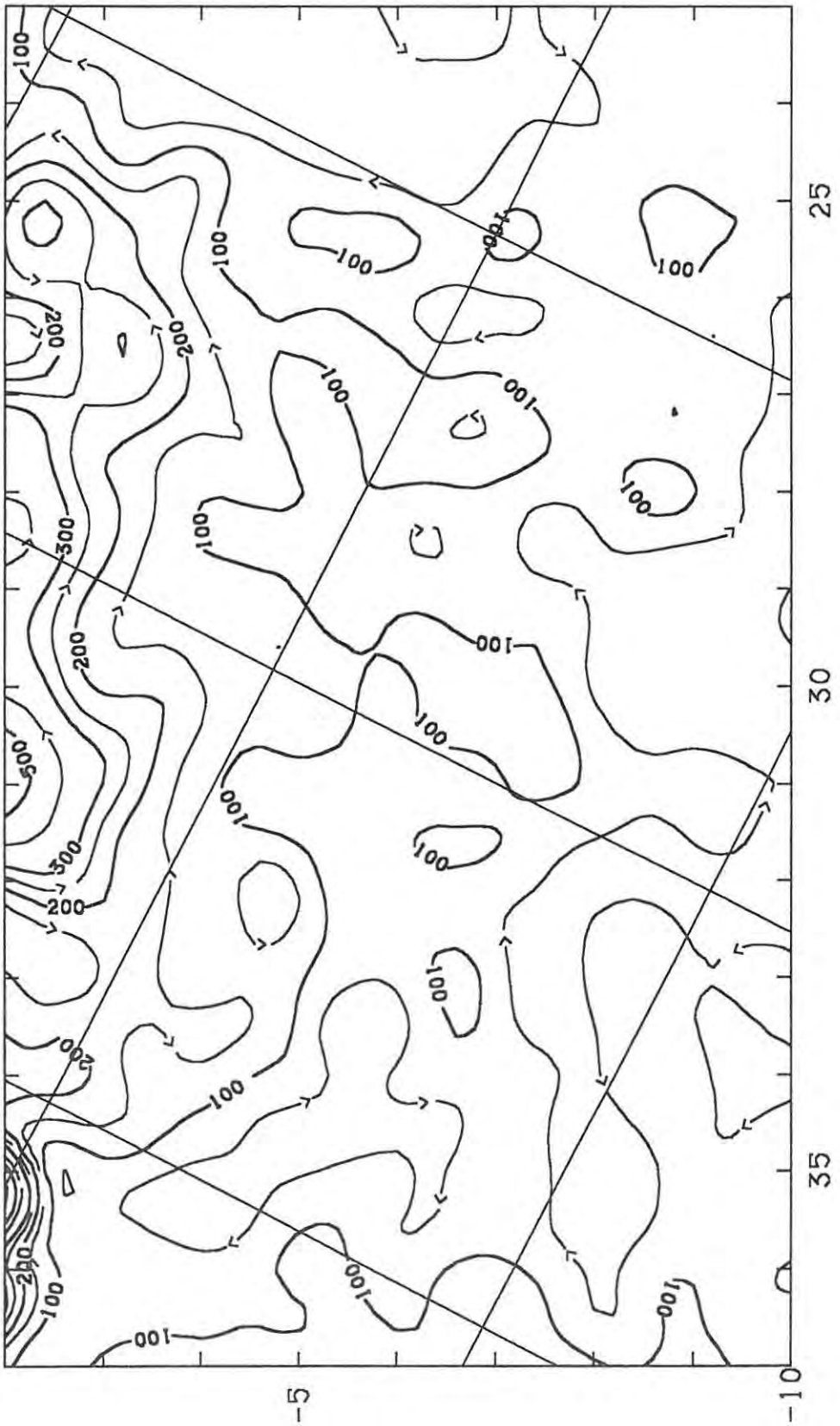

Figure A2.3 - North Polar Spur (Map C1)

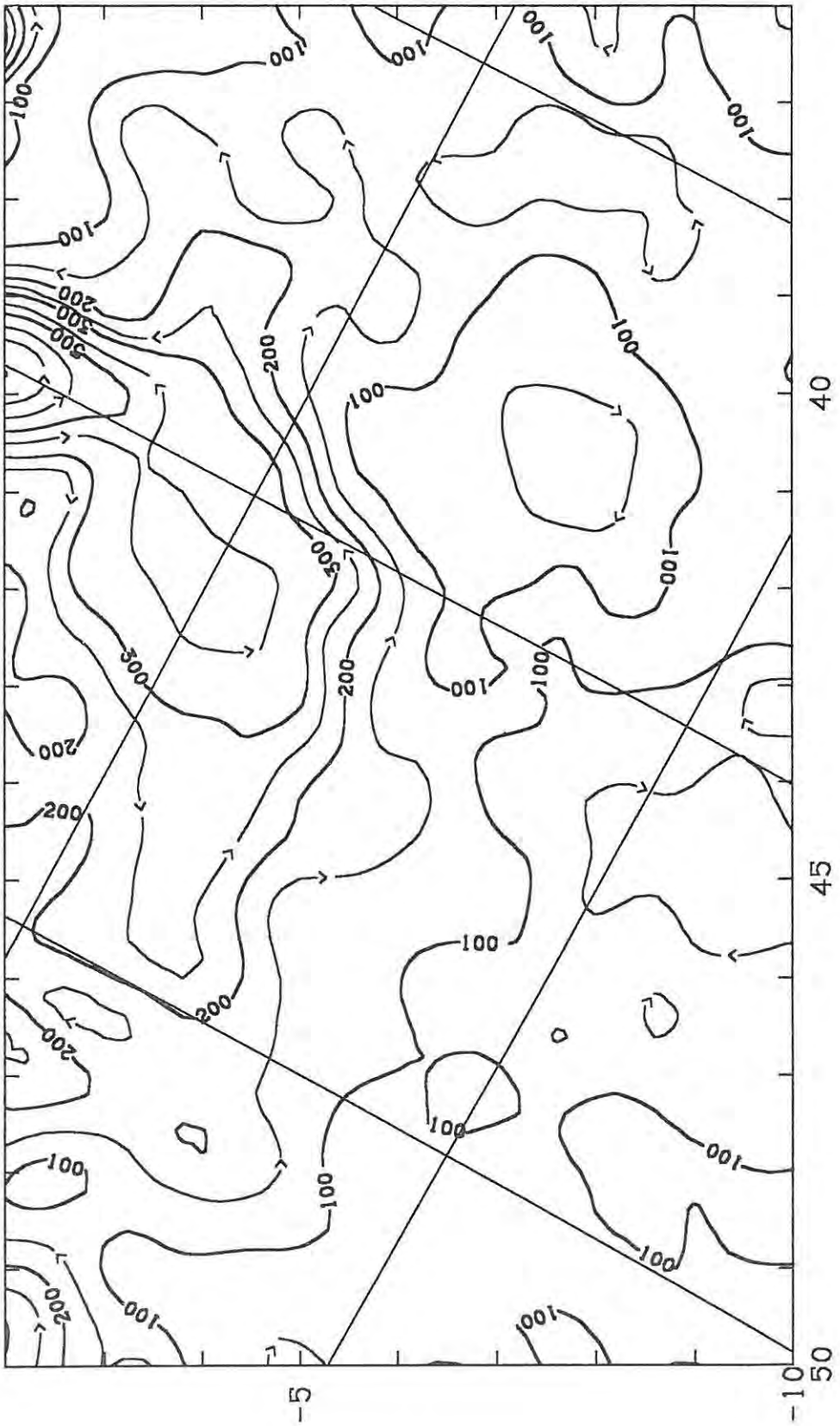

Figure A2.4 - North Polar Spur (Map A2)

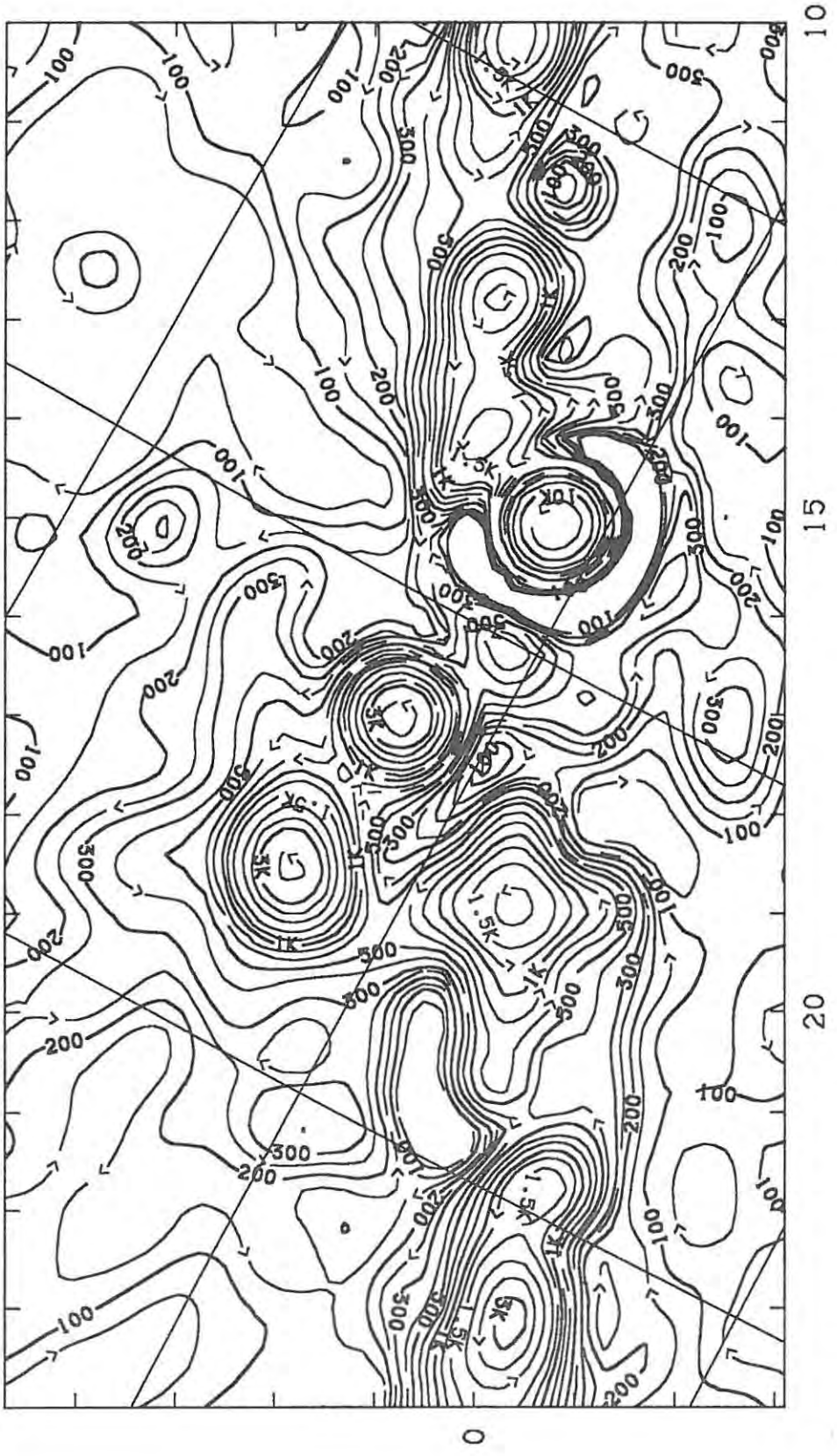

Figure A2.5 - North Polar Spur (Map B2)

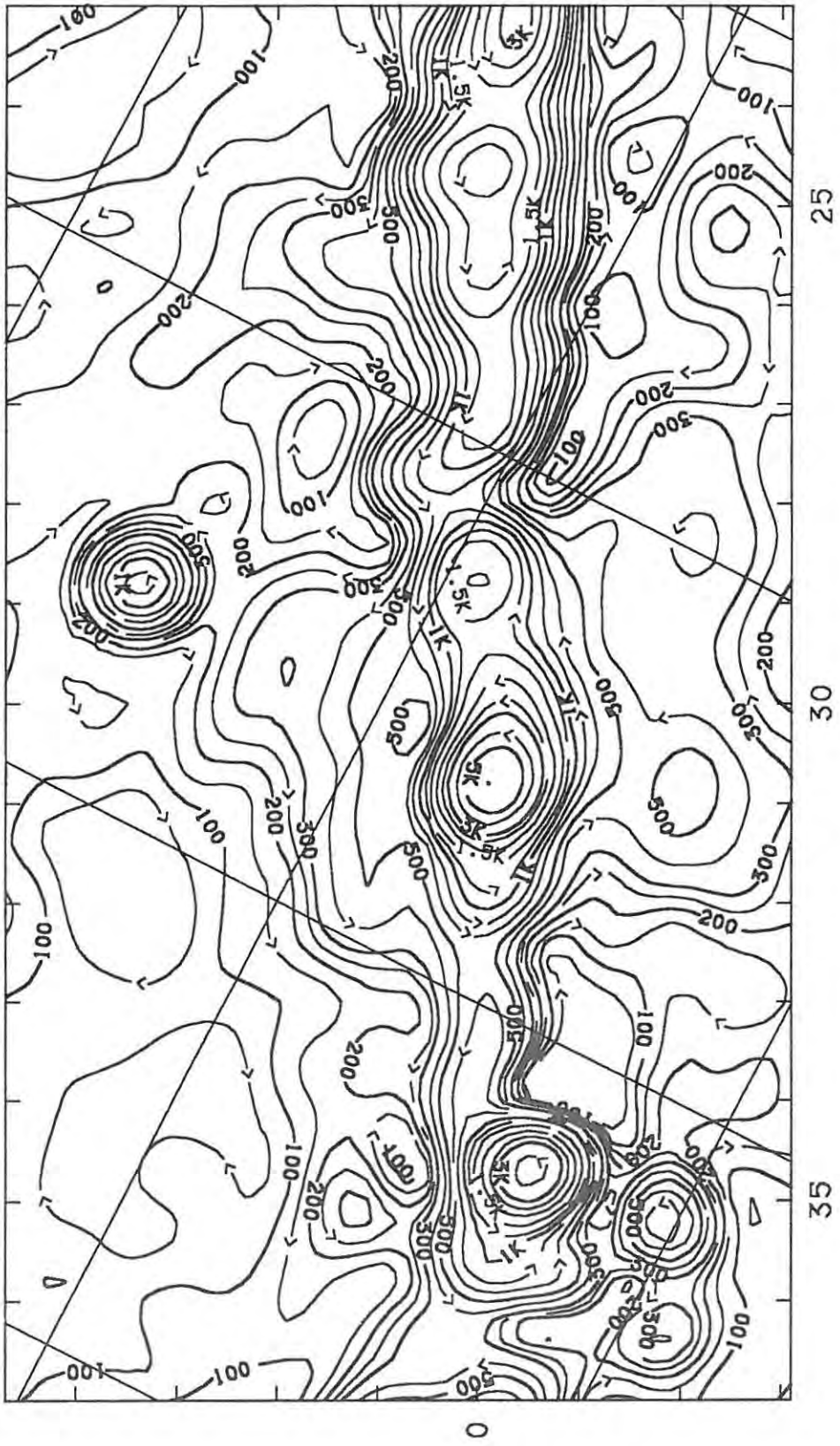

Figure A2.6 - North Polar Spur (Map C2)

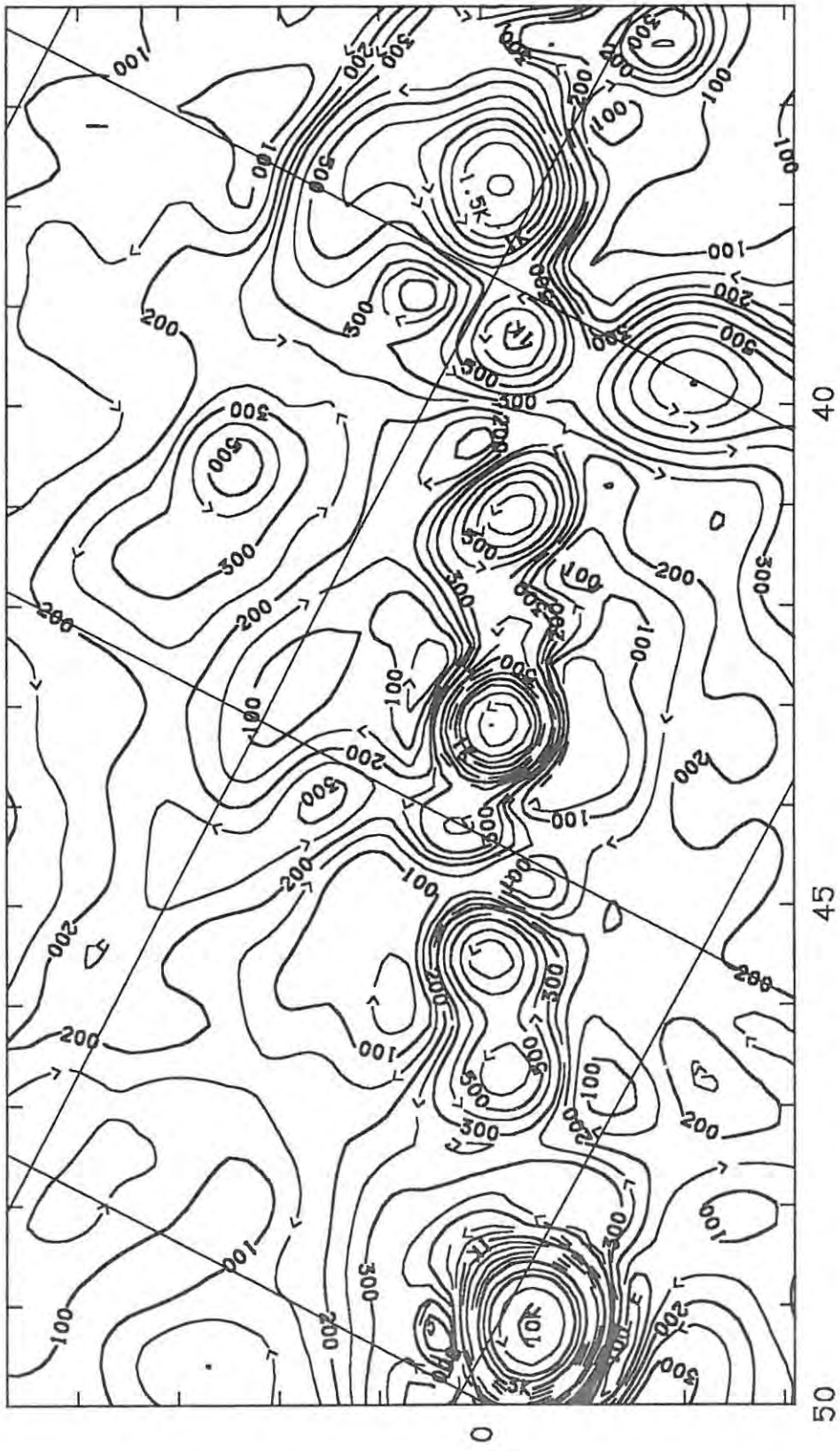

Figure A2.7 - North Polar Spur (Map A3)

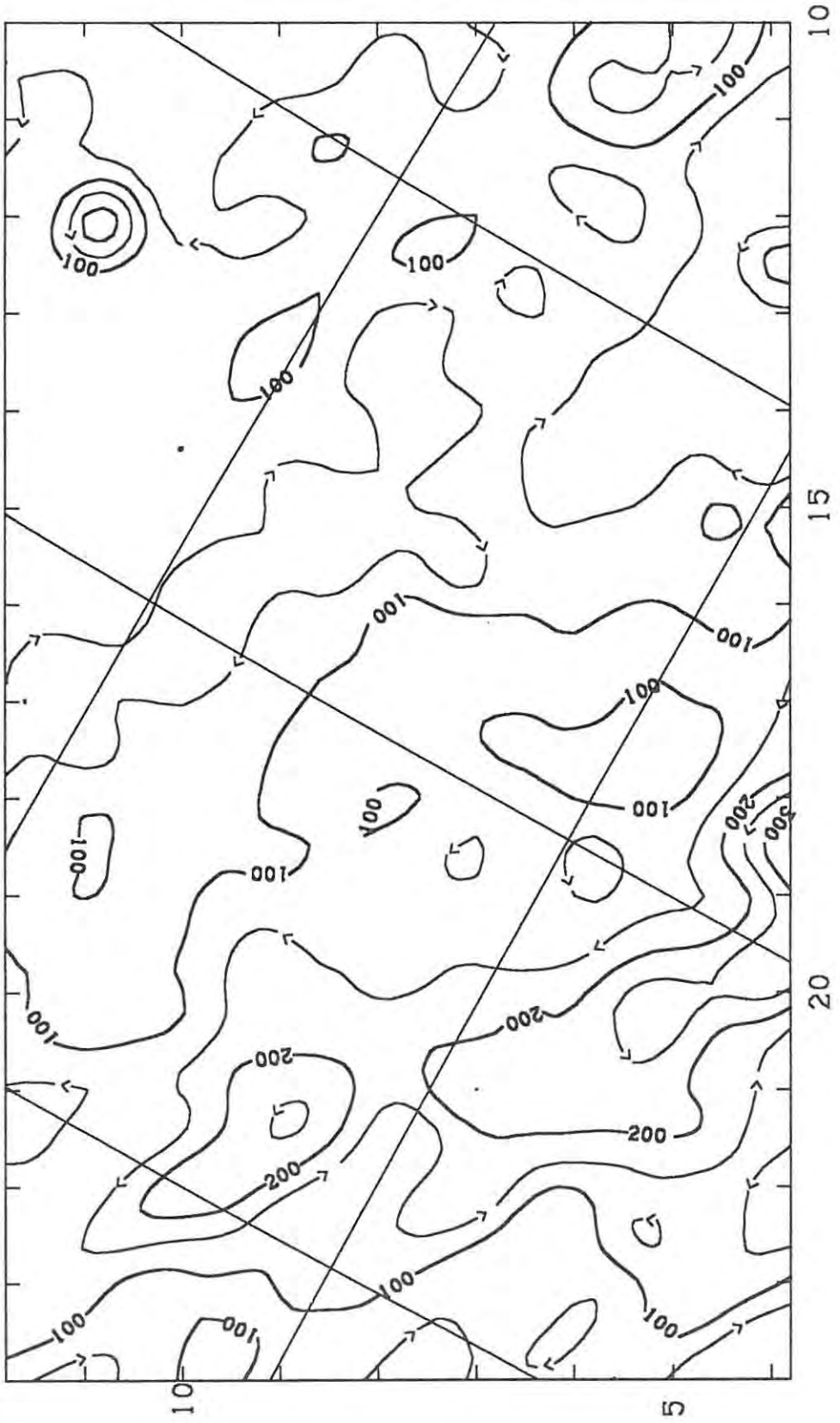

Figure A2.8 - North Polar Spur (Map B3)

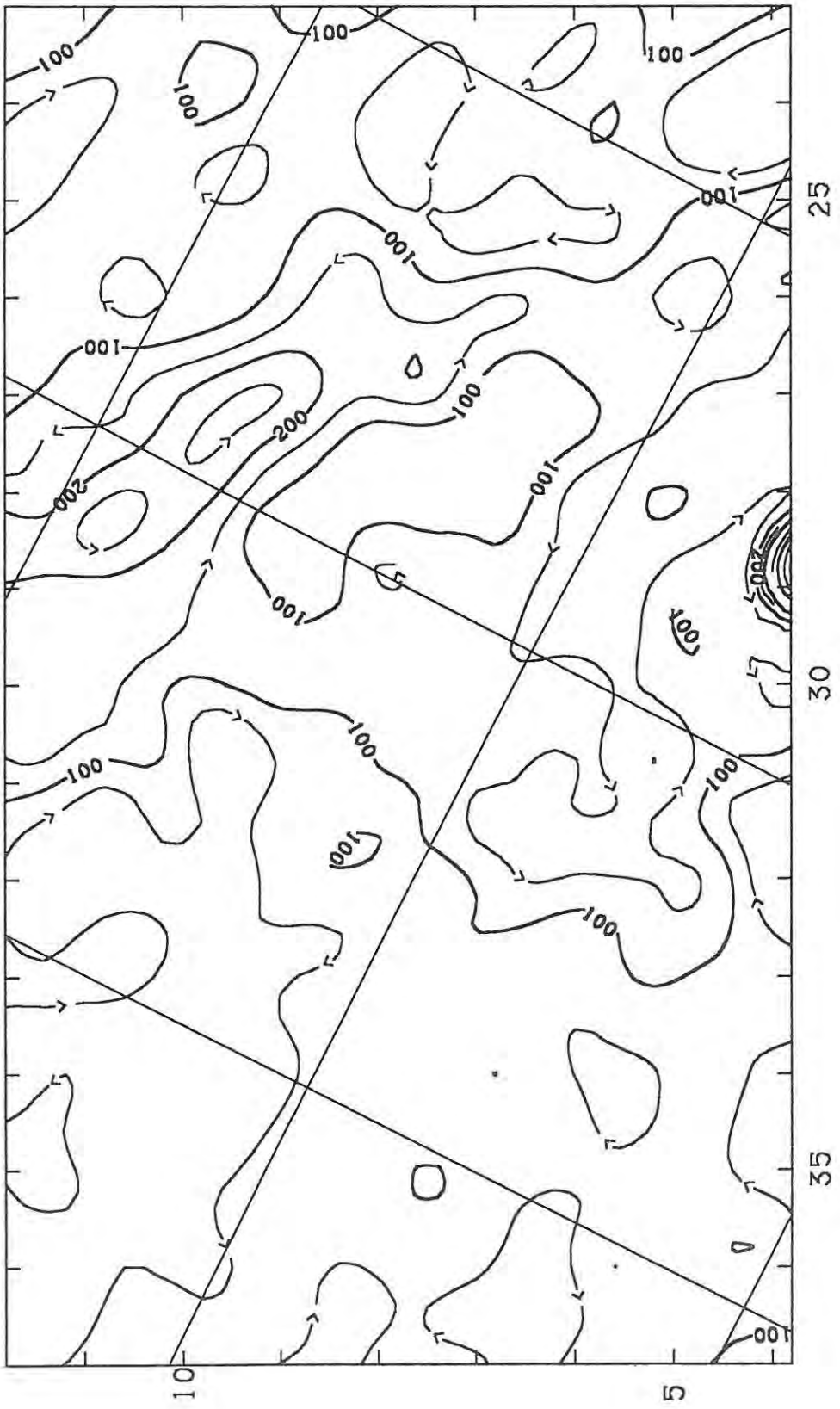

Figure A2.9 - North Polar Spur (Map C3)

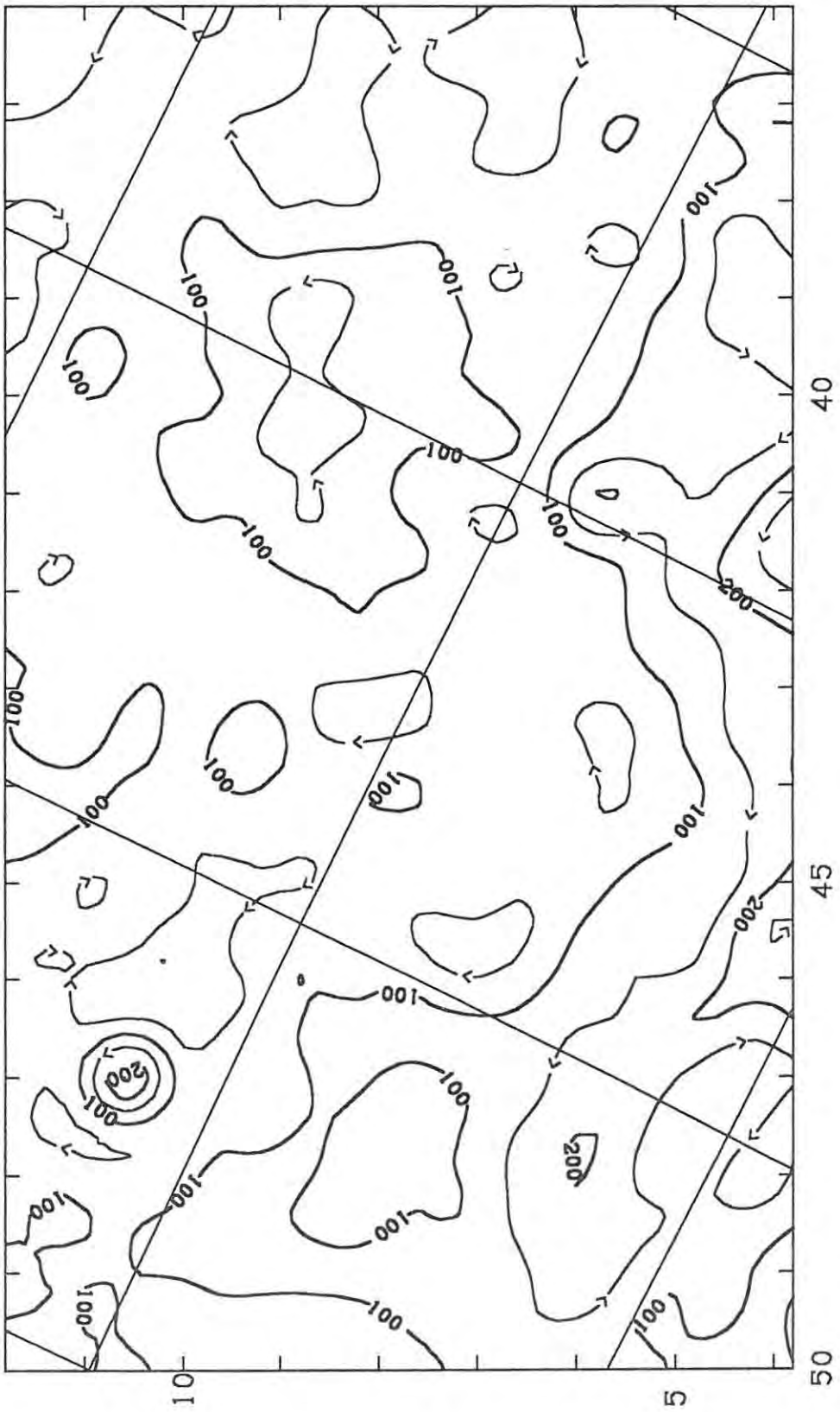

Figure A2.10 - North Polar Spur (Map A4)

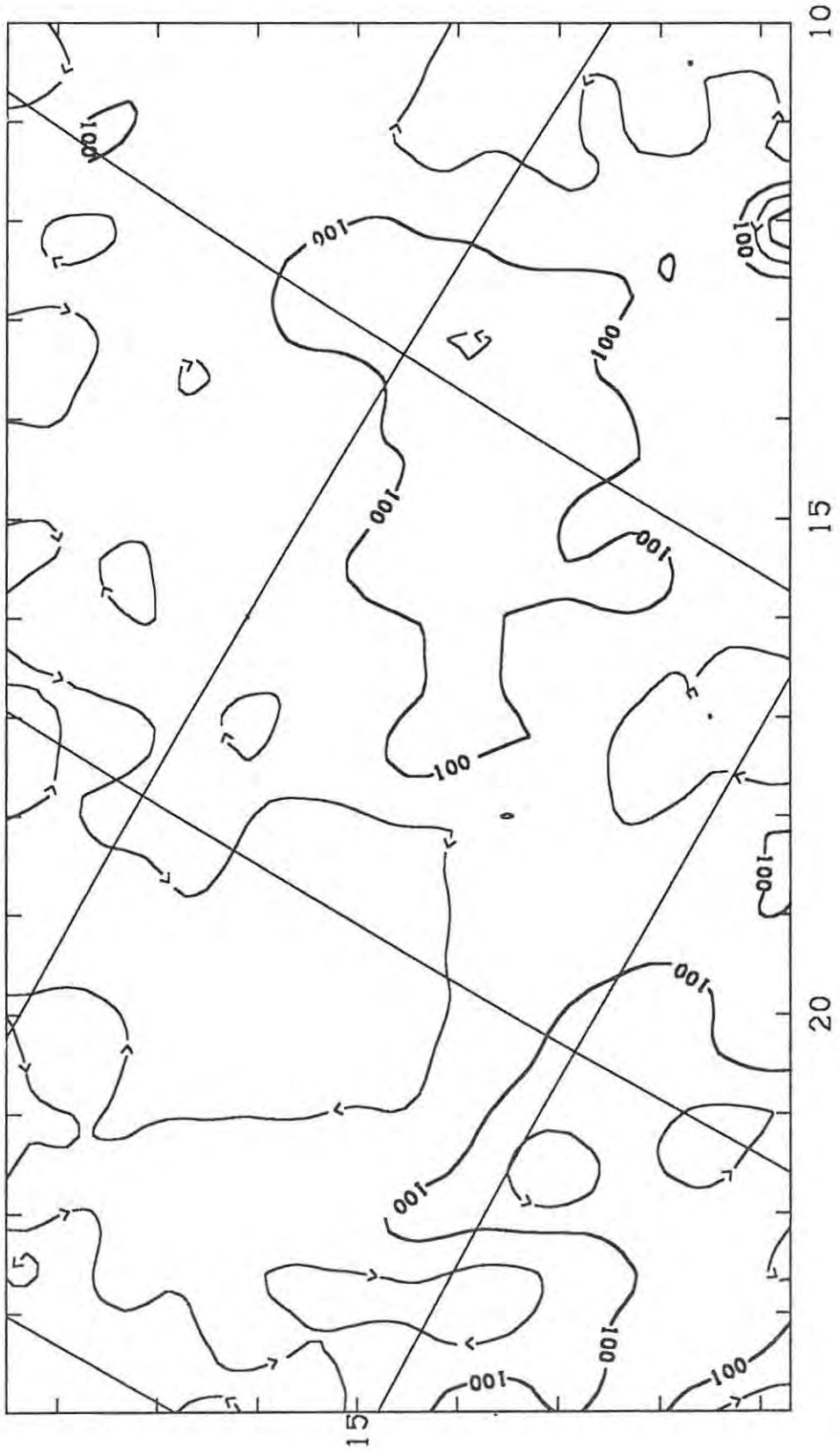

Figure A2.11 - North Polar Spur (Map B4)

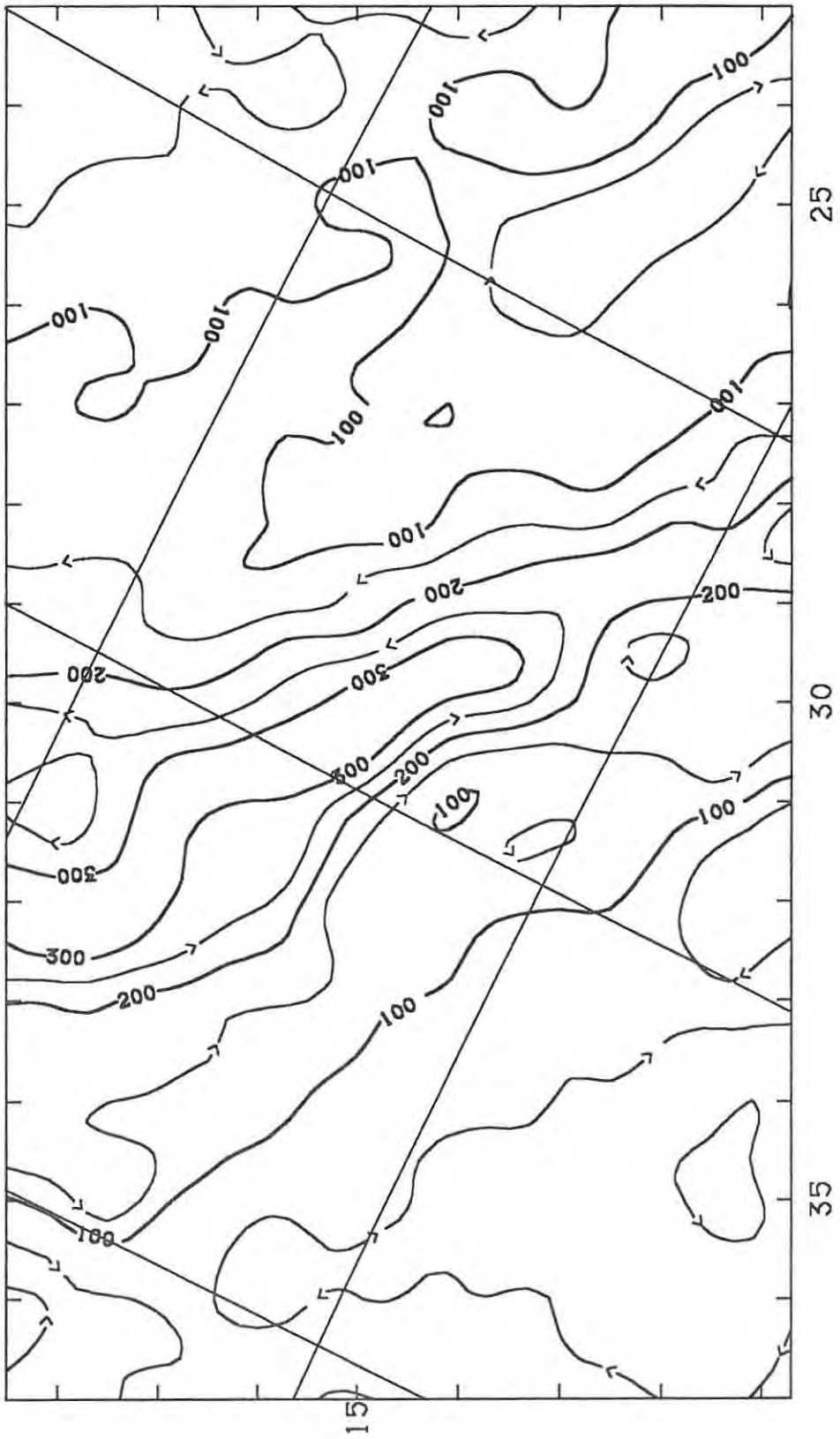

Figure A2.12 - North Polar Spur (Map C4)

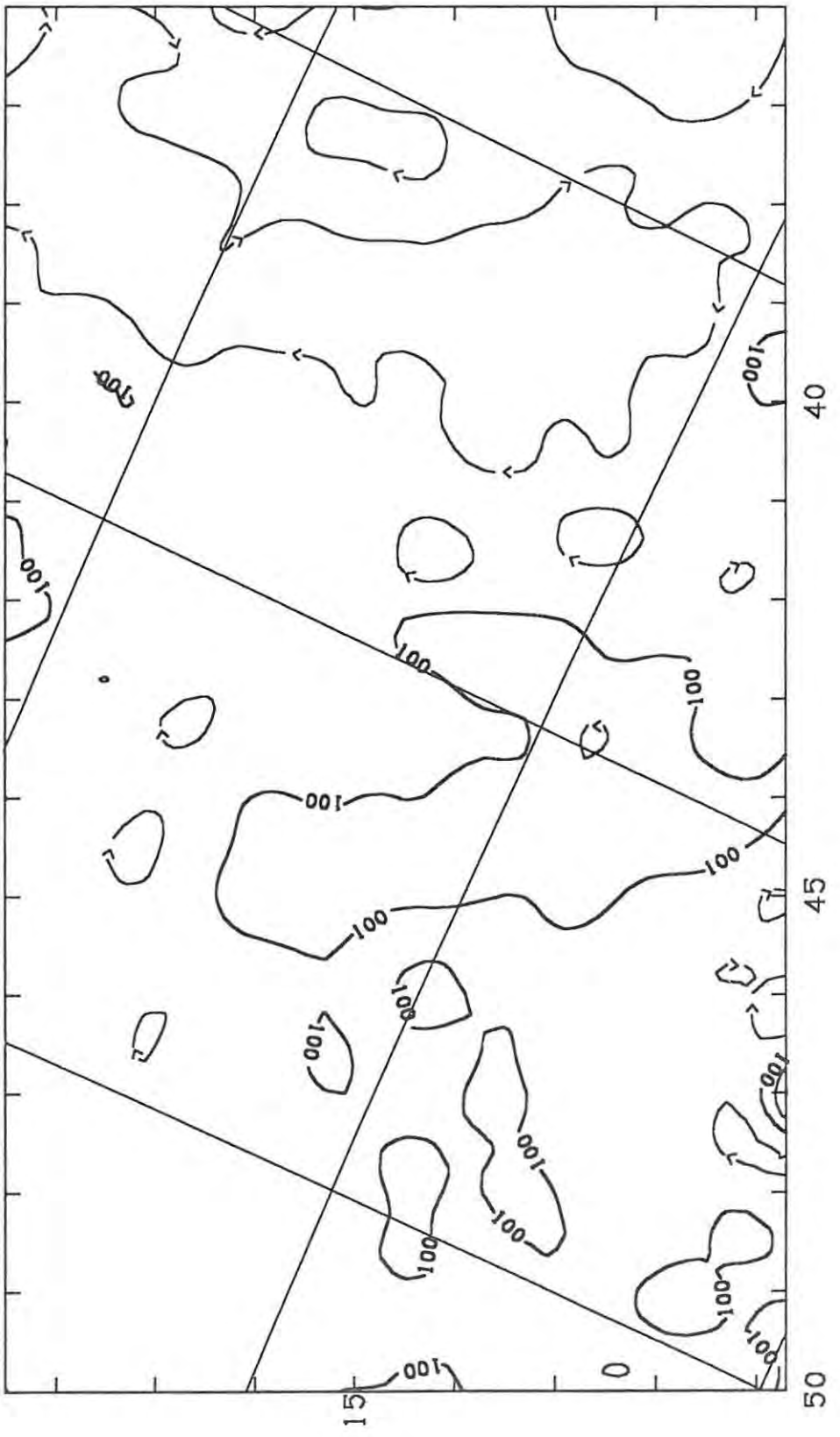

Figure A2.13 - North Polar Spur (Map A5)

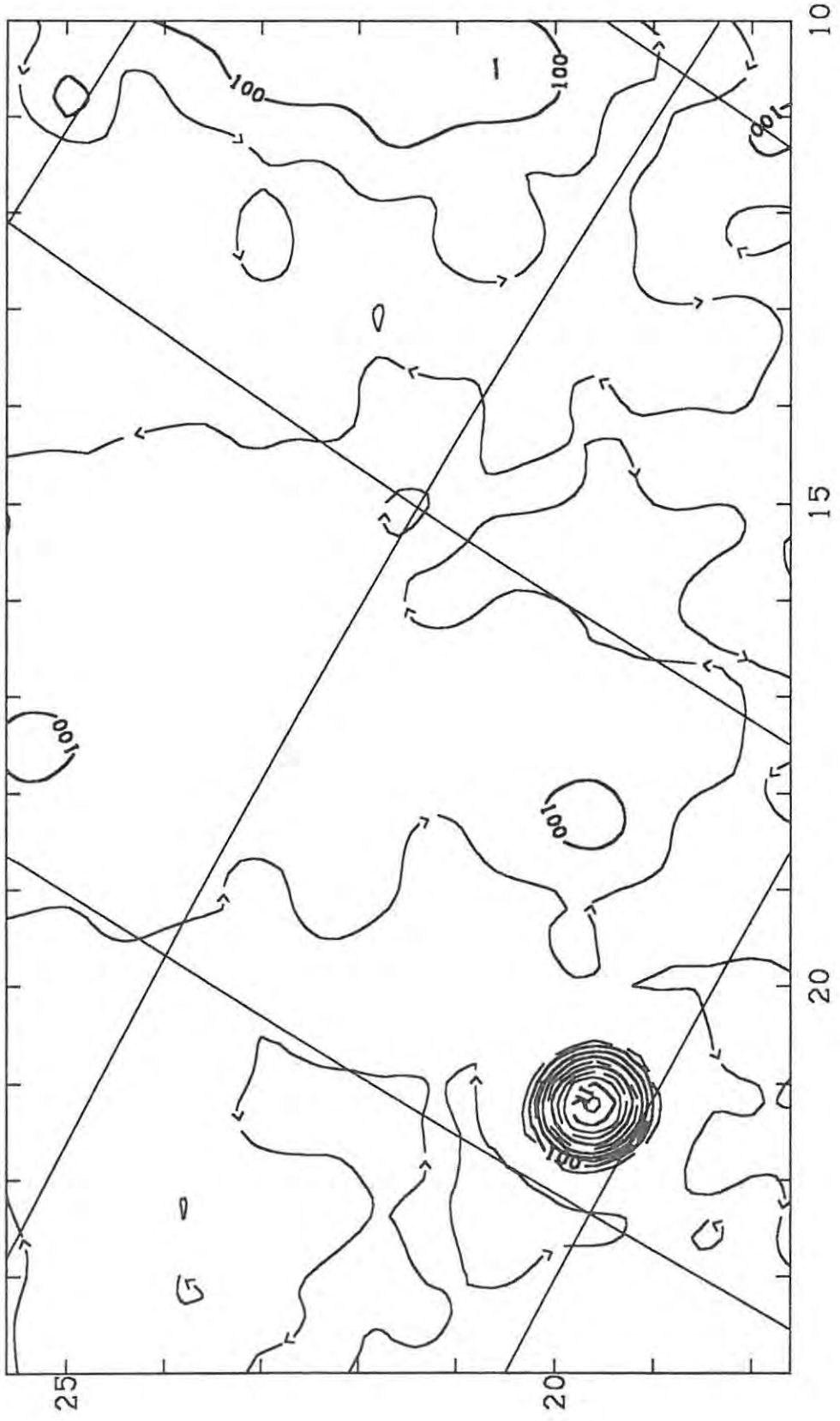

Figure A2.14 - North Polar Spur (Map B5)

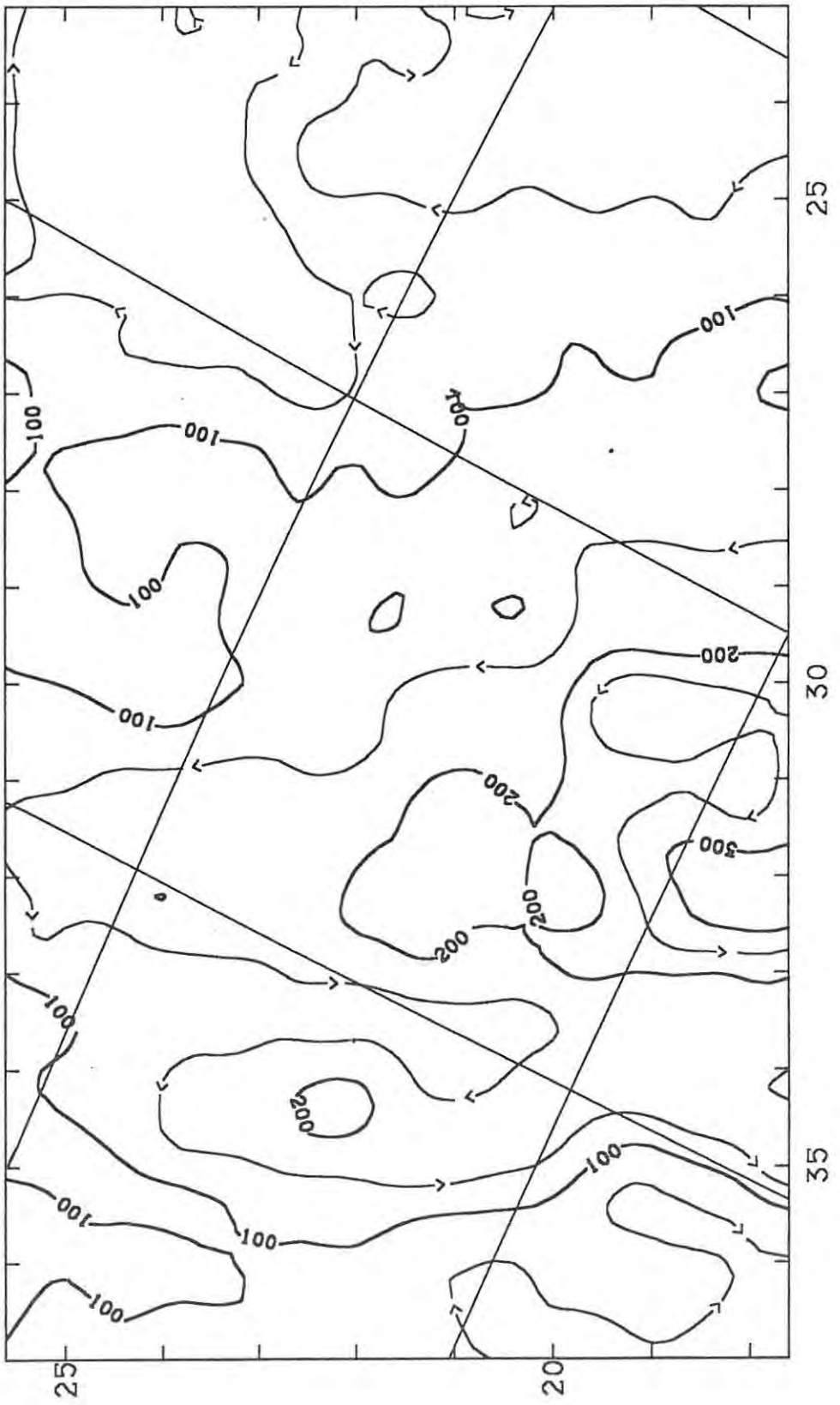

Figure A2.15 - North Polar Spur (Map C5)

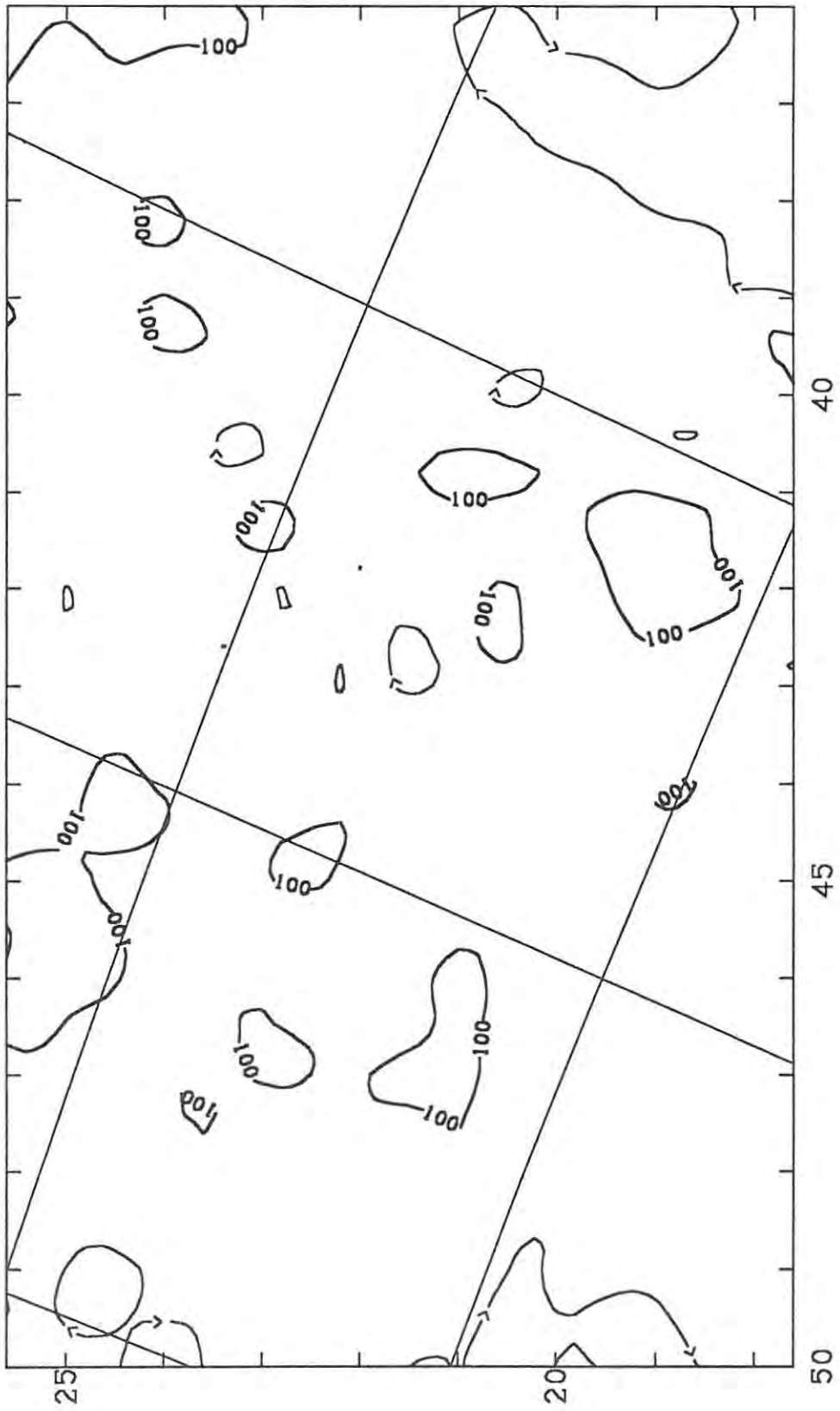

Figure A2.16 - North Polar Spur (Map A6)

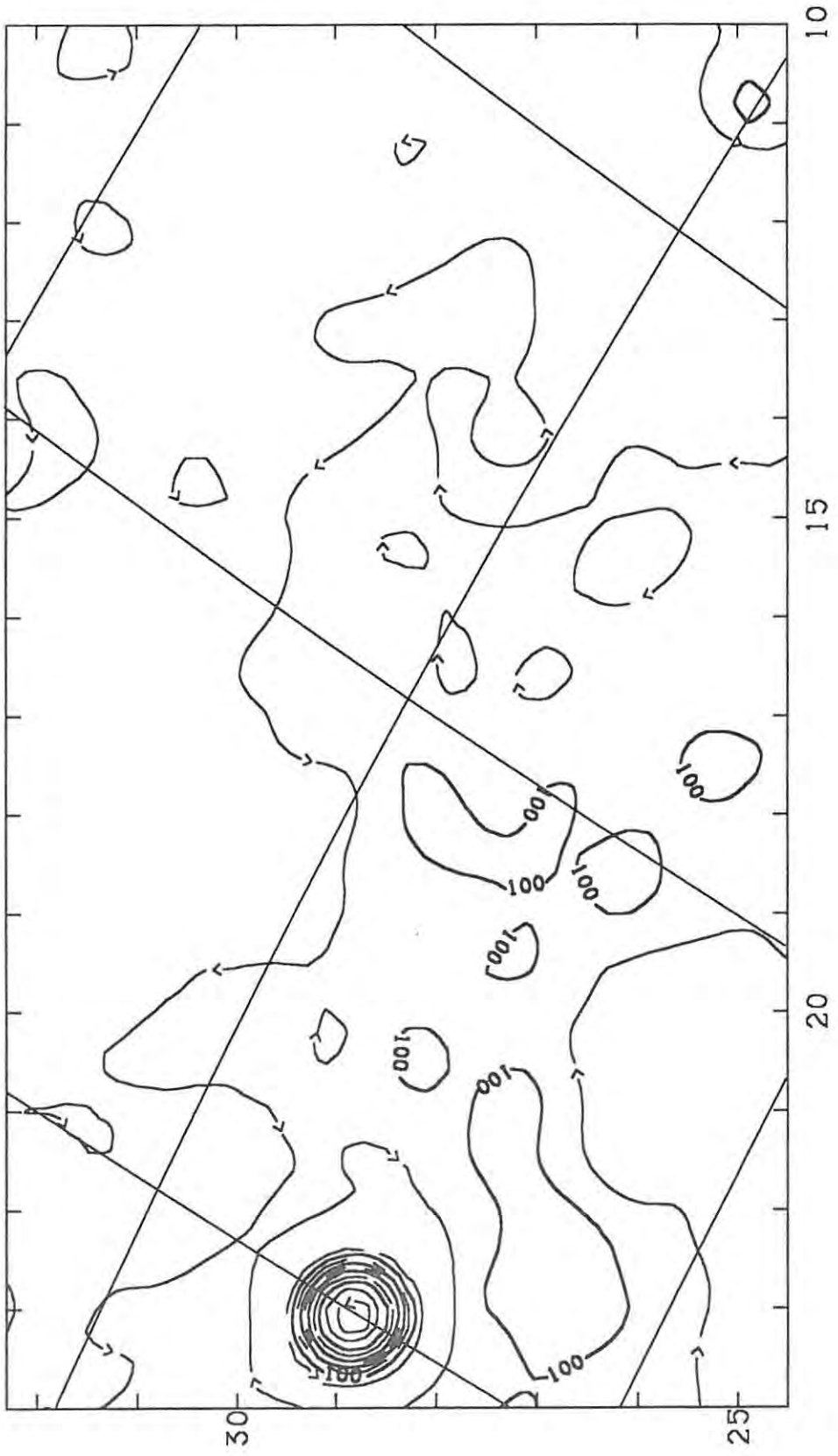

Figure A2.17 - North Polar Spur (Map B6)

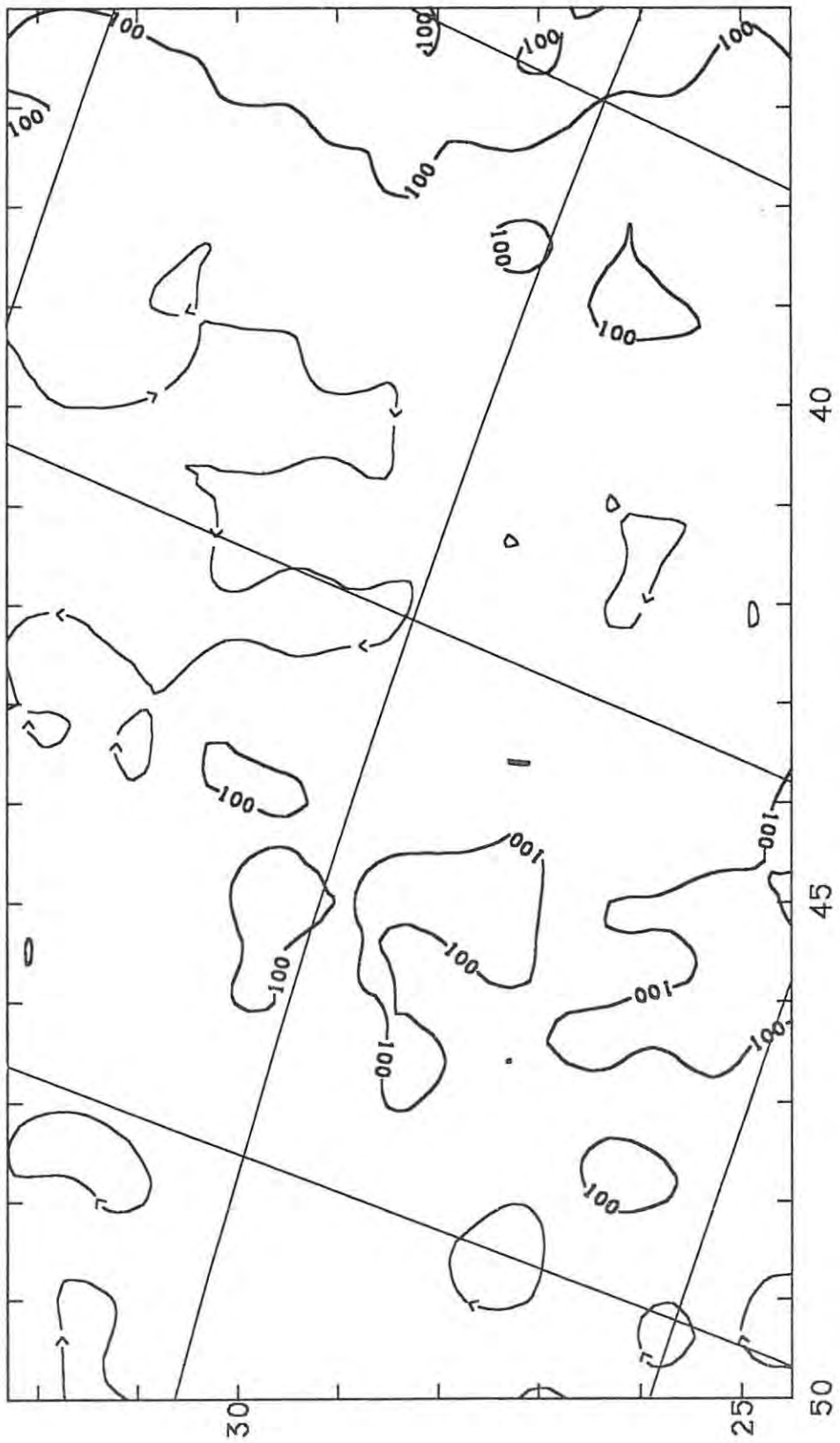

Figure A2.18 - North Polar Spur (Map C6)

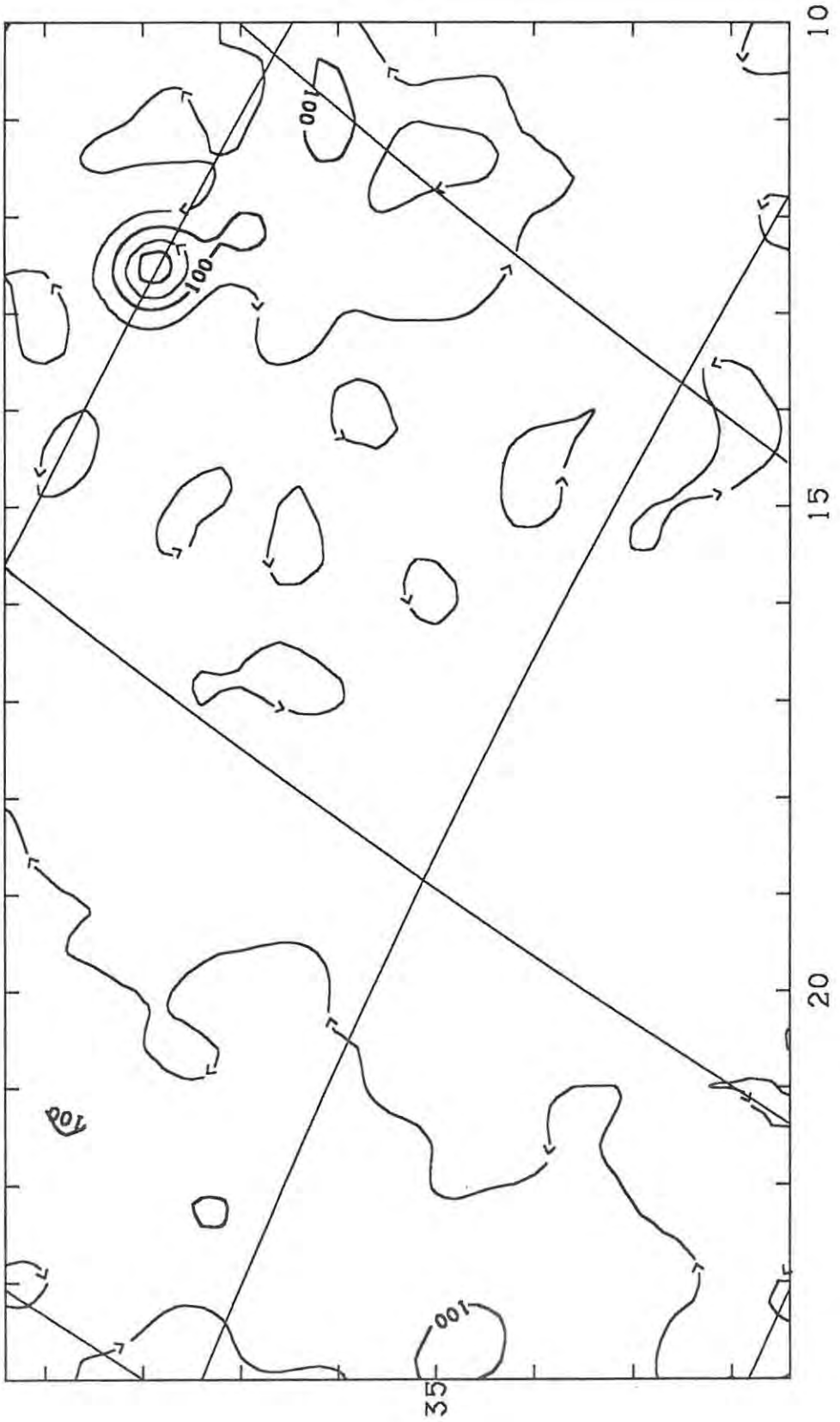

Figure A2.19 - North Polar Spur (Map A7)

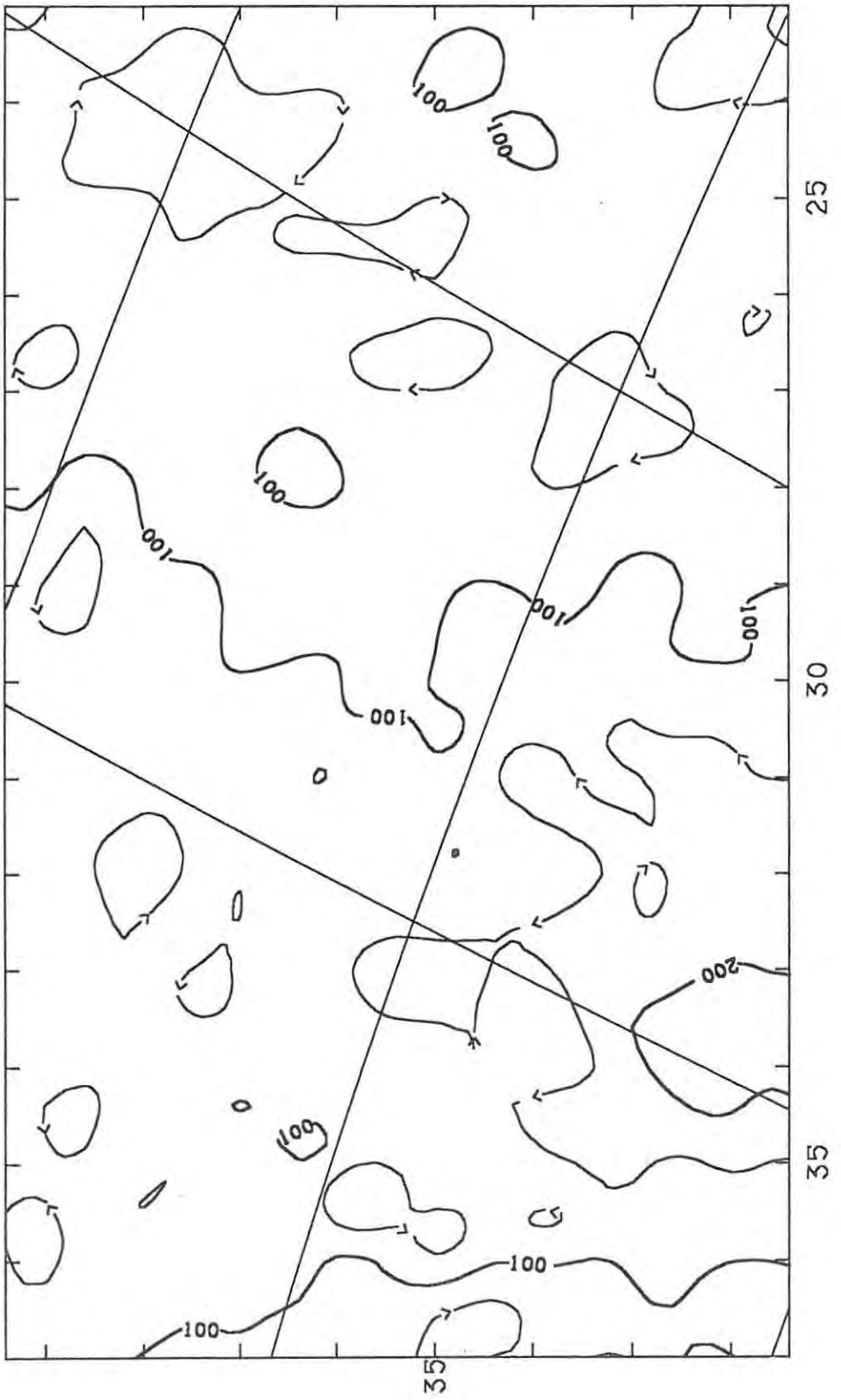

Figure A2.20 - North Polar Spur (Map B7)

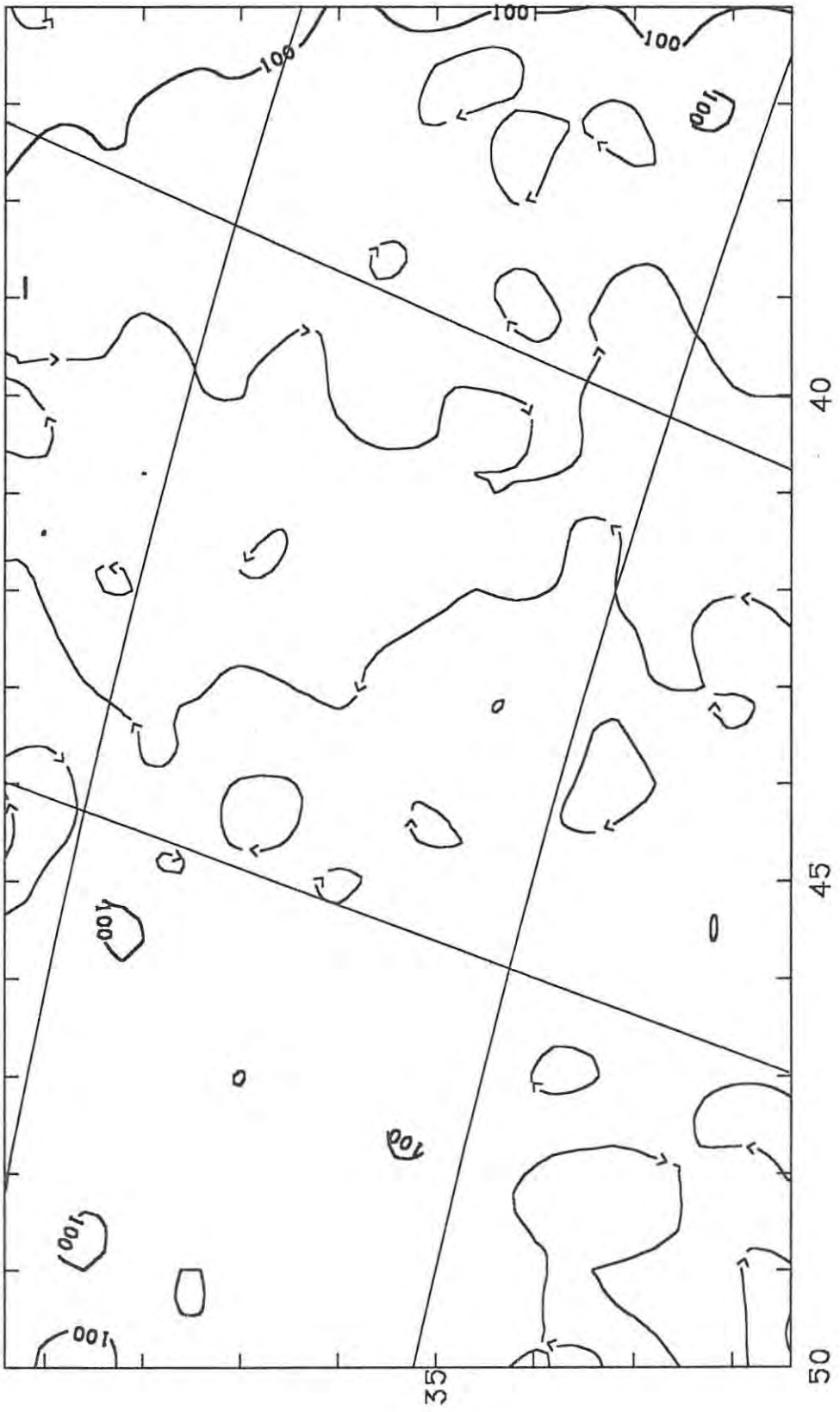

Figure A2.21 - North Polar Spur (Map C7)

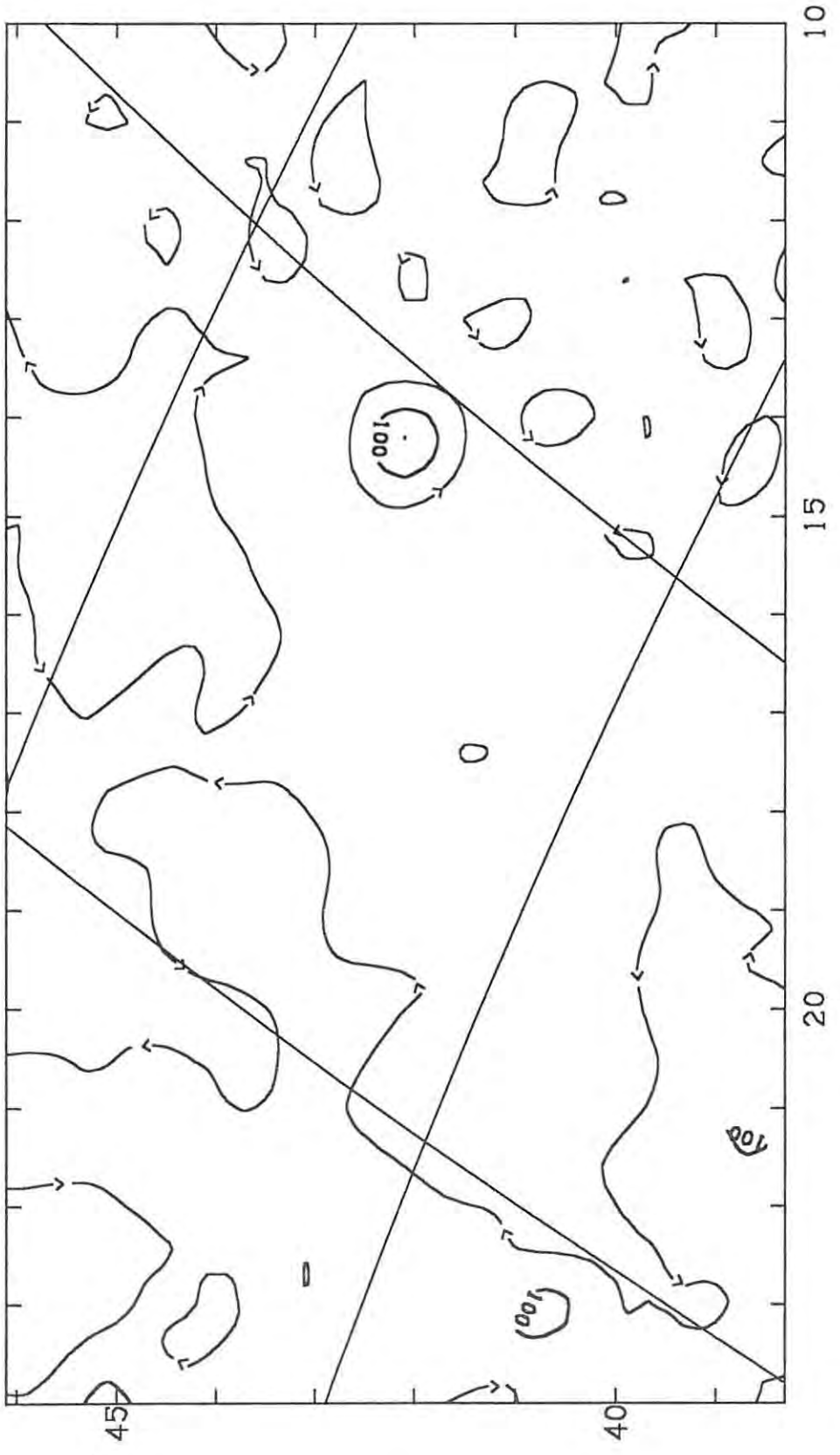

Figure A2.22 - North Polar Spur (Map A8)

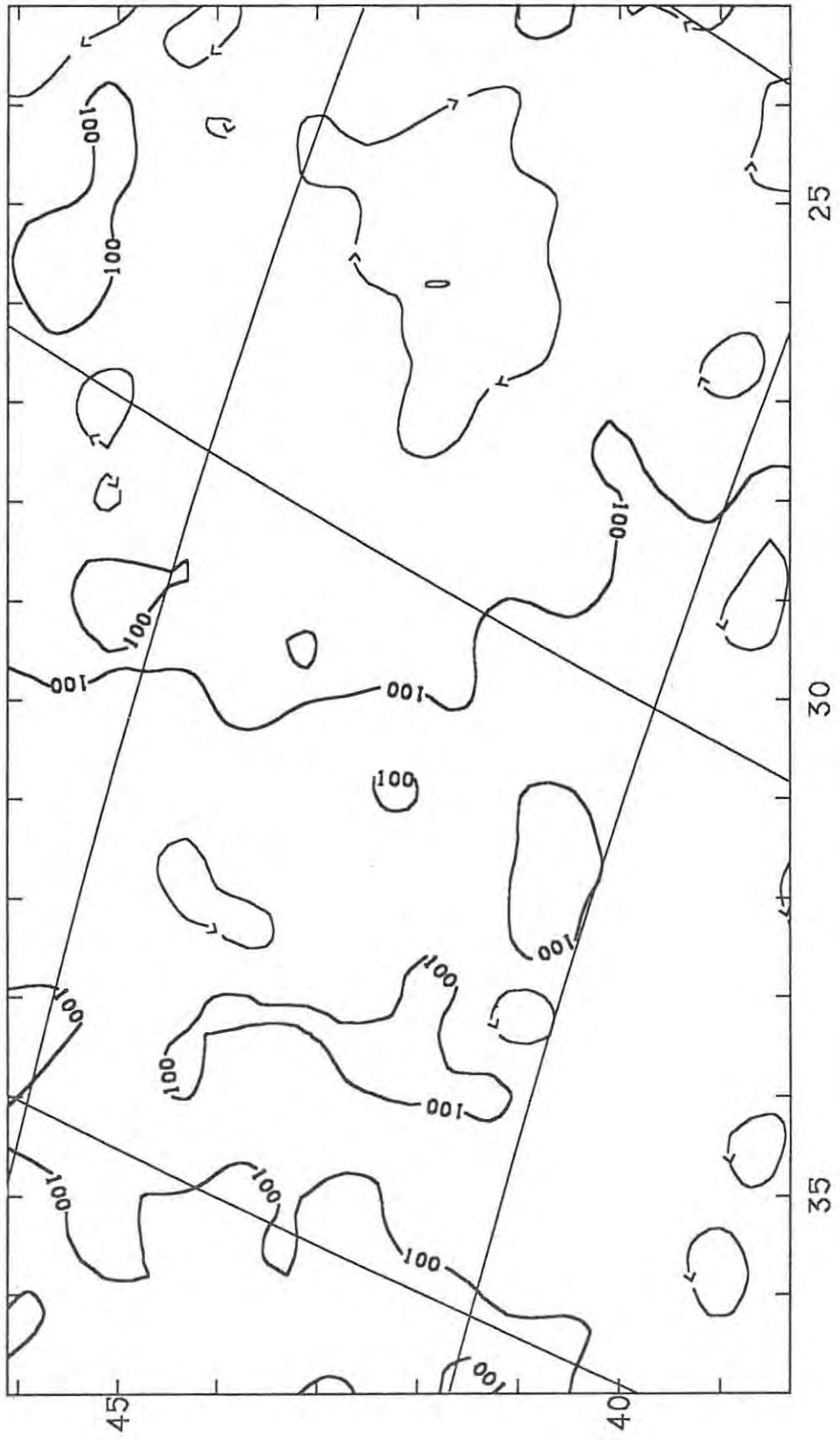

Figure A2.23 - North Polar Spur (Map B8)

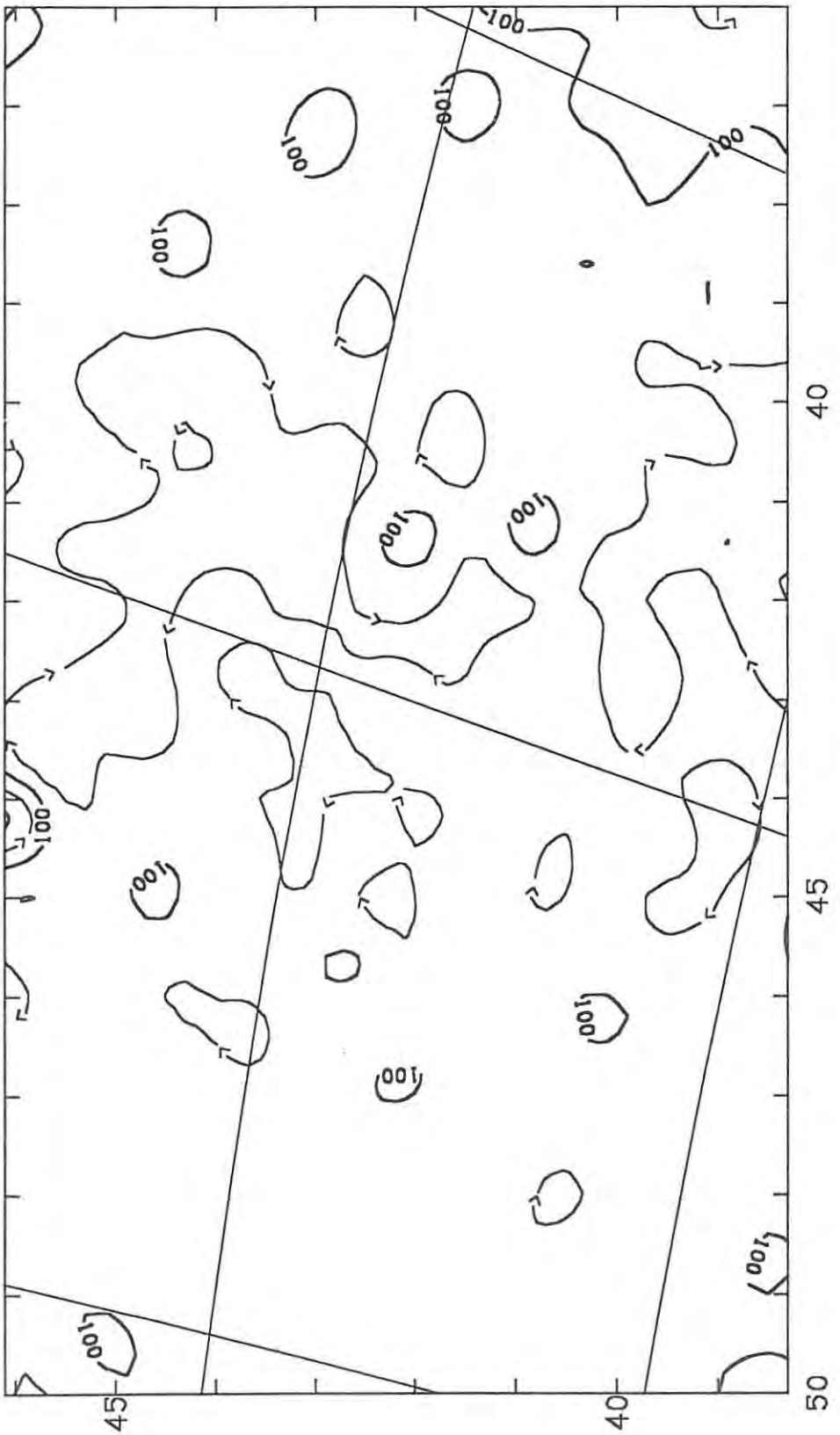

Figure A2.24 - North Polar Spur (Map C8)

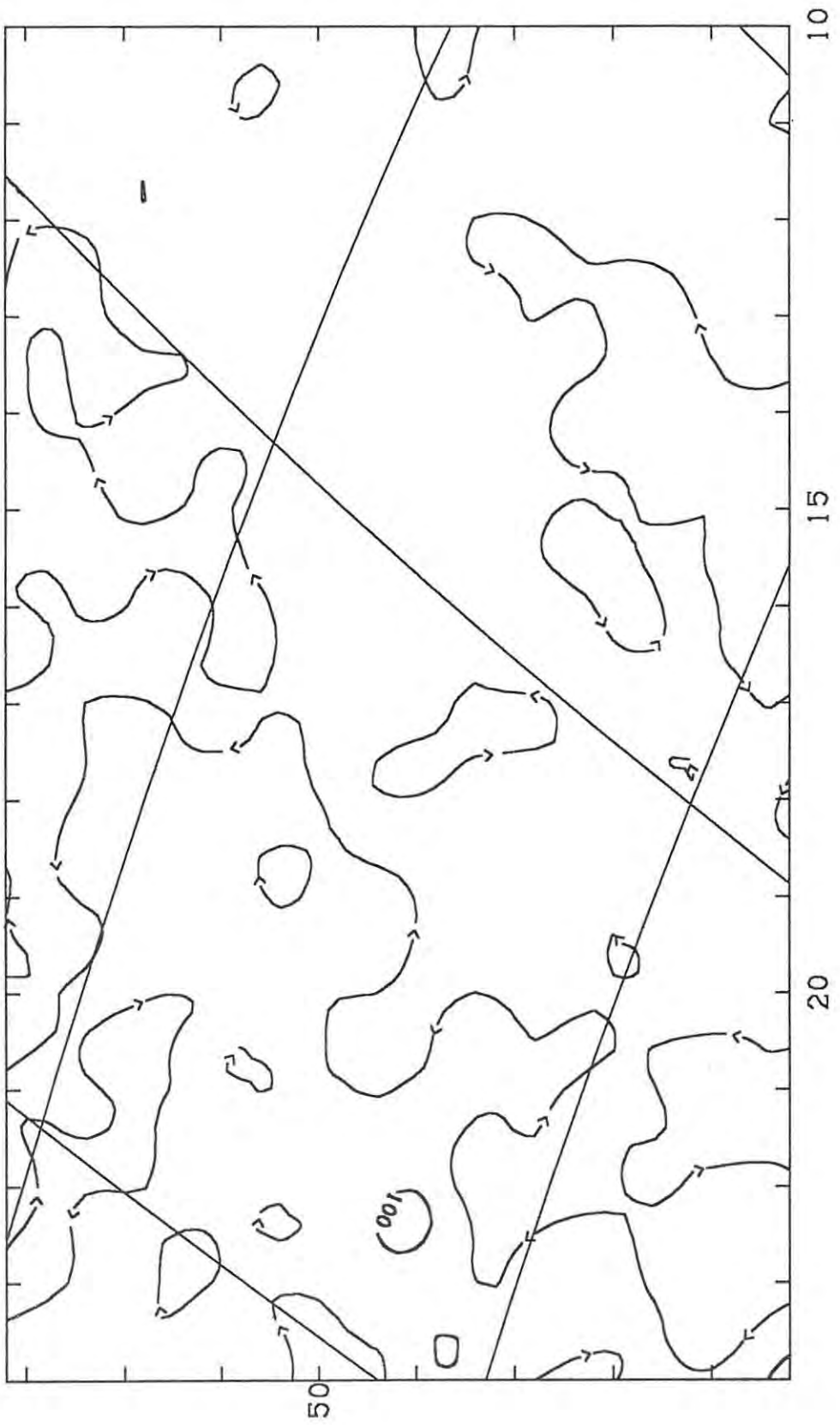

Figure A2.25 - North Polar Spur (Map A9)

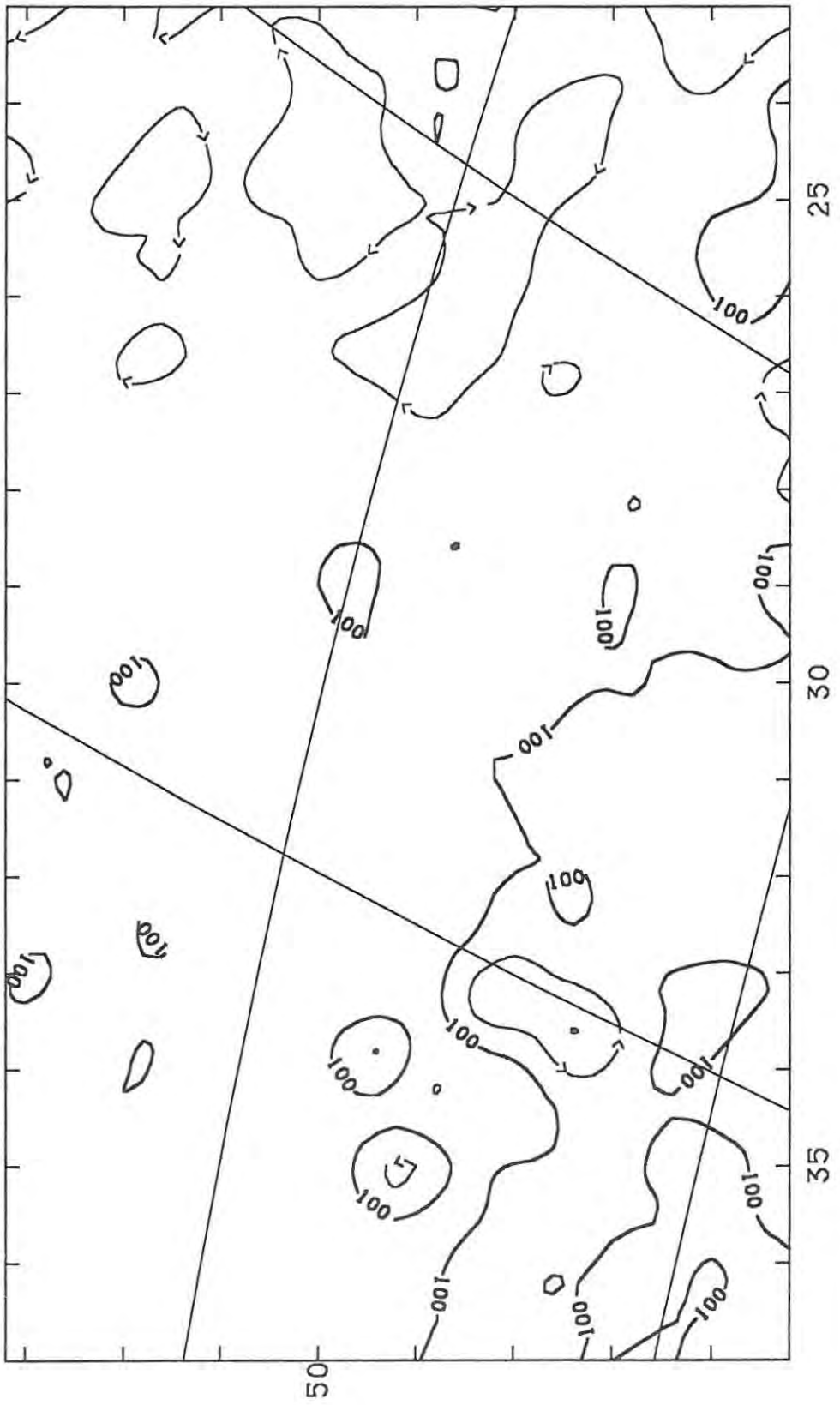

Figure A2.26 - North Polar Spur (Map B9)

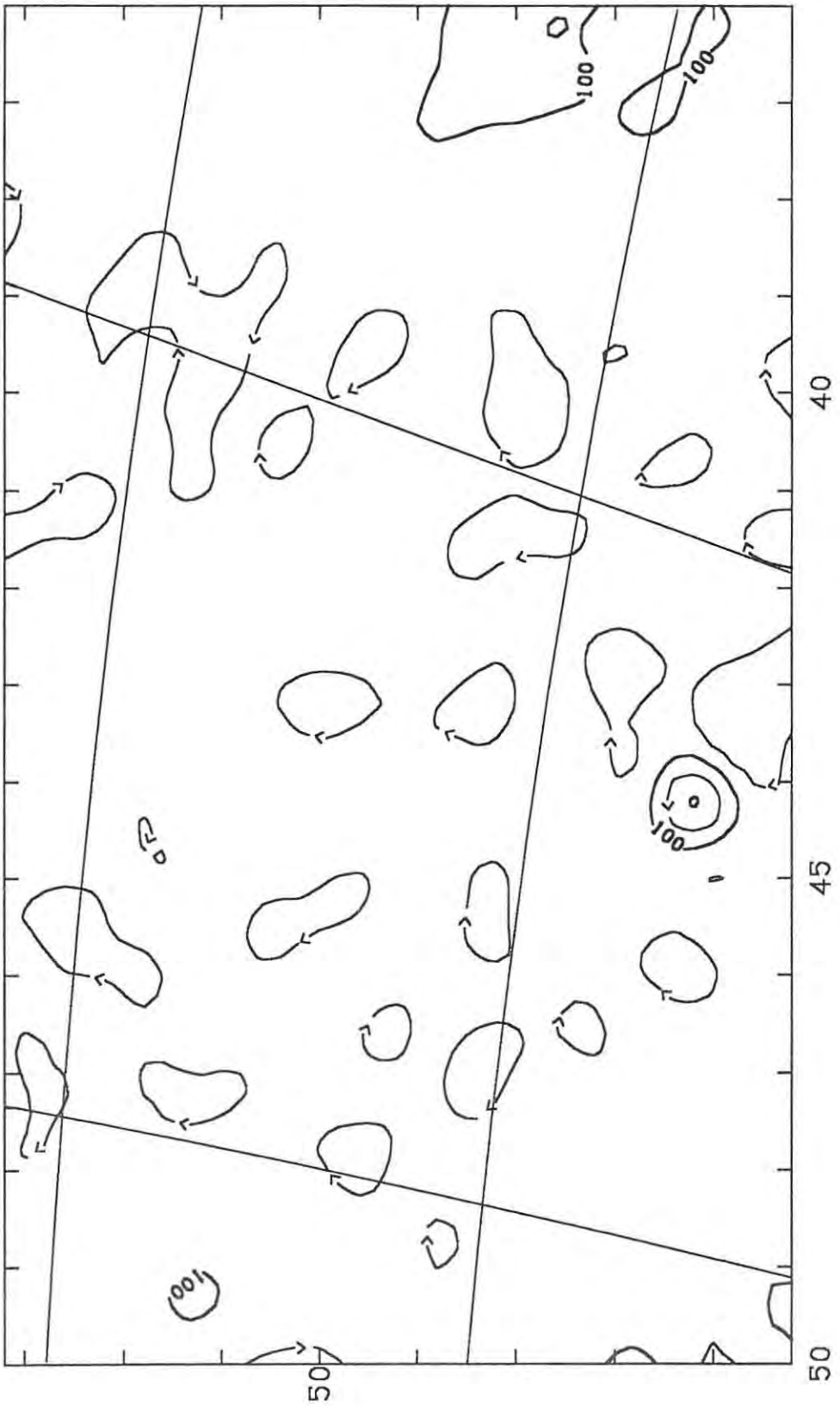

Figure A2.27 - North Polar Spur (Map C9)

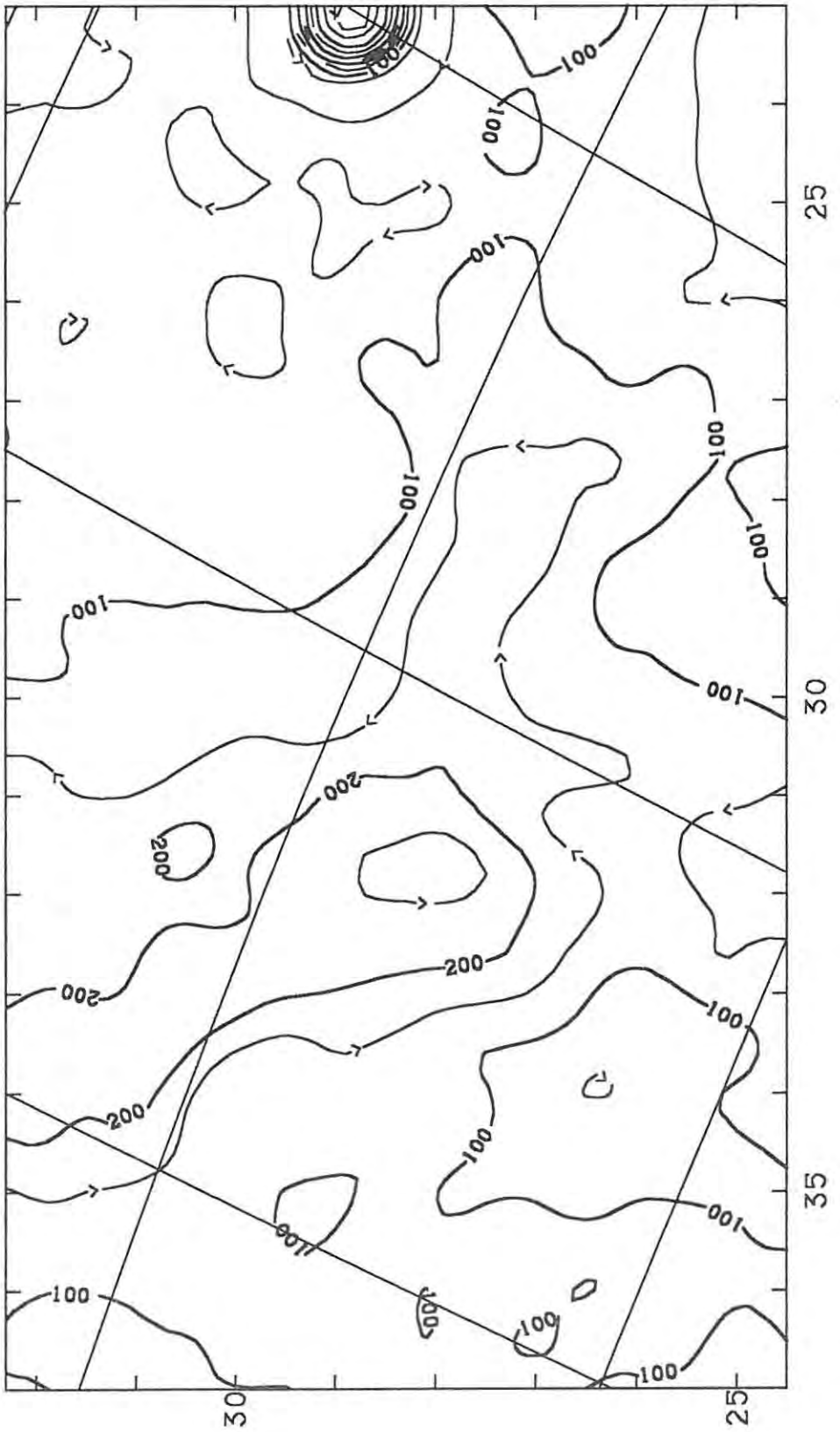

Appendix Three - Calibrators

The contour maps presented in Appendix One represent the measured antenna temperature throughout the region surveyed. As was stated in the preliminary explanation to Appendix One, the beam sensitivity for these maps was 12.26 Jy/K. This means that, in order to convert antenna temperature to flux for any point on the map, the antenna temperature (in Kelvin) must be multiplied by the beam sensitivity to obtain the flux in Janskys. This is essentially only true for point sources since, for an extended source, the angular size of the source needs to be taken into account. This appendix discusses in detail how the beam sensitivity value was obtained.

The flux density of a point source is related to the antenna temperature of the source by the following expression (equation 4.18)

$$S = (2k\Omega_A / R\lambda^2) T_a(max) \qquad \ldots\ldots A3.1$$

where S is the flux density, k is Boltzmann's constant, Ω_A is the full beam solid angle, R is an ohmic-loss factor, λ is the wavelength and $T_a(max)$ is the peak antenna temperature. In this expression, the loss factor and the full beam solid angle are unknown, but both should remain constant for any given source. Therefore, the term in parentheses is a constant (C, say), and equation A3.1 can be written

$$S = C \,.\, T_a(max) \qquad \ldots\ldots A3.2$$

So, if the peak antenna temperature of any point source is known, the corresponding flux density can be calculated from equation A3.2, if a value for the constant C may be found. A method of finding this value is to use a number of point sources as calibrators. These sources must be situated in cold sky (far removed from any large scale structure normally associated with the Galactic disc) and reasonably accurate determinations of their flux densities at other frequencies must be available. From these flux densities, the flux densitys at 2.3 GHz can be found and, using the peak antenna temperatures obtained from the data, a value for C can be found. The constant C is called the beam

sensitivity, and has the units of Janskys per Kelvin (Jy/K).

Five suitable sources were chosen from the data in order to find C. In the following pages, each source will be discussed in detail and, for each source, a value of the beam sensitivity will be found. The average of these beam sensitivities is the value that appears in Appendix One (12.26 Jy/K). The flux densities quoted below are from the Parkes Master Catalogue of Radio Sources (Bolton *et al* 1979) except for the second 408 MHz flux density from the Molonglo Reference Catalogue of Radio Sources (Large *et al* 1981) and the 1400 MHz flux density from Pacholczyk (1978).

Note that the antenna temperatures quoted for each of the sources are the peak temperatures *after* a base surface was removed. This base surface was found in the following way. By taking profiles of a number of point sources (note that point sources are merely any source which is a great deal smaller in angular extent that the half power beam width of the telescope, and not idealized delta functions! Such point sources appear on the contour maps as a series of concentric contours - see chapter 4 for further details) it was noted that the radius to the first null was, in all cases, approximately 0.5°. Side lobes were evident outside of this limit. Taking this value as a standard for all point sources on the map, including the calibrators, a program was written to find the average antenna temperature for an annulus 0.1° wide between 0.4° and 0.5° for each source. These temperatures represented the base surfaces for their respective sources and were subtracted from the peak temperatures to find the corrected antenna temperatures.

Calibrator A

Source Designation	0034-014 (3C 15)
Right Ascension (1950)	$00^h\ 34^m\ 30.8^s$
Declination (1950)	-1° 25′ 38″
Optical Identification	Galaxy
Magnitude (m_v)	15.5
Red Shift	0.0733
Flux at 86 MHz	36 Jy
Flux at 178 MHz	15.8 Jy
Flux at 408 MHz	10.0 Jy
Flux at 408 MHz	9.74 Jy
Flux at 1400 MHz	4.30 Jy
Flux at 1410 MHz	4.1 Jy
Flux at 2650 MHz	2.5 Jy
Flux at 5000 MHz	1.56 Jy

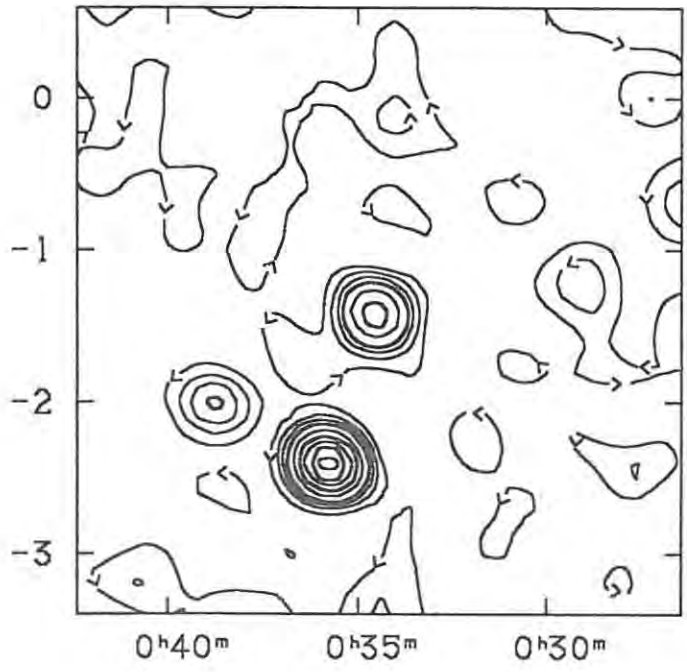

Figure A3.1 - Map of 0034-014.

From the above information, the spectral index was found to be 0.73, resulting in a flux density at 2.3 GHz of 2.82 Jy. The peak antenna temperature was found to be 219.9 mK, and therefore the beam sensitivity is 12.82 Jy/K for this source.

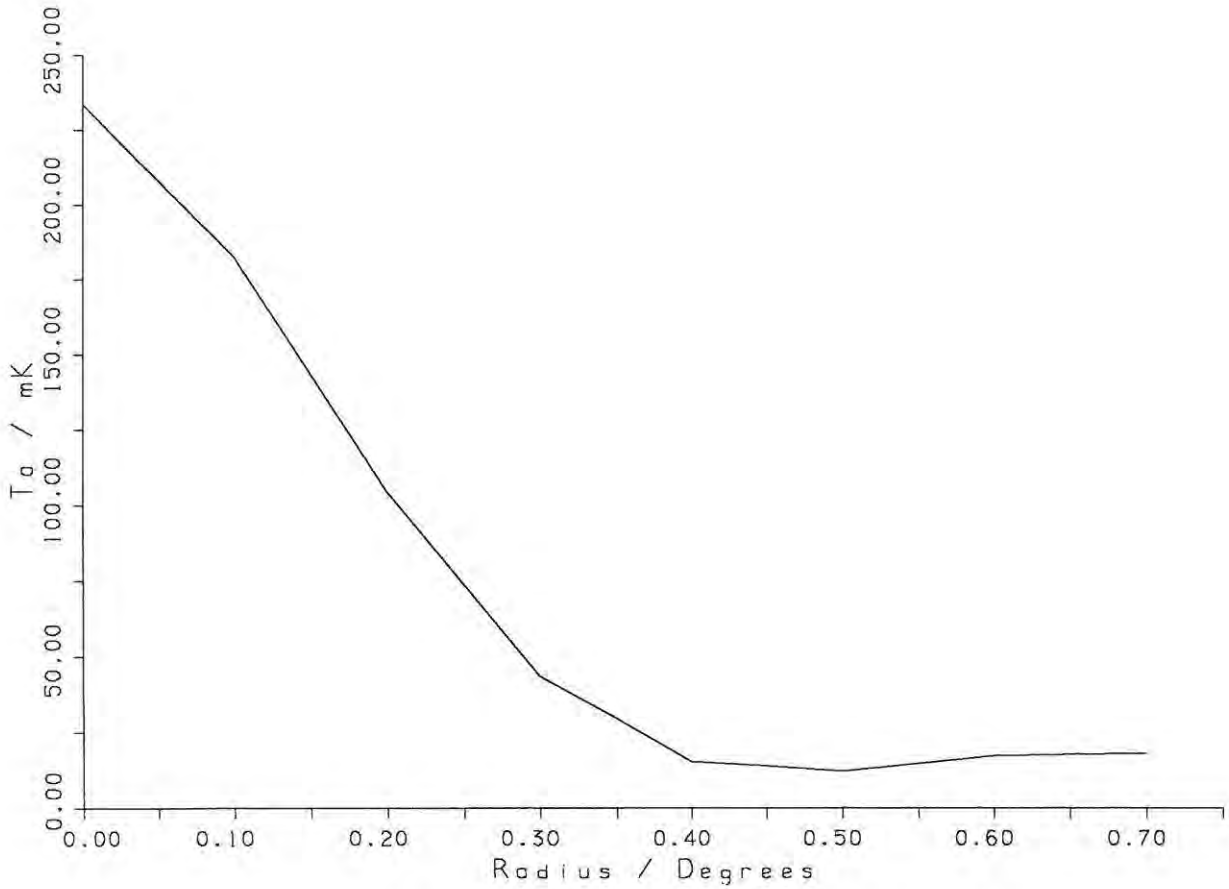

Figure A3.2 - Radial profile of 0034-014. The first null of the profile has occured at 0.5°, just before contamination by the source to the south (0035-024).

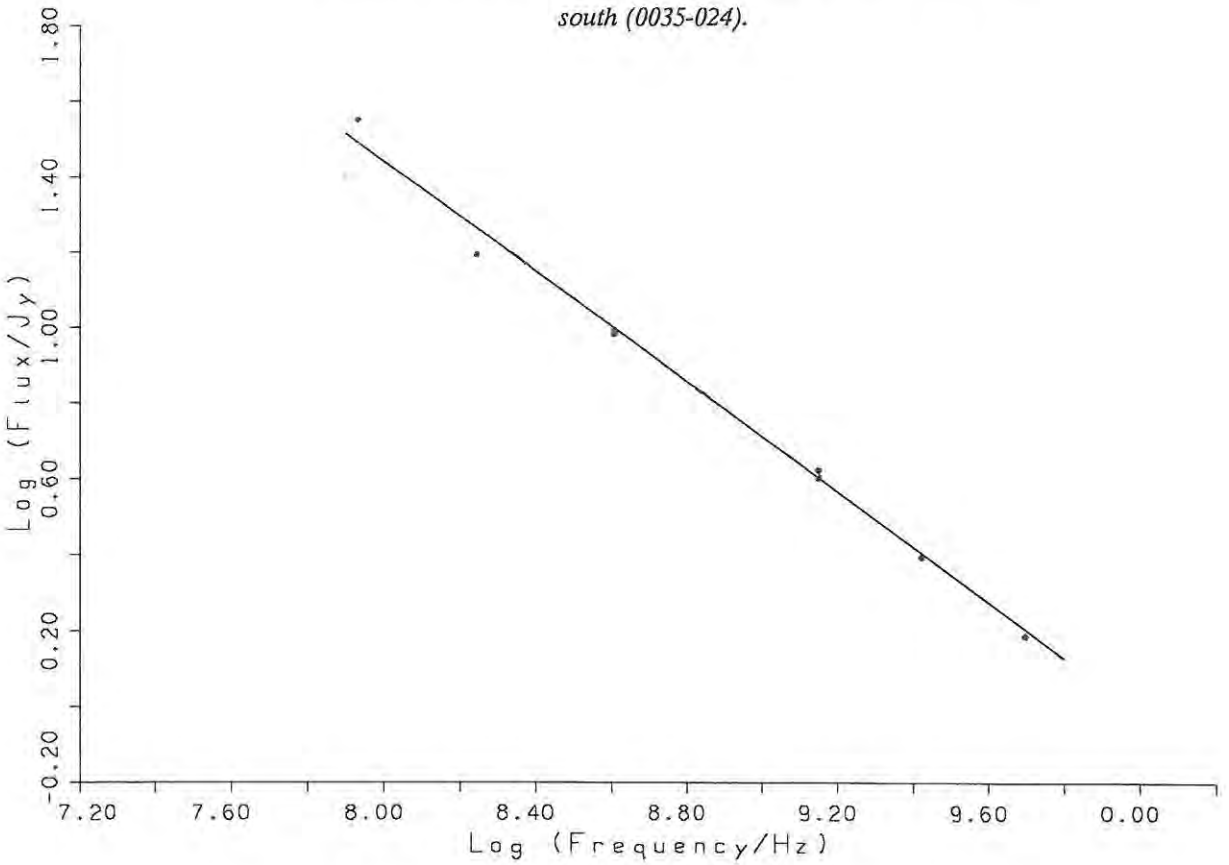

Figure A3.3 - Spectrum of 0034-014.

Calibrator B

Source Designation	0035-024 (3C 17)
Right Ascension (1950)	$00^h\ 35^m\ 47.1^s$
Declination (1950)	-2° 24′ 08″
Optical Identification	Galaxy
Magnitude (m_v)	18.5
Red Shift	0.2201
Flux at 86 MHz	46
Flux at 178 MHz	20.0
Flux at 408 MHz	13.1
Flux at 408 MHz	16.53
Flux at 1400 MHz	6.25
Flux at 1410 MHz	6.1
Flux at 2650 MHz	4.1
Flux at 5000 MHz	2.65

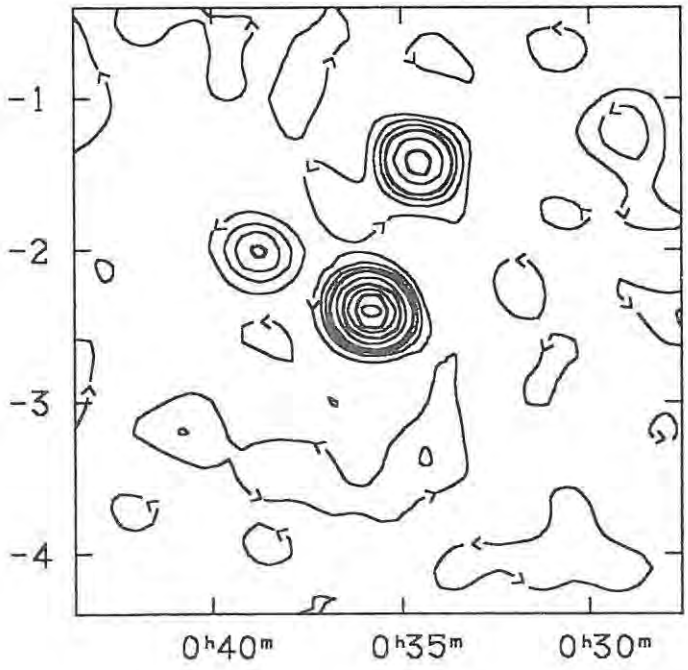

Figure A3.4 - Map of 0035-024.

From the above information, the spectral index was found to be 0.66, resulting in a flux density at 2.3 GHz of 4.47 Jy. The peak antenna temperature was found to be 364.7 mK, and therefore the beam sensitivity is 12.26 Jy/K for this source.

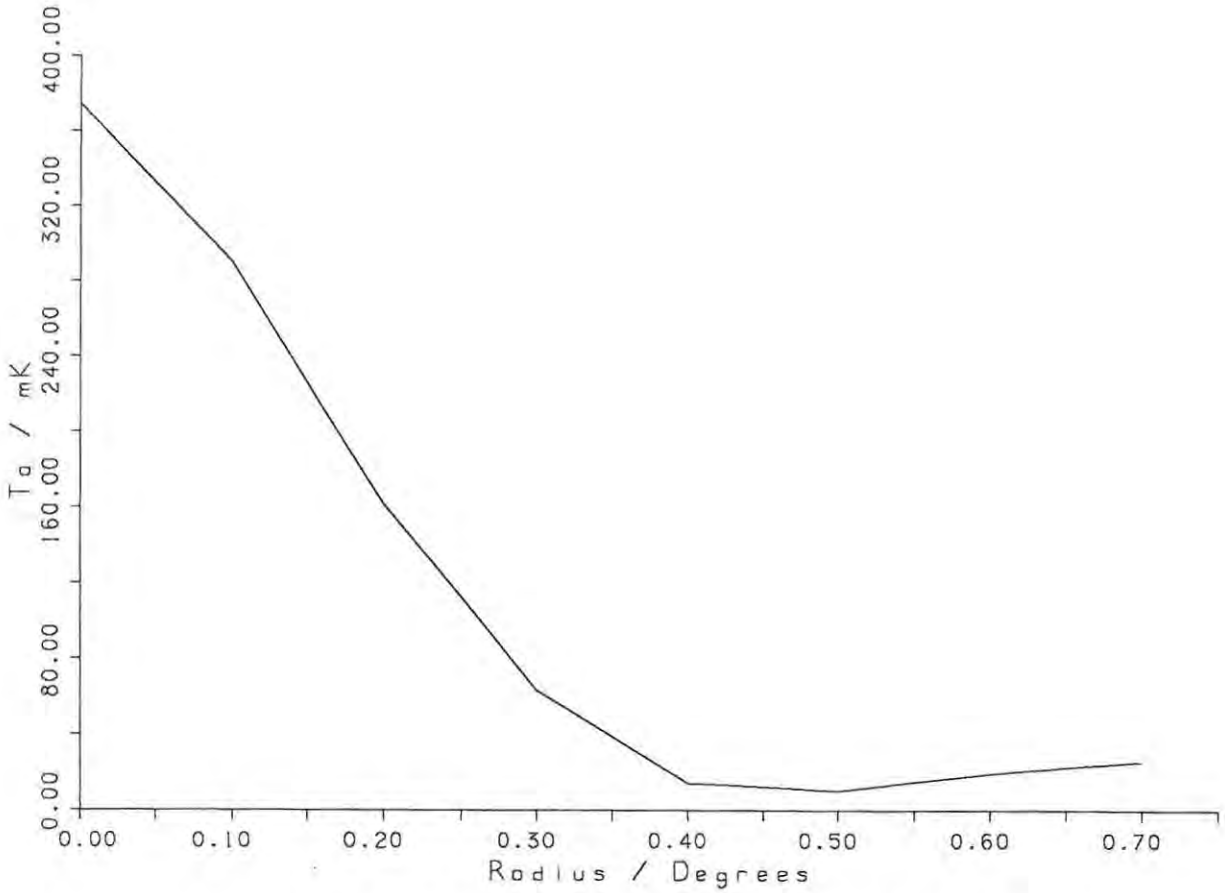

Figure A3.5 - Radial profile of 0035-024. The first null of the profile has occured at 0.5°, just before contamination by the source to the north (0034-014).

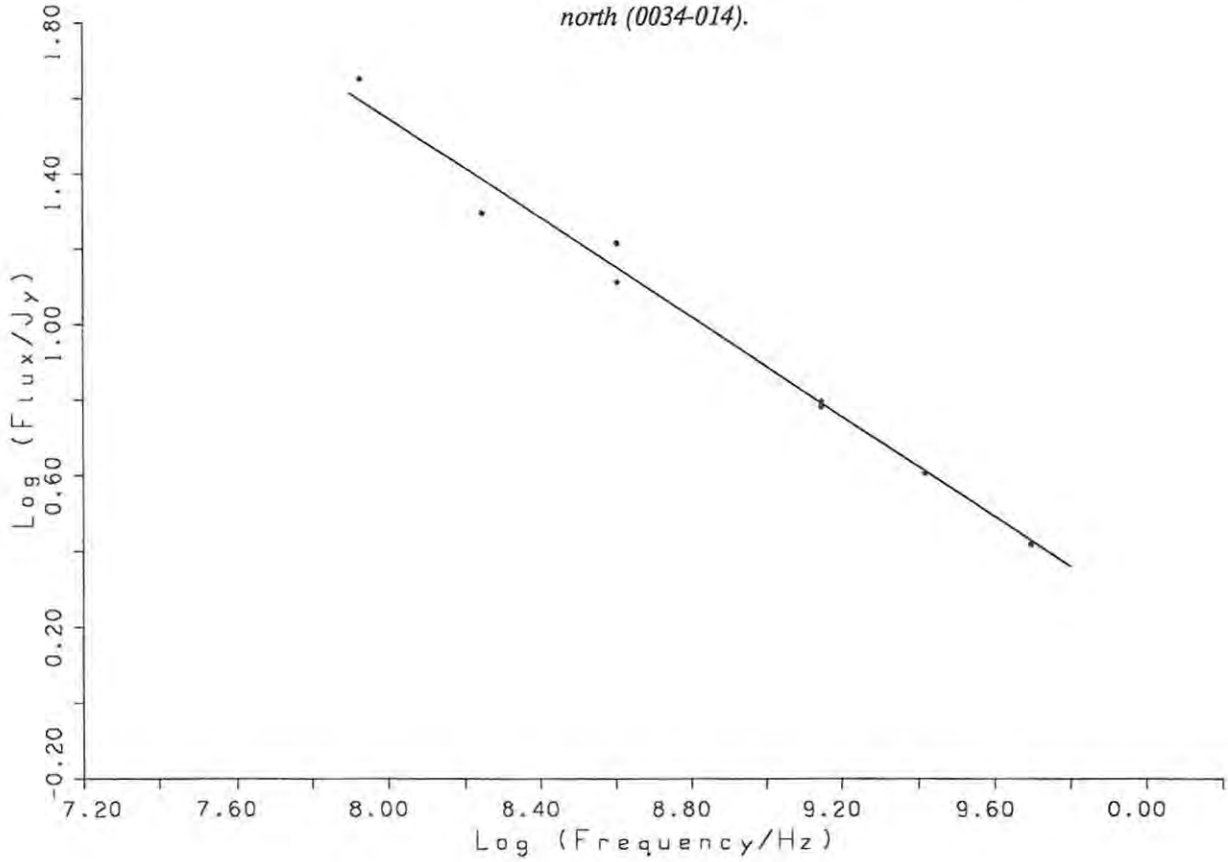

Figure A3.6 - Spectrum of 0035-024.

Calibrator C

Source Designation	0038+097 (3C 18)
Right Ascension (1950)	$00^h\ 38^m\ 14.8^s$
Declination (1950)	+9° 26′ 17″
Optical Identification	Galaxy
Magnitude (m_v)	18.5
Red Shift	
Flux at 86 MHz	37
Flux at 178 MHz	19.8
Flux at 408 MHz	12.2
Flux at 408 MHz	11.54
Flux at 1400 MHz	4.26
Flux at 1410 MHz	4.7
Flux at 2650 MHz	2.8
Flux at 5000 MHz	1.62

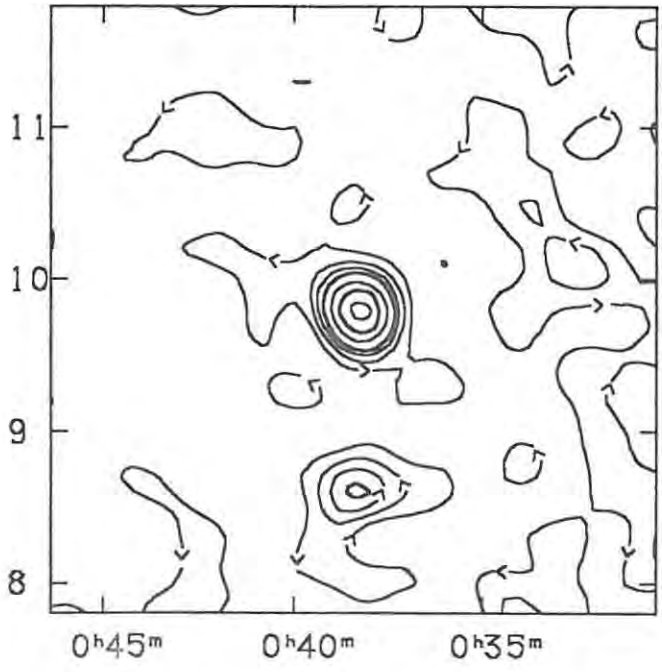

Figure A3.7 - Map of 0038+097.

From the above information, the spectral index was found to be 0.76, resulting in a flux density at 2.3 GHz of 2.95 Jy. The peak antenna temperature was found to be 259.7 mK, and therefore the beam sensitivity is 11.36 Jy/K for this source.

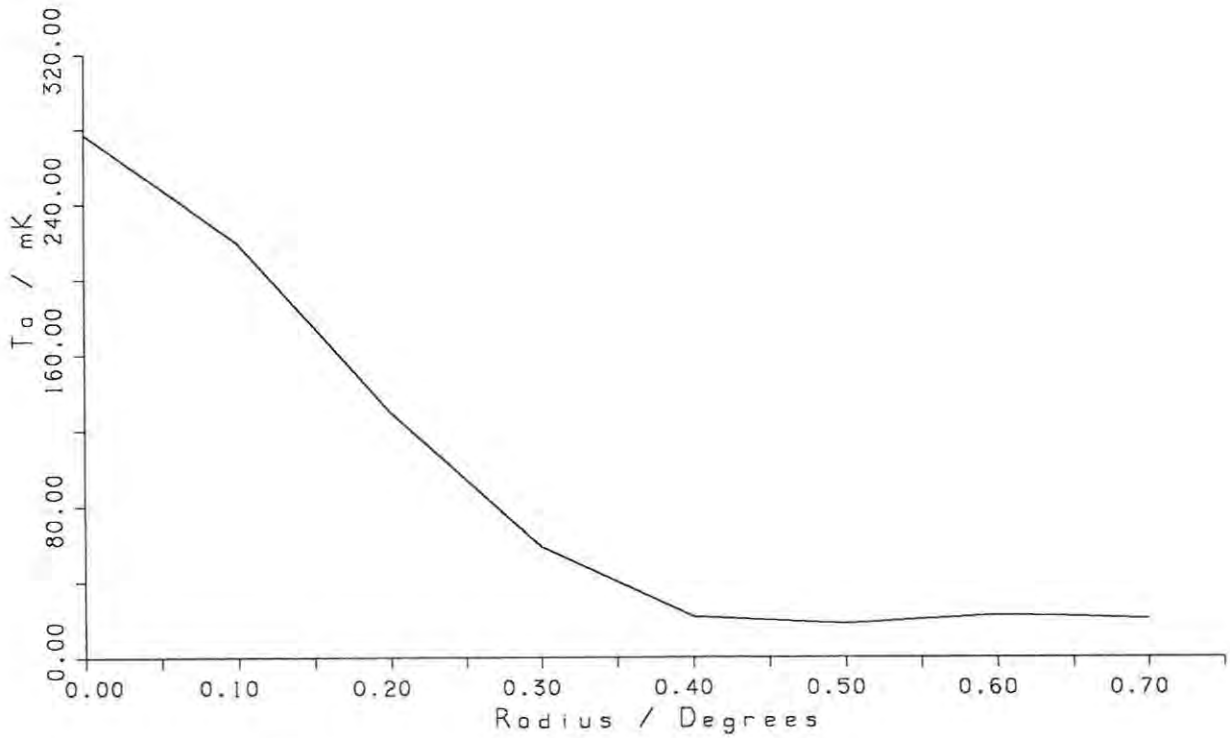

Figure A3.8 - Radial profile of 0038+097. The first null of the profile has occured at 0.5°, and the first side lobe is clearly present.

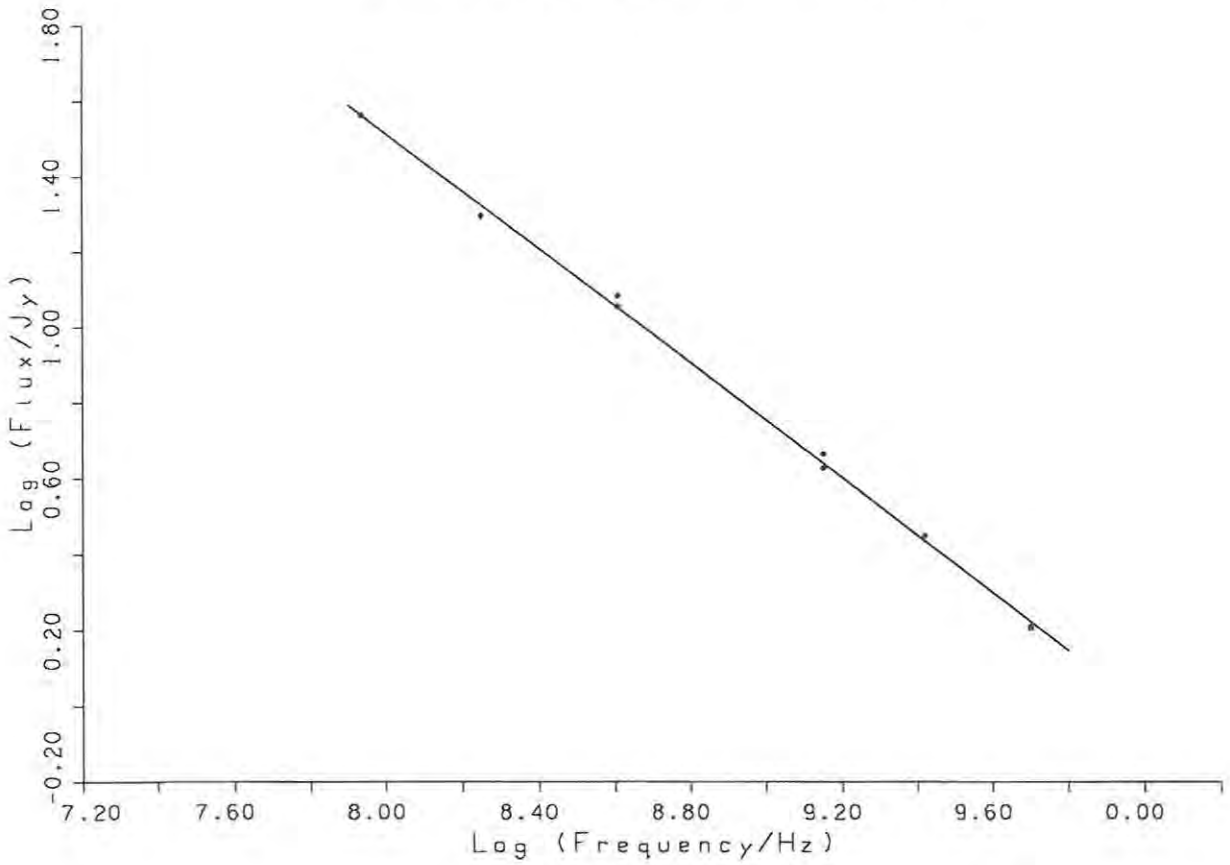

Figure A3.9 - Spectrum of 0038+097.

Calibrator D

Source Designation	0055-016 (3C 29)
Right Ascension (1950)	$00^h\ 55^m\ 01.6^s$
Declination (1950)	-1° 39′ 44″
Optical Identification	Galaxy
Magnitude (m_v)	13.0
Red Shift	0.0450
Flux at 86 MHz	33
Flux at 178 MHz	15.1
Flux at 408 MHz	12.1
Flux at 408 MHz	10.88
Flux at 1400 MHz	5.22
Flux at 1410 MHz	5.4
Flux at 2650 MHz	3.6
Flux at 5000 MHz	2.58

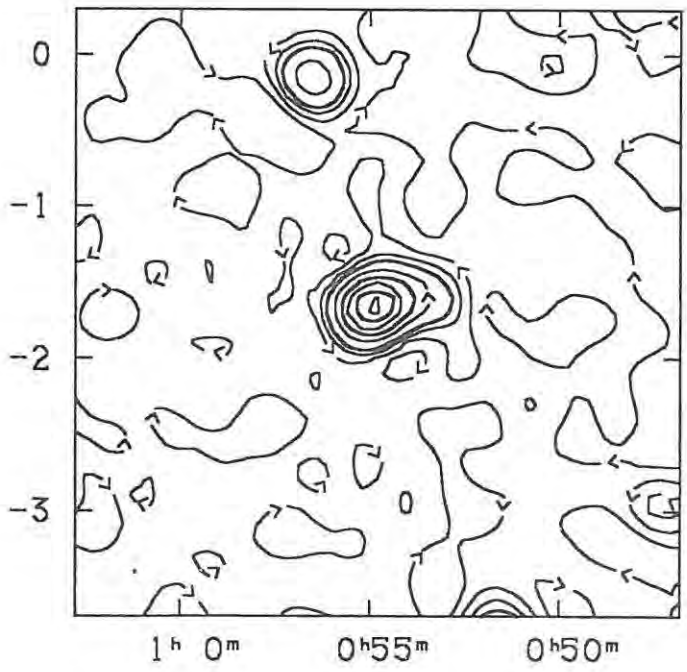

From the above information, the spectral index was found to be 0.60, resulting in a flux density at 2.3 GHz of 4.07 Jy. The peak antenna temperature was found to be 315.9 mK, and therefore the beam sensitivity is 12.88 Jy/K for this source.

Figure A3.10 - Map of 0055-016.

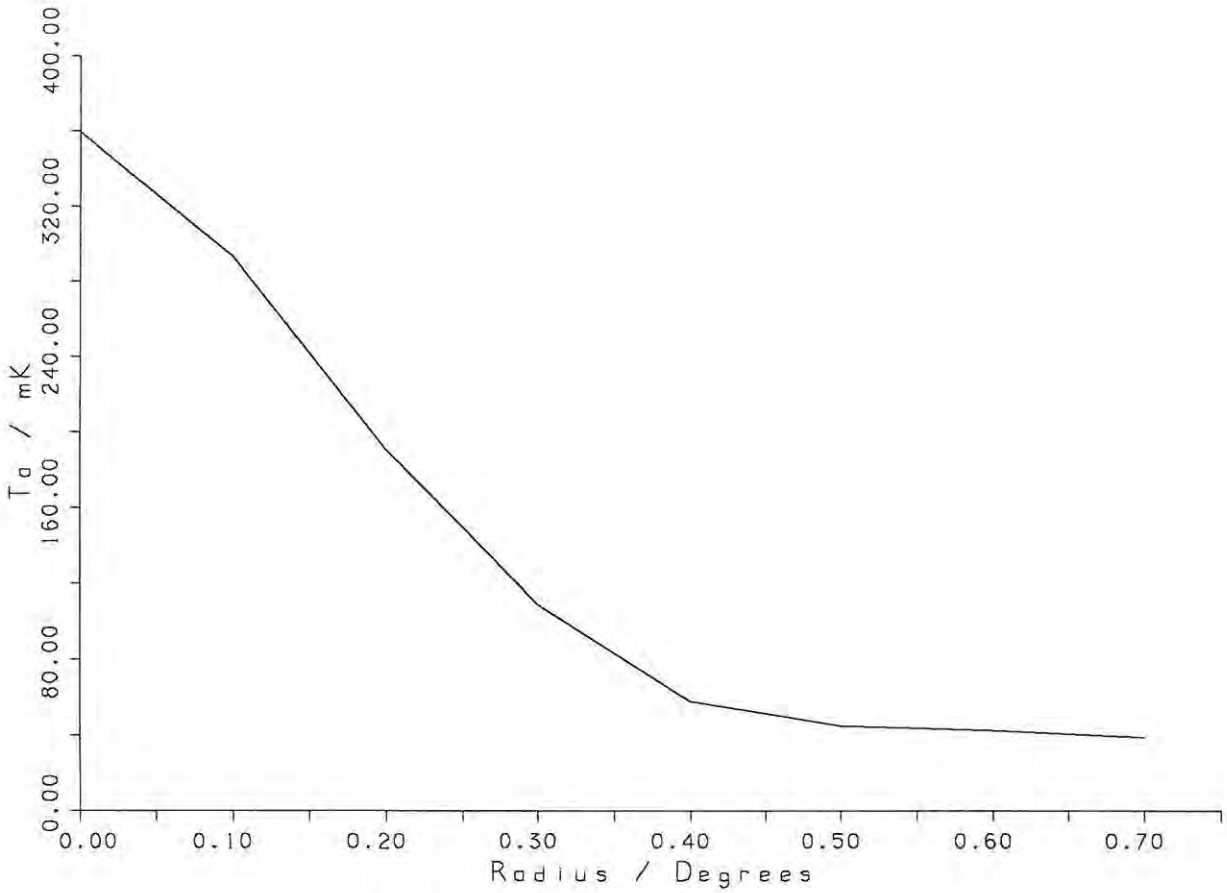

Figure A3.11 - Radial profile of 0055-016. The first null of the profile has occured at 0.5°, but is distorted slightly due to the fact that the source is not circularly symmetric.

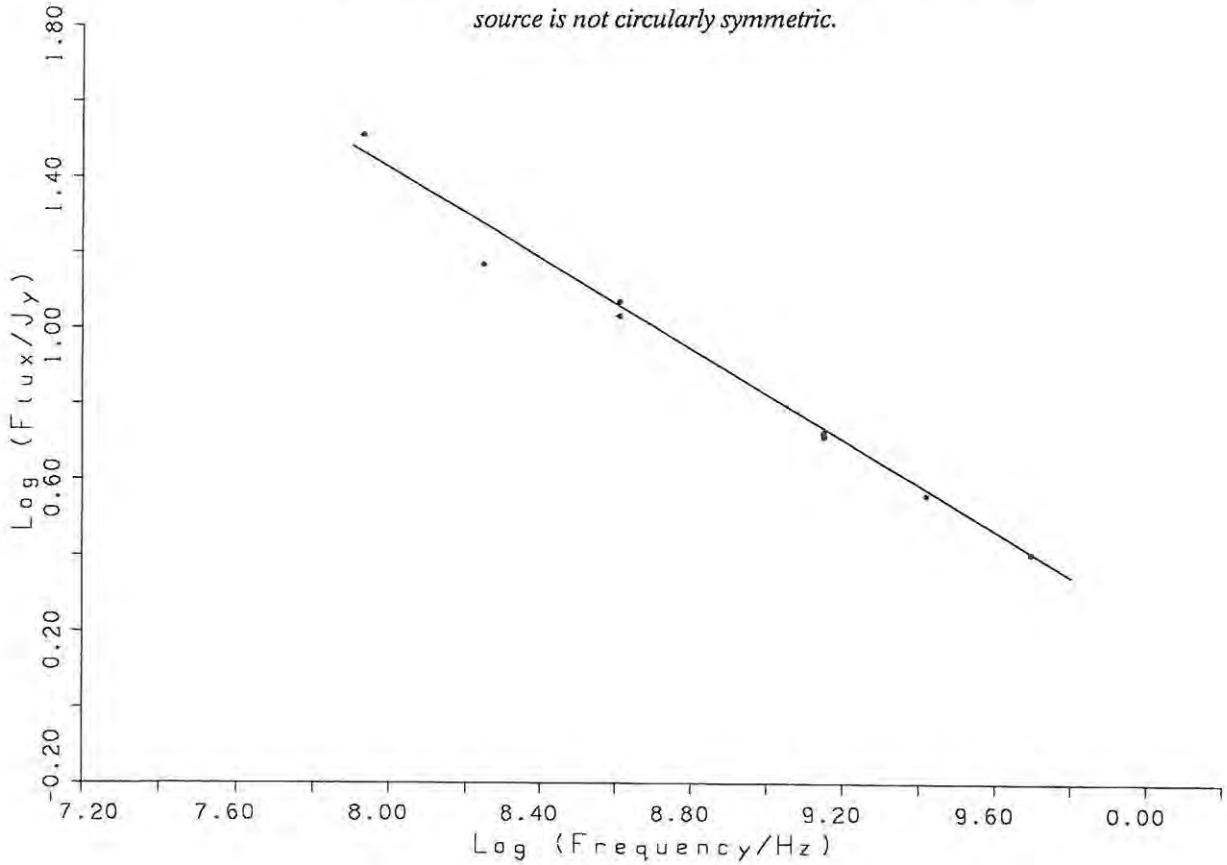

Figure A3.12 - Spectrum of 0055-016.

Calibrator E

Source Designation	0218-021
Right Ascension (1950)	$02^h\ 18^m\ 21.7^s$
Declination (1950)	-2° 10′ 40″
Optical Identification	Galaxy.
Magnitude (m_v)	18.5
Red Shift	0.20
Flux at 86 MHz	34
Flux at 178 MHz	19.1
Flux at 408 MHz	12.4
Flux at 408 MHz	11.77
Flux at 1400 MHz	3.32
Flux at 1410 MHz	3.54
Flux at 2650 MHz	1.70
Flux at 5000 MHz	0.80

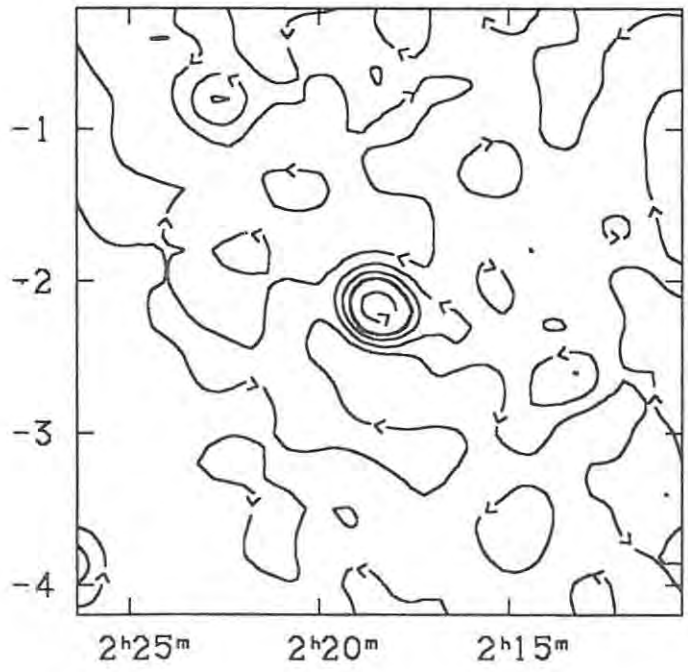

Figure A3.13 - Map of 0218-021.

From the above information, the spectral index was found to be 0.93, resulting in a flux density at 2.3 GHz of 1.97 Jy. The peak antenna temperature was found to be 164.7 mK, and therefore the beam sensitivity is 11.96 Jy/K for this source.

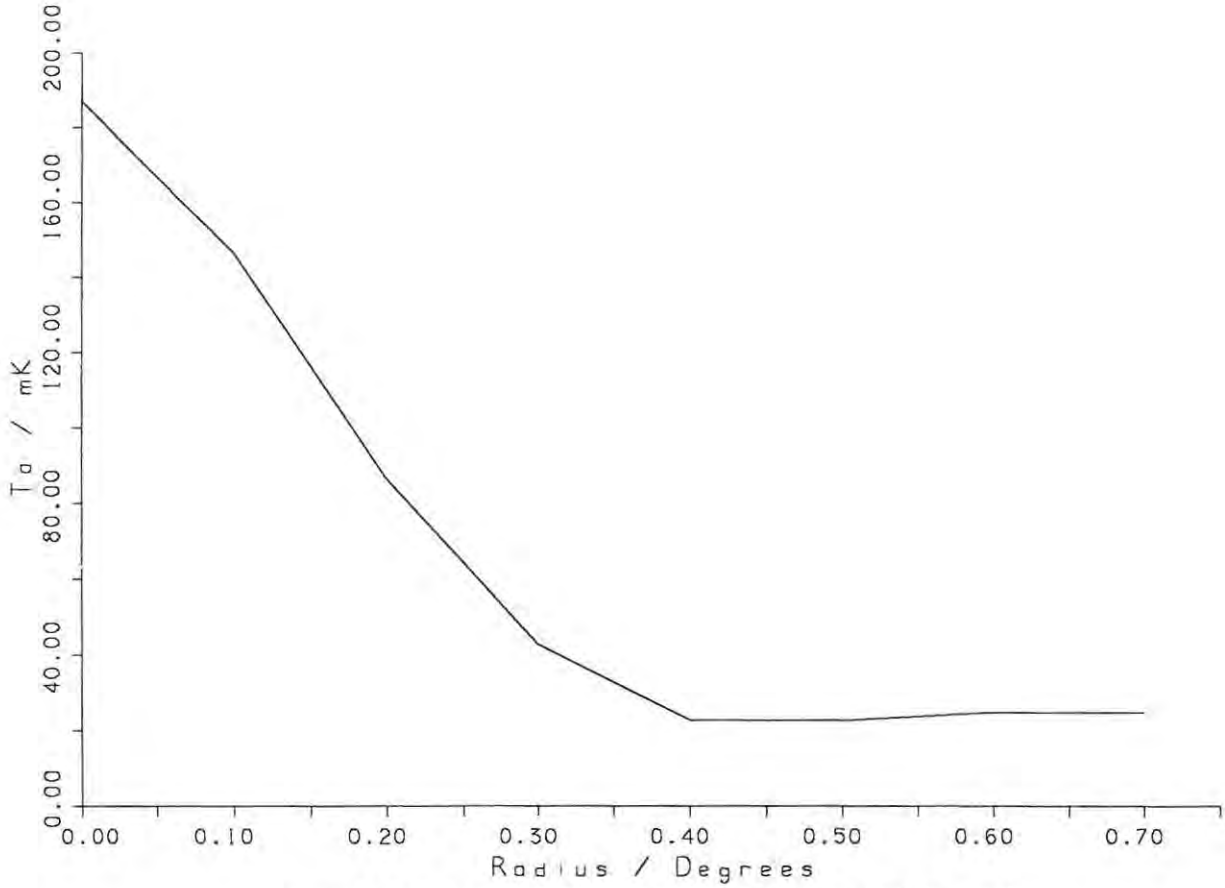

Figure A3.14 - Radial profile of 0218-021. The first null of the profile has occured at either 0.4° or 0.5°. The first side lobe is slightly evident.

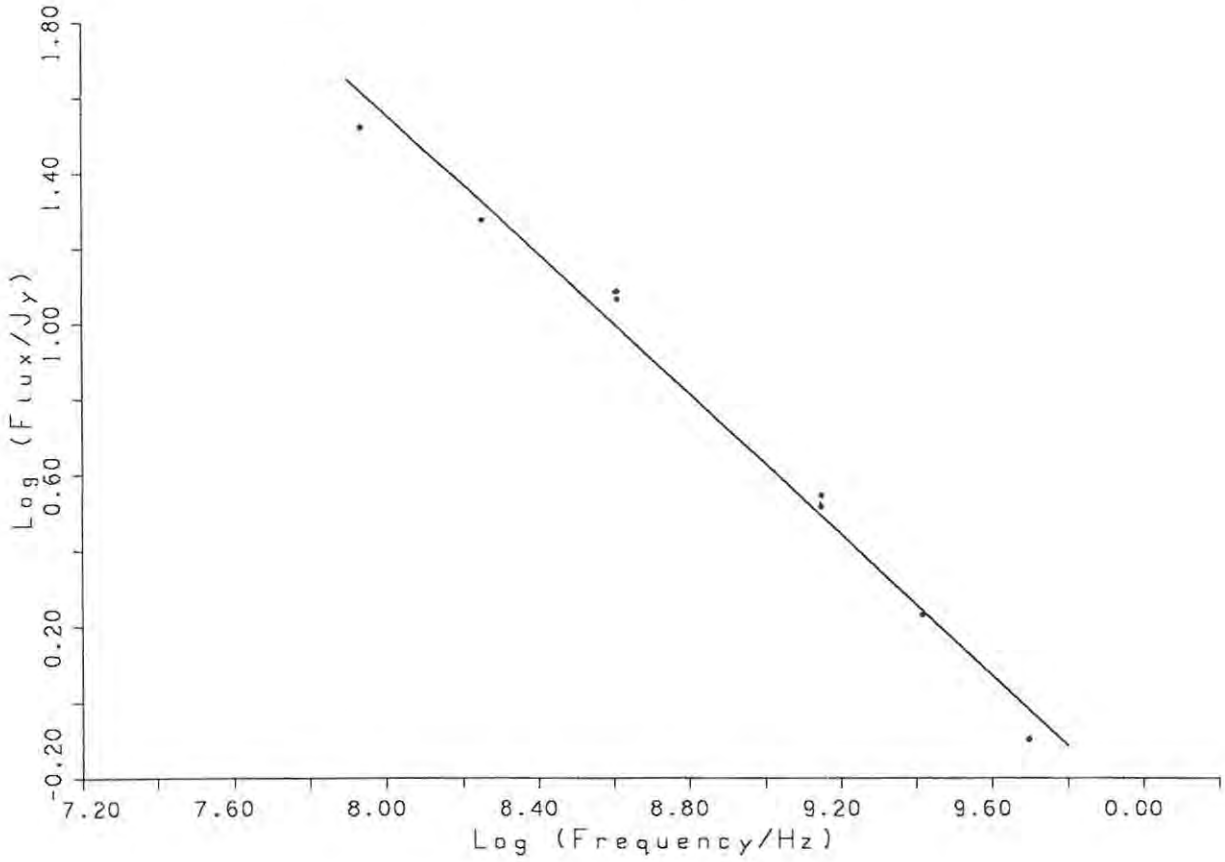

Figure A3.15 - Spectrum of 0218-021.

Appendix Four - Source List

The following pages contain a listing of all the "point sources" in the maps of Appendix One. This listing was compiled in the following manner:

A routine was written which searched sequentially through the data to find peaks with antenna temperatures greater than zero. If a higher peak was found to be situated less than 0.5 degrees from any one peak, then the routine preferentially chose the higher peak, and the lower peak was not included in the listing. Once a source was located, the routine then subtracted a base surface (see Appendix Three) and measured the resulting peak antenna temperature. This peak temperature was then multiplied by the beam sensitivity factor, discussed in Appendix Three, to find the flux density of the source. If the resulting flux density was found to be lower than 0.5 Jy, the source was not included in the listing.

Column 1 (IAU Name) - Note that these are not necessarily the officially recognized names or designations for the sources. These names were "calculated" directly from the measured positions of the sources in the 2.3 GHz data set. In a vast majority of the cases, however, they are within one or two digits of the equivalent Molonglo and Parkes source names.

Column 2 (X) - This column contains the right ascensions of the sources in degrees and tenths of a degree.

Column 3 (Y) - This column contains the declinations of the sources in degrees and tenths of a degree.

Column 4 (Ta) - The absolute peak antenna temperature (before the subtraction of any base surface) is quoted for each source. Note that these temperatures are in mK.

Column 5 (Flux) - This column contains the calculated flux density of the sources in Janskys. Note

that the routine had no way of discerning between point sources and extended sources, so there will be a number of extended sources included in this listing. No attempt has been made to remove such sources by hand or even indicate the presence of such a source. Note also that sources situated in or close to the Galactic plane are likely to be inaccurate due to the effect of other nearby sources and the Galactic disc emission itself.

The listing contains 1105 sources in order of increasing right ascension, starting from $13^h\ 59^m$, proceeding through $00^h\ 00^m$, and ending at $02^h\ 26^m$.

Table A4.1 - Source listing.

IAU Name	X / deg	Y / deg	Ta / mK	Flux / Jy	Base
1359-114	209.8	-11.4	139.2	1.15	45.4
1359-149	209.9	-14.9	94.2	0.59	46.2
1400-185	210.2	-18.5	102.9	0.60	53.6
1401-200	210.3	-20.0	99.9	0.55	55.2
1401+092	210.3	9.2	65.9	0.65	12.7
1401-125	210.4	-12.5	92.0	0.56	46.6
1401-044	210.4	-4.4	79.8	0.78	16.4
1401+000	210.4	0.0	63.7	0.63	12.0
1402-140	210.5	-14.0	88.5	0.53	45.1
1403-086	210.8	-8.6	102.7	0.70	45.8
1403-024	210.8	-2.4	64.6	0.52	22.4
1404-209	211.1	-20.9	117.0	0.61	66.9
1406-230	211.5	-23.0	128.6	0.55	83.7
1406+104	211.5	10.4	55.1	0.51	13.9
1406-076	211.6	-7.6	102.0	0.66	48.4
1410-020	212.6	-2.0	79.1	0.51	37.3
1411-238	212.8	-23.8	160.2	0.66	106.5
1411-201	212.8	-20.1	131.6	0.70	74.8
1411-069	212.8	-6.9	124.2	1.06	38.1
1411-057	212.8	-5.7	106.0	0.74	45.8
1411+095	212.9	9.5	93.6	0.92	18.2
1412-149	213.1	-14.9	115.3	0.60	66.4
1412-107	213.1	-10.7	85.2	0.51	43.2
1412-257	213.2	-25.7	143.1	0.94	66.7
1414-213	213.6	-21.3	162.5	1.12	71.3
1414+074	213.6	7.4	98.3	0.95	20.9
1414+110	213.6	11.0	281.2	3.23	18.1
1414-038	213.7	-3.8	120.7	1.15	27.2
1415-256	214.0	-25.6	170.0	1.26	66.9
1415-085	214.0	-8.5	99.5	0.67	44.9
1416-157	214.1	-15.7	166.0	0.99	84.9
1416-141	214.2	-14.1	126.0	0.60	77.2
1416+067	214.2	6.7	293.1	3.21	31.0
1417-192	214.3	-19.2	183.3	1.24	81.9
1418-109	214.5	-10.9	104.6	0.50	63.7
1418-065	214.6	-6.5	96.4	0.77	33.5
1420-181	215.2	-18.1	116.5	0.57	69.7
1420-137	215.2	-13.7	127.7	0.55	82.8
1420-091	215.2	-9.1	114.7	0.72	55.7
1421-220	215.3	-22.0	142.5	0.56	96.7
1422-192	215.5	-19.2	120.8	0.50	79.7
1422-032	215.6	-3.2	75.3	0.59	27.3
1423-177	215.8	-17.7	155.9	1.06	69.4
1423-256	216.0	-25.6	156.1	1.03	72.1
1424-232	216.2	-23.2	161.4	0.59	113.0
1424+036	216.2	3.6	72.3	0.50	31.2
1425-118	216.3	-11.8	130.7	0.60	81.5
1425+120	216.4	12.0	87.4	0.64	34.9
1426-012	216.5	-1.2	190.0	1.82	41.4
1426+030	216.7	3.0	87.0	0.56	41.1
1427-162	216.8	-16.2	110.6	0.65	57.8
1427+075	216.9	7.5	152.4	1.61	20.7
1427+109	216.9	10.9	117.4	1.01	35.3
1428-035	217.1	-3.5	109.1	0.57	62.6
1429+033	217.4	3.3	85.6	0.55	40.9
1430-178	217.6	-17.8	185.0	1.24	83.4
1432+066	218.0	6.6	86.8	0.67	32.2
1433-040	218.3	-4.0	119.2	0.67	64.2

Table A4.1 - Source listing continued.

IAU Name	X / deg	Y / deg	Ta / mK	Flux / Jy	Base
1434+036	218.6	3.6	237.8	2.12	65.2
1434-077	218.7	-7.7	114.7	0.55	69.6
1435-219	218.9	-21.9	160.1	0.79	95.7
1436-070	219.1	-7.0	141.5	0.85	71.8
1436-255	219.2	-25.5	141.3	0.62	91.1
1436-168	219.2	-16.8	177.9	1.20	79.8
1437-039	219.3	-3.9	104.4	0.51	62.8
1440-184	220.1	-18.4	155.2	0.61	105.2
1442-162	220.7	-16.2	156.4	0.67	101.9
1442+102	220.7	10.2	184.2	1.79	38.4
1443-137	220.9	-13.7	110.7	0.54	66.7
1443+125	220.9	12.5	88.2	0.51	46.6
1444-198	221.0	-19.8	171.0	0.54	126.8
1444-086	221.0	-8.6	118.5	0.60	69.2
1444+077	221.1	7.7	88.9	0.60	39.6
1445-161	221.4	-16.1	185.9	0.93	110.1
1445+005	221.5	0.5	119.0	0.68	63.4
1446+030	221.6	3.0	87.6	0.52	45.3
1446+042	221.6	4.2	104.2	0.57	57.5
1447-055	221.9	-5.5	133.1	0.50	91.9
1449-169	222.3	-16.9	167.9	0.55	123.3
1449-150	222.3	-15.0	147.7	0.59	99.6
1449-131	222.5	-13.1	178.4	1.15	84.9
1451-192	222.9	-19.2	173.4	0.63	121.7
1451+049	222.9	4.9	94.1	0.56	48.5
1451+098	222.9	9.8	87.2	0.53	43.9
1452-042	223.1	-4.2	183.9	1.34	74.8
1453-109	223.3	-10.9	291.9	2.62	78.2
1453-054	223.3	-5.4	119.2	0.64	67.2
1454-061	223.6	-6.1	143.3	0.85	74.2
1454-248	223.7	-24.8	223.1	0.94	146.8
1454-126	223.7	-12.6	135.2	0.53	92.3
1454-035	223.7	-3.5	126.0	0.65	73.1
1456-165	224.1	-16.5	210.1	1.21	111.1
1456+045	224.1	4.5	107.6	0.78	44.2
1456-180	224.2	-18.0	161.9	0.53	118.9
1458-198	224.7	-19.8	186.6	0.80	121.7
1459-078	224.8	-7.8	115.9	0.54	71.6
1500-257	225.0	-25.7	166.8	0.96	88.3
1501-148	225.3	-14.8	158.3	0.55	113.8
1501+127	225.4	12.7	95.6	0.52	53.3
1502+107	225.5	10.7	236.9	2.22	55.5
1502-001	225.7	-0.1	120.8	0.76	58.9
1502+038	225.7	3.8	100.3	0.57	54.1
1503-091	225.8	-9.1	147.7	0.74	87.1
1503-222	226.0	-22.2	194.4	0.66	140.9
1504-167	226.1	-16.7	382.0	3.17	123.4
1506-112	226.6	-11.2	152.1	0.67	97.3
1506-074	226.6	-7.4	130.0	0.63	78.4
1507-247	226.9	-24.7	204.5	0.55	159.6
1507-255	227.0	-25.5	201.3	0.79	137.2
1508-055	227.1	-5.5	298.2	2.56	89.4
1508+081	227.2	8.1	214.2	1.99	51.9
1510-089	227.5	-8.9	257.9	1.86	106.2
1510+015	227.5	1.5	163.1	1.28	59.0
1511-100	227.8	-10.0	196.0	1.14	102.8
1512-054	228.2	-5.4	136.6	0.65	83.8
1514+004	228.5	0.4	230.0	2.01	66.2

Table A4.1 - Source listing continued.

IAU Name	X / deg	Y / deg	Ta / mK	Flux / Jy	Base
1514-140	228.6	-14.0	177.8	0.53	134.8
1514+056	228.6	5.6	95.8	0.53	52.2
1514+072	228.6	7.2	284.3	2.83	53.7
1514-242	228.7	-24.2	336.6	2.31	148.3
1514-165	228.7	-16.5	206.4	1.00	124.7
1515-132	228.8	-13.2	185.3	0.64	133.2
1515-121	228.8	-12.1	165.2	0.61	115.7
1515+101	228.9	10.1	99.9	0.54	55.8
1515-257	229.0	-25.7	166.3	1.01	84.0
1517-052	229.3	-5.2	125.7	0.51	84.0
1518+047	229.7	4.7	284.9	2.76	60.1
1519-049	230.0	-4.9	141.5	0.73	81.8
1519+028	230.0	2.8	107.7	0.52	65.2
1520-120	230.1	-12.0	140.1	0.51	98.1
1522+112	230.5	11.2	109.8	0.62	59.6
1522-188	230.6	-18.8	178.1	0.54	134.3
1523+033	230.8	3.3	169.8	1.33	61.2
1524-257	231.1	-25.7	182.3	1.05	96.9
1524-137	231.1	-13.7	286.2	1.98	124.6
1526-083	231.5	-8.3	150.5	0.62	99.9
1527-088	231.9	-8.8	143.7	0.52	100.9
1527+061	232.0	6.1	112.9	0.58	65.8
1529-168	232.3	-16.8	177.4	0.70	120.0
1529-160	232.3	-16.0	182.1	0.65	129.0
1530-132	232.5	-13.2	165.5	0.64	113.5
1530-061	232.5	-6.1	136.1	0.61	86.6
1531+073	232.9	7.3	126.5	0.59	78.2
1532+017	233.1	1.7	159.5	1.16	64.5
1533-082	233.3	-8.2	136.4	0.58	89.3
1534-074	233.6	-7.4	132.7	0.57	86.5
1534-153	233.7	-15.3	154.0	0.62	103.7
1534-128	233.7	-12.8	173.2	0.75	112.2
1534+126	233.7	12.6	112.3	0.51	71.1
1536+005	234.0	0.5	121.4	0.78	57.9
1537-207	234.4	-20.7	188.9	0.56	143.4
1538+082	234.6	8.2	153.0	0.77	89.9
1538+010	234.7	1.0	102.2	0.53	59.3
1539-093	234.9	-9.3	168.9	0.99	88.5
1540-078	235.1	-7.8	193.2	1.30	87.3
1541-134	235.3	-13.4	170.9	0.93	95.4
1542+043	235.6	4.3	120.1	0.64	67.7
1542-166	235.7	-16.6	198.0	0.69	142.0
1542-054	235.7	-5.4	136.4	0.69	80.3
1543-247	235.8	-24.7	203.7	0.56	158.3
1543-240	235.8	-24.0	200.8	0.53	157.2
1543+020	235.8	2.0	128.5	0.83	61.0
1543+006	235.9	0.6	198.2	1.61	67.3
1544-112	236.0	-11.2	169.8	0.58	122.3
1544+118	236.2	11.8	134.5	0.63	83.1
1545-121	236.4	-12.1	260.2	1.64	126.3
1547-021	236.8	-2.1	99.5	0.50	58.6
1547+028	236.8	2.8	148.9	1.05	62.9
1547-254	236.9	-25.4	258.2	0.63	206.6
1547-173	236.9	-17.3	221.0	0.52	178.8
1547-166	236.9	-16.6	220.3	0.51	178.9
1548+056	237.0	5.6	307.1	2.85	74.8
1548+114	237.0	11.4	149.5	0.62	99.0
1549-211	237.3	-21.1	198.5	0.61	149.1

Table A4.1 - Source listing continued.

IAU Name	X / deg	Y / deg	Ta / mK	Flux / Jy	Base
1552-095	238.2	-9.5	155.8	0.52	113.7
1553-062	238.3	-6.2	160.3	0.77	97.1
1553-224	238.4	-22.4	300.7	0.54	256.5
1553+113	238.4	11.3	167.0	0.70	110.1
1555-257	238.8	-25.7	294.7	1.78	149.5
1555+073	238.8	7.3	135.6	0.72	76.5
1555-141	238.9	-14.1	251.0	0.73	191.3
1555+001	238.9	0.1	137.4	0.78	74.1
1556-246	239.0	-24.6	323.5	0.75	262.5
1556-215	239.1	-21.5	416.5	1.71	277.0
1556-238	239.2	-23.8	347.2	0.77	284.4
1557+033	239.3	3.3	126.6	0.50	85.6
1557+115	239.3	11.5	189.9	0.79	125.6
1557-005	239.4	-0.5	135.8	0.62	85.3
1558+088	239.6	8.8	139.2	0.68	83.7
1559-151	239.9	-15.1	270.7	1.02	187.5
1600+021	240.0	2.1	543.2	5.81	69.3
1601-222	240.3	-22.2	357.5	0.73	297.8
1601-175	240.5	-17.5	254.8	0.97	175.8
1601-018	240.5	-1.8	133.0	0.62	82.4
1601+014	240.5	1.4	280.6	2.45	81.2
1602-242	240.6	-24.2	330.2	0.67	275.6
1602-093	240.7	-9.3	295.3	2.46	94.3
1602+039	240.7	3.9	125.5	0.50	84.5
1603+001	240.9	0.1	232.0	1.40	117.6
1604-207	241.2	-20.7	358.3	0.79	293.5
1605-163	241.4	-16.3	261.1	0.61	211.0
1606-147	241.5	-14.7	222.2	0.51	180.4
1606+107	241.6	10.7	257.6	1.59	127.7
1606-041	241.7	-4.1	148.5	0.62	98.1
1607-091	241.9	-9.1	200.5	0.81	134.3
1607+127	242.0	12.7	146.2	0.53	103.3
1609-163	242.3	-16.3	271.4	0.82	204.6
1609-142	242.3	-14.2	274.5	0.98	194.4
1609+078	242.3	7.8	164.8	0.50	124.0
1610-214	242.6	-21.4	374.8	0.96	296.7
1611+043	242.9	4.3	156.2	0.78	92.3
1612-008	243.0	-0.8	136.6	0.56	90.6
1614+051	243.5	5.1	143.8	0.67	89.5
1614-100	243.7	-10.0	273.1	0.89	200.9
1615-147	243.8	-14.7	251.0	0.69	194.8
1615+029	243.8	2.9	135.3	0.50	94.5
1616-030	244.2	-3.0	148.9	0.57	102.5
1616+064	244.2	6.4	183.4	0.87	112.3
1617-253	244.4	-25.3	694.6	3.26	428.3
1617-042	244.4	-4.2	176.8	0.90	103.4
1617-235	244.5	-23.5	340.8	0.93	264.9
1618+109	244.7	10.9	179.5	0.54	135.2
1619-215	244.8	-21.5	361.7	0.88	290.1
1621-115	245.3	-11.5	357.9	1.77	213.6
1621-138	245.4	-13.8	238.6	0.52	195.8
1622-207	245.6	-20.7	353.1	0.86	283.0
1622-254	245.7	-25.4	497.1	1.54	371.8
1623-228	245.8	-22.8	365.1	0.97	286.1
1623-072	246.0	-7.2	277.5	0.68	221.9
1625-081	246.4	-8.1	283.3	0.62	232.5
1625-150	246.5	-15.0	228.6	0.51	187.3
1625-094	246.5	-9.4	328.8	0.90	255.1

Table A4.1 - Source listing continued.

IAU Name	X / deg	Y / deg	Ta / mK	Flux / Jy	Base
1627+012	246.8	1.2	147.2	0.50	106.4
1627-069	246.9	-6.9	266.7	0.52	224.0
1628-117	247.0	-11.7	343.6	0.82	276.4
1629+121	247.3	12.1	249.2	1.16	154.6
1629-107	247.4	-10.7	351.7	0.88	279.6
1629+082	247.4	8.2	229.6	0.51	188.1
1630-022	247.7	-2.2	177.5	0.51	136.3
1631+073	247.8	7.3	210.1	0.55	165.2
1632-089	248.1	-8.9	343.2	0.51	301.5
1633-083	248.3	-8.3	351.2	0.60	302.3
1633-105	248.4	-10.5	318.3	0.50	277.3
1633-072	248.4	-7.2	279.2	0.50	238.1
1634+086	248.5	8.6	227.5	0.52	185.2
1634-016	248.6	-1.6	186.3	0.56	140.5
1635-143	248.9	-14.3	360.1	1.03	276.4
1636-234	249.0	-23.4	394.5	0.79	329.8
1636-031	249.0	-3.1	198.1	0.62	147.8
1636-125	249.1	-12.5	319.9	0.60	270.9
1636-100	249.1	-10.0	332.1	0.75	270.9
1636+107	249.1	10.7	206.0	0.86	136.0
1637-257	249.4	-25.7	429.5	2.42	231.7
1637-025	249.5	-2.5	242.0	1.22	142.8
1638+124	249.6	12.4	308.0	1.60	177.6
1639-063	249.8	-6.3	374.5	2.54	167.0
1639-109	249.9	-10.9	355.9	0.79	291.5
1639+031	250.0	3.1	206.6	0.51	165.1
1640-232	250.2	-23.2	429.3	1.07	342.3
1641-153	250.3	-15.3	314.4	0.74	254.3
1641+074	250.4	7.4	233.7	0.60	185.1
1642+095	250.5	9.5	208.5	0.51	167.2
1643-223	250.8	-22.3	480.3	1.76	336.8
1643+023	250.8	2.3	253.8	1.05	167.9
1643-097	250.9	-9.7	338.1	0.69	281.7
1644-106	251.2	-10.6	422.9	1.65	288.4
1645+028	251.5	2.8	282.8	1.13	190.3
1645+127	251.5	12.7	267.2	0.65	214.1
1647+065	251.9	6.5	227.8	0.72	169.0
1648+015	252.1	1.5	273.1	1.03	189.1
1648-092	252.2	-9.2	351.6	0.64	299.0
1648+051	252.2	5.1	2320.2	26.57	153.0
1648+073	252.2	7.3	227.1	0.62	176.2
1649-062	252.3	-6.2	287.9	1.41	173.0
1649+127	252.3	12.7	272.7	0.55	228.1
1649-126	252.4	-12.6	332.9	0.58	285.5
1650-106	252.5	-10.6	340.5	0.54	296.1
1650-040	252.5	-4.0	236.0	0.71	178.1
1650+004	252.6	0.4	273.5	0.91	199.0
1652-108	253.2	-10.8	321.0	0.56	274.9
1653-090	253.5	-9.0	361.7	1.07	274.2
1654-137	253.6	-13.7	310.1	0.91	236.0
1655-201	253.8	-20.1	377.3	0.54	333.3
1655+078	253.9	7.8	305.3	1.03	221.6
1655-076	254.0	-7.6	292.9	0.96	214.8
1656+054	254.1	5.4	317.6	1.31	211.0
1657-203	254.3	-20.3	385.9	0.52	343.8
1657-228	254.4	-22.8	501.8	0.74	441.4
1700-179	255.0	-17.9	368.0.	0.72	308.8
1700+056	255.0	5.6	263.2	0.51	222.0

Table A4.1 - Source listing continued.

IAU Name	X / deg	Y / deg	Ta / mK	Flux / Jy	Base
1700-205	255.1	-20.5	409.4	0.54	365.2
1700-122	255.2	-12.2	303.9	0.53	260.5
1701-015	255.3	-1.5	244.1	0.53	200.9
1701-247	255.5	-24.7	585.6	2.03	420.0
1701-137	255.5	-13.7	325.4	0.72	266.5
1704+019	256.2	1.9	221.6	0.65	168.9
1705-225	256.3	-22.5	565.2	0.63	513.5
1705-027	256.3	-2.7	270.1	0.53	226.9
1705-103	256.4	-10.3	342.6	0.62	292.1
1705+114	256.4	11.4	432.0	0.51	390.5
1706-174	256.6	-17.4	401.6	0.55	357.2
1707-087	256.9	-8.7	291.6	0.52	249.1
1708+007	257.1	0.7	274.3	0.99	193.6
1708-237	257.2	-23.7	558.4	0.58	511.4
1709+100	257.3	10.0	367.6	0.61	317.6
1710-250	257.6	-25.0	1045.4	5.94	561.0
1710-082	257.6	-8.2	345.8	1.03	261.5
1711+006	257.9	0.6	255.3	0.66	201.2
1712-034	258.2	-3.4	332.4	0.77	269.5
1713-121	258.3	-12.1	373.6	0.84	304.7
1713-218	258.4	-21.8	569.9	0.63	518.7
1713-047	258.4	-4.7	310.0	0.52	267.3
1714+061	258.5	6.1	298.3	0.57	252.2
1714-020	258.6	-2.0	282.8	0.80	217.2
1715-112	258.9	-11.2	370.3	0.58	322.7
1715-097	259.0	-9.7	392.0	0.64	339.7
1716-143	259.2	-14.3	414.1	1.21	315.7
1716-128	259.2	-12.8	350.7	0.51	308.8
1716+006	259.2	0.6	324.4	1.22	224.6
1716+066	259.2	6.6	331.3	0.59	283.4
1717-070	259.4	-7.0	372.1	0.89	299.6
1717-254	259.5	-25.4	760.9	0.76	698.7
1717-009	259.5	-0.9	3430.5	39.58	201.8
1717+035	259.5	3.5	258.9	0.55	214.3
1718-100	259.6	-10.0	421.3	0.77	358.8
1719-243	259.8	-24.3	801.6	1.06	715.3
1719-045	259.8	-4.5	310.5	0.61	260.8
1720+001	260.1	0.1	272.7	0.51	231.3
1720+073	260.1	7.3	355.4	0.83	287.8
1720+102	260.1	10.2	436.9	0.73	377.3
1722-242	260.5	-24.2	803.4	0.72	744.5
1722-049	260.5	-4.9	337.0	0.63	285.8
1722-027	260.5	-2.7	400.4	1.79	254.0
1722+045	260.5	4.5	288.1	0.53	245.1
1722-147	260.6	-14.7	388.7	0.53	345.2
1722+065	260.6	6.5	331.7	0.52	289.5
1723-205	260.8	-20.5	522.6	0.50	481.4
1724-110	261.2	-11.0	458.8	0.65	405.8
1725-199	261.5	-19.9	566.3	0.61	516.4
1725+123	261.5	12.3	383.3	0.81	317.1
1726-238	261.6	-23.8	873.6	2.21	693.6
1726-038	261.6	-3.8	307.6	0.65	254.4
1727-215	261.9	-21.5	1431.8	10.86	545.8
1730-131	262.6	-13.1	894.9	6.09	397.7
1730-050	262.7	-5.0	328.9	0.55	284.4
1731+081	262.8	8.1	472.7	0.78	409.5
1731+110	263.0	11.0	430.2	0.73	371.0
1732-162	263.1	-16.2	468.8	0.50	427.9

Table A4.1 - Source listing continued.

IAU Name	X / deg	Y / deg	Ta / mK	Flux / Jy	Base
1732-093	263.1	-9.3	527.6	1.59	398.2
1732+094	263.1	9.4	476.0	1.07	389.0
1732-081	263.2	-8.1	440.8	0.79	376.4
1732-059	263.2	-5.9	381.6	0.55	336.9
1734-075	263.6	-7.5	417.1	0.62	366.7
1735+002	263.8	0.2	339.1	0.52	296.6
1735+064	263.8	6.4	525.6	1.00	444.2
1735+035	263.9	3.5	406.2	1.08	318.4
1736-149	264.1	-14.9	533.2	0.59	484.8
1736+109	264.2	10.9	406.1	0.64	354.1
1737-026	264.3	-2.6	398.9	0.60	350.0
1737-159	264.4	-15.9	549.5	0.64	497.3
1739-138	264.8	-13.8	551.9	0.77	489.4
1739-054	264.8	-5.4	461.0	0.70	403.6
1739+060	264.8	6.0	501.2	0.56	455.5
1739-128	264.9	-12.8	549.2	0.82	482.4
1739+106	264.9	10.6	403.4	0.62	353.2
1741-038	265.3	-3.8	581.0	1.76	437.5
1741+099	265.3	9.9	412.4	0.62	361.9
1742-087	265.5	-8.7	459.6	0.51	417.8
1742-079	265.7	-7.9	539.2	1.26	436.7
1744+075	266.0	7.5	562.9	0.64	510.7
1744-194	266.1	-19.4	996.1	2.27	810.6
1744+115	266.1	11.5	282.5	0.51	240.7
1744-153	266.2	-15.3	625.2	0.72	566.7
1744-070	266.2	-7.0	512.0	0.68	456.8
1744+056	266.2	5.6	569.3	0.88	497.4
1745+095	266.5	9.5	427.4	0.87	356.2
1747-043	266.8	-4.3	540.6	0.68	484.8
1747-014	266.9	-1.4	458.8	0.71	401.0
1748-022	267.1	-2.2	470.6	0.57	424.0
1748+032	267.1	3.2	475.2	0.99	394.7
1749+097	267.3	9.7	495.9	2.02	330.8
1749+047	267.4	4.7	621.8	1.04	536.6
1749+061	267.4	6.1	558.1	1.11	467.9
1750-101	267.5	-10.1	605.9	0.64	553.5
1750-093	267.6	-9.3	593.0	0.59	545.1
1751-163	267.8	-16.3	739.7	0.87	668.7
1751+037	267.9	3.7	613.8	0.96	535.2
1752-073	268.1	-7.3	631.2	0.53	588.2
1752-251	268.2	-25.1	4322.5	11.29	3401.4
1753-112	268.3	-11.2	676.8	0.93	601.2
1753+033	268.4	3.3	612.0	0.92	536.7
1753-052	268.5	-5.2	694.1	1.06	607.3
1755-015	268.9	-1.5	489.7	0.64	437.3
1755-163	269.0	-16.3	1031.2	2.97	789.1
1755-062	269.0	-6.2	719.5	0.74	659.1
1756+063	269.1	6.3	393.4	0.65	340.8
1758-233	269.5	-23.3	10366.3	66.19	4967.8
1758-036	269.5	-3.6	592.9	1.07	505.9
1758+045	269.6	4.5	429.9	0.58	382.7
1800-051	270.0	-5.1	610.2	0.51	568.2
1800-021	270.1	-2.1	573.1	1.11	483.0
1800-244	270.2	-24.4	12635.6	113.12	3409.0
1801-099	270.3	-9.9	758.2	0.92	683.2
1801-073	270.3	-7.3	780.0	1.06	693.9
1801+042	270.3	4.2	426.6	0.52	384.0
1801+010	270.5	1.0	676.7	1.61	545.2

Table A4.1 - Source listing continued.

IAU Name	X / deg	Y / deg	Ta / mK	Flux / Jy	Base
1802-216	270.6	-21.6	6532.1	27.17	4315.8
1802+100	270.6	10.0	347.8	0.90	274.5
1803-142	270.8	-14.2	1299.7	4.27	951.0
1803-035	270.8	-3.5	583.5	0.57	537.3
1803-078	270.9	-7.8	859.1	1.35	749.3
1804-068	271.0	-6.8	778.8	1.03	695.0
1804-004	271.1	-0.4	692.3	0.95	615.2
1805+016	271.3	1.6	569.4	0.83	501.6
1805+063	271.3	6.3	365.2	0.98	285.6
1805-012	271.4	-1.2	707.2	1.04	622.2
1806-239	271.6	-23.9	2416.8	7.88	1774.2
1806-203	271.6	-20.3	9082.4	66.39	3667.0
1807-089	271.8	-8.9	916.1	0.74	855.9
1807-193	272.0	-19.3	4340.2	11.58	3395.8
1808+103	272.1	10.3	338.6	0.73	279.2
1808-040	272.2	-4.0	648.7	0.91	574.2
1809-078	272.3	-7.8	864.9	0.80	799.8
1809-097	272.4	-9.7	1022.5	1.14	929.7
1809+068	272.5	6.8	349.9	0.72	290.8
1810-021	272.7	-2.1	741.3	1.39	628.1
1810+046	272.7	4.6	454.7	1.43	337.9
1811-180	272.8	-18.0	8083.3	53.74	3699.8
1811+093	272.9	9.3	339.3	0.74	279.0
1812-054	273.2	-5.4	729.7	0.62	679.5
1812-028	273.2	-2.8	709.2	0.74	648.9
1813-001	273.3	-0.1	631.9	0.98	552.2
1813-062	273.4	-6.2	829.1	1.24	727.7
1814-241	273.5	-24.1	1543.6	5.05	1131.9
1814-163	273.5	-16.3	6277.1	28.65	3940.3
1814-034	273.6	-3.4	714.8	0.51	673.3
1814-196	273.7	-19.6	2019.0	4.30	1667.9
1815-119	273.8	-11.9	6777.0	43.91	3195.3
1815-010	273.8	-1.0	613.8	0.50	572.8
1815-138	274.0	-13.8	10628.2	92.75	3063.3
1816-030	274.2	-3.0	789.6	1.34	680.6
1817-162	274.4	-16.2	52983.6	613.92	2908.8
1817-255	274.5	-25.5	1066.5	1.98	905.0
1818-148	274.6	-14.8	4252.2	14.32	3084.0
1818+127	274.6	12.7	308.0	1.29	203.1
1820-040	275.1	-4.0	882.2	0.92	807.3
1820-221	275.2	-22.1	1304.2	1.14	1211.1
1821-238	275.3	-23.8	1160.4	3.19	900.6
1821-204	275.3	-20.4	1290.0	1.50	1167.5
1821-194	275.3	-19.4	1249.2	0.98	1169.6
1821+018	275.4	1.8	707.0	1.68	569.6
1821+051	275.4	5.1	462.8	0.59	415.0
1821+107	275.4	10.7	435.0	1.35	324.6
1822-132	275.6	-13.2	5163.9	24.97	3126.9
1823-008	275.9	-0.8	748.5	0.66	694.9
1823-126	276.0	-12.6	6577.2	38.62	3427.2
1824-119	276.2	-11.9	4643.5	16.38	3307.6
1825+093	276.3	9.3	448.2	0.64	395.8
1825+004	276.5	0.4	782.0	1.03	697.7
1826-109	276.6	-10.9	4437.3	20.99	2725.6
1826-239	276.7	-23.9	837.3	0.99	756.6
1827-153	276.8	-15.3	1467.6	1.94	1309.5
1827+014	276.9	1.4	710.5	0.51	668.7
1828-038	277.0	-3.8	1036.8	0.53	993.6

Table A4.1 - Source listing continued.

IAU Name	X / deg	Y / deg	Ta / mK	Flux / Jy	Base
1828-021	277.2	-2.1	3802.8	34.78	965.9
1830-102	277.6	-10.2	5590.6	33.20	2882.6
1830+012	277.6	1.2	778.0	1.24	676.8
1830-211	277.7	-21.1	1781.2	11.92	809.0
1831-033	277.8	-3.3	1149.2	0.79	1085.0
1831+069	277.8	6.9	471.0	0.56	425.1
1831+087	277.9	8.7	508.8	0.67	454.3
1831-237	278.0	-23.7	716.0	0.72	657.5
1831-087	278.0	-8.7	6923.8	34.05	4146.7
1832+079	278.2	7.9	491.0	0.59	442.5
1833-074	278.4	-7.4	6419.4	27.90	4144.1
1834+088	278.5	8.8	506.6	0.56	460.9
1835-179	278.9	-17.9	660.5	0.61	610.8
1835-068	278.9	-6.8	6308.2	31.59	3731.6
1836-126	279.1	-12.6	1061.0	1.36	950.5
1836-169	279.2	-16.9	683.3	0.71	625.4
1837-195	279.4	-19.5	616.6	0.57	570.0
1837+097	279.5	9.7	518.7	0.69	462.6
1838-051	279.6	-5.1	4646.2	20.87	2944.2
1838+044	279.6	4.4	660.6	0.56	614.8
1840-038	280.2	-3.8	5261.3	24.79	3239.2
1843+098	280.8	9.8	756.1	2.88	521.2
1845-020	281.3	-2.0	14533.1	123.74	4440.4
1845+125	281.3	12.5	458.7	0.79	394.6
1845-112	281.4	-11.2	733.8	0.76	671.9
1846-073	281.7	-7.3	1109.8	0.75	1048.7
1848-170	282.1	-17.0	513.1	0.60	464.5
1849-220	282.3	-22.0	429.1	0.67	374.1
1849-195	282.3	-19.5	453.8	0.52	411.6
1849-001	282.3	-0.1	3309.9	11.93	2336.5
1849-242	282.4	-24.2	455.8	0.64	403.8
1850+006	282.5	0.6	3577.5	14.57	2388.7
1853+013	283.4	1.3	10279.8	95.42	2496.8
1853-204	283.5	-20.4	435.3	0.77	372.8
1853-193	283.5	-19.3	452.4	0.58	405.2
1853+022	283.5	2.2	3797.3	15.56	2528.4
1853+078	283.5	7.8	1681.5	8.78	965.0
1855-252	283.9	-25.2	388.9	0.52	346.6
1858-081	284.6	-8.1	670.0	0.84	601.8
1858+041	284.6	4.1	4412.2	20.42	2746.7
1859+012	284.8	1.2	2571.8	18.21	1086.4
1859-051	284.9	-5.1	752.1	0.69	696.2
1900-236	285.0	-23.6	508.7	2.28	323.0
1900-074	285.0	-7.4	643.4	0.52	601.0
1900+022	285.2	2.2	1515.9	5.87	1037.1
1901+054	285.4	5.4	3411.6	17.24	2005.5
1902-257	285.7	-25.7	390.7	0.77	328.3
1903+126	285.9	12.6	685.2	2.62	471.4
1904-163	286.1	-16.3	400.1	0.56	354.2
1904-026	286.1	-2.6	777.5	0.84	708.6
1904+071	286.2	7.1	3409.2	20.22	1759.6
1907-055	286.9	-5.5	608.7	0.62	557.9
1907-040	287.0	-4.0	615.0	0.61	565.1
1907+090	287.0	9.0	7235.4	68.87	1617.8
1908-202	287.1	-20.2	486.6	2.23	304.6
1908+051	287.1	5.1	1754.5	4.34	1400.9
1908-173	287.2	-17.3	366.7	1.00	285.0
1908+009	287.2	0.9	672.7	0.50	631.6

Table A4.1 - Source listing continued.

IAU Name	X / deg	Y / deg	Ta / mK	Flux / Jy	Base
1909-059	287.3	-5.9	599.7	1.00	518.0
1909+099	287.3	9.9	1879.9	4.52	1511.1
1909-100	287.5	-10.0	435.8	0.75	374.6
1909-084	287.5	-8.4	463.6	0.63	412.6
1912+024	288.0	2.4	738.7	0.60	689.7
1912+111	288.0	11.1	2662.9	14.81	1454.8
1912+002	288.1	0.2	693.9	0.79	629.2
1913-024	288.4	-2.4	565.8	0.60	516.9
1914+015	288.5	1.5	692.7	0.56	647.0
1914+030	288.5	3.0	753.5	0.58	706.2
1915-249	288.8	-24.9	358.3	0.71	300.3
1915-122	288.8	-12.2	428.0	1.06	341.4
1915+062	288.9	6.2	958.6	1.01	876.6
1915+120	288.9	12.0	2268.8	11.13	1361.0
1916-022	289.1	-2.2	528.9	0.67	474.6
1916-221	289.2	-22.1	343.3	0.65	290.6
1917-079	289.4	-7.9	364.3	0.66	310.6
1917-002	289.4	-0.2	585.3	0.60	536.5
1917-041	289.5	-4.1	459.0	0.73	399.4
1918-109	289.7	-10.9	380.5	0.51	338.6
1920-212	290.2	-21.2	346.2	0.83	278.2
1920-078	290.2	-7.8	401.5	1.25	299.8
1920-031	290.2	-3.1	446.1	0.64	393.9
1921-107	290.3	-10.7	379.3	0.51	337.4
1921+029	290.3	2.9	612.8	0.58	565.6
1921-159	290.4	-15.9	309.3	1.16	214.9
1922+011	290.6	1.1	615.2	1.02	532.1
1923-257	290.8	-25.7	296.4	0.58	249.4
1923-187	290.8	-18.7	284.2	0.71	226.6
1923-147	290.8	-14.7	320.7	0.78	256.8
1923-092	290.8	-9.2	337.0	0.51	295.5
1923+005	290.9	0.5	611.3	1.34	502.3
1925+010	291.5	1.0	520.3	0.77	457.1
1926-012	291.6	-1.2	490.4	1.27	386.4
1926-073	291.7	-7.3	293.1	0.50	252.1
1927-153	291.9	-15.3	285.7	0.80	220.5
1928-142	292.2	-14.2	295.1	0.66	241.1
1929-227	292.3	-22.7	286.4	0.53	243.3
1929-197	292.3	-19.7	288.6	0.73	228.7
1929-116	292.4	-11.6	362.9	0.52	320.7
1930-083	292.6	-8.3	338.9	1.09	249.7
1930+007	292.7	0.7	485.1	0.68	430.0
1931+051	292.8	5.1	460.0	0.52	417.8
1931+074	293.0	7.4	516.0	0.67	461.4
1933-165	293.3	-16.5	258.9	0.54	215.1
1933+058	293.3	5.8	449.8	0.51	408.4
1934-124	293.5	-12.4	305.2	0.56	260.0
1934-005	293.5	-0.5	412.2	0.86	342.4
1935+093	293.8	9.3	447.8	0.76	385.8
1936+047	294.1	4.7	430.6	0.63	379.1
1937-102	294.3	-10.2	362.8	0.98	283.1
1937-231	294.4	-23.1	294.8	0.87	224.0
1937-036	294.4	-3.6	300.4	0.76	238.6
1938-155	294.6	-15.5	562.7	4.23	217.5
1938-012	294.7	-1.2	325.4	0.71	267.5
1939-053	294.8	-5.3	269.7	0.75	208.4
1939+103	294.9	10.3	403.5	0.65	350.1
1941-182	295.3	-18.2	272.1	0.93	196.5

Table A4.1 - Source listing continued.

IAU Name	X / deg	Y / deg	Ta / mK	Flux / Jy	Base
1941-094	295.4	-9.4	278.2	0.62	227.6
1941-075	295.4	-7.5	310.3	0.66	256.1
1942-053	295.7	-5.3	275.1	0.76	213.2
1942+127	295.7	12.7	326.5	1.86	174.5
1944+002	296.0	0.2	366.6	1.14	273.8
1945+036	296.3	3.6	352.2	0.50	311.4
1945-095	296.4	-9.5	313.7	1.14	220.9
1946-236	296.6	-23.6	265.6	0.97	186.9
1946+108	296.7	10.8	357.7	0.57	311.0
1947-201	296.8	-20.1	256.3	0.93	180.3
1947+125	296.9	12.5	328.3	0.72	269.6
1947-047	297.0	-4.7	328.0	1.55	201.9
1947+080	297.0	8.0	375.1	1.02	291.9
1948-100	297.2	-10.0	273.9	0.70	217.0
1949+024	297.4	2.4	654.2	4.26	307.0
1950-014	297.5	-1.4	306.9	1.03	223.0
1950+116	297.5	11.6	373.8	0.93	297.7
1950-214	297.6	-21.4	243.9	0.78	180.0
1952-196	298.1	-19.6	209.3	0.59	161.4
1952-071	298.1	-7.1	253.6	0.56	208.1
1952+008	298.2	0.8	307.3	0.59	259.4
1953-167	298.4	-16.7	218.7	0.55	173.9
1953-127	298.4	-12.7	217.9	0.57	171.1
1953-077	298.4	-7.7	285.6	1.12	194.0
1955-208	299.0	-20.8	198.2	0.57	151.6
1955-059	299.0	-5.9	233.5	0.60	184.7
1957-195	299.3	-19.5	197.1	0.52	154.9
1957-013	299.3	-1.3	250.2	0.64	197.6
1958-180	299.5	-18.0	289.0	1.75	146.5
1958-136	299.5	-13.6	213.3	0.73	153.9
1958+102	299.7	10.2	281.0	0.55	235.7
1959+088	299.8	8.8	303.3	0.64	251.4
1959+116	299.8	11.6	251.8	0.52	209.4
1959-151	299.9	-15.1	199.2	0.58	151.9
1959+125	299.9	12.5	245.4	0.54	201.4
2001+103	300.5	10.3	270.5	0.73	211.2
2002-185	300.6	-18.5	185.2	0.54	140.8
2003-025	300.9	-2.5	306.9	1.48	186.5
2004+118	301.1	11.8	258.7	0.88	187.2
2005-104	301.3	-10.4	231.7	0.91	157.3
2005-044	301.4	-4.4	220.8	0.62	170.2
2006-005	301.5	-0.5	230.2	0.57	183.5
2006+127	301.5	12.7	201.8	1.21	103.4
2007+063	302.0	6.3	226.1	0.52	183.4
2008-159	302.1	-15.9	204.1	0.85	134.5
2008-069	302.1	-6.9	334.3	2.16	158.4
2012-018	303.2	-1.8	232.3	0.93	156.2
2013-036	303.3	-3.6	265.5	1.44	148.0
2014+126	303.6	12.6	190.8	0.82	123.8
2015+084	303.9	8.4	233.1	0.56	187.2
2019+051	304.8	5.1	240.8	0.68	185.6
2019+115	304.8	11.5	208.8	0.63	157.1
2019+099	304.9	9.9	314.2	1.83	164.6
2021+127	305.3	12.7	171.4	0.98	91.4
2022+105	305.6	10.5	211.1	0.59	163.2
2022-077	305.7	-7.7	209.5	0.97	130.2
2022+032	305.7	3.2	198.5	0.57	151.7
2022+120	305.7	12.0	231.5	0.92	156.4

Table A4.1 - Source listing continued.

IAU Name	X / deg	Y / deg	Ta / mK	Flux / Jy	Base
2024-218	306.1	-21.8	215.6	0.96	136.9
2025-206	306.3	-20.6	169.1	0.52	127.0
2025-156	306.4	-15.6	187.7	0.82	121.1
2027+000	306.9	0.0	205.6	0.78	142.2
2028-079	307.1	-7.9	203.3	0.89	131.0
2029-042	307.3	-4.2	164.3	0.53	121.0
2029+121	307.4	12.1	218.5	0.82	151.2
2030-230	307.6	-23.0	276.0	1.87	123.2
2032-177	308.2	-17.7	166.9	0.53	123.9
2032+127	308.2	12.7	161.2	0.96	82.6
2033+108	308.3	10.8	221.2	0.90	147.7
2034-067	308.5	-6.7	226.8	1.02	143.2
2034+120	308.6	12.0	184.4	0.52	141.9
2035-092	308.9	-9.2	176.7	0.53	133.6
2036-203	309.0	-20.3	185.1	0.65	131.9
2036-109	309.0	-10.9	171.3	0.57	124.9
2037-254	309.3	-25.4	183.5	0.61	133.7
2037-086	309.3	-8.6	188.7	0.61	138.6
2039-047	309.8	-4.7	159.4	0.50	118.3
2039-237	310.0	-23.7	184.3	0.53	140.9
2040-035	310.1	-3.5	169.1	0.51	127.2
2041-105	310.3	-10.5	166.9	0.51	125.1
2041+071	310.4	7.1	198.7	0.59	150.3
2043-099	310.9	-9.9	187.1	0.74	126.7
2044-169	311.1	-16.9	172.2	0.60	123.3
2044-028	311.2	-2.8	254.7	1.71	114.9
2045+068	311.5	6.8	260.4	1.35	150.1
2046-072	311.6	-7.2	167.0	0.62	116.3
2046+126	311.7	12.6	193.7	1.06	107.2
2048-148	312.1	-14.8	217.4	1.26	114.9
2049+000	312.4	0.0	155.7	0.56	109.8
2052-106	313.1	-10.6	159.7	0.53	116.2
2052-096	313.1	-9.6	160.3	0.58	113.0
2053-201	313.3	-20.1	279.5	1.77	135.0
2054-127	313.7	-12.7	168.4	0.58	121.1
2055+055	314.0	5.5	195.0	0.83	127.3
2056+028	314.1	2.8	172.8	0.64	120.8
2057-149	314.3	-14.9	179.4	0.75	118.3
2058-180	314.7	-18.0	184.6	0.62	133.7
2059-228	314.8	-22.8	199.2	0.64	147.4
2059-214	314.8	-21.4	196.3	0.60	147.0
2059-135	314.8	-13.5	203.6	1.02	120.5
2059+035	314.8	3.5	177.8	0.79	113.8
2059-095	314.9	-9.5	181.8	0.68	126.4
2101-214	315.4	-21.4	194.2	0.60	145.6
2101-115	315.4	-11.5	195.7	0.90	122.0
2104+124	316.0	12.4	211.5	1.20	113.6
2104-256	316.1	-25.6	770.1	7.66	144.9
2104-243	316.1	-24.3	199.0	0.57	152.8
2105-072	316.4	-7.2	162.8	0.63	111.7
2107-233	316.8	-23.3	193.1	0.54	149.0
2107-106	316.9	-10.6	207.7	1.11	117.1
2108-017	317.1	-1.7	162.4	0.54	118.5
2110-161	317.7	-16.1	169.7	0.77	107.0
2112+077	318.2	7.7	141.8	0.56	96.1
2113+034	318.4	3.4	147.0	0.58	99.8
2114-211	318.5	-21.1	260.0	1.72	119.5
2114-070	318.5	-7.0	170.7	0.56	125.3

Table A4.1 - Source listing continued.

IAU Name	X / deg	Y / deg	Ta / mK	Flux / Jy	Base
2114+055	318.7	5.5	147.8	0.54	103.5
2116-118	319.2	-11.8	190.7	0.94	113.8
2118-150	319.6	-15.0	181.7	0.62	131.5
2120-167	320.0	-16.7	215.3	0.92	140.0
2120+126	320.0	12.6	136.0	0.89	63.8
2120-103	320.1	-10.3	161.4	0.51	119.7
2120+099	320.2	9.9	167.9	0.81	101.5
2121-015	320.3	-1.5	158.0	0.71	99.9
2121+054	320.3	5.4	315.0	2.60	103.3
2121+029	320.4	2.9	148.0	0.51	106.4
2123+007	320.8	0.7	145.2	0.51	103.4
2125-237	321.3	-23.7	162.8	0.50	121.6
2125-066	321.4	-6.6	183.2	0.74	123.1
2126-159	321.6	-15.9	207.5	1.09	118.7
2126-243	321.7	-24.3	170.9	0.75	109.6
2126-230	321.7	-23.0	178.0	0.84	109.5
2126-186	321.7	-18.6	228.4	1.34	118.7
2126+073	321.7	7.3	206.1	1.41	91.2
2127-097	321.9	-9.7	195.6	0.76	133.2
2128+048	322.0	4.8	349.6	3.26	83.9
2128-208	322.1	-20.8	225.0	1.46	105.6
2128+090	322.2	9.0	134.3	0.59	86.0
2129-123	322.3	-12.3	280.0	1.97	119.2
2131-021	322.9	-2.1	267.4	1.81	119.8
2131-143	323.0	-14.3	143.4	0.55	99.0
2132-178	323.1	-17.8	161.0	0.63	109.9
2134+005	323.5	0.5	636.7	6.71	89.3
2135-209	323.8	-20.9	308.2	2.58	98.0
2135-148	323.8	-14.8	304.2	2.46	103.3
2135+126	323.9	12.6	136.4	0.86	66.6
2136-251	324.0	-25.1	171.0	0.79	106.7
2136-184	324.0	-18.4	243.9	1.58	115.3
2136+117	324.0	11.7	163.6	0.59	115.1
2137-165	324.4	-16.5	154.4	0.63	103.1
2137-069	324.4	-6.9	169.8	0.57	123.3
2139-048	325.0	-4.8	144.8	0.60	95.5
2139+028	325.0	2.8	124.0	0.60	75.0
2141+125	325.4	12.5	131.9	0.62	81.5
2142+043	325.7	4.3	140.4	0.82	73.5
2143+110	325.8	11.0	141.1	0.53	97.9
2143-157	325.9	-15.7	190.9	1.09	101.8
2144-179	326.0	-17.9	163.1	0.66	109.0
2144+093	326.1	9.3	132.5	0.50	91.3
2145-200	326.3	-20.0	145.3	0.56	99.8
2145+067	326.4	6.7	273.6	2.52	68.1
2146-133	326.7	-13.3	224.4	1.40	110.4
2147-194	326.8	-19.4	144.7	0.52	102.6
2148+069	327.2	6.9	135.5	0.76	73.2
2148+120	327.2	12.0	160.5	0.70	103.7
2149-200	327.3	-20.0	206.2	1.20	108.1
2150+054	327.7	5.4	145.6	0.80	80.5
2150+079	327.7	7.9	113.3	0.51	71.8
2150+125	327.7	12.5	148.6	0.81	82.6
2151-114	327.9	-11.4	156.7	0.50	115.6
2153-010	328.3	-1.0	121.8	0.54	77.9
2153-017	328.5	-1.7	153.0	0.98	72.9
2154-184	328.6	-18.4	263.9	2.05	96.6
2154-117	328.6	-11.7	192.1	0.97	113.1

Table A4.1 - Source listing continued.

IAU Name	X / deg	Y / deg	Ta / mK	Flux / Jy	Base
2154-081	328.6	-8.1	136.3	0.52	94.3
2154-062	328.6	-6.2	143.9	0.55	99.1
2155-153	328.9	-15.3	267.8	2.09	97.5
2156-100	329.2	-10.0	135.7	0.53	92.7
2158+070	329.6	7.0	105.4	0.59	57.1
2159+043	329.9	4.3	139.4	0.89	67.0
2203-188	330.9	-18.8	554.7	5.62	96.6
2203+057	330.9	5.7	108.9	0.66	54.7
2204-092	331.1	-9.2	153.5	0.55	108.9
2204+126	331.2	12.6	118.4	0.77	56.0
2206-238	331.7	-23.8	202.0	1.46	83.1
2206+020	331.7	2.0	128.9	0.85	59.6
2207-047	331.8	-4.7	109.9	0.52	67.5
2207+125	331.8	12.5	119.6	0.64	67.4
2208-137	332.2	-13.7	166.2	0.98	86.3
2209+081	332.4	8.1	174.9	1.22	75.7
2209-257	332.5	-25.7	178.9	1.13	86.6
2209+016	332.5	1.6	212.6	2.00	49.5
2210-092	332.6	-9.2	132.9	0.54	88.9
2210-045	332.7	-4.5	109.4	0.55	64.2
2211+089	332.8	8.9	126.6	0.68	71.3
2212-173	333.0	-17.3	514.0	5.30	81.8
2212+070	333.0	7.0	120.4	0.63	69.2
2212+127	333.1	12.7	92.8	0.57	46.5
2215+021	333.9	2.1	102.7	0.62	52.3
2215-001	334.0	-0.1	95.7	0.55	50.8
2216-039	334.1	-3.9	277.4	2.65	61.1
2217-251	334.5	-25.1	129.5	0.76	67.9
2217+018	334.5	1.8	104.0	0.64	52.0
2220-031	335.0	-3.1	133.3	0.88	61.8
2220+119	335.0	11.9	127.7	0.58	80.0
2220+014	335.2	1.4	85.7	0.51	44.5
2221-024	335.3	-2.4	384.5	4.00	58.0
2221-117	335.4	-11.7	119.6	0.51	77.6
2222-139	335.5	-13.9	130.9	0.62	80.4
2222+052	335.5	5.2	121.8	0.68	66.7
2222+041	335.6	4.1	123.5	0.67	69.2
2223-052	335.8	-5.2	523.7	5.65	62.9
2226-197	336.6	-19.7	137.2	0.57	90.7
2226-211	336.7	-21.1	171.6	1.18	75.2
2226-088	336.7	-8.8	135.3	0.87	64.1
2229-087	337.3	-8.7	128.9	0.82	61.6
2229+067	337.3	6.7	133.6	0.84	65.2
2230-150	337.5	-15.0	115.0	0.56	69.6
2230+115	337.6	11.5	493.0	5.34	57.3
2231-129	337.8	-12.9	122.4	0.59	74.0
2232-233	338.2	-23.3	128.8	0.60	80.1
2234-148	338.5	-14.8	130.7	0.71	73.1
2234-253	338.7	-25.3	137.8	0.88	66.1
2235-120	338.8	-12.0	161.8	1.26	59.5
2236-143	339.0	-14.3	123.7	0.57	77.6
2236-176	339.1	-17.6	197.1	1.36	85.8
2237+101	339.3	10.1	107.6	0.57	61.0
2238+114	339.7	11.4	122.0	0.68	66.2
2238+127	339.7	12.7	86.8	0.61	36.9
2239-105	339.8	-10.5	112.1	0.57	65.8
2239+096	339.8	9.6	110.8	0.69	54.7
2241-164	340.3	-16.4	119.3	0.57	73.1

Table A4.1 - Source listing continued.

IAU Name	X / deg	Y / deg	Ta / mK	Flux / Jy	Base
2243-191	340.8	-19.1	119.6	0.55	74.6
2243-124	340.9	-12.4	239.1	2.23	57.1
2243-033	340.9	-3.3	155.4	1.03	71.3
2243+048	340.9	4.8	115.3	0.64	63.1
2244-097	341.1	-9.7	103.5	0.57	56.8
2245+029	341.4	2.9	119.1	0.63	67.5
2247+113	341.8	11.3	239.0	2.12	66.2
2247-233	341.9	-23.3	120.5	0.63	69.4
2247+126	342.0	12.6	92.0	0.67	37.5
2248-123	342.1	-12.3	121.5	0.79	57.3
2248+068	342.1	6.8	151.5	1.12	60.0
2249+047	342.3	4.7	115.4	0.71	57.8
2250-211	342.5	-21.1	113.3	0.53	69.9
2252+113	343.0	11.3	126.4	0.77	63.9
2252-090	343.2	-9.0	126.0	0.73	66.8
2254-250	343.7	-25.0	142.7	0.93	66.7
2254-187	343.7	-18.7	120.8	0.64	68.5
2255+061	343.8	6.1	104.3	0.55	59.1
2255+092	343.8	9.2	125.0	0.77	62.0
2257-202	344.4	-20.2	162.8	1.15	68.7
2258+034	344.6	3.4	107.6	0.64	55.5
2258+084	344.7	8.4	116.0	0.52	73.5
2300-189	345.1	-18.9	155.4	0.93	79.4
2303-053	345.9	-5.3	130.0	0.70	73.2
2305+022	346.4	2.2	98.8	0.51	56.9
2306-233	346.5	-23.3	119.1	0.56	73.3
2306+095	346.5	9.5	122.5	0.61	72.9
2307+106	346.9	10.6	131.7	0.81	65.8
2307+073	347.0	7.3	152.6	1.13	60.6
2308+018	347.1	1.8	108.8	0.61	59.4
2308-109	347.2	-10.9	112.4	0.64	60.6
2309+090	347.5	9.0	185.9	1.58	56.7
2310+050	347.6	5.0	205.5	1.88	52.2
2311-222	347.9	-22.2	117.6	0.62	66.9
2312+124	348.2	12.4	100.9	0.70	43.4
2313+102	348.3	10.2	125.2	0.93	49.6
2313-182	348.4	-18.2	131.5	0.83	63.4
2313-166	348.4	-16.6	117.1	0.67	62.8
2313-122	348.4	-12.2	166.6	1.29	61.1
2314-144	348.5	-14.4	118.4	0.72	59.7
2314+013	348.5	1.3	116.1	0.77	52.9
2314+038	348.5	3.8	262.7	2.47	61.2
2317-223	349.4	-22.3	127.5	0.77	64.7
2317+050	349.5	5.0	143.4	1.07	55.9
2318-166	349.6	-16.6	173.0	1.40	58.6
2319+127	349.9	12.7	67.4	0.56	21.5
2320+080	350.0	8.0	118.6	0.84	49.8
2320-021	350.1	-2.1	90.3	0.50	49.3
2322-234	350.6	-23.4	103.3	0.51	62.0
2322-124	350.7	-12.4	129.2	1.02	45.8
2322-052	350.7	-5.2	116.0	0.80	50.7
2322-040	350.7	-4.0	163.5	1.41	48.4
2324-023	351.1	-2.3	170.7	1.56	43.4
2325-052	351.4	-5.2	97.8	0.53	54.4
2325-254	351.5	-25.4	100.7	0.51	59.0
2325-152	351.5	-15.2	214.4	1.95	55.3
2326-214	351.7	-21.4	149.1	1.06	62.5
2327-196	351.8	-19.6	144.2	0.85	74.7

Table A4.1 - Source listing continued.

IAU Name	X / deg	Y / deg	Ta / mK	Flux / Jy	Base
2328+108	352.0	10.8	118.8	0.98	39.2
2329-162	352.3	-16.2	132.1	0.90	59.0
2329-252	352.4	-25.2	108.4	0.64	56.3
2329-191	352.4	-19.1	108.3	0.55	63.3
2329-102	352.4	-10.2	128.4	1.05	42.6
2329-048	352.4	-4.8	184.6	1.73	43.5
2331-094	352.8	-9.4	103.1	0.85	33.7
2331-240	352.9	-24.0	145.0	1.01	63.0
2331+073	352.9	7.3	106.1	0.87	34.7
2332-018	353.2	-1.8	93.6	0.60	44.4
2334-042	353.5	-4.2	340.9	3.61	46.5
2334+085	353.5	8.5	99.0	0.68	43.4
2334-092	353.6	-9.2	77.9	0.52	35.5
2335-182	353.9	-18.2	123.4	0.85	54.0
2335-028	353.9	-2.8	89.4	0.53	46.3
2335+031	353.9	3.1	126.4	1.07	39.5
2336-045	354.2	-4.5	112.0	0.94	35.2
2337-063	354.3	-6.3	120.2	0.95	42.5
2337+062	354.4	6.2	81.8	0.57	35.1
2338+042	354.6	4.2	110.1	0.77	47.3
2338-166	354.7	-16.6	117.3	0.82	50.1
2338+029	354.7	2.9	81.9	0.56	36.2
2339-002	354.8	-0.2	86.9	0.61	37.3
2340-220	355.2	-22.0	110.6	0.74	49.8
2342-162	355.6	-16.2	83.9	0.54	39.6
2343-077	355.9	-7.7	99.9	0.78	36.3
2344+092	356.0	9.2	195.8	2.01	32.0
2344-192	356.1	-19.2	112.2	0.74	52.0
2345-200	356.3	-20.0	98.0	0.54	54.3
2345-168	356.4	-16.8	231.6	2.28	45.3
2345+061	356.5	6.1	92.5	0.77	30.0
2347+079	356.9	7.9	77.1	0.57	30.6
2347-252	357.0	-25.2	121.7	0.85	52.7
2347-027	357.0	-2.7	124.4	1.16	29.4
2349-014	357.4	-1.4	109.2	0.96	30.8
2350+057	357.5	5.7	75.5	0.59	27.1
2352-155	358.0	-15.5	113.9	0.87	43.2
2352-216	358.1	-21.6	101.1	0.65	48.1
2352+097	358.2	9.7	86.3	0.69	29.9
2353-185	358.4	-18.5	107.2	0.74	46.6
2354-117	358.7	-11.7	172.9	1.70	34.5
2355+042	358.9	4.2	66.6	0.51	24.6
2355-106	359.0	-10.6	90.4	0.70	33.7
2355-088	359.0	-8.8	70.0	0.52	27.7
2358-173	359.6	-17.3	88.6	0.55	44.1
2358+108	359.7	10.8	83.8	0.60	35.2
2359-160	359.8	-16.0	87.7	0.57	41.0
0000-144	0.0	-14.4	93.3	0.66	39.5
0000-149	0.1	-14.9	94.7	0.69	38.5
0000-250	0.2	-25.0	87.3	0.50	46.2
0000-177	0.2	-17.7	174.5	1.61	43.2
0001-234	0.4	-23.4	102.2	0.72	43.2
0001-122	0.4	-12.2	81.5	0.66	27.9
0002+125	0.6	12.5	127.8	1.19	30.7
0003-066	0.9	-6.6	144.2	1.59	14.9
0004-003	1.0	-0.3	228.1	2.61	15.5
0004-239	1.2	-23.9	86.1	0.56	40.4
0006-146	1.5	-14.6	75.0	0.53	31.7

Table A4.1 - Source listing continued.

IAU Name	X / deg	Y / deg	Ta / mK	Flux / Jy	Base
0006-062	1.5	-6.2	82.7	0.72	24.0
0007+125	1.8	12.5	144.2	1.44	27.0
0010+006	2.7	0.6	85.3	0.88	13.7
0011-257	2.9	-25.7	81.5	0.56	35.7
0011-096	2.9	-9.6	80.8	0.71	22.6
0011+055	2.9	5.5	87.5	0.76	25.7
0012-184	3.2	-18.4	94.2	0.78	30.2
0013-198	3.4	-19.8	76.9	0.63	25.6
0013-005	3.4	-0.5	77.3	0.67	22.5
0016-130	4.1	-13.0	128.8	1.20	30.8
0016-107	4.1	-10.7	68.7	0.51	26.8
0018-092	4.5	-9.2	69.0	0.60	19.9
0018-205	4.6	-20.5	90.2	0.70	33.4
0018-195	4.7	-19.5	87.3	0.68	32.2
0018-012	4.7	-1.2	76.3	0.81	9.9
0019-073	4.8	-7.3	59.0	0.51	17.4
0020+000	5.0	0.0	169.4	1.97	9.0
0020-253	5.2	-25.3	164.9	1.60	34.3
0020-082	5.2	-8.2	62.6	0.51	21.0
0023-131	5.9	-13.1	106.3	0.95	29.1
0023+010	5.9	1.0	53.0	0.50	11.9
0024-203	6.0	-20.3	88.0	0.67	33.2
0024-101	6.0	-10.1	59.1	0.59	11.3
0024+126	6.2	12.6	67.7	0.63	16.1
0026-007	6.5	-0.7	77.1	0.84	8.8
0027+080	6.8	8.0	72.0	0.51	30.6
0027-024	6.9	-2.4	51.0	0.53	7.4
0027+056	6.9	5.6	88.3	0.73	28.4
0029-012	7.3	-1.2	69.8	0.70	12.4
0030+062	7.6	6.2	83.7	0.70	26.3
0030-220	7.7	-22.0	72.2	0.59	24.1
0031-213	7.9	-21.3	76.8	0.68	21.1
0031-078	7.9	-7.8	69.0	0.59	21.0
0032+011	8.0	1.1	70.6	0.62	20.0
0032-203	8.1	-20.3	104.8	1.04	20.1
0032+101	8.1	10.1	71.8	0.57	25.2
0033-168	8.3	-16.8	65.8	0.62	15.4
0034-001	8.5	-0.1	60.1	0.56	14.2
0034+078	8.5	7.8	58.0	0.51	16.7
0034-014	8.6	-1.4	233.4	2.70	13.5
0035-253	8.9	-25.3	85.7	0.81	20.0
0035-024	8.9	-2.4	374.3	4.47	9.6
0035+122	8.9	12.2	104.6	1.04	19.4
0036-216	9.1	-21.6	69.8	0.57	22.9
0036-082	9.2	-8.2	69.0	0.58	22.1
0036+031	9.2	3.1	148.5	1.56	21.3
0037+047	9.4	4.7	78.4	0.63	26.9
0038-156	9.6	-15.6	49.5	0.55	4.3
0038+086	9.6	8.6	111.8	1.17	16.0
0038+098	9.6	9.8	277.0	3.18	17.3
0038-020	9.7	-2.0	112.4	1.16	18.2
0040-065	10.0	-6.5	91.0	0.94	14.3
0041-163	10.4	-16.3	78.4	0.87	7.2
0044+060	11.1	6.0	60.8	0.59	12.6
0045-255	11.3	-25.5	365.2	4.35	10.2
0047-030	11.8	-3.0	87.2	0.80	21.6
0047-104	11.9	-10.4	65.0	0.53	21.4
0048-124	12.0	-12.4	105.4	1.11	14.9

Table A4.1 - Source listing continued.

IAU Name	X / deg	Y / deg	Ta / mK	Flux / Jy	Base
0048-098	12.1	-9.8	98.1	0.93	22.2
0048-071	12.2	-7.1	87.7	0.81	21.9
0050-253	12.7	-25.3	58.0	0.58	10.4
0051-038	12.9	-3.8	144.7	1.51	21.2
0054-017	13.7	-1.7	359.6	3.87	43.7
0055-059	13.9	-5.9	76.3	0.64	24.0
0056-243	14.0	-24.3	63.8	0.69	7.3
0056-002	14.1	-0.2	189.0	2.03	23.3
0056-173	14.2	-17.3	91.8	0.91	17.8
0057-181	14.4	-18.1	86.7	0.87	15.8
0057-141	14.4	-14.1	63.8	0.54	20.1
0059-151	14.8	-15.1	95.1	0.97	15.9
0100-118	15.1	-11.8	64.6	0.53	21.8
0101-128	15.4	-12.8	141.7	1.30	35.3
0102-245	15.7	-24.5	54.8	0.52	12.2
0102-072	15.7	-7.2	65.4	0.51	24.0
0106-163	16.5	-16.3	213.0	2.46	12.7
0106-123	16.5	-12.3	79.2	0.74	18.4
0106-009	16.5	-0.9	94.9	0.83	27.2
0106+013	16.5	1.3	420.1	4.85	24.5
0108-079	17.1	-7.9	78.9	0.57	32.7
0108-142	17.2	-14.2	100.2	0.97	21.4
0109+027	17.4	2.7	83.1	0.63	31.4
0111+020	17.8	2.0	85.5	0.69	29.0
0112-017	18.2	-1.7	139.6	1.37	28.2
0113-119	18.4	-11.9	171.4	1.86	19.5
0114-211	18.6	-21.1	219.5	2.47	18.2
0114+075	18.7	7.5	105.9	1.04	20.9
0115-191	19.0	-19.1	87.8	0.94	10.8
0115+027	19.0	2.7	122.7	1.04	38.2
0116+083	19.1	8.3	191.3	2.04	25.0
0116-219	19.2	-21.9	64.3	0.59	16.1
0117-156	19.5	-15.6	291.9	3.26	25.9
0118+035	19.6	3.5	83.3	0.60	34.1
0119+105	19.8	10.5	63.5	0.52	21.4
0119+115	19.8	11.5	93.2	0.86	22.9
0119+041	19.9	4.1	97.8	0.78	34.6
0120-046	20.0	-4.6	108.5	0.93	32.4
0122-255	20.6	-25.5	58.8	0.57	12.6
0122-004	20.7	-0.4	149.9	1.51	26.4
0123-016	20.9	-1.6	368.0	4.17	28.1
0123-226	21.0	-22.6	66.0	0.66	11.9
0123-118	21.0	-11.8	73.2	0.58	25.5
0124+090	21.2	9.0	119.6	1.15	26.0
0125-143	21.3	-14.3	149.8	1.66	14.2
0127+053	21.9	5.3	71.6	0.50	30.6
0128+040	22.2	4.0	142.8	1.31	35.8
0128+061	22.2	6.1	93.2	0.72	34.3
0129-072	22.4	-7.2	125.3	1.20	27.6
0130-172	22.6	-17.2	77.4	0.79	12.7
0131-244	22.9	-24.4	63.0	0.65	9.9
0131-003	23.0	-0.3	101.4	0.87	30.1
0132-098	23.1	-9.8	97.8	0.82	30.6
0132+079	23.2	7.9	153.8	1.46	34.6
0133-204	23.3	-20.4	56.6	0.59	8.9
0134+092	23.7	9.2	80.2	0.61	30.6
0135-248	23.8	-24.8	78.0	0.89	5.3
0137+013	24.3	1.3	107.4	0.95	29.6

Table A4.1 - Source listing continued.

IAU Name	X / deg	Y / deg	Ta / mK	Flux / Jy	Base
0138+074	24.5	7.4	82.9	0.59	35.2
0139-097	24.8	-9.7	102.1	1.02	18.6
0139-167	24.9	-16.7	62.5	0.63	11.5
0139-080	25.0	-8.0	63.8	0.58	16.6
0140-015	25.2	-1.5	81.4	0.64	28.9
0141+020	25.3	2.0	72.3	0.52	29.8
0144-060	26.0	-6.0	108.6	1.05	23.3
0144-023	26.0	-2.3	104.8	0.93	29.3
0146+103	26.5	10.3	69.3	0.54	25.4
0146+057	26.7	5.7	141.7	1.16	47.4
0148-093	27.1	-9.3	58.3	0.60	9.6
0152+033	28.2	3.3	123.3	1.08	35.3
0153-053	28.4	-5.3	56.1	0.52	13.4
0153+053	28.4	5.3	93.3	0.78	30.0
0155-110	28.8	-11.0	126.0	1.56	-1.4
0155-212	28.9	-21.2	49.5	0.69	-7.0
0156-145	29.1	-14.5	95.4	1.17	-0.3
0159-118	29.9	-11.8	159.4	1.87	6.7
0200-256	30.1	-25.6	126.2	1.59	-3.4
0201+113	30.3	11.3	139.8	1.07	52.5
0201+088	30.5	8.8	141.4	1.23	40.8
0202-173	30.6	-17.3	79.4	1.01	-2.6
0202-195	30.7	-19.5	27.2	0.50	-13.8
0202-183	30.7	-18.3	58.3	0.68	2.5
0203-054	30.9	-5.4	62.0	0.57	15.5
0203-224	31.0	-22.4	40.8	0.56	-4.7
0204+067	31.1	6.7	139.4	1.36	28.1
0205-011	31.5	-1.1	72.3	0.57	25.9
0206-102	31.7	-10.2	54.0	0.53	10.6
0206+127	31.7	12.7	77.4	0.64	25.2
0207-079	31.8	-7.9	48.7	0.55	4.1
0207-018	31.8	-1.8	71.2	0.56	25.1
0207+096	31.8	9.6	98.2	0.71	40.1
0208-224	32.0	-22.4	73.3	1.00	-8.2
0208-194	32.0	-19.4	37.9	0.54	-6.0
0208-112	32.0	-11.2	88.0	0.97	9.2
0208+041	32.0	4.1	93.8	0.72	34.8
0208-069	32.1	-6.9	76.4	0.88	4.9
0208+106	32.2	10.6	83.8	0.51	42.1
0209-241	32.3	-24.1	44.8	0.57	-1.6
0209-102	32.3	-10.2	60.1	0.61	10.2
0210-076	32.7	-7.6	47.7	0.53	4.6
0213-132	33.3	-13.2	292.7	3.68	-7.7
0213-026	33.3	-2.6	76.2	0.60	27.3
0214+109	33.6	10.9	114.5	0.99	33.6
0215+015	33.8	1.5	89.1	0.63	37.8
0215-168	33.9	-16.8	46.2	0.64	-5.8
0216-250	34.1	-25.0	55.7	0.79	-8.9
0217+111	34.5	11.1	131.4	1.13	39.6
0218-133	34.6	-13.3	39.6	0.53	-3.4
0218-022	34.6	-2.2	187.0	2.02	22.3
0219+127	34.8	12.7	75.0	0.59	27.0
0219+082	34.9	8.2	154.6	1.38	42.1
0221+067	35.5	6.7	110.3	0.90	36.7
0222-234	35.7	-23.4	78.0	1.08	-10.0
0222-008	35.7	-0.8	78.1	0.75	17.1
0223+013	35.9	1.3	73.5	0.64	21.6
0223+095	35.9	9.5	84.6	0.66	30.8

Table A4.1 - Source listing continued.

IAU Name	X / deg	Y / deg	Ta / mK	Flux / Jy	Base
0224-175	36.2	-17.5	61.6	0.88	-9.9
0225-241	36.3	-24.1	37.6	0.60	-11.5
0226-247	36.6	-24.7	29.1	0.52	-13.5

Number of sources = 1105

Appendix Five - Telescope Parameters

Contained in this appendix is a listing of all the essential parameters of the telescope and other apparatus used to collect the data for the Skymap survey. A majority of these parameters were calculated in the first section of Chapter Four, while a few were calculated in Chapter Two and Appendix Three. While this listing does not offer a complete description of the telescope, it is adequate for the purposes of the Skymap survey in general and this thesis in particular. it is important to note that many of the parameters listed below are approximate - the number of significant figures quoted gives a fair indication of the accuracy of the values.

Site of the observations	Hartebeesthoek RAO
Type of antenna	Parabolic, Cassegrain reflector
Type of mounting	Equatorial
Diameter of antenna	26m
Physical aperture of antenna (A_p)	$531m^2$
Operating frequency (ν) [1]	2.3 GHz
Half-power beam width (θ_{HP})	20′
Pointing accuracy	Better than 1′
Type of receiver	GaAsFET
System noise temperature (T_{sys})	41.1K
System bandwidth (B)	38.5 MHz
Noise diode temperature (T_n)	71K
Minimum detectable temperature (dT_e)	14.8 mK
Method of observation	Raster scanning method
Main-beam solid angle (Ω_M)	5.0×10^{-5} ster
Effective aperture (A_e)	$250m^2$
Loss factor (R)	1.51
Full beam solid angle (Ω_A)	10.2×10^{-5} ster
Beam efficiency (ε_M)	49.0%

Aperture efficiency (ε_A)	47.0%
Calibration factor (C)	12.26 JyK^{-1}
Resolution of the final map	22.8′
Rms noise level of final map [2]	10.8 mK

1 This is the frequency applicable to the Skymap observations.

2 The rms noise level of the final map was found by calculating the standard deviation of 3000 data points located in a region of cold sky.